The Dissertation Committee for Stephanie P. Vega Certifies that this is the approved version of the following dissertation:

Development and Utilization of a Bioengineered 3D Human Lung Model to Study Pathogenesis of Lung Disease

Committee:

Joan E. Nichols, Ph.D.,
Chair and Mentor

Joaquin Cortiella, M.D.

Tonyia Eaves-Pyles, Ph.D.

Rick Pyles, Ph.D.

Jason Sakamoto, Ph.D.

Dean, Graduate School

Development and Utilization of a Bioengineered 3D Human Lung Model to Study Pathogenesis of Lung Disease

By

Stephanie Priscilla Vega, B.S.

Dissertation

Presented to the Faculty of the Graduate School of

The University of Texas Medical Branch

in Partial Fulfillment

of the Requirements

for the Degree of

Doctor of Philosophy

The University of Texas Medical Branch

August, 2018

Development and Utilization of a Bioengineered 3D Human Lung Model to Study Pathogenesis of Lung Disease

Publication No._____

Stephanie Priscilla Vega

The University of Texas Medical Branch, 2018

Supervisor: Joan E. Nichols

There is a great need for research models that mimic human lung physiology and lung pathologies such as chronic lung diseases and respiratory infections. The morbidity and mortality associated with lung disease and respiratory infections represent a global burden. Pathogenesis of these diseases and infections remains elusive. Lack of experimental models that recreate important aspects of human disease has been a major obstacle in the progress of scientific advancements. Tissue-engineering technologies provide a new approach for development of novel 3D *in vitro* models that can mimic human disease. Production of tissue-engineered 3D human respiratory tract models requires the selection of an appropriate (1) size scale for the model, (2) cell source and cell types (3) scaffold that provides structural support (4) culture support platform and (5) methods for validation and assessment of the model.

We have developed a decellularization procedure for native human lungs to produce whole human acellular (AC) lung scaffolds that contain the desired anatomical

structures and morphological structures that provide a 3D configuration and biological cues that facilitate production of tissue-engineered lung tissue. We demonstrate that whole AC pediatric lung scaffolds and cells isolated from discarded human lungs can be used to bioengineer whole-organ constructs with functional characteristics similar to native human lungs. Small-scale human lung constructs can also be developed and used as models for repetitive standardized testing. The 3D bioengineered human lung construct we developed is composed of human AC lung scaffold and primary or immortalized human lung cells isolated from donor lung tissue. We provide data to support the ability of this 3D engineered human lung construct to be used as an *in vitro* model to examine early pathological changes associated with acute lung injury and initiation of pulmonary fibrosis (PF). After exposure to the PF-inducing agent bleomycin, only constructs containing macrophages exhibited excessive collagen deposition and developed PF. Bleomycin exposure resulted in production of pro-inflammatory cytokines IFN-γ, TNF, IL-1β, and IL-6. MMP-7 expression was found in alveolar epithelial cells post-bleomycin exposure. M2 macrophages expressing tissue inhibitor of matrix metalloproteinases-1 (TIMP-1) were consistently present in areas with excessive collagen deposition that resembled fibrotic foci.

TABLE OF CONTENTS

List of Tables

List of Figures

List of Abbreviations

AC	Acellular
ALI	Acute Lung Injury
AEC	Alveolar Epithelial Cells
ACE	Angiotensin Converting Enzyme
AQP5	Aquaporin 5
BMMSC	Bone Marrow-Derived Mesenchymal Stem Cells
BAL	Bronchoalveolar Lavage
CFSE	Carboxyfluorescein Succinimidyl Ester
CHAPS	(3-((3-cholamidopropyl) dimethylammonio)-1-propanesulfonate)
COPD	Chronic Obstructive Pulmonary Disease
CT	Computed Tomography
EGM	Endothelial Growth Medium
eNOS	Endothelium Nitric Oxide Synthase
EHS	Engelbreth-Holm-Swarm
ERG1	Early Growth Response Protein 1
ECM	Extracellular Matrix
FSP-1	Fibroblast Specific Protein-1
HRCT	High Resolution Computed Tomography
hESC	Human Embryonic Stem Cells
HFLC	Human Fetal Lung Cells
HLA	Human Leukocyte Antigen
HoC	Human Organ Construct
HUV-EC-C	Human Umbilical Vein Endothelial Cells
HAG	Hydroxyethyl methacrylate-Alginate-Gelatin
IPF	Idiopathic Pulmonary Fibrosis
iHLC	Immortalized Human Lung Cells
I-lung	Immortalized Lung Cells
iPSC	Induced Pluripotent Stem Cells
IACUC	Institutional Animal Care and Use Committee
IRB	Institutional Review Board
LYVE-1	Lymphatic Vessel Endothelial Receptor-1
MHC	Major Histocompatability Complex
MMP	Matrix Metalloproteinases
MHRI	Methodist Hospital Research Institute
μ-human	Micro-human
ml-human	Milli-human
MNL	Mononuclear Lymphocytes
MPM	Multi-Photon Microscopy
mESC	Murine Embryonic Stem Cells
PL	Pediatric Lungs
PBS	Phosphate-Buffered Saline
PECAM	Platelet Endothelial Cell Adhesion Molecule

PRP	Platelet-rich Plasma
PF-127	Poloxamer PF-127
PGA	Polyglycolic Acid
PLGA	Poly-lactic-co-glycolic Acid
PET-CT	Positron Emission Tomography–Computed Tomography
PHAEC	Primary Human Alveolar Epithelial Cells
pHLC	Primary Human Lung Cells
P-lung	Primary Lung Cells
PL-VASC	Primary Lung Vascular Cells
Pro-SPC	Pro-Surfactant Protein C
PF	Pulmonary Fibrosis
PFT	Pulmonary Function Test
ROI	Region of interest
SHG	Second Harmonic Generation
SL	Single Lungs
SAGM	Small Airway Growth Medium
α-SMA	α-Smooth Muscle Actin
SDS	Sodium Dodecyl Sulfate
SLPC	Somatic Lung Progenitor Cells
SP-A	Surfactant Protein-A
SP-C	Surfactant Protein-C
SP-D	Surfactant Protein-D
TIMP	Tissue Inhibitors of Metalloproteinases
3D	Three-Dimensional
TTF-1	Transcription Termination Factor-1
TGF-β	Transforming Growth Factor-β
TEM	Transmission Electron Microscopy
2D	Two-Dimensional
UTMB	University of Texas Medical Branch
UIP	Usual Interstitial Pneumonia
VE-cadherin	Vascular Endothelial Cadherin
VEGF	Vascular Endothelial Growth Factor

CHAPTER 1*

The Need for Better Research Models: Development of 3D Respiratory Tract Models for Research Use

INTRODUCTION

Our understanding of the underlying mechanisms of human developmental, physiological and pathological processes is heavily dependent on experimental models designed to mimic these processes. The most commonly used experimental models for biomedical research are static two-dimensional (2D) *in vitro* cell culture systems and animal models. The use of 2D cell culture has been fundamental for examinations of basic cell functions, examination of cell-specific products and basic cellular interactions. The usefulness of 2D cell culture is limited by the fact that these static cultures do not accurately reflect the cell-cell and cell-matrix interactions that happen at the tissue-interface *in vivo*. For example, cell gene expression profiles have been shown to change when cells are cultured in a 2D environment vs. a three-dimensional (3D) environment [1]. Animal models are essential for research use but they often fail to provide data that can be directly translated to humans for clinical use. It is estimated that 90% of newly developed drugs fail to show efficacy in clinical trials despite being effective in animal models [2]. Recent advances in tissue-engineering technologies have provided a new approach for the

Chapter* published and taken from:
Nichols, J.E., Niles, J.A., Vega, S.P., Argueta, L.B., Eastaway, A. and Cortiella, J., 2014. Modeling the lung: Design and development of tissue engineered macro-and micro-physiologic lung models for research use. *Experimental biology and medicine*, *239*(9), pp.1135-1169.

development of novel 3D *in vitro* models that can mimic the physiological conditions within the *in vivo* environment. These models can be bioengineered to resemble the morphological structures of a tissue or organ, perform key functional characteristics and recreate specific human responses in a normal physiologic or pathologic setting.

Of critical importance is the need for better research models of human lung physiology and lung pathologies such as chronic lung diseases and respiratory infections. Although extensive research on the normal physiological processes of the human lungs has been done, we are just beginning to understand how wound healing and tissue repair are orchestrated to maintain tissue integrity during normal lung homeostasis. Much less is known about how the disruption of these highly regulated processes can lead to disease. A wide range of progressive lung diseases exist that interfere with normal lung function , have no cure and can ultimately lead to death from respiratory failure. One of the most common is chronic obstructive lung disease which is the third leading cause of death in the United States [3]. The others are restrictive interstitial lung diseases (ILD) which represent a large group of over 200 disorders characterized by lung inflammation or fibrotic lung scarring [4]. The most common type of ILD is pulmonary fibrois (PF), a debilitating disease with a poor prognosis. The damaging effects of respiratory infections are also a concerning matter because globally, more than 4 million deaths per year are attributed to respiratory infections [5, 6]. Viral respiratory infections such as the ones caused by influenza viruses, can spread rapidly through human populations and result in epidemics. The morbidity and mortality associated with lung disease and respiratory infections represent a global burden. The pathogenesis of many of these diseases and infections remains elusive and much more work is needed to better understand the mechanisms that

drive these pathologies. The lack of experimental models that can recreate important aspects of human disease has been a major obstacle in the progress of scientific advancements. Development of 3D *in-vitro* human respiratory tract models would greatly improve our opportunities for advancements toward effective strategies to diagnose, treat, prevent or cure these diseases.

PARAMETERS TO CONSIDER FOR THE DEVELOPMENT OF 3D RESPIRATORY TRACT MODELS FOR RESEARCH USE

It is important to consider the unique anatomical structures and physiological functions of the human respiratory tract when designing 3D tissue mimics so that we can create *in vitro* models that help to increase our understanding of chronic lung diseases and respiratory infections or help us to identify new targets for drug development. In order to reconstruct key functional characteristics of a tissue or organ, certain parameters must be considered. Production of tissue-engineered 3D human respiratory tract models requires the selection of an appropriate (1) size scale for the model, (2) cell source and cell types (3) scaffold that provides structural and anatomical support (4) culture support platform and (5) methods for validation and assessment of the model. The design of the model must reflect the cell phenotypes, morphological structures and functional properties of the region of the respiratory tract the model is mimicking. In the following sections we will discuss these parameters in detail.

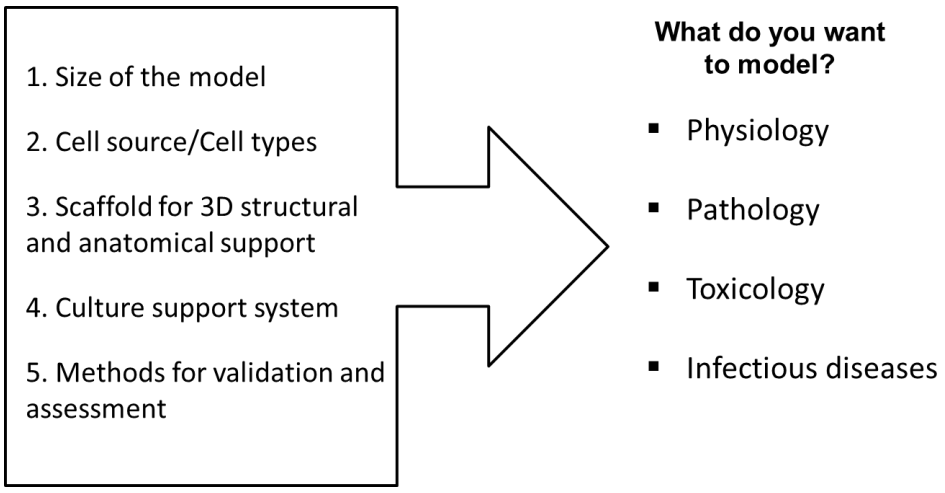

Figure 1.1 Parameters to consider for model development. The design of the model will be dependent on the type of studies the model will be used for, whether physiological, pathological, toxicological or infectious disease studies.

Size of the Model

When designing respiratory tract models, the size of the system is important to consider. The size of a model system is dependent on a variety of factors, such as the numbers of cells, cellular homogeneity or heterogeneity, the presence or absence of tissue-like morphological structures and the type of culture support platform used. The size of model systems can greatly vary and exact specifications of the size can sometimes be difficult to estimate due to various components incorporated in the design. Terms such as micro-human (µ-human), milli-human (ml-human) or larger-scale human organ constructs (HoC) can be used to describe the general overall size of each system [7]. Human organs-on-chips are considered µ-human models and are usually characterized by having less than 1 million cells and usually one or two cell types. Microfluidic platforms are used for culture of µ-human models. The small volumes of reagents needed for µ-human models and their cost-effective production make them good options for use as standardized testing platforms for high-throughput experiments. One disadvantage is that the size of µ-human models can

limit their ability to model complex diseases. Ml-human models often contain 1- 5 million cells while HoC are characterized as more complex model systems that can contain several million cells [8]. Platforms for culture support of ml-human models include tissue culture plates or transwell plates. HoC can be cultured in tissue culture plates, small rotary bioreactors or whole organ perfusion bioreactors. Ml-human and HoC models can be bioengineered with several different cell types and can therefore be used to as physiological, pathological or infectious disease models.

Allometric scaling of organs has been used to approximate a suitable size for model systems but this approach does not always provide valid parameters since the scaling of a model system must be compared to the scaling of organs as a function of human body mass [7]. For example, if the size of the model system is entirely based on allometric scaling, the diameters of the human trachea, bronchi, bronchioles or alveoli must be taken into consideration in order for the model to approximate a scaled fraction of these lung regions [7]. Allometric scaling suggests that in a µ-human lung model, the estimated alveolar diameter should be 21 µm, which is an order of magnitude less than the average estimated diameter of 200 µm in a human alveolus [7]. The problem with this is that a diameter of 21 µm would further limit the number of cells used in a µ-human alveolus model. Because the average diameter of a type I alveolar epithelial cell is estimated to be 20 µm, this would only allow space for a single cell within a reconstructed µ-human alveolus-like structure [7].

Functional scaling is a more reasonable approach for determining the size of model system because critical functional parameters for a specific organ can be identified and implemented in the design [7]. Unfortunately, appropriate scaling of model systems can be

a challenge because the physical dimensions, cellular composition and structural organization must support the overall functional performance of the model. The relative size of the model system will depend on the physiological responses or pathological conditions that are to be modeled and if these responses or conditions will be recreated in a simplified or complex system in order to mimic a particular function(s).

Cell Sources and Cell Types

The human respiratory tract is a complex organ that contains about 40 different cell types distributed throughout each of its specialized regions [9]. For development of a respiratory tract model, the cell types used are extremely important to ensure functionality of the model. Selection of cell types for development of respiratory tract models is dependent on the specific region of the respiratory tract the model represents and on the type of model being developed (physiological, pathological, toxicological, or infectious disease models). Many different cell types have been used for the development of respiratory tract models. **Table 1.1** lists some of the main human cell types that have been used for development of respiratory tract models along with advantages and disadvantages of each. Human physiologic respiratory tract models require the presence of cell types that are involved in normal physiological functions within the specialized regions of the lungs. If respiratory tract models are developed for pathological studies, published data from patient case-studies should be taken into consideration to help identify key cell types that may need to be used in order to recreate a similar scenario *in vitro*. Human infectious disease models of the respiratory tract must contain cell types that are permissive to bacterial or viral pathogens and support the replication of these pathogens. Often,

heterogeneous cell populations are needed to recreate human responses in normal physiological or pathological settings.

Primary cells isolated directly from their tissue of origin, accurately represent physiological *in vivo* conditions and are considered the "gold standard" to which all other cells types are compared [8]. The genotypic and phenotypic profiles of primary cells are a reflection of their characteristics and specialized functions within native tissues, thus making them good predictors of cellular responses that are physiologically relevant. Human primary cells are often used by pharmaceutical companies during the early pre-clinical drug discovery process in order to generate data that is clinically relevant and representative of a particular human population [10]. Some 3D respiratory tract models have been developed using only human primary cells isolated from donor tissues [11, 12, 13], while others have been developed using mixtures of human primary cells and transformed cell lines [14, 15, 16]. Even though the use of primary cells can offer many advantages, issues related to their acquisition and handling can limit their use. Some of the main issues associated with use of primary cells include difficulties in procuring human tissues, problems with transport or delays in acquisition of human tissues that directly affect cell viability, difficulties in the isolation of cells and their limited lifespan.

Transformed cell lines are widely used for 2D cell cultures and some have been used for production of 3D respiratory tract models [8]. The popularity of transformed cell lines arises from their ease of use and their ability to divide indefinitely which can provide misleading results due to their cancerous origin. Chromosomal abnormalities and undefined mutations in transformed cell lines severely alter their genotypic and phenotypic profiles making them unreliable for use in studies of normal cellular responses. As a result,

transformed cell lines should not be used for the development of respiratory tract models designed to mimic normal lung physiological conditions. Some studies have used transformed cell lines derived from cancerous lung tissue (e.g. A549) for development of tissue-engineered 3D lung cancer models. Resistance to ionizing radiation [17] and the association of gene expression profiles in cancer prognosis [18] have been examined in 3D lung cancer models developed using the A549 cell line. Although the use of transformed cell lines may seem applicable for use in 3D lung cancer models, a better option would be to use primary cells isolated directly from patients' tumors.

In contrast to transformed cell lines, immortalized cells are modified to have an extended replicative capacity but without yet having other cancerous characteristics. Immortalization of primary cells may be an option to circumvent replicative senescence that limits the use of primary cells for use in long-term cultures for extended experiments. Ideally, immortalization of primary cells can give rise to immortalized cell populations that may still maintain the genotypic and phenotypic profile of the native tissue. Methods for immortalization of cells include viral transduction by using lentiviral, adenoviral or retroviral vectors to inactivate tumor suppressive genes or to induce expression of telomerase reverse transcriptase protein in order to prevent replicative senescence.

Although the renewable capacity and differentiation ability of stem cells makes them an attractive option for use in the development of respiratory tract models, our understanding of how these cells can be induced to become specialized cells *in vitro* is still limited. Human embryonic stem cells (hESC) [19] and human induced pluripotent stem cells (iPSC) [20, 21] have been used to generate lung epithelial cells in 2D *in vitro* cell cultures. One study has reported the generation of alveolar-like 3D structures produced

from differentiation of hESC into surfactant-secreting cells [22]. Currently there are no reports of the use of iPSC in the production of lung tissue or for the production of 3D respiratory tract models. The capacity of murine embryonic stem cells (mESC) to generate bronchial or alveolar epithelium has been demonstrated by our laboratory [23] and another research group [24].

Scaffolds

Development of 3D respiratory tract models, requires the selection of an appropriate scaffold that can mimic key structural characteristics of the native tissue-specific extracellular matrix (ECM). The scaffold selected must also be biocompatible and support cell attachment, cell viability, cell growth, and tissue formation. Aside from providing structural support, the native tissue-specific ECM is a biologically active matrix that directly influences cellular responses. For this reason it is important to remember that the type of scaffold used for development of respiratory tract models may have different effects on cellular behavior. For development of 3D respiratory tract models, scaffolds must possess the strength, elasticity and structural architecture similar to that of native lungs. It is also important to remember that within the different regions of the respiratory tract such as the trachea, bronchial airways or alveoli, the architectural structure and protein composition of the ECM can vary.

Many natural and synthetic hydrogels such as Matrigel, type I collagen gel, Poloxamer F-127 (PF-127), polyglycolic acid (PGA), poly-lactic-co-glycolic acid (PLGA) and hydroxyethyl methacrylate-alginate-gelatin (HAG) have been used as scaffolds in the production of respiratory tract models. The composition, cross-link configurations, permeabilities, degradability and mechanical capabilities of hydrogels can vary. Some of

these characteristics are used to classify hydrogels into two major categories: reversible/physical hydrogels or permanent/chemical hydrogels [25]. Hydrogels in the reversible/physical category are cross-linked by ionic bonds, hydrogen bonds or hydrophobic interactions which gives them the ability to change from solutions to gels depending on the physical conditions they are exposed to. Hydrogels in the permanent/chemical category are cross-linked by covalent bonds, making their junctions permanent [25, 26]. Native lung-derived acellular (AC) matrices from a variety of animal species have also been used as scaffolds for development of respiratory tract models. **Table 1.2** lists many of the currently available respiratory tract models and the type of scaffolds used in production of each model. In the following sections, we describe the characteristics of some of these hydrogels and AC matrices and discuss how they have been used as scaffolds for development of respiratory tract models.

MATRIGEL

Matrigel is a solubilized basement membrane preparation extracted from Engelbreth-Holm-Swarm (EHS) mouse sarcoma tumors. The major ECM protein components of Matrigel include laminin, collagen IV, and entactin. Some Matrigel preparations may contain growth factors such as transforming growth factor-β (TGF-β) epidermal growth factor, insulin-like growth factor, platelet-derived growth factor and fibroblast growth factor which are naturally found in EHS tumors [27]. When using Matrigel as a scaffold it is important to read specifications provided by the manufacturer to be aware of the exact composition because the presence of these growth factors or even other undefined components will influence cellular behavior. Matrigel has been used as a scaffold to produce alveolar-like structures *in vitro* [28, 29]. In these studies, culture of

undifferentiated fetal rabbit lung cells on a thick coating of Matrigel, initiated differentiation of cells into cuboidal cells containing lamellar bodies that polarized with their apical surfaces, some containing microvilli, facing a central opening that resembled a lumen [28, 29]. A mixture of Matrigel, type I collagen and alginate-poly-l-lysine-alginate (APA) microcapsules has also been used to develop an alveolus – like structure *in vitro* [30]. Culture of feta pulmonary cells from mice on this scaffold mixture, resulted in the differentiation of cells that contained lamellar bodies and expressed surfactant protein-C (SP-C) [30].

GELFOAM

Gelfoam is a compressed pliable surgical sponge produced from purified porcine skin gelatin. Gelfoam is commonly used for would care, as it is considered to have hemostatic properties. The porous structure of Gelfoam has also made it an option for use as a scaffold in development of distal lung models. Gelfoam was used as a scaffold for fetal lung cells to examine fetal lung differentiation and developmental lung growth in some studies [31, 32, 33]. Gelfoam has also been used to examine lung regeneration. One study used Gelfoam as a scaffold for culture of fetal rat lung cells to examine the potential of cell-scaffold techniques for *in vivo* lung regeneration in adult rats [34]. Gelfoam that was seeded with fetal rat lung cells and implanted into adult rat lungs formed alveolar-like structures [34]. This study also claimed that the shape and pore size of Gelfoam is similar to that of alveolar structures in adult rat lungs.

POLOXAMER PF-127

PF-127 is a non-ionic diblock copolymer composed of polyoxyethylene and polyoxypropylene. The trade name for PF-127 hydrogels is Pluronic®. PF-127 is an aqueous solution that can undergo thermoreversible gelation at temperatures > 15˚C. PF-127 has been widely used for a variety of studies because of its reverse thermal gelation, high drug loading capabilities, cell encapsulating capabilities and ability to gel in physiological conditions at relatively low concentrations [35, 36]. PF-127 hydrogel is often used as a vehicle to facilitate cell transport, cell attachment and cell aggregation for tissue-engineering [25]. PF-127 has been used as a scaffold for culture of ovine somatic lung progenitor cells (SLPC) in *in vitro* cultures for *in vivo* implantation. Both *in vitro* and *in vivo* cultures of ovine SLPC with PF-127 demonstrated that cells had differentiated and expressed Clara cell 10 protein, a marker of Clara cells and SP-C a marker for type II AEC and the resulting morphological structures looked similar to bronchial and alveolar epithelium [37].

POLYGLYCOLIC ACID

Polyglycolic acid is a synthetic biodegradable polymer composed of glycolic acid. PGA is degraded by non-enzymatic hydrolysis and the degradation products are not toxic [38, 39]. PGA fibers can be woven together to create a PGA mesh that can be used as a scaffold. Several studies have used PGA mesh scaffolds for development of lung models. A study from our laboratory used PGA mesh as a scaffold to culture SLPC and examine cell differentiation and development of lung tissue both *in vitro* and *in vivo* [37]. *In vitro* and *in vivo* culture of SPLC on PGA mesh scaffolds resulted in differentiation of cells expressing Clara cell protein 10, cytokeratin and SP-C. The morphological structure of the

engineered tissue resembled that of terminal bronchi and alveoli [37]. However, results from the *in vivo* experiments showed that implantation of engineered tissue produced from PGA mesh and SPLC induced a foreign body response in a sheep model [37]. In *in vivo* experiments, engineered lung tissue produced from PF-127 and SPLC, had less of an inflammatory response when compared to lung tissue produced from PGA mesh [37].

ACELLULAR (AC) LUNG SCAFFOLDS

Native lung-derived AC lung scaffolds are produced by decellularization procedures that remove all cells and nucleic material from the native tissue leaving only the ECM. Decellularization can alter the composition of the ECM by causing degradation of some of the structural proteins ultimately affecting the physical characteristics of the ECM. Different reagents can be used for decellularization, some of these include chemical agents (acids and bases), hypotonic and hypertonic solutions, detergents or alcohols along with enzymatic or physical processes [40]. An effective decellularization procedure would be one that removes all cellular material while retaining key structural components of the ECM. A variety of decellularization reagents and procedures have been used to produce AC scaffolds of different tissues or organs but none of these were specifically developed for lung decellularization. One of the first studies to describe the production of fragments of AC human lung scaffold for the development of a 3D lung model to examine the influence of the lung ECM on cell attachment and morphology was done by Lwebuga-Mukasa and colleagues in 1986 [41]. When rat type II AEC were seeded on these AC human lung scaffold fragments they attached and their morphological characteristics changed, as they lost lamellar bodies and appeared to undergo cytoplasmic flattening [41]. Since then, there was no progress in the development of AC lung scaffolds until 2010 when

several studies reported the production of whole AC lung scaffolds produced from mice [42] or rat lungs [23, 43, 44]. Production of these whole AC lung scaffolds from mice or rat lungs helped to gain insight about which decellularization reagents and processes would be applicable for use in lung tissue. There are only a few lung decellularization procedures available but these have only been validated for the production of mice or rat whole AC lung scaffolds with the exception of an earlier method for production of small fragments of AC human lung scaffolds [41]. Most of these decellularization procedures utilize detergents but each procedure differs in the type of detergent used, the length of time it takes for decellularization and the composition of the remaining ECM **[**23, 42, 43, 44]. Examinations of the rat AC whole lung scaffolds revealed that the hierarchical lung architecture was preserved [23, 43, 44]. The ability of these AC lung scaffolds to support cell attachment has been examined *in vitro*. Studies from our laboratory have shown that rat whole AC lung scaffolds were able to support and retain attachment of mESC and also guide site-specific differentiation of mESC into lung-specific lineages including type II AEC and Clara cells [23]. Rat AC whole lung scaffolds have been shown to support attachment of neonatal rat lung epithelial cells and microvascular lung endothelial cells [44], A549 cells, rat fetal lung cells and HUVEC [43]. Although these mice or rat AC lung scaffolds were all shown to support the attachment of cells, recellularization was not complete and some areas were not repopulated with cells. AC lung scaffolds have been produced from Rhesus monkey lungs and were shown to support differentiation of hESC into surfactant-secreting cells [22].

The benefit of using AC lung scaffolds lies in the tissue–specific ECM that they are composed of, which possesses all the characteristics required to support and promote *in*

vitro lung tissue development. The natural lung ECM is a dynamic structure that constantly undergoes regulated remodeling in order to maintain the structural and functional integrity of lung tissue. The composition of the native ECM consists of fibrous proteins and proteoglycans that are highly conserved throughout multiple species [45]. The main protein components include collagens, elastins, fibronectin, laminin and glycosaminoglycans [45, 46]. The ECM provides biomolecular and biomechanical cues that facilitate communication between adjacent cells, modulate mechanical changes in response to the microenvironment, and contribute to the maintenance of optimal organ function by influencing cellular responses [45, 47]. Studies done by atomic force microscopy have shown that local differences in the strength and elasticity of the ECM dictate its ability to influence and regulate the spatial distribution, function and differentiation of cells [48]. In contrast to other natural or synthetic scaffolding materials, natural lung-derived AC lung scaffolds already contain the desired anatomical structures and morphological structures that provide an adequate 3D configuration and biological cues that facilitate production of tissue-engineered lung tissue [45, 47].

Culture Support Platforms

Most of the currently available respiratory tract models **(Table 1.2)** have been cultured on simple culture support platforms such as 6-, 12- or 24-well tissue culture plates **(Figure 1.2 A)** with **(Figure 1.2 B)** and without transwell inserts or on slide chambers **(Figure 1.2 C)**. These simple platforms are cost-effective, are already sterilized and allow for simultaneous replicate cultures making their ease of use an attractive option for use in a wide range of experiments. Tissue culture plates and slide chambers are suitable for ml-human respiratory tract models. The use of transwell inserts allows for submerged cultures

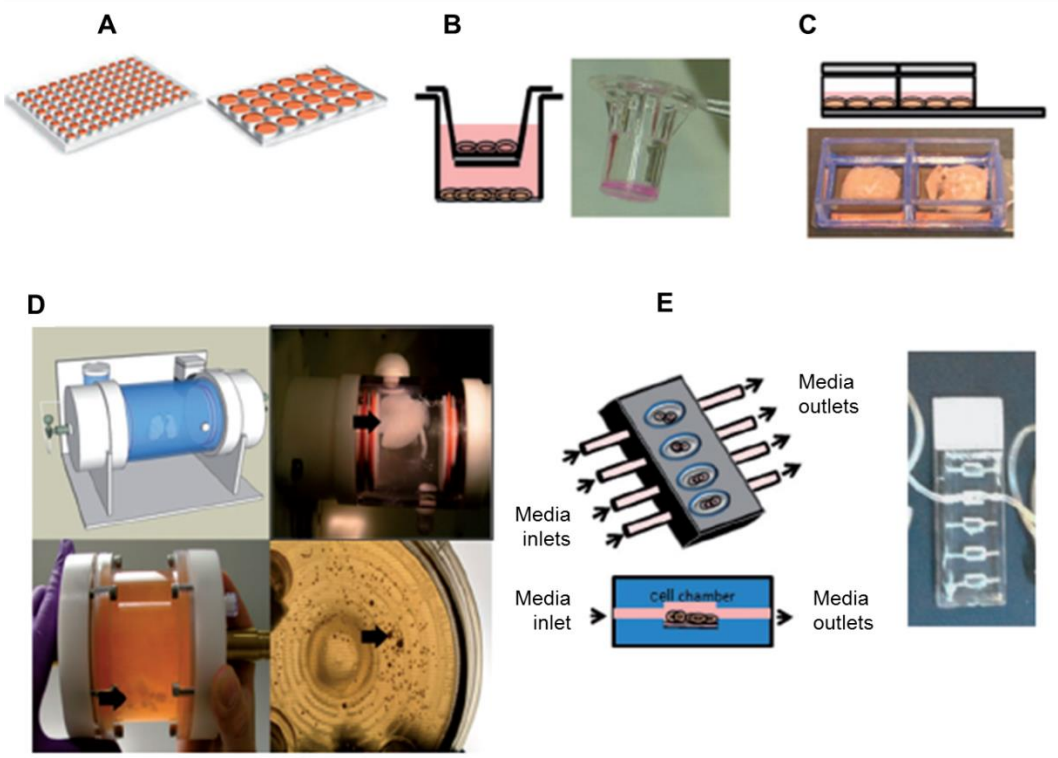

or air-liquid interface cultures of respiratory tract models. Transwell inserts can be coated with different types of collagen, fibronectin or Matrigel to provide an ECM-like structure to support the examination of cell adhesion, cell migration, cell invasion, cell transport across a membrane or for permeability studies. Medium replenishment and removal of metabolic wastes must be done manually in most of these simple culture platforms. Manual maintenance of multiple cultures can be time consuming and also increases the risk of contamination.

Figure 1.2 Platforms used in the development of 3D lung tissue models. (A) 12 -, 24 -, 96-well format plates. **(B)** Transwell type culture platform. **(C)** Slide chamber platform for support of imaging of 3D lung tissue. **(D)** Rotary bioreactor for culture of 3D lung constructs. Black arrow points to either whole lung culture (top right) or aggregate cultures of alveolar type I and II epithelial cells (bottom right). **(E)** Diagram of a basic microfluidic system with media inlet and outlet ports Reproduced with permission from Nichols *et al.* 2014.

Complex platforms such as perfusion bioreactor systems are designed to provide fluidic support during culture and are used for a variety of biotechnological applications.

Bioreactors can range in size and configuration. Bioreactor chambers can hold volumes between 1-500 ml of culture medium, supporting small-scale through large-scale culture systems. Bioreactors are used for culture of HoC. The use of bioreactors as culture platforms in the bioengineering of lung tissue and development of respiratory tract models **(Figure 1.1 D)** offers many advantages when compared to the simple culture platforms such as tissue culture plates that are static. Bioreactors allow (1) precise control of material transfer rates (2) regulation of shear stress within the culture vessel (3) maintenance of constant pH, gas partial pressures (pO_2, pCO_2) and nutrient levels (4) control and adjustment strategies that meet the changing needs of tissue constructs during longer culture periods [8].

Recently developed micro-fluidic based culture platforms have been designed to meet the needs for miniaturization, automation, integration and parallelization of model systems [49]. The use of micro-fluidic platforms allows for single-cell analysis [50], cell-cell evaluations at a micro-scale [51], or high-throughput *in-vitro* diagnostic studies or drug screening for biotechnology market segments [49]. Microfluidic platforms can be categorized by the type of liquid propulsion principle they utilize, which includes, pressure driven, capillary, centrifugal, electrokinetic, or acoustic [49]. Micro-fluidic platforms are produced using different microfabrication techniques such as photolithography [52, 53, 54], microprinting [52], and replica molding [42, 53]. Many configurations of micro-fluidic platforms can be tailored to contain multiple fluidic channels or inner chambers for cell culture. **Figure 1.1 E** shows an example of a multiple chamber platform produced from polydimethylsiloxane (PDMS). PDMS is one of the most common materials used for microfabrication of platforms because it is inexpensive, easy to mold, its transparency

facilitates visual and microscopic observations of the inner chambers and it is highly permeable to gases [54, 55]. Precision of micro-scale volume flow streams, the flexibility of programming automated handling and maintenance protocols and ability to design multiple integrated microfluidic platforms are all reasons why these platforms are attractive options for use in high –throughput studies. Many of the currently available µ-human respiratory tract models that have been developed with microfluidic platforms, are designed to mimic the alveolar-capillary interface [56, 57, 58, 59].

Although most µ-human respiratory tract models that use microfluidic platforms are considered 3D, cells are usually cultured as monolayers within the micro-channels or chambers of the platforms. To provide an ECM-like three dimensionality, micro-channels can be coated with collagen gels before cells are added [56]. One of the commonly encountered problems with the use of microfluidic platforms is the formation of gas bubbles that can cause experimental sensory errors and interfere with the flow stream which can increase the shear stress within the system and be damaging to the cells cultured within the channels or chambers. Before microfluidic platforms are used for cell culture, bubble trapping should be set up for in-line removal of gas bubbles. Another disadvantage is the that the small numbers of cells and small fluid volumes used in microfluidic culture platforms limit the amount of biological samples that can be collected and used for further evaluations.

Methods for Evaluation and Validation

Tissue-engineered respiratory tract models require appropriate methods for evaluation and validation in order to measure and ensure the functionality of the system. Many of these evaluations are based on the cellular constituents of the model systems.

Assessments of the cell phenotypes, cell responses and generation of cell products are needed as a measure of functionality. For example, in physiologic respiratory tract models, products of lung epithelial cells can be used to indicate the ability of lung epithelial cells to function. For type II AEC some of these products include surfactant proteins A-D which are essential for normal lung function. Expression of surfactant proteins can be used as markers for identification of type II AEC. For bronchial epithelial cells such as Clara cells, production of Clara cell 10 protein (CC10) and some surfactant proteins, reflects their secretory role in the bronchial epithelium. Mucin production by tracheal or bronchial cells, such as goblet cells is indicative of their function. If the model also contains a vascular component, expression of endothelial markers such as vascular endothelial growth factor (VEGF), platelet endothelial cell adhesion molecule (PECAM) or vascular endothelial (VE) cadherin must be examined. In developmental respiratory tract models produced using fetal lung cells or embryonic stem cells, transcription factor-1 (TTF-1) has been shown to be expressed by immature lung epithelial cells and as these cells mature they start to express SP-C [23, 60]. Respiratory tract models used for toxicological studies assess cell viability and induction of apoptosis to examine cell responses after exposure to drugs or other agents. For evaluations of respiratory tract models used for pathological or infectious disease studies an understanding of the critical cell types involved in these pathological responses is needed to examine if these models are able to recreate these responses *in vitro*. For some of these models it may be possible to recreate these pathological responses in a deconstructed manner by using the fewest cell types required to elicit a specific response. Even in simplified pathogenesis models, heterogeneous cell types are needed to recreate a pathological response and all cell types used in the model will need to be characterized.

For some pathology models, structural changes of the ECM induced by pathological responses such as in lung cancer, asthma or pulmonary fibrosis (PF) must also be examined and measured. Each pathological condition will present specific kinetics for lung injury which will require different read-out assays for data analysis. Different methods can be used for validation of lung-specific protein expression, lung lineage cell products or gene expression profiles. Some of the most commonly used methodologies include gel electrophoresis, PCR, fluorescent microscopy and flow cytometry but many other methods and technologies also can be used.

After a respiratory tract model is produced it must be standardized. Standardization of small-scale systems such organs-on chips models, can be fairly easy because these usually have less than one million cells, are often composed of one or two cell types and the microfluidic platforms are automated. Standardization of HoC is more difficult because these model systems are composed of several million cells, contain many different cell types and also have 3D structural features. All of these components must be considered in order to standardize the model system. Respiratory tract models that require a reconstituted immune response to recreate specific cell responses also are difficult to develop and standardize. The use of innate immune cells (e.g. macrophages, neutrophils) from one donor in respiratory tract models produced from cells of a different donor, does not require human leukocyte antigen (HLA) matching because these cells are part of the non-specific immune response. In contrast, T and B lymphocytes from different donors will not be able to be used in respiratory tract models that are not HLA-matched. One option would be to use cells that are an HLA half-match but the process of identifying possible cell candidates would be even more challenging. As part of standardization, evaluations of the precision

of each model also must be done to validate their reproducibility and their use as experimental testing platforms. For each model system, examinations of intra- and inter-variability must be done to show that results are reproducible each time the model is tested. Intra-assay variation should be examined within data produced from a single experiment while inter-assay variation should be examined in experimental replicates. The use of appropriate controls for each experimental unknown is also important to measure the reproducibility of data. These assessments will be good indicators of the reproducibility of the model system and will help to understand how the system functions as a reliable testing platform.

Table 1.1 Commonly used cell types for production of respiratory tract models

Cell Type	(+) Advantages	(-) Disadvantages
Primary NHBE Normal Human Bronchial/Tracheal Epithelial Cells [61]	-Can manipulate growth and differentiation through use of epinephrine and TGF-β. -Can be immortalized through expression of hTERT, Cdk4 and E6/E7 to serve as a model to study molecular pathogenesis of lung cancer.	-Must be obtained within 12h postmortem though it becomes progressively more difficult to establish a culture should the postmortem interval exceed 6h. -Alternative method to obtain cells is via bronchoscopy though it offers a much lower yield. -Potential for microbial contamination. -Limited passage
HBSM(C)/HASM Human Bronchial/Airway Smooth Muscle Cells [62]	-Used in 3D models to study asthma on cross-sectioned airway segments. -Presence of C3a and C5a receptors makes these cells useful in	-Underlying factor(s) of hyperplasia/hypertrophy of these cells remain unidentified. -Inevitable phenotypic modulations occur in culture.

	modeling sepsis as well as asthma. -Express transcripts for IL-4 α , IL-13R α I, and IL-13R α II and high affinity for IgE. -Capable of influencing airway inflammation and growth factors via the production of prostanoids and chemokines (IL-11, IL-6, IL-8, RANTES, eotaxin). -Ability to modify airway modeling by the production of matrix-degrading enzymes (metalloproteinases). -Synthesize VEGF protein.	-Contaminating epithelial cells; difficulty in obtaining a pure population. -Donor genetics
16HBE14o- Human Bronchial Epithelial Cell Line [63]	-Forms polarised cell layers *in vitro.* -Provide a discriminatory barrier to solute transport (suitable barrier properties by day 6 in culture). -Grown on monofibrillar collagen because of ease of application, reproducibility, and uniformity of layers. -Express drug transport systems that are also present in the human bronchus *in vivo* (P-gp, LRP, and Cav-1) -Retains many features of differentiated bronchial epithelial cells.	-How culture conditions effect expression of airway-specific transport mechanisms is not fully understood. -Passage history is unknown

	-Form tight junctions (ZO-1 & occludin positive stains).	
Calu-3 Human submucosal adenocarcinoma cell line [64]	-Readily available cell line. -Well-characterized cell line. -Differentiates into monolayers of polarized cells of varying phenotypes in 3D. -Their morphological features, presence of transport systems, efflux pumps, and metabolic pathways allows for qualitative prediction of the fate drugs exposed to the lung. -Impact airway surface liquid, mucins, etc.. -Can be grown at air-liquid interface. -Functional intracellular tigh junctions mediate monolayer restrictiveness (observed by staining of the ZO-1 protein), thus high TEER value -Maximum TEER values were achieved around days 10-14 after monolayers were seeded onto collagen-coated filter membranes. -Exhibit passive diffusion an to a lower degree also low-affinity mediated transport of antibiotics at the apical and basolateral cell membranes.	-Non-inducible P450 enzymes. -The transport of Gly-Ser and other peptide substrates as well as insulin, requires further investigation before use for pulmonary drug absorption models. -Little is known about how these cells secrete multidrug-resistant proteins (MRPs). -Extensive passage -Mycoplasma contamination

Primary AECs Human alveolar epithelial type I & II mix of primary cells [65]	-Used as the "gold standard for comparison of other cell types." -Accurately demonstrate *in vivo* behavior. -Controllable cell division. -Capable of TGF-ß1 induced epithelial-mesenchymal transition in culture -Metabolically active. -Harbor necessary cell surface receptors for signaling.	-Time consuming isolation -High risk for bacterial or fungal contamination following isolation. -Never 100% pure isolation. -Financial cost for reagents used in isolation (collagenase, dispase, etc). -Cells cannot be passaged repeatedly. -Cells can be growth dependent and need to be maintained at an adequate seeding density.
A549 Human lung adenocarcinoma alveolar basal cell line [66]	-Consistent AECII metabolic/transport properties -They are genetically homogenous. -Can be grown in large quantities. -They produce confluent monolayers with AECII morphology & lamellar bodies present. -Has inducible P450 enzymes (IA1 & IIB6) consistent with *in vivo* AECIIs.	-Monolayers formed are leaky because they lack tight junctions. -Very low trans-epithelial electrical resistance (TEER) values which make it difficult to measure the transport of low molecular weight molecules. -Cells are genetically and phenotypically homogenous.
HUVEC Human umbilical vein endothelial cells [67]	-Constitutively express appropriate cell markers (ICAM-1, PECAM-1, MHC I). -TNFα inducible expression of adhesion molecules (VCAM-1, E-selectin). -All major signaling pathways present/intact -Proper cytokine responses. -Isolation/culture methods exist.	-Low yields when isolated. -Possibility of contamination with other cell types at isolation. -Can be difficult to culture. -Can express altered expression of endothelial markers during *in vitro* propagation.

	-Form a monolayer of density-inhibited cells with a cobblestone-like morphology when grown on Matrigel diluted 1:3 in serum-free cell culture medium in a 24-well plate. -Appropriate expression of von Willebrand factor (vWF).	
HuLECs/HPMECs Primary human (lung/pulmonary) microvascular endothelial cells [68]	-Published isolation methods exist. -Purity can be achieved using a highly specific selective marker, Ulex Europaeus Agglutin-1 (UEA-1). -There is high constitutive production of vWF, PECAM-1/CD31. -Cells express two vascular endothelial growth factor receptors Flt-1 & KDR. -*In vitro* responses to TNFα, LPS, and IL-1β by induction of cell adhesion molecules (ICAM-1/CD54, VCAM-1/CD106, & E-selectin) and secretion of proinflammatory cytokines (IL-6, IL-8, MCP-1, & GM-CSF) via AEC interactions. -Capable of responding to infectious agents via Toll-like receptors	-Need to prevent overgrowth. -Contaminating fibroblasts, pericytes, smooth muscle cells. -Require considerable cell expansion, manipulation, and *in vitro* culture time.

	expressed on their cell surface.	
MRC-5 Human fetal lung fibroblast cell line [69]	-Grow as adherent cells in culture. -Exhibit fibroblast morphology. -Well-characterized and well-defined non-tumorigenic phenotype. -Widely used human diploid cell line.	Develop into fibroblasts but no other cell types.
W1-38/CCL-75 Human fetal lung fibroblast cell line [70]	-Grow as adherent cells in culture. -Can be used to test anti-virals. -Well-characterized and well-defined non-tumorigenic phenotype. -Widely used human diploid cell line.	Develop into fibroblasts but no other cell types.
hESC Human Embryonic Stem Cells [71]	-Ability to differentiate into progeny with differentiated phenotypes (pluripotency) -Production of all normal lung cell types -Cells provide a renewable source for population of models. -Potential for self-renewal & plasticity is excellent.	-Cells can be highly unstable. -In culture cells often form teratomas. -There are indications of genetic instability after prolonged culture time (aneuploidy). -There can be frequent epigenetic errors (SSEA-4/STAT4 expression, TGFβ signaling, telomere length, collagen down-regulation, etc.).
iPS Induced Pluripotent Stem Cells [72]	-Circumvents the difficulties faced when generating patient- or disease-specific embryonic stem cells.	-Cell production using retrovirus transduction to force expression of c-Myc, Klf4, Oct 3/4, and Sox2 can lead to transcription of undesired genes and an

	-Express many un-differentiated embryonic cell-marker genes at equivalent or elevated levels: OCT3/4, SOX2, NANOG, GDF3, FGF4, ESG1, DPPA2, DPPA4, & hTER; thus these cells have high flexibility. -High telomerase activity and exponential proliferation for at least 4 months with a doubling time equivalent to human embryonic cells (~46 hours). -Ability to form 3 germ layers *in vitro* observed by embryoid-body formation. -Lineage-directed differentiation has been limited and at low efficiency to lung lineages.	increased risk of tumor formation. -Existing alternative methods that do not utilize transgenes often have a low yield. -Cell programming is dependent upon the original cell type being transformed. -Cell generation efficiency remains low despite efforts to improve yield.

Table 1.2 Review of currently available respiratory tract models

Author	Model Description	Type of Model	Cell Source	Scaffold	Culture Platform	Final Cell Type Produced
Lwebuga-Mukasam, 1986 [73]	Model used to study the modulating effect of the lung basement membrane on the morphology and function of type II pneumocytes.	Physiologic	Primary rat type II pneumocytes	Human lung acellular alveolar fragments	48-well tissue culture plates	Type II AEC (lamellar bodies)
Blau, 1988 [28]	Development of alveolar-like structures (ALS) with central lumens. Model used to study the effects of a reconstituted basement membrane on fetal cell differentiation and long term culture of pneumocytes.	Developmental Physiologic	Fetal rabbit cells from 29 day gestation	Engelbreth-Holm-Swarm (EHS) tumor membrane thick and thin gels	24-well culture plates	Type II AEC (lamellar bodies) Cells with microvilli facing central cavities
Sugihara, 1993 [74]	Model used to study type II pneumocyte differentiation on a three-dimensional (3D) matrix and pulmonary disorders affecting alveoli.	Developmental Physiologic Pathologic	Primary rat type II pneumocytes from 21 -23 day old rats	Collagen gel matrix	12-well tissue culture plates	Type II AEC
Chinoy, 1994 [29]	Formation of alveolar-like structures	Developmental Physiologic	Fetal rabbit type II pneumocytes 22 day gestation	Engelbreth-Holm-Swarm (EHS) tumor membrane or Matrigel	24-well tissue culture plates	Type II AEC

Pugin, 1998 [14]	Development of an *in vitro* "plastic lung" model with the ability to perform cyclic pressure-stretching of cells in culture. Model used to study the inflammatory response of a variety of lung cells including alveolar macrophages (AM) during mechanical ventilation-induced inflammation.	Physiologic Pathologic	A459 cells, EA.hy926 endothelial cells, human bronchial BET-1A cells, human primary lung fibroblasts, human AM isolated from lavage of lungs with cancer, Human monocyte-derived macrophages (MDMs) from peripheral blood, Nonadherent promonocytic human THP-1 cells		Plastic lung made from transparent Plexiglas with a bottom chamber containing double 6-well plates. Bottom of wells contain Bioflex Silastic membranes	Type II AEC, endothelial cells, fibroblasts, bronchial epithelial cells AM (main source of inflammatory mediators - TNF-α, IL-8, IL -6 and matrix metalloproteinase-9)
Chakir, 2001 [11]	Model of engineered human bronchial mucosa (EHBM) in air-liquid interface used to study mechanisms of inflammation,	Physiologic Pathologic	Human bronchial epithelial cells and fibroblasts isolated from bronchial	Human fibroblasts incorporated into a collagen gel matrix	Petri dishes (35-mm diameter) containing an anchorage	EHBM with normal cells presented a pseudostratified ciliated epithelium with the presence of

	airway repair, and cellular interactions in asthma.		biopsy specimens of asthmatic and normal subjects. T lymphocytes isolated from the peripheral blood of asthmatic patients			mucus secretory cells. Percentage of IL-5^{+} lymphocytes was significantly higher in EHBM with asthmatic cells.
Hermanns, 2004	Co-culture system of human distal lung. Model used to study the alveolar-capillary barrier in the pathogenesis and recovery from acute lung injury.	Physiologic Pathologic	Primary human pulmonary microvascular endothelial cells (HPMEC) isolated from normal portions of lung specimens from patients who underwent lobectomies for early stage lung cancer. Human lung adenocarcinoma		24-Transwell plates with a collagen type I coated filter	Type II AEC (TTF-1, SP-A, SP-B, SP-C, SP-D, E-cadherin, lamellar bodies) HPMEC (CD 31, VE-cadherin)

			cell lines, A549 and NCI H441.			
Paquette, 2004	Production of bronchial equivalents (BE). Model used to study mechanisms involved in asthma.	Physiologic Pathologic	Primary human bronchial epithelial cells (HBEC) and human bronchial fibroblastic cells (HBFC) isolated from biopsies of normal and asthmatic lungs	Mesenchymal layer composed of type I collagen gel with a HBFC suspension.	Petri dishes (35-mm diameter) containing peripheral anchorage (sterile ring of Whatman paper) and an internal elevated support	HBEC (Keratin, Gelatinase A MMP-2, Gelatinase B MMP-9) HBFC (vimentin) Numerous cilia in HBEC of normal lungs. Sparsely distributed cilia in HBEC from asthmatic lungs.
Matrosovich, 2004	*In vitro* cell culture models of human airway epithelium. Model used to study cellular tropism of human and avian influenza viruses.	Pathologic	Primary human epithelial cells from tracheal/ bronchial and nasal tissues		Transwell culture plates	Non-ciliated human tracheal epithelial cells (2-6-linked sialic acid receptors) Ciliated cells (2-3-linked sialic acid receptors) Secretory cells (identified by Alcian blue-periodic

						acid Schiff staining)
Chen , 2005	Formation of lung histotypic alveolar-like structures. Model used to facilitate the study of strategies for preparing collagen-glycosaminoglycan (GAG) scaffolds for the regeneration of lung tissue.	Physiologic	Primary fetal lung cells from rats 16 and 19 days gestation.	Disk-like samples of type I collagen - (GAG) sheets	Agarose-coated 12-well tissue culture plates	Type II AEC Pseudo-stratified ciliated columnar epithelial cells 19 day cells surrounding alveolar-like structures expressed alpha smooth muscle actin and were able to contract.
Coraux, 2005	Culture model of airway epithelium in an air-liquid interface from differentiated murine embryonic stem (ES) cells. Model used to study methods of cell therapy to reconstitute airway epithelium in airway diseases, such as bronchopulmonary dysplasia, cystic fibrosis, or bronchiolitis obliterans.	Developmental Physiologic	Undifferentiated mouse ES cell line CGR8		Petri dishes - type I collagen-coated, gelatin-coated, type IV collagen-coated, or type VI collagen-coated. Milicell-HA porous membranes placed on dishes.	Basal cells (GS-I-B4) Ciliated cells (tubulin β) Intermediate cells nonciliated Clara cells (CC10, SP-D, abundant rough endoplasmic reticulum, numerous mitochondria and electron-dense

						secretory granules)
Choe, 2006	Model of human bronchial mucosa cultured at an air-liquid interface that mimics anatomical and functional features of the airway wall. Model used to study airway remodeling, transepithelial transport, and inflammatory cell interactions.	Physiologic Pathologic Toxicological	Normal human bronchial epithelial cells (NHBEs) Human fetal lung fibroblasts (HLFs)	Type 1 collagen gel	6-well Transwell plates with porous polymeric wells	Ciliated cells Mucus secreting cells
Cortiella, 2006	Alveolar tissue growth *in vitro* and *in vivo* from differentiated ovine somatic lung progenitor cells (SLPCs) capable of generating lung tissue. Model used to study the potential of progenitor stem cells and scaffold-based methods in the generation of lung tissue.	Developmental, Physiologic	Primary ovine SLPCs isolated from lung tissue	Polyglycolic acid (PGA) matrix Pluronic F-127 (PF-127) matrix	175ml flasks	Clara cells (CC10) Type II AEC (SP-C Cytokeratin)
Mondrinos, 2006	Pulmonary tissue constructs that mimic distal lung architecture by formation of alveolar forming units (AFU) and branching morphogenesis. Model used to study the generation of distal pulmonary tissue	Developmental Physiological, Pathological	Primary murine embryonic day 18 fetal pulmonary cells (FPC)	Porous foams and nanofibrous matrices of Matrigel hydrogel, Poly-lactic-co-glycolic	55mL rotating wall vessel bioreactor	Type II AEC (SP-C, lamellar bodies) Mesenchymal cells (vimentin) Mesenchymal-derived morphogenic inducer of

	for replacing diseased lung tissue such as in neonatal pulmonary hypoplasia.			acid (PLGA), Poly-L-lactic-acid (PLLA)		the epithelium (FGF 10), epithelial morphogenetic receptor (FGFr2)
Mondrinos, 2007	Model of fetal distal lung tissue in which an epithelial-endothelial interface is observed. Model used to study lung development and for methods of generating lung constructs for lung augmentation in pediatric pulmonary pathologies.	Developmental Physiological Pathological	Primary murine embryonic day 17.5 FPC	Type I collagen gel matrix	24-well culture plates	Type II AEC (pro-SP-C, cytokeratin) Endothelial cells (CD 31, PECAM-1, VEGFR1, VEGFR2, isolectinB4) Mesenchymal cells (vimentin, tropoelastin) Epithelial-endothelial interfacing (FGF10/7/2)
Andrade, 2007	Generation of porous structures that are similar to alveolar units. Model used to study the potential of cell- and scaffold-based techniques for lung regeneration.	Developmental Physiological	Rat fetal lung cells	Gelfoam sponge	Gelfoam implantation into rat lungs	Type II AEC (pro-SP-C) Clara cells (CCSP) Endothelial cells (von Willebrand factor) Infiltrating leukocytes (CD45)

Birkness, 2007	Rounded cellular aggregates of human cells used as a model to study granuloma formation and cellular and immunological responses during *Mycobacterium tuberculosis* infection.	Pathologic	Peripheral blood mononuclear cells (PBMCs) isolated from whole blood of healthy donors.		24-well culture plates	Macrophages (CD68) T lymphocytes (CD3)
Zani, 2008	*In vivo* airway injury model using collagen matrices engrafted with human epithelial and endothelial cells. Model used to study airway injury and repair.	Physiologic Pathologic	Human bronchial epithelial (EP) cells, human aortic endothelial cells (EC) HUVECs Normal human lung fibroblast cell line (NHLF)	Tissue culture polystyrene (TCPS) coated with Gelfoam	15-ml polypropylene tubes 48-well plates Matrices implanted into rabbit tracheas	Cuboidal basal cells Squamous mucus cells EP and EC cells (sICAM-1 production, production of pro-inflammatory cytokines)
Cortiella, 2010	Generation of 3D upper and lower respiratory tract lung tissue using differentiated murine embryonic stem cells (mESC) on a whole natural lung matrix. Model used to study the effects of natural lung matrix on ESC differentiation into lung-specific lineages.	Developmental Physiologic	mESC	Whole acellular (AC) rat lung matrix	50mL rotary bioreactor	Ciliated epithelial cells (cytokeratin-18) Clara cells (CC10) Type II AEC (pro-SP-C) Developing epithelium (TTF-1)

						Endothelial cells (CD31, PECAM-1) Smooth muscle cells (α-SMA)
Huh, 2010	Biomimetic microsystem with an air-liquid interface that reconstitutes the alveolar-capillary interface of the lung. Microengineered system used as a model to study cellular interactions and responses to nanoparticles. Systems may also be used as models for high-throughput screening of drugs, toxins, or pathogens.	Physiologic Pathologic Toxicological	Cell line of human microvascular endothelial cells, HUVEC, human alveolar epithelial cells (NCI H441), A549, E10 (an immortalized, non-tumorigenic cell line derived from alveolar type II pneumocytes), human dendritic cells isolated from whole blood of healthy donors	microporous PDMS membranes coated with collagen gel or fibronectin	Microfluidic device with microchannels that is integrated with computer-controlled vacuum to produce cyclic stretching	Type II AEC (lamellar bodies surfactant production) Endothelial cells (ICAM-1, VE-cadherin)

Miller, 2010	Development of a human lung cylindrical-shaped bronchiole model in an air-interface. Model used to study mechanisms of airway remodeling	Physiologic	Human primary normal lung fibroblasts (CC2512) Human airway smooth muscle cells (CC2576) Human small airway epithelial cells (CC2547)	Type I collagen gel matrix with embedded human lung fibroblasts	Bioreactor that contains a polytetrafluoroethylene (PTFE) mould unit	Human lung fibroblasts (β-tubulin) Human small airway epithelial cells (cytokeratin-18, collagen IV, mucin, K-19, production of cilia) Smooth muscle cells (α-SMA, smooth muscle myosin heavy chain, vimentin)
Ott, 2010	*In vitro* formation of lung tissue constructs that contain epithelial and endothelial lung tissue. Regenerated lung constructs were transplanted into orthotopic position and assessed for *in vivo* function. Model used to study methods of lung regeneration.	Developmental Physiologic	A549 Rat fetal lung cells HUVEC	Whole acellular rat lung matrix	Bioreactor	Type II AEC (pro-SP-C, SP-A, Ttf1) Caveolin-1 Type I AEC (T1-α) Fibroblasts (vimentin)
Petersen, 2010	Engineered lungs that display many microarchitectural features of native lung and that function in gas	Developmental, Physiological	Mixed populations of neonatal rat lung epithelial	Decellularized rat lung	Bioreactor	Ciliated columnar epithelial cells

	exchange for short periods of time when implanted into rats. Model used to study if lung tissue can be regenerated *in vitro* using decellularized tissues as scaffolds.		cells Microvascular lung endothelial cells			Clara cells (CCSP) Type I AEC (AQP 5) Type II AEC (pro-SP-B, pro-SP-C) Endothelial cells (CD31)
Price, 2010	Development of a bioreactor system to produce natural lung matrices from decellularized tissues. Model used to study components of a decellularized lung matrix and its ability to support lung tissue development.	Developmental Physiologic	Mice embryonic day 7 fetal lung cells	Decellularized mice lungs	Culture flask filter cap bioreactor system	Type II AEC (pro-SP-C) Type I AEC (AQP 5) Endothelial cells (CD31) Fibroblasts (vimentin)
Zhang , 2011	Development of an alveolus-like structure to examine fetal lung cell differentiation	Developmental Physiologic	Mice fetal pulmonary cells	Collagen, Matrigel and alginate-poly-l-lysine-alginate (APA) microcapsules		Type II AEC (Pan-cytokeratin, vimentin and SpC positive cells)
Nguyen, 2012	Generation of an organotypic model of the human airway mucosa. Model used to study the influence of the tissue microenvironment	Physiologic	Human lung fibroblast cell line, MRC-5 derived from normal	Collagen gel matrix seeded with fibroblasts	6-well plates with 3.0-μm Transwell inserts	DC (DC-SIGN, positive for CD1a and negative for CD14)

	on regulating dendritic cell (DC) functions during homeostasis or an inflammatory response.		lung tissue of a 14-wk-old male fetus. 16HBE, an immortalized human bronchial epithelial cell line Human monocyte-derived DC isolated from whole blood.			
Huh, 2012	Development of a microfluidic device with air and fluid flow that mimics the alveolar-capillary interface of the human lung. Microfluidic device used as a model of pulmonary edema.	Physiologic Pathologic Toxicological	Human alveolar epithelial cell line NCI-H441 Cell line of human pulmonary microvascular endothelial cells	Porous membranes coated with fibronectin	Microfluidic device with upper and lower microchannels	AEC II Microvascular endothelial cell junctional proteins (VE-cadherin, occludin)
Kloxin, 2012	Cell culture platform in which the geometry and connectivity of the cellular microenvironment is controlled	Physiologic	A549 cell line isolated from human lung	Hydrogel layers on photolabile, enzyme-labile	12-well culture plates	AEC II (pro-SP-C) AEC I (T1-α)

	spatiotemporally. Model used to study how cellular interactions are affected by static or evolving environmental cues and how this modulates tissue development.		adenocarcinoma Primary AEC II isolated from rat distal lung tissue	base material		
Patel, 2012	Dynamic cell growth system to mimic the mechanical environment of the lung. Model used to study pneumocyte proliferation and oxidative and inflammatory response to multi-walled carbon nanotubes (MWCNT) in dynamic versus static growth conditions.	Physiologic Pathologic	A549 cell line that is type II epithelial-like in morphology and originates from a human lung adenocarcinoma		6-well BioFlex plates with a Tension Plus 4000T system	AEC II
Booth, 2012	Culture system of acellular human lung matrices from normal lungs and fibrotic lungs seeded with human cells to create lung constructs. Model used to study how the extracellular matrix of normal and fibrotic lungs influences fibroblast phenotype	Physiologic Pathologic	Primary human lung fibroblasts were isolated	Biopsy punch cylinders of decellularized lung matrices from normal healthy lungs and from interstitial pulmonary fibrosis patients	24-well culture plates	Myofibroblasts (α-SMA, cellular fibronectin)
Bonvillain, 2012	Development of a non-human	Developmental Physiologic	Rhesus primary	Lower lobes of	6-well plates	BMSC and ASC

	primate lung model using decellularized Rhesus macaques lungs and mesenchymal stem cells. Model used to study the effects of decellularized lung matrix on cell attachment, elongation and proliferation.		bone marrow-derived mesenchymal stem cells (BMSC) and adipose-derived mesenchymal stem cells (ASC)	acellular Rhesus macaque lungs with an agarose mixture as a vehicle for seeding cells		(assessment of proliferation ; Ki67- and TUNEL-positive)
Horie, 2012	3D co-culture assay of human lung cancer cells. Model used to study the tumor-promoting abilities of cancer-associated fibroblasts (CAFs) when compared to normal fibroblasts (NF)	Physiologic Pathologic	Human lung adenocarcinoma cell line A549 Primary human lung fibroblasts isolated - patient-matched CAFs and NFs from tumoral and non-tumoral portions of resected lung tissue from lung cancer patients.	Type I collagen gel matrices	6-well culture plates	CAFs (α-SMA, enhanced collagen gel contraction,) Both CAF and NF (vimentin, pan-keratin)

Nichols, 2013	Development of lung tissue constructs using acellular pig and human lung matrices seeded with a variety of different cell types. Model used to support *in vitro* development of lung tissue using natural lung matrices.	Physiologic	Murine embryonic stem cells (mESC), human fetal lung cells (HFLC), pig bone marrow-derived mesenchymal stem cells (BMMSCs) and primary human alveolar epithelial type II cells (HAEC), which are predominantly AEC II.	0.5 cm^3 pieces of acellular porcine and human lungs, Matrigel, or Gelfoam	24-well culture plates	AEC II (pro-SP-C) AEC I (AQU 5)
Mishra, 2013	Development of an *ex vivo* lung cancer model using natural lung matrix with human cancer cells. Model forms tumor modules and is used to study progression of tumor growth.	Pathologic	Human alveolar basal epithelial cell line A549	Decellularized rat lungs	Bioreactor	AEC II
Nichols, 2017	Cell-scaffold lung constructs to examine cell numbers and pre-treatment of	Physiologic	Primary human lung cells	2.5 cm^3 AC human lung	Bioreactor	AEC II (pro-SPC) AEC I (AQP 5)

	scaffolds in lung tissue development			scaffold pieces		
Nichols, 2018	Cell-scaffold constructs to examine lung tissue development for bioengineered lungs before transplant	Physiologic Pathologic	Primary porcine lung cells	AC porcine lung scaffold	Bioreactor	AEC I AEC II Endothelial cells

CHAPTER 2*

Production and Assessment of Pig and Human Acellular Whole Lung Scaffolds

INTRODUCTION

Our previous studies have shown that AC whole lung scaffolds can be produced from native rat lungs and that these scaffolds, retain structural components of the lung ECM and have the ability to support tissue development when seeded with murine embryonic stem cells (MESC) [23]. To determine the feasibility of producing large-scale whole AC lung scaffolds with the potential for use in development of human research models for pre-clinical studies or clinical applications such as regenerative medicine, we have developed a decellularization procedure to produce whole AC lung scaffolds from native porcine lungs or native human lungs. If whole AC lung scaffolds are to be developed for research use, or for use in tissue replacement strategies, standard procedures and guidelines for decellularization methods and for post-production assessments will be required. As noted in Chapter 1, it is important to consider are the decellularization reagents, because the use of different detergents may yield varying results for cell removal and alterations of the lung ECM. Results from decellularization of whole mice lungs or whole rat lungs suggested that there are variations in the protein composition of the ECM [23, 42, 43, 44].

Ineffective removal of cellular material can have a direct effect on the immunogenicity of the scaffolds produced and can impede the use of AC lung scaffolds for recellularization. Although

Chapter * published and taken from: Nichols, J.E., Niles, J., Riddle, M., Vargas, G., Schilagard, T., Ma, L., Edward, K., La Francesca, S., Sakamoto, J., Vega, S. and Ogadegbe, M., 2013. Production and assessment of decellularized pig and human lung scaffolds. *Tissue Engineering Part A*, *19*(17-18), pp.2045-2062.

it is believed that removal of cells and nucleic material should prevent induction of an immune response, naturally–derived scaffolds may still contain other components that can make them immunogenic. For this reason, the immunogenicity of AC lung scaffolds must also be examined. As part of these post-production assessments, the effects of decellularization on the mechanical integrity of AC lung scaffolds and the quantitative evaluation of the protein composition in the ECM after decellularization must also be considered. Cell attachment, cell viability and tissue formation also can be affected by AC lung scaffolds that are not well decellularized, contain residual detergent or have not been cleaned properly to ensure there is no contamination.

In this study, we report the first attempt to produce whole AC porcine or human lung scaffolds by perfusion decellularization using a prototype bioreactor (Harvard Apparatus). We provide post-production assessments of the whole AC porcine or human lung scaffolds to show gross structures of the scaffolds and the protein and structural composition of the remaining ECM. Further, we performed pulmonary function tests (PFT) to examine the mechanical function with measurements of static and dynamic compliance of whole AC porcine or human lung scaffolds and compared these measurements to that of normal porcine lungs or normal human lungs. Small cell-scaffold model constructs were produced using AC porcine or human lung scaffolds and a variety of cell types to examine the influence of scaffolds on cellular responses. The human immune response to AC human lung scaffolds produced by different decellularization reagents was examined in cell-scaffold constructs containing human monocyte lymphocytes (MNL) to assess immunogenicity of the scaffolds. Cell attachment and cell viability also were examined in AC porcine or human lung scaffolds produced using different decellularization reagents.

MATERIALS AND METHODS

Decellularization Process

Human lungs obtained for production of whole human lung AC scaffolds were procured as discarded human tissues following protocols approved by Institutional Review Boards (IRB) at UTMB or Methodist Hospital Research Institute. Pig lungs were obtained as part of a tissue-sharing program from Institutional Animal Care and Use Committee (IACUC)-approved studies at UTMB. Upon procurement, porcine and human lungs were stored at -80˚C and were kept in storage at least 1 month prior to decellularization. On the day of decellularization, lungs were thawed in a 45˚C water bath before being placed in a perfusion bioreactor chamber.

To setup the lungs for perfusion, individual cannulas were used to connect the pulmonary artery and trachea to allow for control of separate pumping and waste systems. Day 1 of decellularization was initiated by immersing the lungs in 1% SDS solution and pumping 1% SDS solution into the individual cannulas of the pulmonary artery and trachea. 1% SDS was perfused into the pulmonary artery at a rate of 60 ml/min and into the trachea at a rate of 120 ml/min. 1-3 liters of 1% SDS were used to fill and expand the lungs. Expanded lungs were emptied every hour for 3 hours and at the end of each 3 hour time point, fresh 1% SDS solution was added to the chamber to begin perfusion again. The concertation of SDS was lowered to 0.1% on day 3 of decellularization and the perfusion rates were kept the same. Fresh 0.1% SDS was added to the bioreactor chamber every day for days 4, 5 and 6 of decellularization. By day 7, lungs were perfused with distilled water at a rate of 500 ml/min for 12 hours. Distilled water in the bioreactor chamber was replaced every 3 hours. Lungs were then perfused with 3% H_2O_2 for 1 hour followed by perfusion with sterile water for 12 hours at a rate of 500 ml/h. Sterile water was replaced every 3 hours. Sterile water was then removed from the bioreactor chamber and lungs were perfused

with phosphate-buffered saline (PBS) containing streptomycin (90 µg/ml), penicillin (50 U/ml) and amphotericin (90 µg/ml) for 5 hours at rate of 500 ml/h. Whole AC porcine and human lung scaffolds were stored in fresh PBS containing antibiotic and antimycotic solutions.

Bronchoscopy protocol

A bronchoscope (Olympus, Model BF, Type P160: Olympus Exera CVL-160 light source; and Olympus Exera CV-160 image source) was used for digital bronchoscopic examination of pig and human lungs before and after decellularization. The insertion cord of the bronchoscope was inserted into the trachea and pulmonary artery of the lungs to examine the gross structures of branching airways and vasculature. Digital video recordings and images were taken with a Sony model VRD-MC10 Multifunctional DVD recorder.

Pulmonary Function Tests

Pulmonary function tests (PFT) were done to obtain measurements of static lung compliance and dynamic lung compliance were done for pig and human lungs and for AC pig and human lung scaffolds. PFT measurements for normal pig lungs were done on animals that were being used for other studies with IACUC approval at UTMB. PFT measurements obtained from patients enrolled in past IRB-approved studies at UTMB were used to compare measurements obtained from AC human lung scaffolds. A ventilator (Model 300; Siemens-Elema) was used to ventilate lungs and AC lung scaffolds. A cuffed endotracheal tube was placed inside the trachea and umbilical tape was used to secure it. To seal the cuff within the trachea, the cuff was inflated. The ventilator settings were arranged to deliver sufficient tidal volume to generate a peak pressure of approximately 20 mmHg. Static lung compliance, dynamic lung compliance and peak pressures

were measured. Images from the ventilator screen for measurements obtained from each lung or AC lung scaffold captured.

DNA Analysis after Decellularization

To evaluate DNA content after decellularization, strips of scaffold were cut from the trachea, main stem bronchus, distal lung and pleura and were digested with proteinase K at 37˚C until no visible pieces of scaffold were left [23]. Digested scaffolds were centrifuged to precipitate any remaining proteins and phenol-Chloroform-Isoamyl alcohol (25:24:1) was used to purify supernatants. To isolate DNA, aqueous layers were removed and ethanol was precipitated for 12 hours at -20˚C. DNA extracted from native lung and a decellularized human lung scaffold was run side by side on by electrophoresis on a 3% LMP agarose gel with a 5KD DNA ladder control (Invitrogen). Immunohistochemistry was also done to verify cell removal by staining for major histocompatibility complex-1 (MHC-1) and 4′,6-diamidino-2-phenylindole (DAPI) to evaluate DNA content.

Immunohistochemistry

Immunohistochemistry was done on cell-matrix constructs, native pig and human lungs and AC pig and human lung scaffolds. Tissues, frozen in tissue freezing medium (Triangle Biomedical Sciences) were sectioned using a Micron cryomicrotome (Thermo Scientific). Primary antibodies and dilutions used include: anti-collagen I (goat 1/250; Santa Cruz Biotechnology, Inc.); anti-elastin (1/150; Santa Cruz Biotechnology, Inc.); anti-collagen IV (goat, 1/200 or 1/250; Santa Cruz Biotechnology); anti-laminin (goat, 1/200; Santa Cruz Biotechnology); and anti-fibronectin (goat, 1/250; Chemicon). FITC-conjugated anti-pig MHC-1antibody (murine; Antigenex America, Inc.) and FITC-conjugated anti-human MHC-1 antibody (murine; BD Biosciences) were also used.

Secondary antibodies were conjugated to fluorescein isothiocyanate (FITC), phycoerytherin (PE), or rhodamine (Molecular Probes). DAPI counter-stains were done in all tissue sections for identification of cell nuclei.

Fluorescence Microscopy

A Nikon T300 Inverted Fluorescent Microscope (Nikon Corp.) was used for examination of fluorescent labels. Confocal microscopy was done using a Zeiss LSM 510 UV-META confocal microscope.

Flow Cytometry

A FACSAria flow cytometer (BD Biosciences) was used. Data acquisition and data analysis were done using the FACSDiva program (BD Biosciences).

Multiphoton Microscopy and Second Harmonic Generation

Multiphoton microscopy (MPM) was done using a customized Zeiss 410 Confocal Laser Scanning Microscope with multiphoton excitation and detection of nondescanned optics, as previously described [88]. A femtosecond titanium sapphire laser provided multiphoton excitation with a 5W frequency-doubled Nd:YVO pump laser that routed into the scanhead and through the objective. The pulse width for the operating system was 140 fs prior to the objective (40X, 1.2 N.A., water immersion). Emitted light was collected using an epi-configuration and a cooled PMT placed in a nondescanned configuration (R6060; Hamamatsu) was used to detect it. Autofluorescence excitation was 780 nm and for second harmonic generation (SHG) it was 840 nm. For detection of broadband autofluorescence from the lungs or scaffolds fluorescence emission in the spectral region of 450 – 840 nm was collected. A 420±14 nm bandpass filter in the nondescanned detector path was used to collect SHG. Lung or scaffold samples to be imaged were

placed in an imaging dish with #1.5 coverslip and were immersed in PBS. Several sites throughout the lung or scaffold pieces were chosen. For each of the chosen sites, a z-stack was obtained from the outer surface using a z-interval of 1 μm to depths > 150 μm. 3D image reconstructions of micrograph stacks were constructed using Metamorph (Molecular Devices, Sunnyvale CA) or Image J 3D viewer (http://rsbweb.nih.gov/ij/plugins/3d-viewer/index.html).

Cell Viability Assay

Cell viability was examined in all cell-scaffold constructs after 7 days in culture. Vital fluorescent staining (calcein-AM and ethidium homodimer-1; Molecular Probes) was used as previously descried [23]. For all the cells isolated from each of the cell-scaffold constructs, both live and dead cells were counted. Averages were calculated from the numbers of live cells for each set of cell-scaffold constructs. Cell counts were done using a cell counter (Coulter) and low cytometry was used to assess cell viability.

Evaluation of the Cell Attachment to AC Pig or Human Lung Scaffolds

The ability of AC pig and human lung scaffolds to support cell attachment was examined in cell-scaffold constructs produced using different cell types. Cell types evaluated included (1) mESC, (2) human fetal lung cells (HFLC), (3) pig bone marrow-derived mesenchymal stem cells (BMMSC) and primary human alveolar epithelial type II cells (pHAEC), that were predominately pro-SPC-positive type II AEC. MESCs (C57BL6 (F)) were purchased from Open Biosystems and were maintained as previously described. Before use in experiments, the embryonic stem cells and feeder cell lines were tested and shown to be mycoplasma negative. HFLCs passage 6–20, were grown in Eagle's minimum essential medium containing 10% fetal bovine serum (Intergen Co.), penicillin (100 U/mL), and streptomycin (100 μg/mL) at 37°C in a 5% CO2 in air atmosphere. Pig

BMMSCs were isolated by slicing open the tibia and scooping out the marrow using a sterile curette instrument. Bone marrow was placed in a sterile 50 cc tube filled with DMEM with penicillin (50 U/ml) and streptomycin (90 μg/ml). The tube was gently shaken and then centrifuged to collect the cell pellet and 2×10^6 cells per plate were cultured in a 24-well plate. Cells were cultured in DMEM with penicillin (50 U/mL) and streptomycin (90 μg/ml) and then observed for adherence to the culture dish. After 1 day non-adherent cells were removed and the remaining cells were cultured for 4 more days. On day 5, the adherent cells were trypsinized and collected for evaluation of MSC markers by flow cytometry.

PHAEC were isolated from human lungs. Pieces of human distal lung were cut into $1mm^3$ fragments, and treated with collagenase/dispase (Roche Diagnostics) for 3–5 hours. Cells were collected and filtered through 100 and then 40 micron filters before centrifugation to collect the pHAEC. PHAEC were cultured in small airway growth media (SAGM) (Lonza) plus 1% heat-inactivated human serum, penicillin (100 U/mL), and streptomycin (100 μg/mL) and then were incubated at 37°C and 5% CO2. Non adherent cells were removed after 24 hours.

Individual cell-scaffold constructs were produced using each of the cell types listed above and AC pig or human lung scaffolds, Gelfoam or Matrigel. $2x10^6$ pHAEC were injected with a 20-gauge catheter into the center of each 0.5 cm^3 scaffold piece. After cells were seeded, cell-scaffold constructs were centrifuged at 100 g to help spread cells throughout each scaffold piece. All cell-scaffold constructs were placed in individual wells of 24-well cultures plates containing small airway growth medium (SAGM; Lonza) at 37˚C and 5% CO_2. Cell-scaffold constructs were cultured on the 24-well cultures plates for 24 hours. After 24 hours, sets of 6 same cell-scaffold constructs were placed together in individual small chambers of rotary bioreactors (Synthecon) containing SAGM at 37˚C and 5% CO_2. Cells were isolated from each of the cell-scaffold

constructs after 7 days of culture and the total number of cells and total viable cells were determined.

Evaluation of the Effects of AC Human Lung Scaffolds on pHAEC

PHAEC cellular responses to AC human lung scaffolds produced using different decellularization reagents were examined. PHAEC were isolated from human lungs as previously described [90]. 2 cm^3 pieces of distal lung were cut from native human lung and were decellularized using either 1% SDS, 0.1% SDS, 8mM 3-[(3-Cholamidopropyl) dimethylammonio]-1propanesulfonate (CHAPS), 0.1% triton X-100 plus 2% deoxycholate or 3% triton X-100. After decellularization, scaffold pieces were cut into smaller-sized 1 cm^3 pieces that were used for the experiment. $2x10^6$ PHAEC were injected into the center of each scaffold piece produced by each of the different detergents. Cell-scaffold constructs were done in triplicate and were cultured submerged in SAGM for 7 days at 37˚C and 5% CO_2. After 7 days in culture, PHAEC were isolated from each of the cell-scaffold constructs and the amounts of cells for triplicate cultures were averaged. The number of total cells isolated and total viable cells was determined for scaffolds produced using the detergents mentioned above. Histological evaluations of cell-scaffold constructs were done with H&E stains. Immunohistochemistry was also done to examine expression of lung-specific proteins.

Evaluation of the Human Immune Response to AC Lung Scaffolds

The human immune response to AC human lung scaffolds produced using different detergent decellularization protocols described in the literature was evaluated. 2 cm^3 pieces of distal lung were cut from native human lung and were decellularized using either 1% SDS, 0.1% SDS, 8mM 3-[(3-Cholamidopropyl) dimethylammonio]-1propanesulfonate (CHAPS), 0.1% triton X-100 plus 2% deoxycholate or 3% triton X-100. Five pieces of native human lung were decellularized with each detergent. After decellularization with each of the detergents, all 2 cm^3 lung pieces were cut into smaller 0.5 mm^3 for use in experiments. Peripheral blood was obtained from ten donors through an IRB approved protocol at UTMB or purchased from the UTMB blood bank. Ficoll-hypaque and density gradient centrifugation was used to isolate the mononuclear MNL fraction from whole human blood. Prior to use in experiments, MNLs were either not labeled or labeled with carboxyfluorescein succinimidyl ester (CFSE). Five 0.5 mm^3 lung scaffold pieces produced from each of the different detergents mentioned above, were incubated with 2 x 10^6 CFSE-labeled MNLs and cultured in triplicate, in 24-well tissue culture plates at 37˚C and 5% CO_2 for 5, 7, or 14 days. MNLs were collected from each of the triplicate cultures after each time point and were stained with 20 µl of anti-CD3 antibody conjugated to PE to identify any CD3-positive T-cells. After staining, all cells were fixed in 2% paraformaldehyde and were analyzed by flow cytometry.

MNLs that were not CFSE-labeled were used to examine chemokine production. 2 x 10^6 MNLs from each of the ten donors were added to individual 0.5 mm^3 pieces of AC lung scaffolds produced using each of the detergents mentioned above. Triplicate cultures were placed in 24-well plates and were incubated at and 5% CO_2 for 5 days. After 5 days, supernatants from each of the cultures were collected and a Cytometric Bead Array human chemokine kit (BD Biosciences) was

used to examine the production of the chemokines, CCL2/MCP-1, CCL5/RANTES, CXCL9/MIG, and CXCL10/IP-10. The protocol was performed as described by the manufacturer (BD Biosciences). A FACSort flow cytometer was used for analysis.

Statistical Analysis

GraphPad In-STAT software (version 2003) was used for statistical analysis. Mean values and standard deviations are reported. Analysis of variance (ANOVA) was performed and data was subjected to Tukey-Kramer multiple comparison test. Mean differences were considered significant when p was less than 0.05.

RESULTS

Evaluations of AC Pig Lung Scaffolds

Perfusion decellularization facilitated the removal of cells, cell debris and blood from pig lungs. The process of decellularization was documented from start **(Figure 2.1 A, B)** to finish **(Figure 2.1 J)** for pig lungs. After the first few hours of decellularization, the 1% SDS solution in the bioreactor chamber became dark, due to the presence of hemolyzed red blood cells and cell debris **(Figure 2.1 C)**. Lungs started turning a lighter color on days 2 and 3 of decellularization, as more blood and cells were being removed **(Figure 2.1 D, E)**. On day 4 of decellularization distal regions of the lungs began to turn white **(Figure 2.1 F)**. By day 5 of decellularization only small areas of the lungs retained some blood and cell debris **(Figure 2.1 G)** but by day 6 these areas also turned white, indicating they had been decellularized **(Figure 2.1 H, white arrow)**. By day 7, lungs had a white glassy appearance that indicated that decellularization was complete **(Figure 2.1 I, J)**. Pleural tears were sealed with fibrin glue **(Figure 2.1 K, black arrows)** and one these were properly sealed, they did not prevent the scaffolds from being inflated **(Figure 2.1 L)**. After

decellularization, bronchoscopic examination of the bronchial airways **(Figure 2.1 M)** and branching vasculature **(Figure 2.1 N, O)** indicated that these gross structures were intact and there was no evidence of structural damage. Pulmonary function tests of porcine lungs before decellularization and after decellularization indicated that were no statistically significant differences in peak pressure, dynamic compliance or static compliance between native porcine lungs and the AC lung scaffolds **(Figure 2.2 A, B)**.

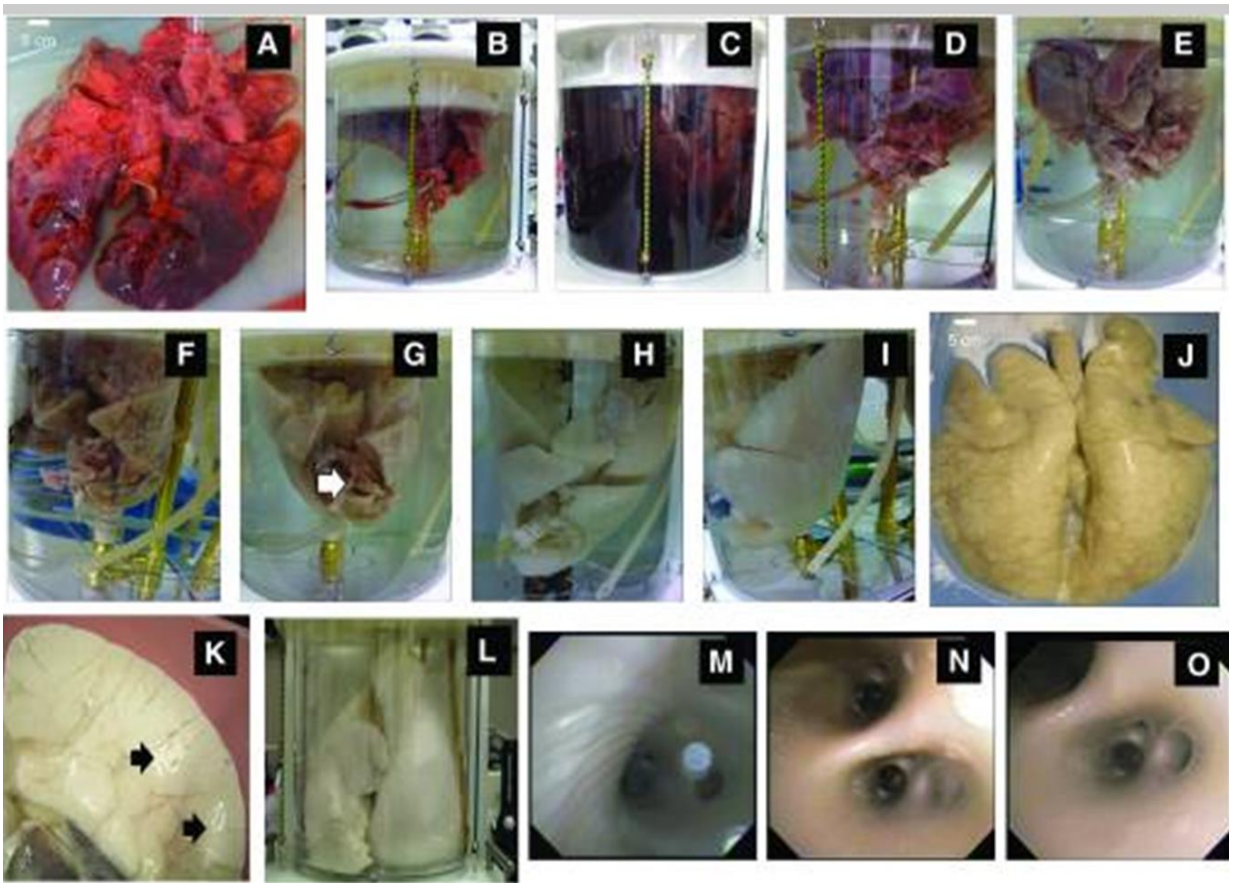

Figure 2.1 Processing procedure for the decellularization of a whole pig lungs. **(A)** Whole pig lung prior to processing. **(B)** Placement of cannulas into trachea and PA. **(C)** Start of decellularization process on day 1 showing discoloration of the SDS in the tank due to the presence of hemolyzed blood and cell debris. **(D)** Day 2 of process. **(E)** Day 3 of process. **(F)** Day 4 of process. Note the white regions where decellularization has taken place. **(G)** Day 5 of process. Note white arrow showing regions near the carina that have not been fully decellularized. **(H)** Day 6 of process. **(I)** Day 7 of process and **(J)** completely decellularized lung removed from tank on day 7, anterior view. **(K)** Posterior view of one lobe showing sites of fibrin glue repair of pleura (black arrows). **(L)** Lungs were expanded to examine elasticity and for PFT testing. **(M)** Bronchoscopic examination of main stem bronchus and branching airways and **(N, O)** use of same scope to view branching vessels of AC lung scaffold. Reproduced with permission from Nichols *et al*. 2013.

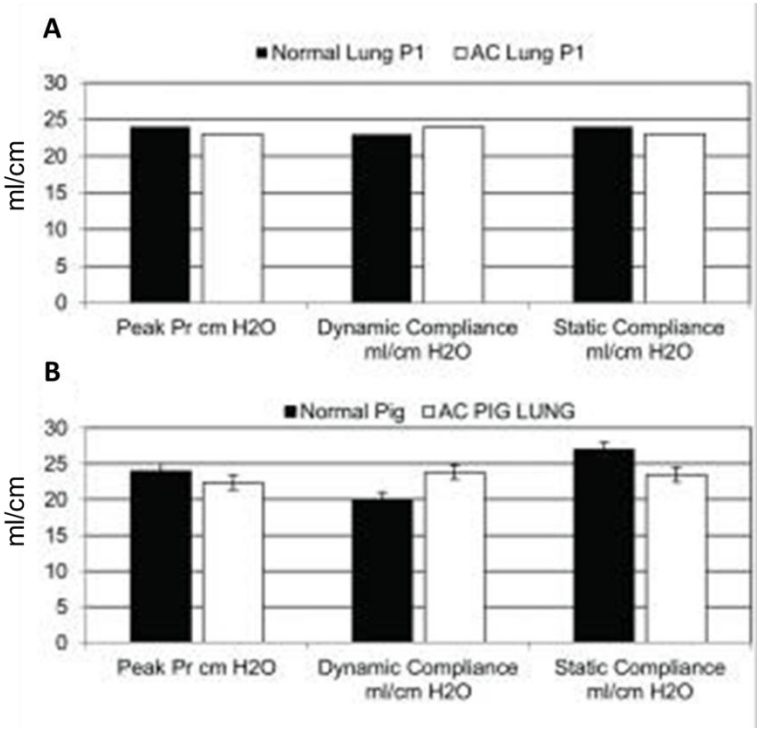

Figure 2.2 Evaluation of mechanics of lung function. (A) Representative examination of the peak pressure, dynamic compliance, and static compliance for a single pig lung pre and post decellularization. **(B)** Averaged data for peak pressure, dynamic compliance, and static compliance for *n*=8 pig lungs measured pre and post decellularization. Reproduced with permission from Nichols *et al*. 2013.

MPM and SHG were used to examine the collagen and elastin content in AC pig lung scaffolds after decellularization. Assessments also were done in native pig lungs as a comparison. MPM and SHG 3D reconstruction images show the collagen content in native pig lungs (**Figure 2.3 A-D**) and decellularized AC pig lung scaffolds (**Figure 2.3 E-H**). Using MPM and SHG, regions of interest (ROI) were identified and were used to quantitate collagen content in native pig lungs and AC pig lung scaffolds A comparison between the ROIs of native pig lung (**Figure 2.3 C ,D**) and AC pig lung scaffold (**Figure 2.3 G, H**) showed that native lung had higher levels of collagen than AC pig lung scaffolds. Intensities of all selected ROIs from each plane were averaged for volume density analysis to quantify the amount of collagen present in normal pig lungs and decellularized AC pig lung scaffolds. Volume density analysis of the collagen SHG intensity indicated that AC pig lung scaffolds contained significantly less amounts of collagen than native

pig lungs **(Figure 2.3 I).** The volume fraction of the SHG signal was significantly higher in AC lung scaffolds than in native porcine lungs, indicating that the distribution of collagen was more uniform in the scaffolds **(Figure 2.3 J)**.

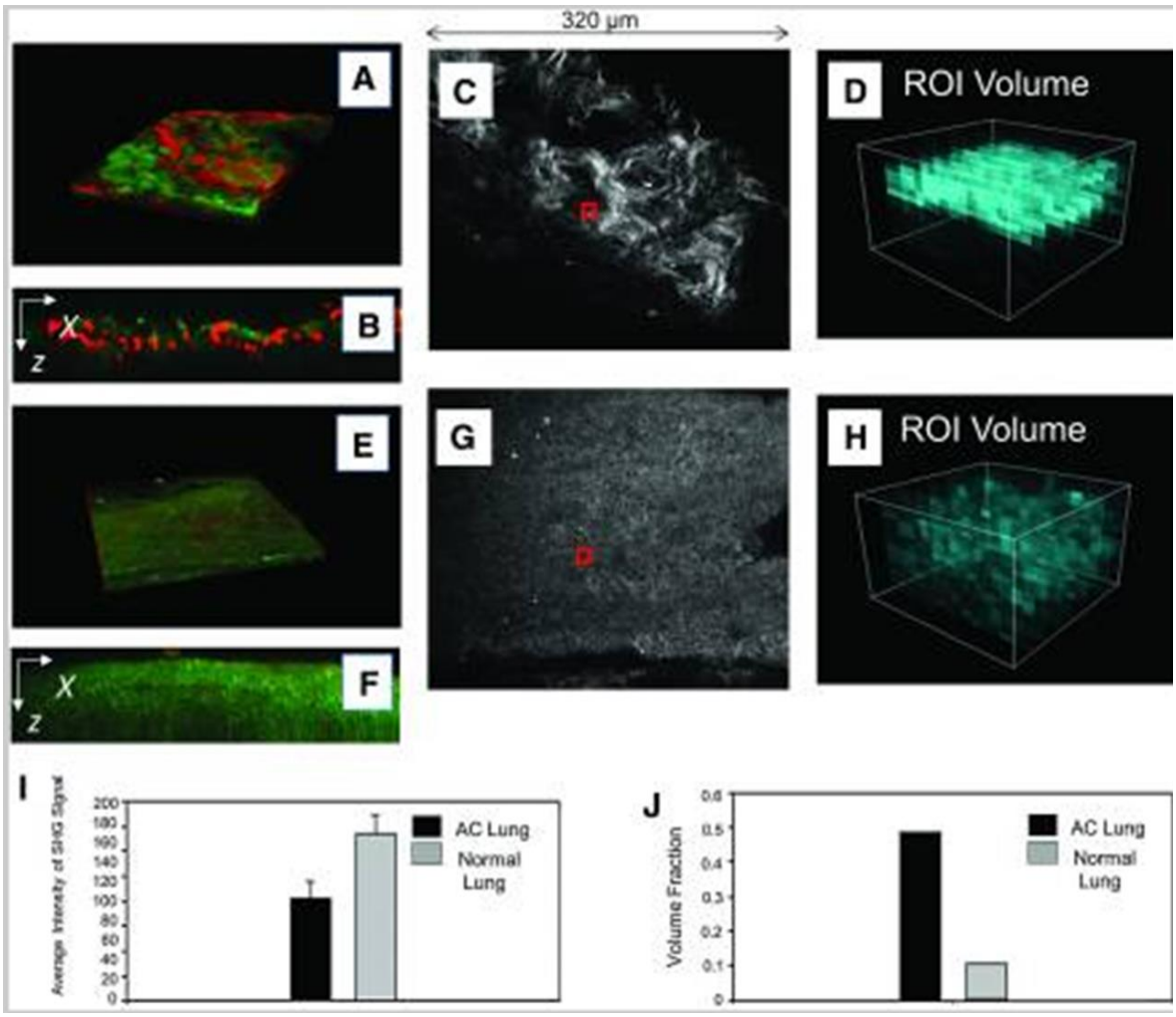

Figure 2.3 MPM-SHG of pig native versus AC lung. (A) MPM 3D reconstruction image of normal lung ECM using SHG to image collagen (green) and AF for elastin (red). **(B)** Single XZ cross section of A. **(C)** A scored ROI (red box) is shown for normal pig lung. **(D)** Volumetric representation of the distribution of the collagen SHG intensity of the region denoted by red box in **(C)**. **(E)** MPM 3D reconstruction image of AC pig lung ECM using SHG to image collagen (green) and AF for elastin (red). **(F)** Single XZ cross section of **(E)**. **(G)** A representative scored ROI (red box) is shown for AC pig lung. **(H)** Volumetric representation of the distribution of the collagen SHG intensity of the region denoted by red box in **(G)**. **(I)** Averaged scoring results for normal versus AC lung based on the average of the SHG intensity from each case. **(J)** Volume fraction of the SHG signal in normal versus AC lung showing that although the intensity of SHG is higher in the native lung, the distribution of collagen is more uniform in the AC lung. Reproduced with permission from Nichols *et al*. 2013

Immunohistological and MPM and SHG examinations of the pleura **(Figure 2.4 A-J)** and distal regions **(Figure 2.5 A-P)** of AC pig lung scaffolds revealed that the remaining ECM in both of these regions was predominately composed of type I collagen and elastin. Some distal areas of the scaffold contained fibronectin **(Figure 2.5 I)**. Pleura, distal lung, trachea and bronchi of AC pig lung scaffolds did not retain collagen IV and laminin. The gross configurations of collagen and elastin were retained in the pleura **(Figure 2.4 G-J)**. Immunohistochemistry of MHC-1 and DAPI confirmed there were no cells or DNA present after decellularization **(Figure 2.4 B)**. Distal lung regions of the scaffolds contained bundles of collagen that had relaxed configuration and only a few elastin fibers interlaced between **(Figure 2.5 A, L)**. In native pig lung, both collagen and elastin were present but collagen fibers had a wavy appearance **(Figure 2.6 A-H)**. In some distal lung regions of AC pig lung scaffolds, the remaining ECM of small blood vessels could be seen **(Figure 2.5 H, K)**. This blood vessel ECM was composed of inner layers of elastin that were surrounded by bundles of collagen (**Figure 2.5 H, K)**.

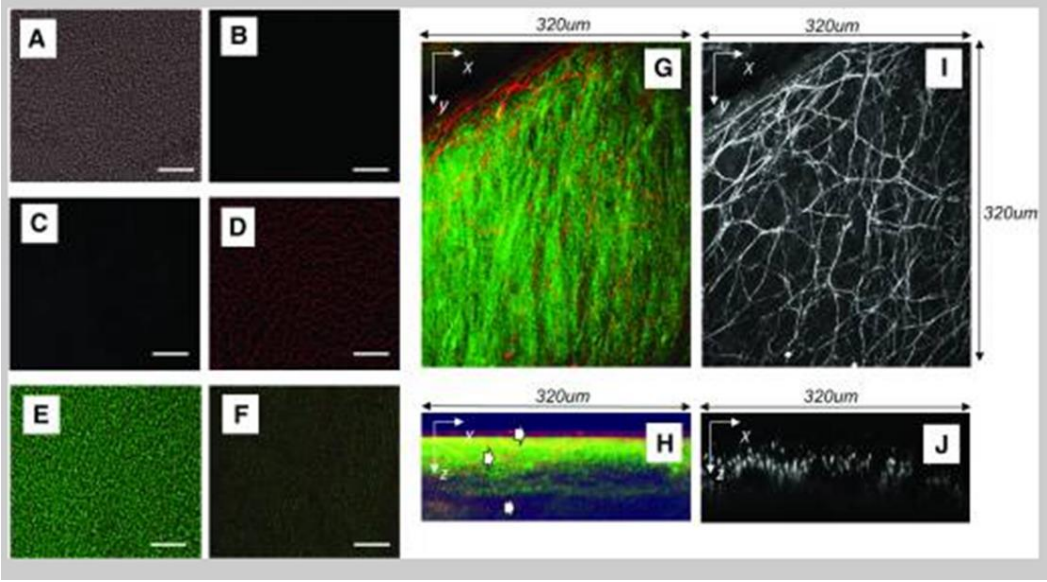

Figure 2.4 MPM and SHG of pig AC lung pleura. (A) Phase contrast microscopic image of AC pig pleura, scale bar=100 μm. **(B)** Evaluation of presence of nuclei, nuclear material using DAPI, or cell debris by staining for pig MHC-1, scale bar=100 μm. **(C)** Staining control for **(D)** and **(E)**. **(D)** Staining for presence of elastin (red) and (E) Collagen (green), scale bar=100 μm. **(F)** Merge of (B) and **(D)**, scale bar=100 μm. **(G)** MPM image of pleura using combined AF of elastin (red) and SHG of collagen (green).

(H) 90° (XZ) cross-sectional view of **(G)**. White arrows indicate elastin fibers between collagen bands. **(I)** MPM AF image of pleura using MPM showing bright elastin fibers. **(J)** Single XZ cross section of I showing depth-resolved structure. Reproduced with permission from Nichols *et al*. 2013

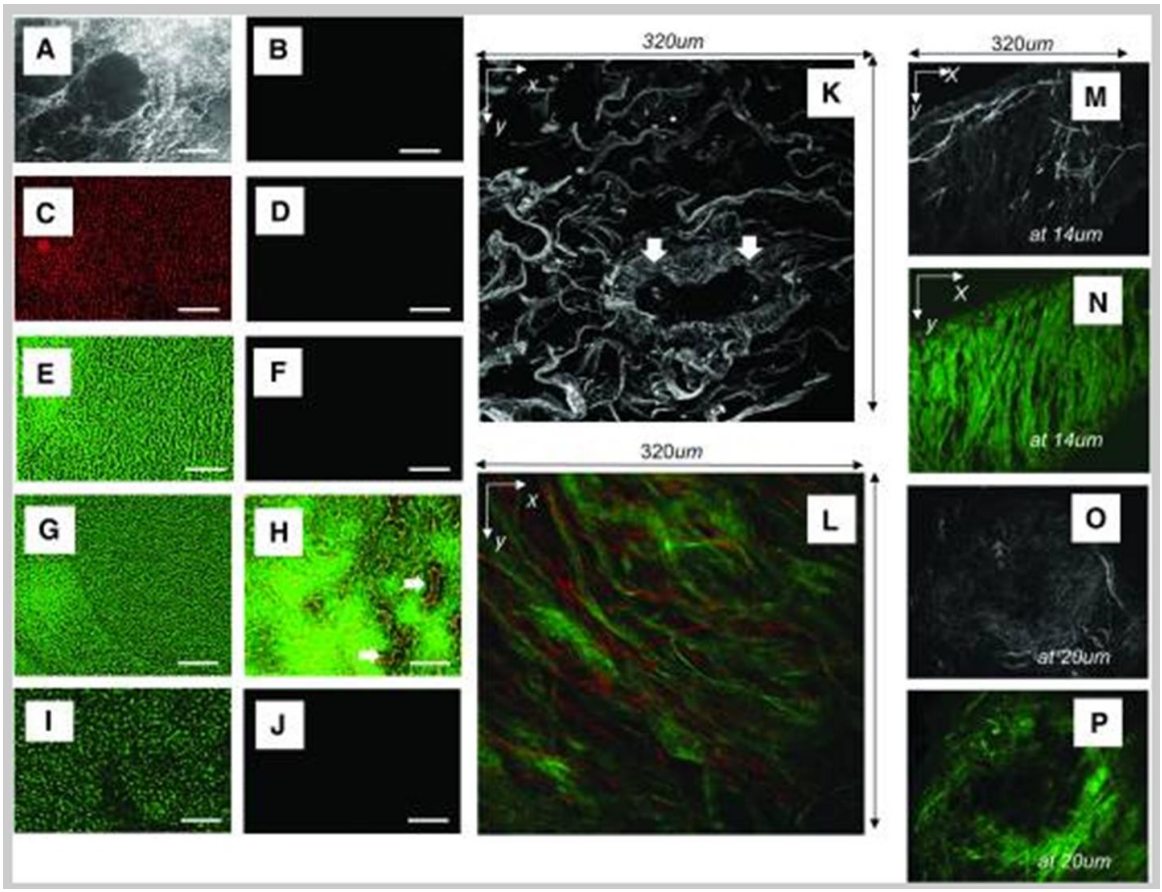

Figure 2.5 Evaluation of AC pig distal lung. (A) Phase contrast microscopic image of AC pig distal lung, scale bar=100 μm. **(B)** Evaluation of presence of nuclei, nuclear material using DAPI, or cell debris by staining for pig MHC-1. **(C)** Staining for presence of elastin (red), scale bar=100 μm. **(D)** Staining control for **(C)**. **(E)** Staining for the presence of collagen (green), scale bar=100 μm. **(F)**Staining control for **(E)**. **(G)** Merge of **(C)** and **(E)**, scale bar=100 μm. **(H)** Merge of section stained for elastin (red) and collagen (green) showing that ECM of small blood vessels remains intact, scale bar=100 μm. White arrows point to blood vessels in AC distal lung. **(I)** Staining for presence of fibronectin (green), scale bar=10 μm. **(J)** Staining control for **(I)**. **(K)** MPM images of distal lung using AF for elastin. White arrows point to ECM of a blood vessel in cross section. **(L)** MPM z-projection of distal lung using combined AF and SHG showing elastin fibers (red) and bundles of collagen (green) imaged to a depth of 140 μm. **(M, N)** Border of AC distal lung using AF at a depth of 14 μm at edge of distal lung indicating high elastin content. **(M)** Bright elastin fibers amid lower intensity collagen (grey background), and **(N)** corresponding SHG of same area in panel **(M)** showing the signal specific to bundles of collagen fibers (green). **(O)** MPM AF at a depth of 20 μm of small bronchiole showing bright elastin fibers and gray background (collagen). **(P)** SHG of same area in **(O)** showing bundles of collagen fibers (green). Reproduced with permission from Nichols *et al*. 2013.

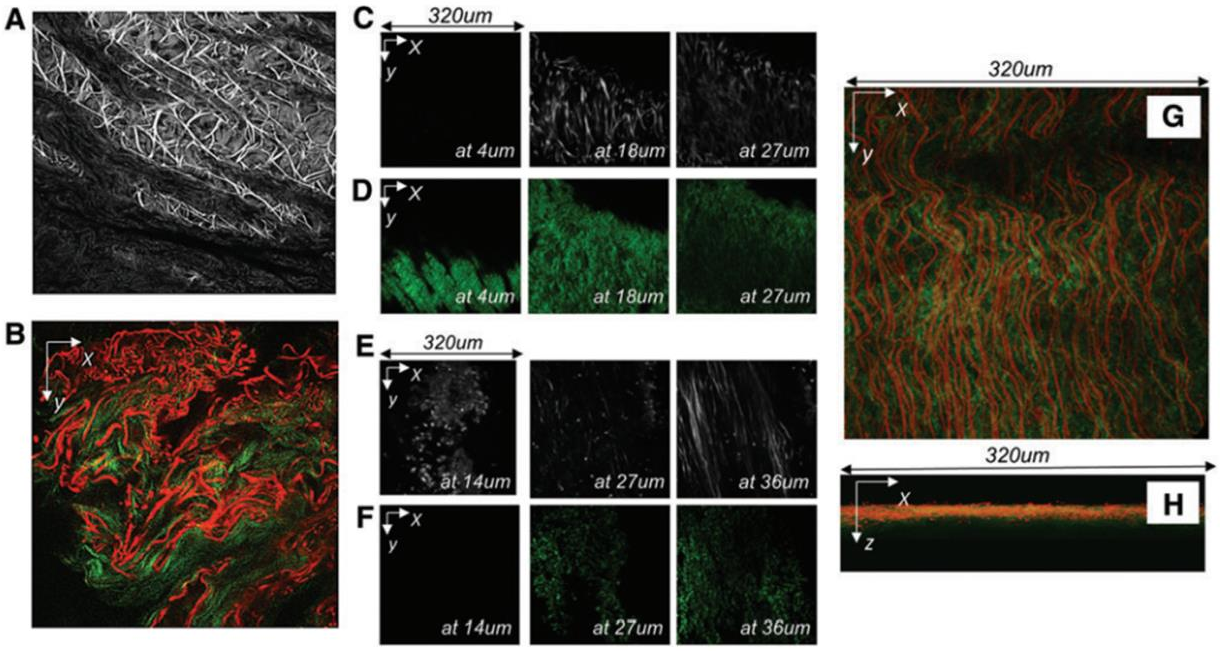

Figure 2.6 Representative MPM images of native pig lung. (A) Distal lung in the expanded state was imaged MPM AF with elastin appearing as thick bright white fibers with less intense collagen AF in the background (grey). The collagen bundles are interlaced with the thick elastin fibers. **(B)** Distal lung in the relaxed state was imaged using SHG for collagen (green) and AF for elastin (red). **(C)** The border of a normal distal pig lung was imaged using MPM AF to show the dense layer of elastin fibers at depths of 4, 18, and 27mm and **(D)** Corresponding SHG (green) images showing collagen fibers in these same regions and at depths of 4, 18, and 27mm. **(E)** AF showing elastin fibers and cells (white) in main stem bronchus from the lumen side at depths of 14 (showing cells in white), 27, and 36mm (showing elastin fibers and cells in white) and **(F)** Corresponding SHG (green) showing collagen fibers in these same regions and at depths of 14, 27, and 36 mm. **(G)** MPM zprojection showing elastin fibers (red) of trachea SHG (green) showing collagen fibers. **(H)** 90 (XZ) cross-sectional view of **(H)**. MPM, multiphoton microscopy. Reproduced with permission from Nichols *et al*. 2013.

Evaluations of AC Human Lung Scaffolds

The bioreactor setup and process of decellularization of human lungs was similar to one used for pig lungs **(Figure 2.7 A-C)**. Examinations of the bronchial airways **(Figure 2.7 D, E)** and branching vasculature **(Figure 2.7 F, G)** indicated these structures did not have any structural damage. Pulmonary function tests of normal healthy patients were compared to those of the AC human lung scaffolds and results showed there no significant differences expect that in the scaffolds, the initial opening pressures were increased **(Figure 2.7 H-J)**. This could have been caused by residual PBS inside the scaffolds.

MPM and SHG 3D reconstruction images showed the collagen content in native human lungs **(Figure 2.8 A-D)** and decellularized AC human lung scaffolds **(Figure 2.8 E-H)**. MPM and SHG were used to identify ROI that were used to quantitate collagen content in native human lungs **(Figure 2.8 C)** and AC human lung scaffolds **(Figure 2.8 D)**. Volumetric representation of ROI volumes for native human lungs **(Figure 2.8 D)** and AC human lung scaffolds **(Figure 2.8 H)** showed that native lungs contained more collagen. Averaged volume density analysis of all ROI intensities from native human lungs and AC human lung scaffolds confirmed that human AC lung scaffolds contained significantly less collagen, that was half the amount in native human lungs **(Figure 2.8 I)**. Similar to pig AC lung scaffolds, the volume fraction of the SHG signal was higher in human AC lung scaffolds **(Figure 2.8 J)**.

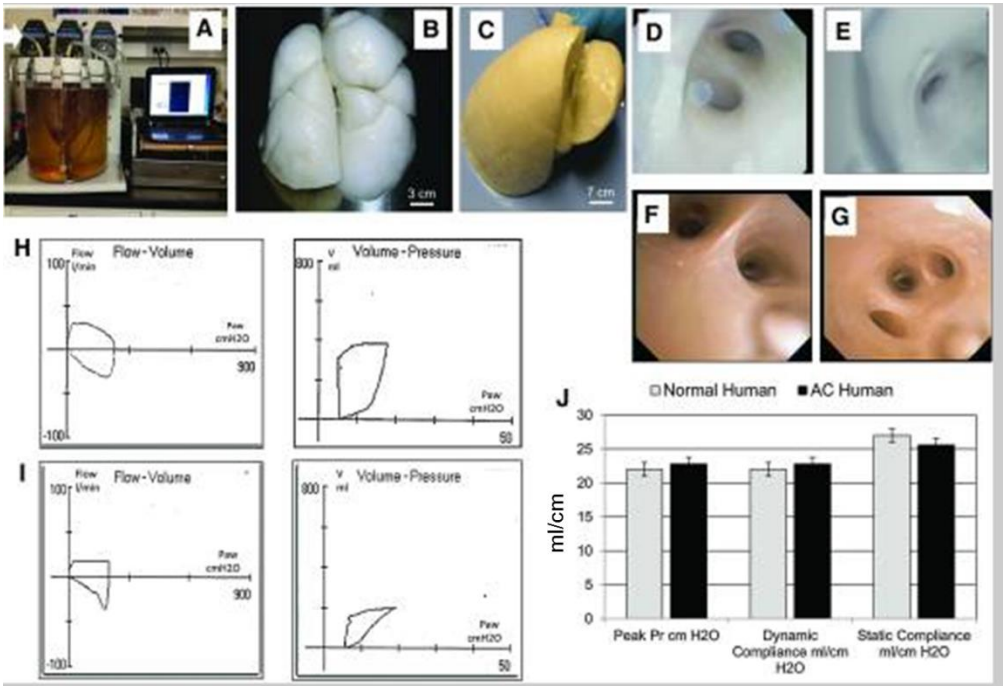

Figure 2.7 Production and evaluation of AC human lung. (A) Image of bioreactor containing an adult lung **(B)** Gross image of an AC pediatric trachea-human lung and **(C)** AC main stem bronchus and lobe of an adult lung. **(D, E)** Bronchoscopic views imaged through right main stem bronchus of the adult AC lobe in panel **(C)** showing the branching airway. **(F, G)** Use of a bronchoscope to view the PA showing branching of blood vessels. **(H, I)** PFTs showing **(H)** normal human ventilation profiles with flow-volume loop (left) and volume-pressure loops (right). **(I)** PFTs of AC human lung showing ventilation profiles and flow-volume loop (left) and volume-pressure loops (right). **(J)** Averaged data for peak pressure, dynamic compliance, and static compliance for *n*=6 adult human lungs measured pre- and post - decellularization. Reproduced with permission from Nichols *et al*. 2013.

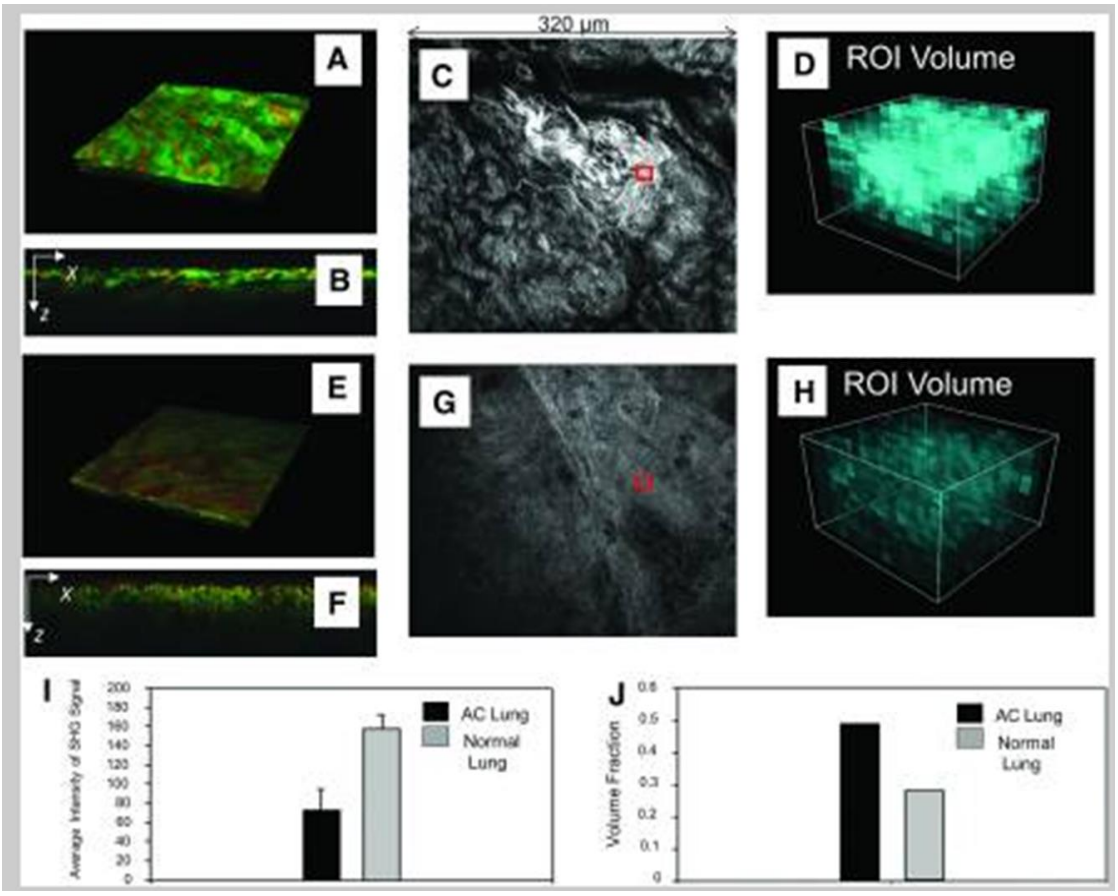

Figure 2.8 MPM-SHG scoring of human native lung versus AC lung. MPM evaluation of normal lung **(A–D)**. **(A)** MPM 3D reconstruction image of normal lung ECM using SHG to image collagen (green) and AF for elastin (red). **(B)** Single XZ cross section of **(A)**. **(C)** SHG to visualize collagen of normal lung. A scored ROI (red box) is shown. **(D)** Volumetric representation of the distribution of the collagen using SHG intensity of the region denoted by red box in **(C)**. **(E–H)** MPM evaluation of AC lung. **(E)** MPM 3D reconstruction image of AC human lung using SHG to image collagen (green) and AF for elastin (red). **(F)** Single XZ cross section of E. **(G)** SHG was used to visualize collagen. A scored ROI (red box) is shown for AC human lung. **(H)** Volumetric representation of the distribution of the collagen SHG intensity of the region denoted by red box in **(G)**. **(I)** Averaged scoring results for normal versus AC lung based on the average of the SHG intensity from each case. **(J)** Volume fraction of the SHG signal in normal versus AC lung showing that although the intensity of SHG is higher in the native lung, the distribution of collagen is more uniform in the AC lung. Reproduced with permission from Nichols *et al*. 2013.

Collagen fibers in AC human lung scaffolds were loosely organized and only a few elastin fibers were present **(Figure 2.9 A, K)**. There are no cells present in the scaffolds **(Figure 2.9 B, H)**. In native human lungs, collagen and elastin fibers are densely packed **(Figure 2.10 A-E)**. Distal regions of the AC human lung scaffold were predominately composed of type I collagen and elastin **(Figure 2.9 C, E, G)**. Fibronectin was also found in distal lung regions of the AC

human lung scaffold **(Figure 2.9 I)**. MPM and SHG examination of the pleura showed the presence of collagen and elastin **(Figure 2.11 A-J)**. The main stem bronchus of the AC human lung scaffold retained its shape and structure **(Figure 2.12 A)** and there were no cells present in the lacunae of the cartilage rings **(Figure 2.12 B-D)**. MPM examination of the main stem bronchus showed the structural configuration of collagen and elastin **(Figure 2.12 E, F)**. Assessments of DNA content after decellularization revealed that the main stem bronchus, pleura and distal lung regions of the AC human lung scaffold contained no DNA **(Figure 2.13 A)**. Even low molecular weight fragmented DNA was removed by decellularization treatment **(Figure 2.13 A)**.

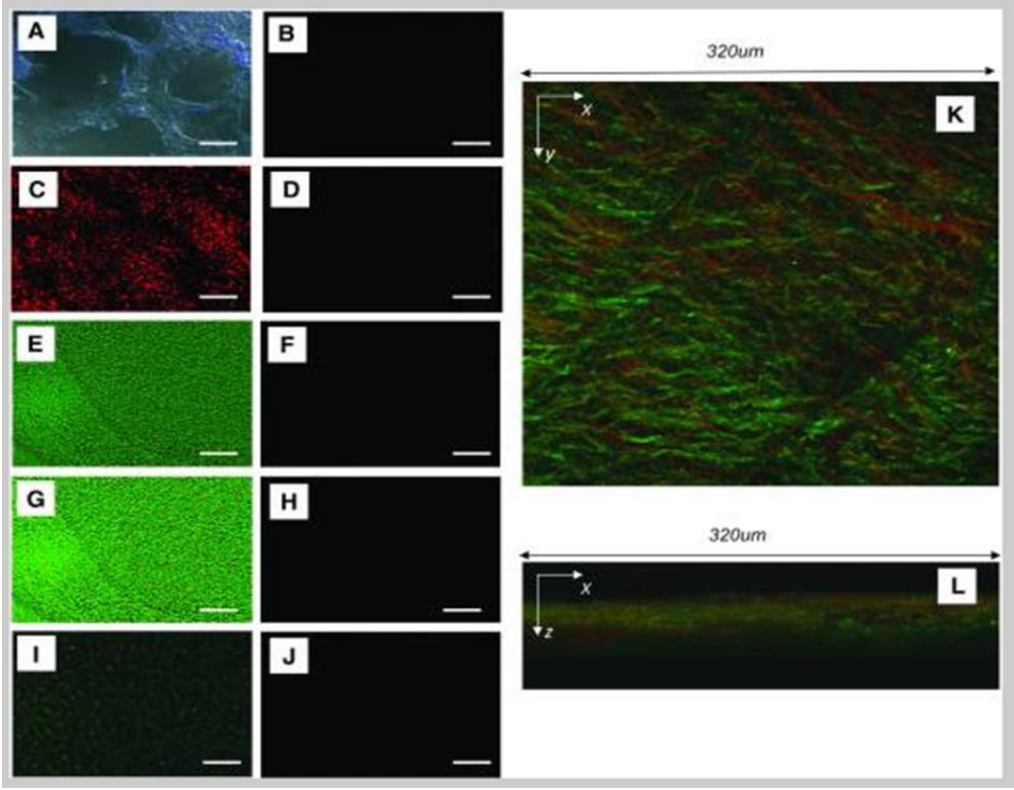

Figure 2.9 Evaluation of AC human distal lung. (A) Phase contrast microscopic image of AC distal lung, scale bar=100 μm. **(B)** Evaluation of presence of nuclei and nuclear material using DAPI. **(C)** Staining for presence of elastin (red), scale bar=100 μm. **(D)** Staining control for C. **(E)** Staining for presence of collagen (green) and cell nuclei using DAPI (blue), scale bar=100 μm. **(F)** Staining control for **(E)**. **(G)**Merge of **(C)** and **(E)**, scale bar=100 μm. **(H)** Evaluation of cell debris using staining for human MHC-1 (green) in AC distal lung, scale bar=100 μm. **(I)** Staining for fibronectin (green), scale bar=100 μm. **(J)** Staining control for **(I)**. **(K)** MPM images of distal lung using combined AF with SHG for elastin (red) and collagen (green). **(L)** 90° (XZ) cross-sectional view of (K). Reproduced with permission from Nichols *et al*. 2013.

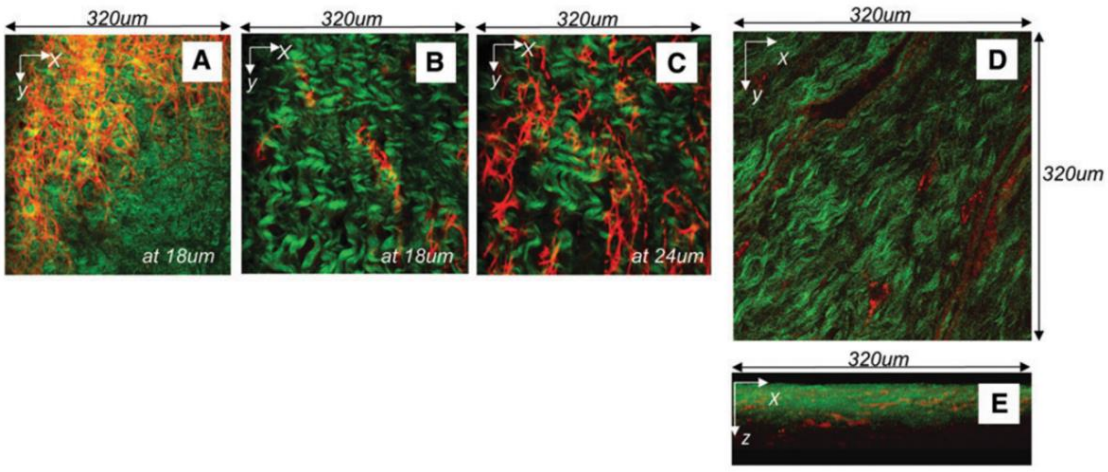

Figure 2.10 Representative MPM images of native human lung tissue. (A) MPM of normal human pleura showing outer elastin mesh network (red) and underlying collagen layer (green). **(B–E)** Regions of distal lung were imaged using AF for elastin fibers or cells (red) and SHG for collagen (green). **(E)** 90 (XZ) cross-sectional view of D. SHG of the corresponding areas at these same depths shows the dense array of wavy collagen fibers found in normal lung tissues, collagen (green) to a depth of 60 mm. Reproduced with permission from Nichols *et al*. 2013.

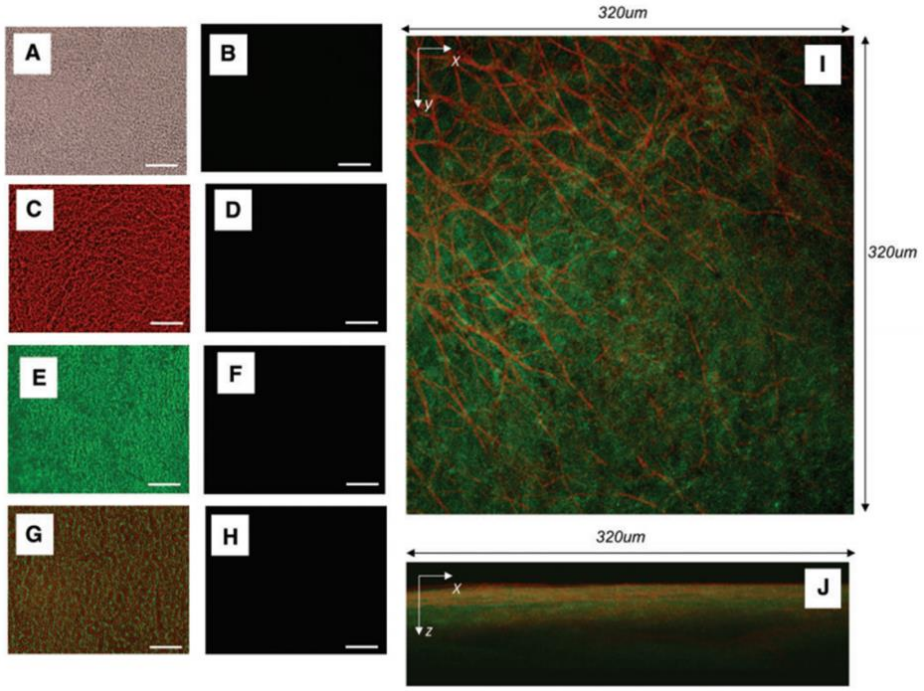

Figure 2.11 Evaluation of AC human pleura. (A) Phase contrast microscopic image of AC human pleura, scale bar = 100 mm. **(B)** Evaluation of residual nuclei and nuclear material in AC pleura using DAPI (blue), scale bar = 100 mm. **(C)** Staining for presence of elastin (red), scale bar = 100 mm. **(D)** Staining control for **(C)**. **(E)** Staining for presence of collagen (green), scale bar = 100 mm. **(F)** Staining control for **(E)**. **(G)** Merge of C and E, showing elastin (red) and collagen (green), scale bar = 100 mm. **(H)** Staining for presence of cell debris using human MHC class-I (green). **(I)** MPM z-projection image of pleura AF with SHG:

elastin (red) and collagen (green). **(J)** 90 (XZ) cross-sectional view of (H). Reproduced with permission from Nichols *et al*. 2013.

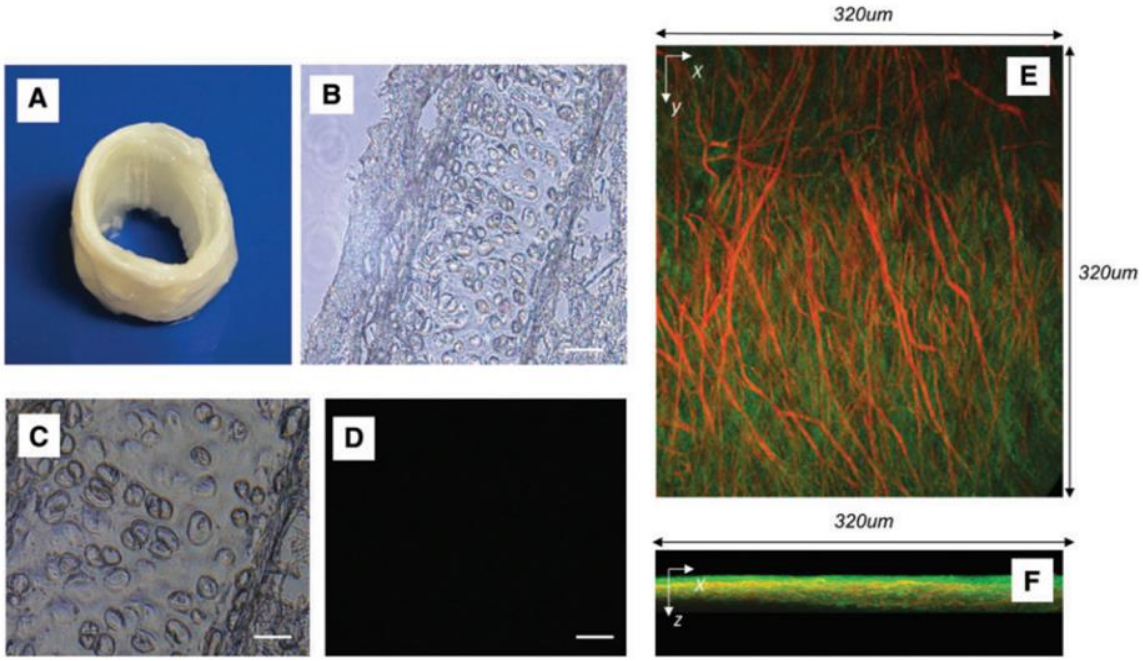

Figure 2.12 Evaluation of AC human main stem bronchus. (A) Gross image of 1'' section of AC human main stem bronchus. **(B, C)** Phase contrast images of AC bronchus showing that there are no cells or nuclei left in the lacunae. **(B)** Scale bar = 20 mm. **(C)** Scale bar = 10 mm. **(D)** Staining for cell debris using human MHC-1 (green) and DAPI (blue), scale bar = 10 mm. **(E)** MPM images of human AC main stem bronchus using combined AF for elastin (red) and with SHG for collagen (green). **(F)** 90 (XZ) cross-sectional view of **(E)**. MHC-1, major histocompatability complex-1. Reproduced with permission from Nichols *et al*. 2013.

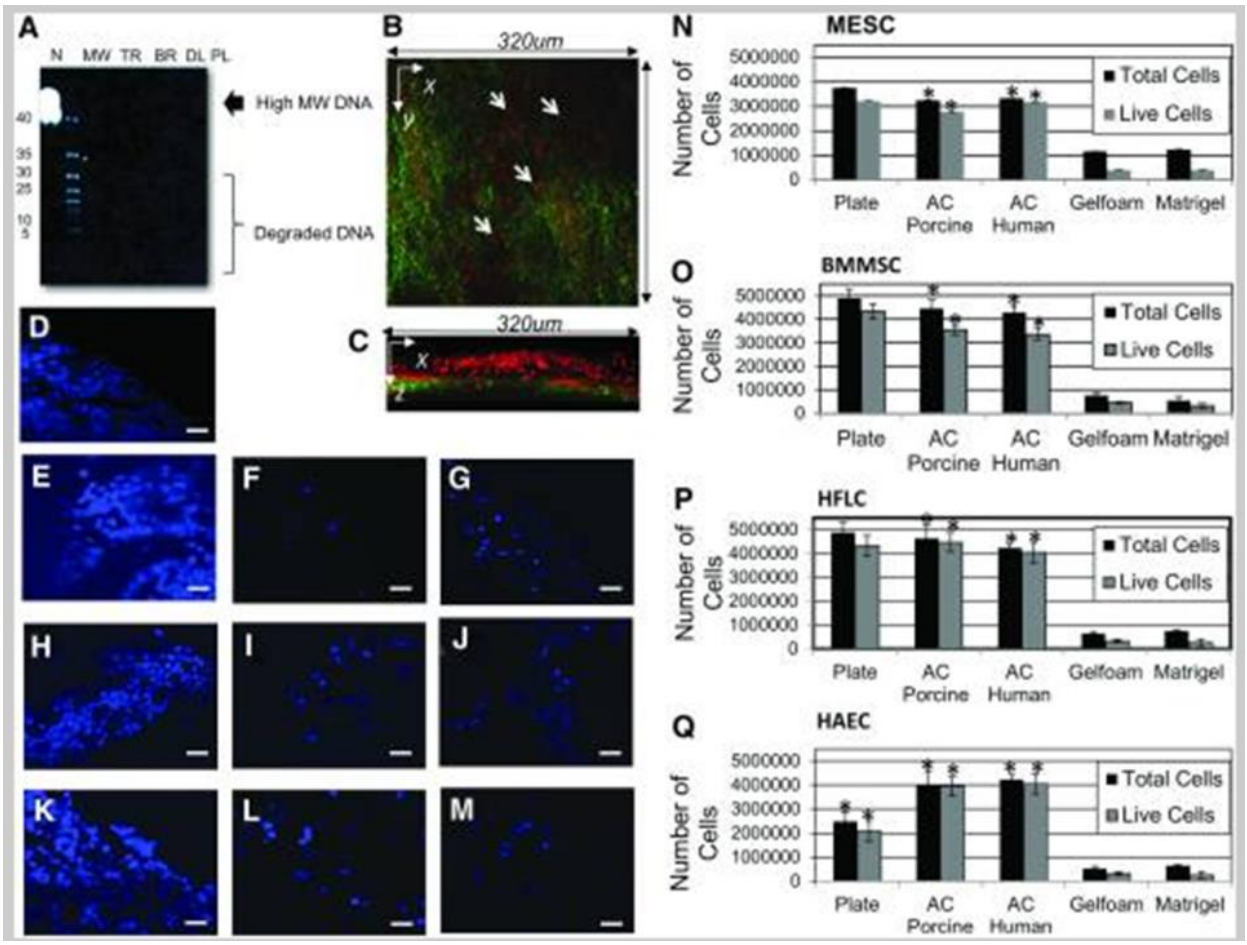

Figure 2.13 Post production DNA content evaluation and assessment of cell viability. (A) Evaluation of residual DNA in a normal human lung pre-decellularization and for one representative human lung post decellularization. **(B)**MPM z-projection of distal recellularized AC Pig lung showing AF arising from elastin fibers and cells (red) and SHG from collagen (green). Cells are also designated by white arrows. **(C)** 90° (XZ) cross-sectional view of **(B)**. Note cells (red) attached to the ECM. **(D)** DAPI staining of normal lung. **(E, F, G)** DAPI staining of MESC nuclei (blue) cultured for 7 days or cells cultured on **(E)** AC pig lung scaffold, **(F)** Gelfoam or **(G)**Matrigel. **(H, I, J)** DAPI staining of HFLC nuclei (blue) cultured on **(H)** AC pig lung, **(I)** Gelfoam or **(J)**Matrigel. **(K, L, M)** DAPI staining of nuclei of pig BMMSC cultured on **(K)** AC pig lung, **(L)** Gelfoam or **(M)**Matrigel. **(N–Q)** Averaged data for evaluation of total number of cells and number of viable cells harvested at 7 days from each scaffold material. Average number of total cells and viable cells at 7 days for **(N)** MESC, **(O)**BMMSC, **(P)** HFLC, or **(Q)** HAEC after culture on AC pig lung, AC human lung, Gelfoam or Matrigel scaffolds. Both AC pig lung and AC human lung had significantly more cells and viable cells at 7 days of culture than either Gelfoam or Matrigel (*p<0.05). HAEC AC pig and AC human scaffold constructs also yielded significantly more intact primary HAEC and more viable HAEC than plate culture (*p<0.05). MESC, murine embryonic stem cells; BMMSC, bone marrow-derived pig mesenchymal stem cells; HFLC, human fetal lung cells; HAEC, human alveolar epithelial type II cells. Reproduced with permission from Nichols *et al*. 2013.

Assessments of Cell Attachment and Cell Viability in Cells Cultured on AC Pig or Human Lung Scaffolds

The ability of AC pig and human lung scaffolds to support cell attachment was examined by culturing different cell types in 0.5 cm^3 scaffold pieces. Cell attachment also was examined in 0.5 cm^3 pieces of Gelfoam and Matrigel scaffolds as a comparison. Cell types used included mESC, HFLC and PBMMSC. Examinations of cell attachment were done after 7 days of culture. All cell types, evaluated mESC, HFLC and PBMMSC were able to attach to AC pig or AC human lung scaffolds **(Figure 2.13 B, C, E, H, K).** Fewer cells attached to Gelfoam and Matrigel when compared to AC pig or human lung scaffolds **(Figure 2.13 F, G, I, J, L, M).** Evaluations of total numbers of cells and total numbers of viable cells isolated from each the cell-scaffold constructs after 7 days of culture are shown for MESC, BMMSC, HFLC, and pHAEC **(Figure 2.13 N-Q)**. Plate cultures of all the individual cell types were used as controls. For all the cell types evaluated, retention of cells and cell viability was significantly higher when cells were cultured in AC pig or human lung scaffolds than in Gelfoam or Matrigel **(Figure 2.13 N-Q)**. Cell-scaffold constructs of pHAEC and AC pig or human lung scaffolds yielded higher numbers of total cells and total viable cells when compared plate cultures **(Figure 2.13 N-Q)**. There were no significant differences in the total number of cells and total number of viable cells between AC pig and human lung scaffolds. When compared to AC human lung scaffolds produced from different detergents, scaffolds produced using 1% had higher numbers of total PHAEC and higher numbers of viable PHAEC **(Figure 2.14 A)**

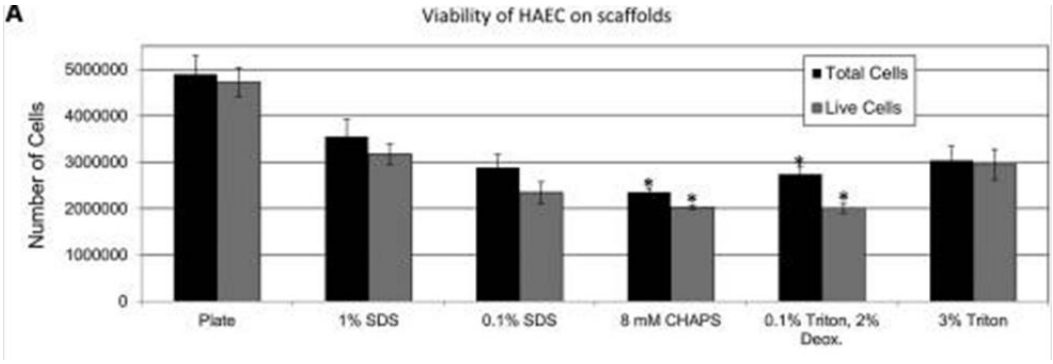

Figure 2.14 Post production assessment of primary HAEC cultured on AC human scaffolds produced using different detergents. (A) Averaged data for evaluation of total number of cells and number of viable primary HAEC harvested at 7 days from scaffolds produced using different detergents. (*$p<0.05$). Reproduced with permission from Nichols *et al*. 2013.

PHAEC attachment to AC human lung scaffolds was further examined, because these are the cell types found in the alveolar epithelium of native lungs. After 7 days of culture, PHAEC had attached and covered a large part of the scaffold **(Figure 2.15 A, B)**. The pHAEC isolated from donor lungs were predominately pro-SPC-positive type II AEC. On day 1 **(Figure 2.15 C, D)**, day 5 **(Figure 2.15 F)** and day 7 **(Figure 2.15 G)** after seeding, pHAEC predominately expressing pro-PSC were found to attach to the scaffold in clumps. Over time, a few pockets of AQP5-positive cells were found in the cell-scaffold constructs, indicating the presence of type I AEC **(Figure 2.15 H)**.

Human Immune Response to AC Human Lung Scaffolds Produced Using Different Detergents

T cell activation and chemokine production was examined in cell-scaffold constructs of human MNL and AC human lung scaffolds produced using different detergents to assess the immunogenicity of scaffold. The different detergents tested are the same as the ones mentioned above, they include 1% SDS, 0.1% SDS, 8mM CHAPS, 0.1% triton X-100 plus 2% sodium deoxycholate or 3% triton X-100. T-cell activation was assessed by measuring CFSE loss in CD3-postive cells and by the production of chemokines CCL2/MCP-1, CCL5/RANTES, CXCL9/MIG,

and CXCL10/IP-10 (some of which are involved in graft rejection, including CCL5, CXCL-9, CCL2, CXCL10). Results from these T-cell activation assays indicated that the percentage of CD3-postive cells with CFSE loss was significantly lower in AC human lung scaffolds produced using 1% SDS ($p<0.05$) than in AC human lung scaffolds produced using 0.1% SDS, 8mM CHAPS, 0.1% triton X-100 plus 2% sodium deoxycholate or 3% triton X-100 **(Figure 2.16 A)**. Production of CCL5, CXCL9, CCL2 and CXCL10 was significantly lower in AC human lung constructs produced using 1% SDS ($p<0.05$) than in AC human lug scaffolds produced using 0.1% SDS, 8mM CHAPS, 0.1% triton X-100 plus 2% sodium deoxycholate but not 3% triton X-100 **(Figure 2.16 B)**. Our results indicate that AC human lung scaffolds produced using 1% SDS were less immunogenic than scaffolds produced using 0.1% SDS, 8mM CHAPS or 0.1% triton X-100 plus 2% sodium deoxycholate.

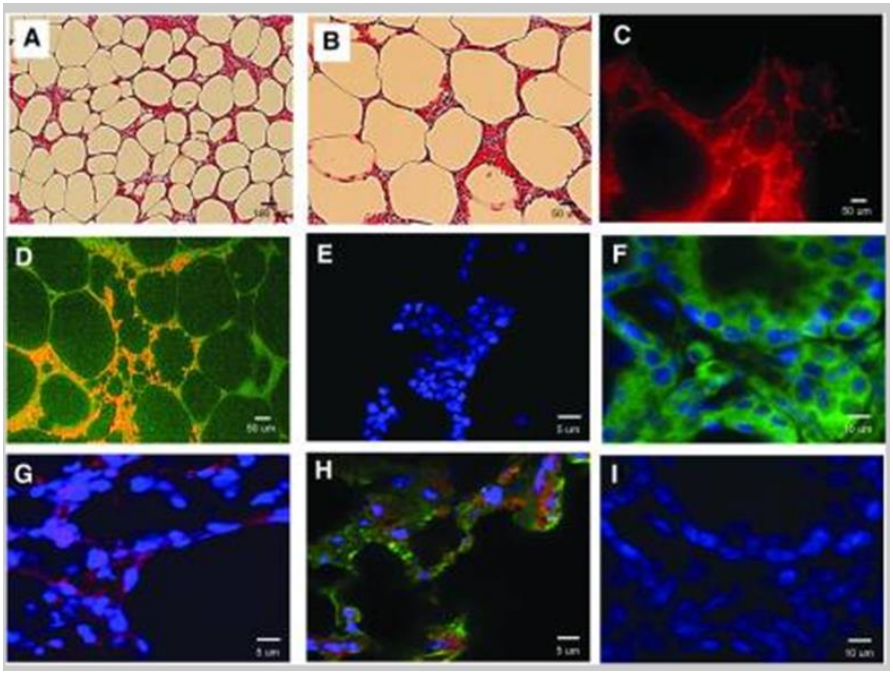

Figure 2.15 Human alveolar epithelial cell culture (A) H&E of HAEC cultured for 7 days on AC human lung, scale bar=100 μm. (B) H& E of HAEC cultured for 7 days on AC human lung, scale bar=50 μm. (C) Examination of section of HAEC on human lung, day 1 post seeding of cells, stained to show pro-SPC (red). Scale bar=50 μm (D) Examination of section of HAEC on human lung, day 1 post seeding of cells, stained to show pro-SPC (red) showing cell adhesion on portions of scaffold. Scale bar=50 μm (E) Staining control for panel (F). Scale bar=5 μm. (F) Examination of section of HAEC on

human lung, 5 days post seeding of cells, stained to show pro-SPC (green). Scale bar=10 μm. (G) Examination of section of HAEC on human lung, 7 days post seeding of cells, stained to show pro-SPC (red). Scale bar=5 μm. (H) Section of HAEC on AC human lung scaffold, 7 days post seeding of cells, stained to show pro-SPC (green) and aquaporin 5 (red). Scale bar=5 μm. (I) Staining control for (C–H). Scale bar=10 μm. pro-SPC, pro surfactant protein C. Reproduced with permission from Nichols *et al*. 2013.

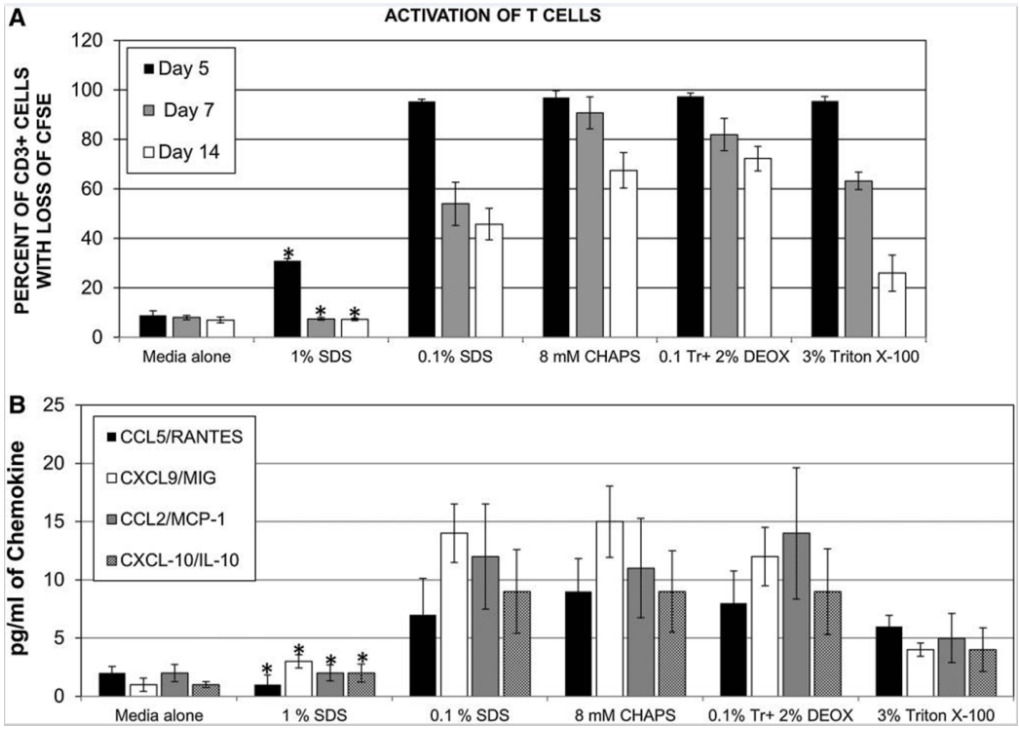

Figure 2.16 Post production assessment of human immune cell activation. **(A)** Culture of human MNL with human AC distal lung produced using 1% SDS, 0.1% SDS, 8 mM CHAPS, and 0.1% Triton X-100 followed by 2% Deoxycholate or 3% Triton X-100 detergents to determine activation of CD3 T Cells. Values from cells isolated from triplicate cultures for each scaffold were averaged to determine loss of CFSE label. Human lung scaffold produced using 1% SDS induced significantly less activation of human MNLs than did scaffolds produced using other detergents. (*p<0.05). **(B)** Examination of chemokine production by MNLs cultured with AC human lung scaffolds produced using different detergents. Lung scaffold produced using 1% SDS induced significantly lower levels of chemokines than did culture of MNLS with AC human lung scaffolds produced using other detergents (*p<0.05). Reproduced with permission from Nichols *et al*. 2013.

DISCUSSION AND CONCLUSION

Not much work has been done in the production of AC human lung scaffolds much less whole lung scaffolds or in the production of whole AC lung scaffolds from larger animal models. In this study, we have developed a decellularization procedure for the production of whole AC

lung scaffolds from porcine or human lungs. We showed that decellularization with SDS in a perfusion bioreactor was effective in removing cells, cell debris and DNA from native pig or human lungs. Post-production assessments of AC pig or human lung scaffolds were done using various methods, including bronchoscopy, PFT, MPM and SHG and histology in order to evaluate gross respiratory tract structures, mechanical function and characterize the structural proteins of the remaining ECM. Our results showed that the AC pig or human lung scaffolds produced retained the ECM of gross structures such as the pleura, trachea, bronchi, distal lung and blood vessels. The remaining ECM was predominately composed of type I collagen and elastin, which are key structural proteins of the native lung ECM that are essential for mechanical functions. Whole AC lung scaffolds contain the necessary structural components to support lung tissue formation.

Evaluations of cell attachment and cell viability using small-scale cell-scaffold constructs indicated that porcine and human AC lung scaffolds produced using 1% SDS supported cell attachment and cell viability better than those produced using other detergents that were better than Gelfoam or Matrigel. To develop a better understanding of how decellularization would affect scaffold immunogenicity, we examined the human immune response to scaffolds by using MNL from 10 donors. Our assessments of the immunogenicity of AC lung scaffolds revealed that scaffolds produced with 1% SDS, did not elicit the activation of T-cells or the production of pro-inflammatory chemokines.

We have shown the feasibility of producing whole AC pig or human lung scaffolds that have the potential to be used for bioengineering lung tissue. Before we can realize the goal of producing bioengineered human lung tissue, we must first examine appropriate cell sources and develop recellularization procedures in order to bioengineer lung tissue with functional capabilities

that closely resemble those of native lungs. The successful *in vitro* bioengineering of human lung tissue can pave the way for the development of 3D HoC that could be used as models for a wide range of studies.

CHAPTER 3*

Production of Human Whole Organ Constructs: Bioengineered Human Pediatric Lungs

INTRODUCTION

In our previous study, detailed in Chapter 2, we developed a decellularization procedure for the production of whole AC human lung scaffolds that retained essential components of the ECM and were capable of supporting cell attachment and maintaining cell viability. In this study, we have utilized primary cells isolated from discarded whole human lungs as a cell source we attempted to recellularize whole AC human lung scaffolds with the goal of bioengineering whole pediatric lungs. Initial use of small-scale cell-scaffold constructs allowed us to examine cellular responses to help gain insight on how the number of cells and pre-treatment of AC lung scaffolds would influence tissue development. These initial assessments in a small-scale construct allowed us to scale up and develop recellularization protocols and examine tissue development in much larger single lung scaffolds and eventually whole lung scaffolds for the production of human bioengineered lungs. The use of single lung scaffolds and surrogate cell populations allowed us to identify the numbers of cells needed for installations, the order the cells were installed or seeded, perfusion flow rates and methods to manage large organ culture in a bioreactor. Upon establishing appropriate cell installation protocols for recellularization, pediatric whole AC lung scaffolds were recellularized using primary human lung tracheal/bronchial epithelial cells, alveolar epithelial cells and endothelial cells. Recellularized pediatric lungs were composed of bronchial and alveolar epithelium with evidence of alveolar-capillary formation. Bioengineered lungs were also capable

Chapter * published and taken from: Nichols, J.E., La Francesca, S., Vega, S.P., Niles, J.A., Argueta, L.B., Riddle, M., Sakamoto, J., Vargas, G., Pal, R., Woodson, L. and Rhudy, J., 2017. Giving new life to old lungs: methods to produce and assess whole human paediatric bioengineered lungs. *Journal of tissue engineering and regenerative medicine*, *11*(7), pp.2136-2152.

of producing surfactant proteins-C and –D. Pulmonary function tests were performed and results indicated normal lung compliance measurements.

MATERIALS AND METHODS

Bioreactor

The prototype Riddle bioreactor was initially used by our laboratory for production of whole AC human lung scaffolds in our previous study [88]. The stand that supports three stepper motors and is used for placement of the chamber was built using star board high-density polyethylene (HDPE) plastic. The three Nema 23 435 oz. 4.25A stepper motors (Longs, Motor, Changzhou City, China) were used to run Materflex Easy-load II L/S peristaltic pump heads (Cole-Parmer, Vernon Hills, IL, USA). A small computer numerical control (CNC) machining mill was built as controller for the bioreactor system. CNC machining software and a break-out board purchased from Probotox (Peoria, IL, USA) were used as controls for the stepper motors. The chamber was constructed from a 3.5 gal Top Fin Brand 180˚-view plastic aquarium (Petco, Houston, Texas, USA). The lid to the chamber was constructed from HDPE plastic and plumbing hardware (Lowes Home Improvement Store, Houston Texas, USA).

Decellularization of Human Lungs

Human lungs were procured as discarded human tissues following protocols approved by Institutional Review Boards (IRB) at UTMB or Methodist Hospital Research Institute. A total of six human lungs were procured. Three adult single lungs (SL), SL-1, SL-2 and SL-3 and three pediatric whole lungs (PL), PL-1, PL-2 and PL-3. SL-1 and SL-2 were larger than PL-3. PL-1 was from a 7-month old child, PL-2 was from a 19-month old child, and PL-3 was from a 5-month old child. Upon procurement, human lungs were stored at -80˚C and were kept in storage at least 1

month prior to decellularization. Decellularization was done as previously described [88, 89] and detailed in Chapter 2. On the day of decellularization, lungs were thawed in a 45˚C water bath before being placed in a perfusion bioreactor chamber. To setup the lungs for perfusion, individual cannulas were used to connect the pulmonary artery and main stem bronchus to allow for control of separate pumping systems.

Day 1 of decellularization was initiated by immersing the lungs in 1% SDS solution and pumping 1% SDS solution into the individual cannulas of the pulmonary artery and trachea. 1% SDS was perfused into the pulmonary artery at a rate of 60 ml/min and into the trachea at a rate of 120 ml/min. 1-3 liters of 1% SDS were used to fill and expand the lungs. Expanded lungs were emptied every hour for 3 hours and at the end of each 3 hour time point, fresh 1% SDS solution was added to the chamber to begin perfusion again. The concertation of SDS was lowered to 0.1% on day 3 of decellularization and the perfusion rates were kept the same. Fresh 0.1% SDS was added to the bioreactor chamber every day for days 4, 5 and 6 of decellularization.

By day 5, lungs were perfused with distilled water at a rate of 500 ml/min for 12 hours. Distilled water in the bioreactor chamber was replaced every 3 hours. Lungs were then perfused with 3% H_2O_2 for 1 hour followed by perfusion with sterile water for 12 hours at a rate of 500 ml/h. Sterile water was replaced every 3 hours. Sterile water was then removed from the bioreactor chamber and lungs were perfused with phosphate-buffered saline (PBS) containing streptomycin (90 µg/ml), penicillin (50 U/ml) and amphotericin (90 µg/ml) for 5 hours at rate of 500 ml/h. AC human lung scaffolds were stored in fresh PBS containing antibiotic and antimycotic solutions.

Isolation of Primary Human Lung Cells and Primary Human Lung Vascular Cells

Human lungs were procured as discarded human tissues following protocols approved by Institutional Review Boards (IRB) at UTMB or Methodist Hospital Research Institute. A total of three adult double-lung sets were used for primary cell isolations. Whole human lungs were flushed with 1 liter of PBS containing 100 µg/ml primocin (InvivoGen, San Diego, CA, USA). The lungs were cut to obtain pieces of human distal lung while avoiding bronchial airways and blood vessels. Pieces of distal lung were then minced into smaller fragments that were treated with 1 mg/ml collagenase/dispase (Roche Diagnostics, Indianapolis, IN, USA) for 7 hours at 4˚C. The inner epithelial lining of the trachea and bronchial airways was stripped off the tissue to isolate the tracheal and bronchial cells. The tracheal and bronchial epithelial lining collected was minced and treated with 1mg/ml collagenase/dispase for 4 hours at 4˚C. After incubation with collagenase/dispase, all cells isolated were filtered sequentially through 100 and then 40 µm sterile filters (BD Falcon, San Jose, CA, USA). The filtered solutions containing the cells were centrifuged to collect the pellets of primary human lungs cells and primary human tracheal/bronchial and do cell counts. P-lung cells were cultured in T75 filtered flasks containing SAGM with 1% heat-inactivated human AB serum and primocin (100 µm/ml). P-TB cells were cultured in T75 filtered flasks containing bronchial epithelial growth medium (BEGM; Lonza, San Jose, CA, USA) with 1% heat-inactivated human AB serum and primocin (100 µm/ml).

Primary human lung vascular (Pl-vasc) cells were isolated by stripping off the inner endothelial lining of blood vessels from the lungs. These endothelial sheets then were finely minced and treated with 1mg/l collagenase/dispase for 4 hours at room temperature. Sterile 100 µm and 40 µm filters were used to filter the cells followed by centrifugation to collect cell pellets.

Primary human vascular cells were cultured in T25 filtered flasks containing endothelial growth medium (EGM; Lonza).

The double-lung set from donor 1 yielded 9.12 x 10^9 primary lung (P-Lung) cells, 2.94 x 10^8 primary lung vascular (PL-Vasc) cells and 1.63 x 10^8 primary tracheal/bronchial (P-TB) cells. The double lung set from donor 2 yielded 2.59 x 10^9 P-Lung cells, 2.41 x 10^8 PL-VASC cells and 2.2 x 10^7 P-TB cells. The double lung set from donor 3 yielded 4.83 x 10^9 P-Lung cells, 2.88 x 10^8 PL-VASC cells and 1.51 x 10^8 P-TB cells.

Creation of Immortalized Human Lung Cells and Immortalized Human Lung Vascular Cells from Primary Cells

PHLC and PHLVC were immortalized when confluence reached 50-70% in culture flasks. Immortalization was done using the PA317 LXSN 16E6E7 cell line (ATCC, Manassas, VA, USA) that produces the pLXSN16E6E7 retrovirus vector. A transduction mixture was prepared with 200 µl PA317 LXSN 16E6E7 cells supernatant, 20 µl protamine sulfate (1 µg/µl; MP Biomedical, Santa Ana, CA, USA) and 1800 µl serum-free SAGM for pHLC or EGM for pHLVC. Medium was aspirated from the flasks and sterile PBS without Ca2+ and Mg2+ was used to rinse the cell monolayers. The transduction mixture was then added to the cells. The volume of the transduction mixture was based on the surface volume of the flasks. Cells were incubated with the transduction mixture for 6 hours at 37˚C with 5% CO_2 and were occasionally rocked. Serum-free SAGM or EGM was then replaced SAGM or EGM containing serum and cells were incubated overnight at 37˚C with 5% CO_2. After 24 hours, medium was replaced with fresh SAGM or EGM. After 48 hours, the medium was changed again and replaced with medium containing 50 µg/ml (G418; Corning Cellgro, Manassas, VA, USA) for selection of transduced cells that contained the neomycin resistance gene from the vector. Immortalized human lung cells (iHLC) and

immortalized human lung vascular cells (iHLVC) were passaged as needed and aliquots of cells were frozen until use for experiments.

Production of Human Platelet-rich Plasma

Whole human blood was purchased form the UTMB blood bank. To isolate the platelet fraction from whole human blood, 50 ml aliquots of blood were centrifuged for 15 minutes at 275 x *g* as previously described [91, 92, 93]. The plasma with platelets was collected from the top portion of the tube. PRP was flash-frozen by liquid nitrogen and stored at -80˚C. PRP samples were then thawed and centrifuged at 3000 x g for 20 minutes at 4˚C to maintain low levels of platelet activation. After centrifugation, two-thirds of the supernatant was removed and the pellet was resuspended in the plasma that remained to calculate platelet concentrations. Platelet concentrations were estimated to be 825.50±25.22 ($x10^4$/µl). PRP was stored at 4˚C to prevent clumping.

Influence of Cell Numbers and Pre-treatment of AC Human Lung Scaffolds on Tissue Development

The effects of pre-treatment of AC human lung scaffolds and the numbers of cells seeded onto the scaffolds were examined using small cell-scaffold constructs to assess tissue development. These small-scale constructs allowed us to perform initial assessments before scaling up and making an effort to recellularize whole human pediatric lungs. A total of forty-five 2.5 cm^3 pieces of AC human lung scaffold were used for this experiment. Fifteen pieces were pretreated by injecting SAGM containing 10% heat-inactivated human AB serum into the center of each scaffold piece. Fifteen other pieces were pre-treated by injecting SAGM containing 10% PRP into the center of each scaffold piece. Another set of fifteen scaffold pieces was not treated. For each of the pre-treatment groups mentioned above, sets of five scaffold pieces were seeded with 100,000

pHLC, 500,000 pHLC or $1x10^6$ pHLC. To do this, pHLC were injected using a 20-gauge catheter, into the center of each scaffold piece. Cell-scaffold constructs were centrifuged at 100 x g to help spread the cells within each scaffold piece. Cell-scaffold constructs were placed into individual wells of a 24-well culture plate containing SAGM and were cultured for 24 hours at 37˚C with 5% CO_2. After 24 hours, each set of 5 cell-scaffold constructs (same pre-treatment, same number of cells) were placed in individual rotary bioreactor chambers and were cultured for 7 days at 37˚C with 5% CO_2. A 0.5 cm^3 slice was taken from each of the cell-scaffold constructs for use in histological examination with H&E staining for evaluation of cell attachment and tissue formation. The remaining piece of cell-scaffold constructs was used to isolate the cells and determine total cell counts and total viable cells. Total cell counts and total viable cells were determined as previously described [88].

Recellularization of Human Lung Scaffolds

Three AC human single-lung scaffolds produced from SL-1, -2 and -3 were used to develop cell installation protocols for recellularization. Cell installation protocols were developed using I-lung, iHLVC, human fetal lung cells (13LU) and human umbilical cord vascular endothelial cells (HUV-EC-C; ATCC, Manassas, VA, USA). Once cell installation protocols were examined, modified and developed using AC human single-lung scaffolds (SL-1, SL-2 and SL-3), AC human lung scaffolds produced from PL-1, -2 and -3 were used for recellularization. Cell installations for all lung scaffolds were done in a perfusion bioreactor. A bronchoscope was used to place a single catheter into the main stem bronchus of single lung scaffolds or whole lung scaffolds. Tygon tubing with a 3/32 inner diameter and a 7/32 outer diameter was placed into the opening of the pulmonary artery and the opening of the pulmonary vein. Tubing attached to the pulmonary vein terminated in a waste receptacle or circulated back to the pulmonary artery following vascular cell installation.

Two separate pumps were used to control perfusion into the pulmonary artery (pump 1) or the main stem bronchus (pump 2) to allow for different medium flow rates to be used for respiratory tract of the lungs, or the vasculature during culture. A third pump was used to pump medium in or out of the bioreactor chamber. Catheter ends were pulled up the main stem bronchus tube to the port controlled by pump 1 and sterile plastic zip ties were used to attach lungs to a metal flange at the bottom of the bioreactor chamber. With this setup, the main stem bronchus ports could be easily accessed for cell installations. Dulbecco's modified Eagle's medium (DMEM)/F-12 containing 10% heat-inactivated human AB serum, streptomycin (90 µg/ml, penicillin (50 U/ml), and amphotericin B (25 µg/ml) was used to fill the bioreactor chamber containing the lung scaffolds and was left in culture at 37˚C with 5% CO_2 overnight to check for contamination of lung scaffolds. Once sterility of the lung scaffolds was verified by overnight culture, cell installations were performed.

Table 3.1 Cell installations protocol for (A) Single lung-1 (B) Single lungs-2 and -3 (C) Pediatric lungs 1-3 Reproduced with permission from Nichols *et al*. 2016.

Day of installation	Cell type installed	Viability (%)			Number of cells installed	Method of installation	Flow rate for cell installation	Flow rate between installations
(A) *SL-1*								
1	13 LU	98			1 installation of 3.5×10^7	Tracheal catheter	5 ml/min	5 ml/h
5	I-Lung	95			1 installation of 3.5×10^7	Tracheal catheter	5 ml/min	5 ml/h
7	I-Lung	98			1 installation of 3.5×10^7	Tracheal catheter	5 ml/min	5 ml/h
10	I-Lung	97			1 installation of 3.5×10^7	Tracheal catheter	5 ml/min	5 ml/h
15	HUVECs	97			1 installation of 3.5×10^7	Pulmonary artery	1 ml/min	1 ml/h
20	HUVECs	97			1 installation of 3.5×10^7	Pulmonary artery	1 ml/min	1 ml/h
(B) *SL-2 and SL-3*								
		SL-2		SL-3				
1	IL-Vasc	97		97	1 installation of 3.5×10^7	Tracheal catheter	0.5 ml/min	0.5 ml/h
5	IL-Vasc	97		97	1 installation of 3.5×10^7	Tracheal catheter	0.5 ml/min	0.5 ml/h
7	IL-Vasc	98		98	1 installation of 3.5×10^7	Tracheal catheter	1 ml/min	1 ml/h
10	I-Lung	97		97	1 installation of 3.5×10^7	Tracheal catheter	1 ml/min	1 ml/h
15	I-Lung	97		97	1 installation of 3.5×10^7	Pulmonary artery	1 ml/min	1 ml/h
20	I-Lung	97		97	1 installation of 3.5×10^7	Pulmonary artery	1 ml/min	1 ml/h
(C) *PL 1–3*								
		PL-2	PL-3	PL-3				
1	PL-Vasc	92	90	95	2 installations of 3.5×10^7	Pulmonary artery	0.5 ml/min	0.5 ml/h
5	PL-Vasc	94	89	93	2 installations of 3.5×10^7	Pulmonary artery	0.5 ml/min	0.5 ml/h
7	PL-Vasc	94	91	92	2 installations of 3.5×10^7	Pulmonary artery	1 ml/min	1 ml/h
10	P- lung	93	86	92	2 installations of 3.5×10^7	Tracheal catheter	1 ml/min	1 ml/h
15	P-lung	93	84	91	2 installations of 3.5×10^7	Tracheal catheter	1 ml/min	1 ml/h
20	P- lung	92	88	90	2 installations of 3.5×10^7	Tracheal catheter	1 ml/min	1 ml/h
25	P-Trachea/ bronchial	97	95	95	3 installations of 5.0×10^6	Tracheal catheter	0.5 ml/min	0.5 ml/h

Before cell installations, lung scaffolds were prepared by initially pumping DMEM F-12 into the lung scaffolds at a rate of 5 ml/min and stopping when the programmed volume reached was 0.5 or 1L, which was dependent on the size of each lung scaffold. The system was then reversed to pump the same volume out of the lungs. This process was repeated four times prior to cell installations. Cell installation protocols varied in the numbers of cells used and the flow rates used for installations. Protocol specifications for the each of the cell types and cell numbers used for installations in the three AC human single-lung scaffolds or AC human whole-lung scaffolds, site of installation, times for cell installations, medium flow rate during cell installations and medium flow rate between cell installations are described in **Table 3.1**.

For cell installations of pHLC, iHLC or 13LU, the tubing to the main stem bronchus was clamped and disconnected from the bioreactor at the lid flange. The catheter ends were attached

to a Minipulse 3 peristaltic pump (Gilson, Middleton, WI, USA). After each cell installation, SAGM with 10% heat-inactivated human AB serum was pumped through the catheter for 3 hours at a rate of 0.5 ml/min, making the lung scaffolds expand slightly and to help disperse cells. The flow rate was then decreased to 1 ml/min.

For installation of vascular cells, HUVEC were suspended in 200 ml EGM containing15% PF-127. For installations of vascular cells into AC human whole-lung scaffolds, PRP preparations were perfused into the pulmonary artery and then incubated for 24 hours prior to pHLVC installations. PHLVC were suspended in to 200 ml EGM containing 10% PRP and 15% PF-127. After installation of vascular cells, the medium flow rate through the pulmonary artery was stopped and the intake was switched to perfuse the cell suspension until cells were installed. After 5 hours, the pump was started again and EGM with 10% heat-inactivated human AB serum was pumped into the pulmonary artery and into the pulmonary vein in a closed loop.

The bioreactor was placed in an incubator and cell-scaffold single-lung or whole-lung constructs were incubated at 37˚C with 5% CO_2 for 30 days. After 30 days of culture, measurements of compliance were done, biopsy samples were taken for evaluations of protein content and histology. The bronchoalveolar lavage from bioengineered lungs was collected to evaluate the presence of microbial contamination.

Immunocytochemistry

Cells were fixed with 2% PAF. Before immunofluorescent staining, cells were washed with PBS to remove PAF. For staining of internal proteins, cells were permeabilized with 1% BD permeabilizing solution (BD Biosciences) for 10 minutes and then were washed with PBS. Antibodies used for immunocytochemistry included anti-AQP-5 (1:200; Santa Cruz Biotechnology, Santa Cruz, CA, USA), anti-proSPC (Chemicon, Temecula, CA, USA), anti-α-

smooth muscle actin (α-SMA; Sigma, St. Louis, MO, USA), anti-fibroblast specific protein-1 (FSP-1; Millipore, Merck, Darmstadt, Germany), anti-CD31 (BD Biosciences, San Jose, CA, USA) and anti-vascular endothelial (VE)-Cadherin (BD Biosciences). For negative controls, corresponding immunoglobulin species matched antibodies were used or the primary antibodies were omitted and only secondary antibodies were used. DAPI counter-stains were done for identification of cell nuclei.

Histology and Immunohistochemistry

To fix bioengineered lungs, 2% PAF was pumped into the main stem bronchus and the pulmonary artery. Lungs were kept in 2% PAF overnight at room temperature. A rotary meat slicer (Weston, Incline Village, NV, USA) was used to slice 2-inch slices of the bioengineered lungs. From these slices, 0.5 cm^3 pieces were cut from different regions of the lungs for immunohistochemistry. Tissue pieces were placed in tissue freezing medium (Triangle Biomedical Sciences) and were sectioned on a Microm cryomicrotome (Thermo Scientific). Tissue was sectioned with a 6-7 μm thickness. Tissue sections were stained with hematoxylin & eosin (H&E) for evaluations of tissue formation. For immunohistochemistry, the antibodies used included anti-AQP-5 (1:200; Santa Cruz Biotechnology, Santa Cruz, CA, USA), anti-proSPC (Chemicon, Temecula, CA, USA), anti-α-smooth muscle actin (α-SMA; Sigma, St. Louis, MO, USA), anti-fibroblast specific protein-1 (FSP-1; Millipore, Merck, Darmstadt, Germany), anti-CD31 (BD Biosciences, San Jose, CA, USA) and anti-vascular endothelial (VE)-Cadherin (BD Biosciences). To block non-specific binding, Tris-buffered saline (TBS) containing 0.1% w/v Tween and defatted milk powder (30mg/ml) was added to the tissue sections for 1 hour. DAPI counter-stains were done in all tissue sections for identification of cell nuclei

Fluorescent Microscopy

A Nikon T300 Inverted Fluorescent Microscope (Nikon Corp.) was used for examination of fluorescent labels.

Flow Cytometry

A FACSAria flow cytometer (BD Biosciences) was used. Data acquisition and data analysis were done using the FACSDiva program (BD Biosciences).

PET-CT Imaging Procedures

Positron emission tomography-computed tomography (PET-CT) was done for bioengineered PL-1. A portion of distal lung from the left lobe was cut about 1 inch above the catheter termination site. The tissue collected was placed in a 50 ml conical tube with 25 ml DMEM/F-12 and 0.91 mCi (100 µl) of clinical grade 2-(^{18}F) fluoro-2-deoxy-D-glucose (FDG) was added to the lung sample and the tube was inverted three times. A dose calibrator set to F-18 was used to place the tube and confirm radioactivity. Every 10 minutes, the tube with the lung sample was inverted three times. The lung tissue sample was incubated with this solution for 30 minutes at room temperature. After 30 minutes, the radioactive medium was replaced with 25 ml of fresh medium and the lung tissue sample was incubated for 15 minutes at room temperature, while being inverted every 5 minutes. After 15 minutes the medium was replaced again with 25 ml of fresh medium for another 15 minutes. The lung tissue sample was then put in a plastic bag to measure radioactivity using the dose calibrator (approximately 30 µCi). A PET-CT scan of the lung tissue sample was done using a murine-dedicated system (Siemens Inveon). Inveon Workstation software was used to process and fuse the images.

Pulmonary Function Tests

Pulmonary function tests (PFT) were done to obtain measurements of static lung compliance for human pediatric lungs after procurement, after decellularization, and after recellularization. A ventilator (Model 300; Siemens-Elema) was used to ventilate lungs and lung scaffolds. A cuffed endotracheal tube was placed inside the main stem bronchus and umbilical tape was used to secure it. To seal the cuff within the trachea, the cuff was inflated. The ventilator settings were arranged to deliver sufficient tidal volume to generate a peak pressure of approximately 20 mmHg. Static lung compliance, dynamic lung compliance and peak pressures were measured. Images from the ventilator screen for measurements obtained from each lung or AC lung scaffold captured.

Evaluation of Vascular Patency

The vascular patency was evaluated by examining capillary development in the bioengineered PL-2. PL-2 was chilled at 4˚C for 3 hours before injection with mixture containing DMEM/F-12, 15% PF-127, and 1:500 solution of rhodamine red (Sigma). This mixture was pumped into the pulmonary artery at a flow rate of 1 ml/min, until the solution began to drip from the pulmonary vein. To allow gelation of PF-127 within the vasculature, the bioengineered PL-2 was warmed to room temperature. Small 1 cm^3 pieces of tissue were then cut and 2% PAF was used to fix overnight at room temperature. Fixed tissue pieces were washed in PBS and prepared for sectioning. Tissue sections (7μm) were used for immunohistochemistry.

Immunoprecipitation

Before bioengineered lungs were fixed, small 1 cm^3 tissue samples were cut from bioengineered SL-1-3 and PL-1-3. Samples of native human lungs were used as a comparison. Individual tissue samples were placed in 1ml cold RIPA lysis buffer (50 mM Tris-HCI, pH 8, 150

mM NaCl, 1% NP-40, 0.5% sodium deoxycholate) containing 1X Protease Inhibitor Cocktail (Sigma). Lysate from each tissue sample was centrifuged at 10 000 x g for 15 minutes. After centrifugation the supernatants were collected. Immunoprecipitation was done for AQP5, SP-C, and β-actin following an Abcam protocol. To pre-clear the lysate, 50 µl of Sepharose protein A slurry (Millipore) was added to 100 µl cell lysate and incubated on ice for 30-60 minutes. After pre-clearing, the lysate was centrifuged at 10,000 x g for 10 minutes at 4˚C and then placed in a fresh microcentrifuge tube. Antibodies were then added to the individual lysates, 10 µg antibody of SP-C, SP-D, AQP5 and β-actin were added and incubated for one hour at 4˚C. Then, 50 µl of Sepharose protein A slurry were added and tubes were placed on a rocking platform and were incubated for one hour at 4˚C. Samples containing sepharose protein A beads were then washed three times with 500 µl lysis buffer to remove non-specific binding. After a third final wash, samples were centrifuged, the supernatant was removed and the beads were collected. Then, 50 µl 1X Laemmli sample buffer was added to the samples containing Sepharose protein A beads. Samples containing sepharose protein A beads were vortexed, and then heated at 90˚-100˚C for 10 minutes to elute proteins from the beads. Samples containing beads were then centrifuged at 10,000 x g for 5 minutes and the supernatants were collected and loaded onto a SDS-PAGE gel. Coomassie blue was used to stain the gels.

Multiphoton Microscopy and Second Harmonic Generation

Multiphoton microscopy (MPM) was done using a customized Zeiss 410 Confocal Laser Scanning Microscope with multiphoton excitation and detection of nondescanned optics, as previously described [88, 89]. A femtosecond titanium sapphire laser provided multiphoton excitation with a 5W frequency-doubled Nd:YVO pump laser that routed into the scanhead and through the objective. The pulse width for the operating system was 140 fs prior to the objective

(40X, 1.2 N.A., water immersion). Emitted light was collected using an epi-configuration and a cooled PMT placed in a nondescanned configuration (R6060; Hamamatsu) was used to detect it. Autofluorescence excitation was 780 nm and for second harmonic generation (SHG) it was 840 nm. For detection of broadband autofluorescence from the lungs or scaffolds, fluorescence emission in the spectral region of 450-650 nm was collected. A 420±14 nm bandpass filter in the nondescanned detector path was used to collect SHG. Lung or scaffold samples to be imaged were placed in an imaging dish with #1.5 coverslip and were immersed in PBS. A z-stack was obtained from every imaging site, using a z-internal of 1 µm to depths > 150 µm using the 40X, water immersion objective that provided a field of view of 320 x 320 µm. Metamorph or Image J viewer were used for image reconstructions.

Statistical Analysis

InSTAT GraphPad software (version 2003) was used for statistical analysis. Mean values and standard deviations are shown. The Student's *t*-test was used to determine statistical significance. Values were considered significant when $p<0.05$.

RESULTS

Phenotypic Profile of the Cells Used For Recellularization of AC Human Lung Scaffolds

As described in the methods section, a bronchoscope was used to help place individual catheters into the main stem bronchus for cell installations. **Figure 3.1 A-E** demonstrates how these catheters were placed and how the lungs were connected to the bioreactor chamber for perfusion. Single human adult lung or whole pediatric lung scaffolds were placed in the bioreactor chamber **(Figure 3.1 F, G)**. The phenotypes of the all the cells used for installations were examined.

Figure 3.1 H shows the phenotypic profile of the vascular cells used for installations in SL-1-3 or PL 1-3. HUV-EC-C, immortalized lung vascular cells (IL-Vasc), and primary lung vascular cells (PL-Vasc) were examined for expression of CD 31, VE-CAD, α-SMA, and FSP-1. The majority of these cells were shown to be positive for vascular endothelial cell markers CD 31 and VE-CAD. **Figure 3.1 I** shows the phenotypic profile of the lung epithelial cells used for installations of SL 1-3 or PL 1-3. Primary lung cells (P-lung) or immortalized lung cells (I-lung) were examined for expression of AQP5, pro-SPC, α-SMA, and FSP-1. Phenotypic profiles for P-lung and I-lung were similar and show that the majority of these cells were positive for pro-SPC, a marker for type II AEC.

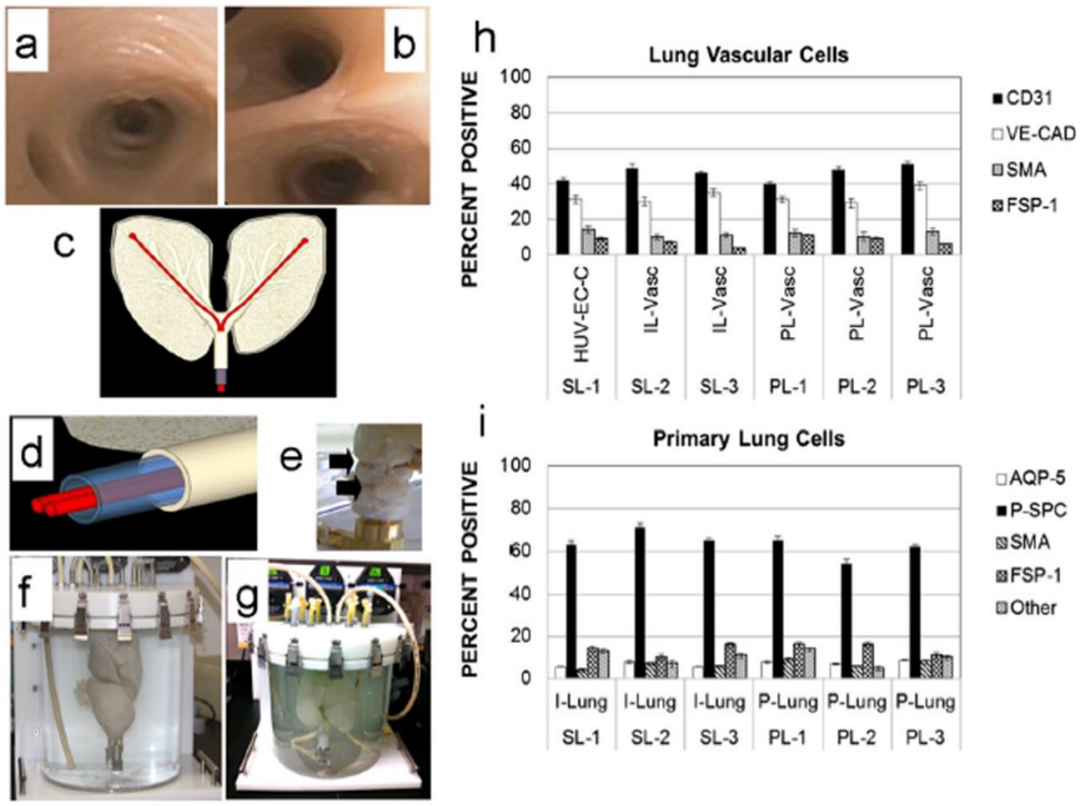

Figure 3.1 Preparation of lung scaffolds for cell installation. (A) Bronchoscopic image of SL-2 used in determining catheter placement. **(B)** Bronchoscopic image of PL-1. **(C)** Cartoon showing catheter placement in lungs. **(D)** Cartoon showing enlargement of catheter placement into the trachea for all lungs. **(E)** Image of trachea of AC scaffold, showing attachment of lung to metal piping system of the bioreactor; black arrows, plastic zip ties used to attach each trachea to bioreactor fluidics system. **(F)** SL-1 in the bioreactor prior to cell installation. **(G)** PL-1 in the bioreactor prior to cell installation. **(H)** Phenotypic

profile of the HUVECs installed in SL-1, the immortalized lung vascular cells (IL-Vasc) or the primary lung vascular cells (PL-Vasc) installed in pediatric lungs 1–3 (PL 1–3): percentages of cells positive for expression of CD31, VE-CAD, α-SMA and FSP-1 are shown. **(I)** Phenotypic profile of the immortalized lung cells (I-lung) installed in adult single lungs (SL) 1–3 or the primary lung (P-lung) cells installed in pediatric double-lung sets (PL) 1–3. I-lung and primary lung cells were predominantly P-SPC-positive type II AECs, although FSP-1-positive fibroblasts, AQP-5-positive type I alveolar epithelial cells and α-SMA-positive cells were also found. Reproduced with permission from Nichols *et al*. 2016.

Initial Assessments of Tissue Development in Small-Scale Cell-Scaffold Constructs

Before attempting to recellularize whole pediatric lung scaffolds, small-scale cell-scaffolds constructs produced from P-lung cells and 2.5 cm^3 pieces of AC human lung scaffold were used for initial assessments of tissue development. The influence of cell numbers used and the effects of pre-treatment of AC human lung scaffolds with PRP or AB serum on tissue developed were examined. Total numbers of cells and total numbers of viable cells isolated from constructs were higher when scaffolds were pre-treated with AB serum ($p<0.005$) or PRP ($p<0.0005$) than in untreated scaffolds **(Figure 3.2 A-I)**. Pre-treatment with PRP resulted in higher total cell and total viable cell numbers when compared to pre-treatment with AB serum **(Figure 3.2 A-I)**. Results show that when 1×10^6 P-lung cells were used to seed the scaffolds, there was better tissue formation than in constructs seeded with less than one million cells **(Figure 3.2 A-I)**. Pre-treatment

of AC human lung scaffolds with PRP or AB serum also resulted in better tissue formation when compared to untreated scaffolds regardless of the numbers of cells used **(Figure 3.2 B,C,E,F,H,I)**.

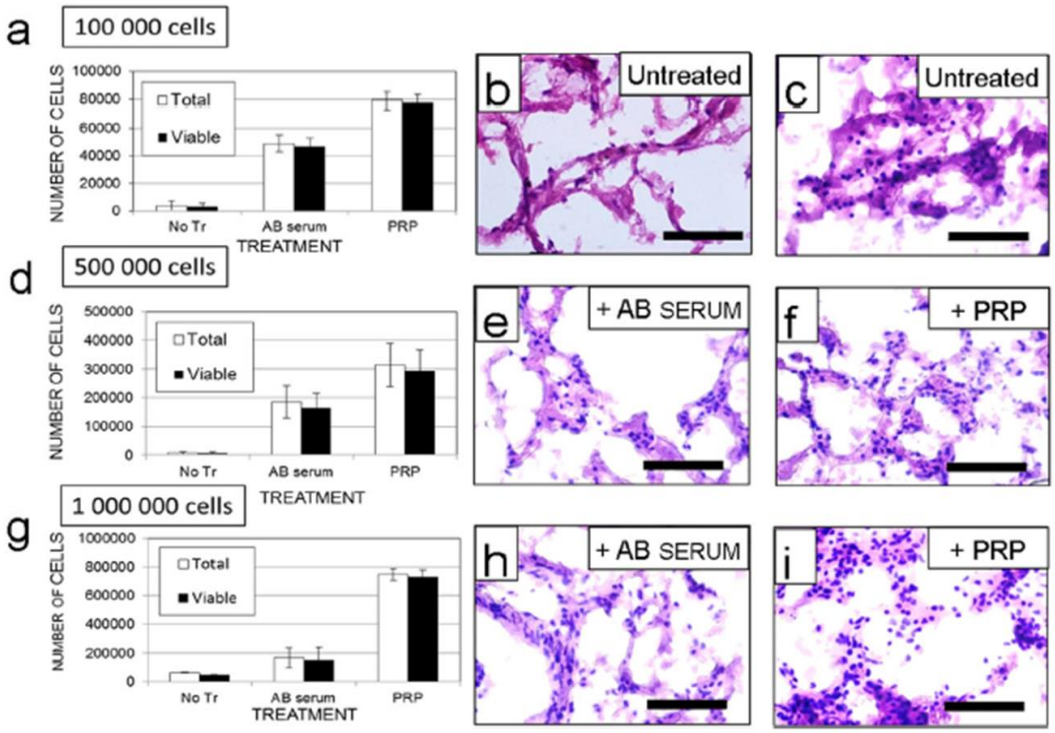

Figure 3.2 Examination of cell numbers and PRP or AB serum pre-treatment (A, D, G) Influence of cell numbers used or pretreatment of AC scaffolds with AB serum or PRP on cell attachment and tissue formation: 2.5 cm3 pieces of AC scaffold were left untreated or treated with AB serum or with PRP and then seeded with **(A–C)** 100 000 primary human lung cells, **(D-F)** 500 000 primary human lung cells or **(G-I)** 1 000 000 primary human lung cells; averaged values for numbers of recovered cells and viable cells are shown. Significantly higher levels of viable cells were collected after 7 days of culture following treatment with AB serum (*p<.005) compared to untreated scaffolds; treatment with PRP (**p<0.0005) was always significantly better than untreated or AB serum-treated samples. Representative 7 μm H&E-stained sections of **(B, C)** untreated, **(E, H)** human AB serum-treated or **(F, I)** PRP-pretreated scaffolds, indicating that increased cell attachment occurred in PRP-treated pieces of AC scaffold. Bar=50 μm **(B, C, E, F, H, I)**. Higher cell numbers combined with PRP pretreatment of scaffolds also produced better tissue formation. Reproduced with permission from Nichols *et al*. 2016.

Evaluation of Lung Tissue Development in Bioengineered Single Lungs 1-3

When examined histologically, AC lung scaffolds did not contain any cells and they did not have a well-organized structure **(Figure 3.3 A)**. Throughout regions of the AC lung scaffolds, the remaining ECM of blood vessels **(Figure 3.3 B)**, or bronchial airways could be seen.

After using the small scale cell-scaffold constructs to do our initial examinations of tissue development, we then scaled up and utilized single lung scaffolds to develop recellularization protocols. SL-1, -2 and -3 were used to develop recellularization methods, by determining the numbers of cells needed for each installation, methods for installations, order of cell installations and perfusion flow rates for the bioreactor. Details for recellularization protocols we developed are described in **Table 3.1**.

Histological evaluations of bioengineered SL-1 -3 indicated that tissue formation was variable between the bioengineered lungs The AC lung scaffold for SL-1 was not pre-treated before cell installations. Bioengineered SL-1 did not have well-distributed cells throughout the scaffolds, which resulted in poor tissue formation **(Figure 3.3 C-G)**. Cell installations for SL-1, included 13LU, followed by I-lung, and HUV-EC-C. Immunohistological examinations revealed the many of the cells in SL-1 were FSP-1-positive fibroblasts **(Figure 3.3 D, F, G)**. The average number of blood vessels/tissue section in SL-1 were 5±1.

In an attempt to improve vascular and lung tissue development in bioengineered, SL-2 and -3, changes were made to the initial recellularization protocol used for SL-1. For recellularization of SL-2 and SL-3, the AC human lung scaffolds were pre-treated with either human AB serum or PRP, the number of cells used for installations was increased and the order of cell installations was modified. The AC human lung scaffold used for SL-2 was pre-treated with human AB serum and the scaffold used for SL-3 was pre-treated with PRP. Unlike the first cell installation in SL-1, the first cell installations for SL-2 and SL-3 were done with IL-Vasc to first seed the vasculature. SL-2 and SL-3 were seeded with twice the number of cells than for SL-1. Cell installations for SL-2 and SL-3 were done at a slower perfusion rate than for SL-1 **(Table 3.1)**.

Bioengineered SL-2 had a better distribution of cells which resulted in better tissue formation than SL-1 **(Figure 3.3 H, I)**. Some areas in SL-2 showed recellularization of blood vessels **(Figure 3.3 H)**. Immunofluorescent staining indicated that SL-2 contained many pro-SPC-positive type II AEC **(Figure 3.3 K)**. The average number of blood vessels/tissue section for SL-2 was 15±4, which was significantly increased ($p<0.005$) when compared to SL-1. Bioengineered SL-3 had a good cell distribution and better tissue formation than SL-1 and SL-2 **(Figure 3.3 L-P)**. Well-formed blood vessels were found throughout SL-3 **(Figure 3.3 M)**. Immunofluorescent staining of SL-3 revealed the presence of pro-SPC-positive type II AEC **(Figure 3.3 O)** throughout the bioengineered lung and small pockets of AQP-5-positive type I AEC were also found **(Figure 3.3 P)**. The average number of blood vessels/tissue section for SL-3 was 57±7, which was also significantly increased ($p<0.0005$) when compared to SL-1.

The modifications made to the recellularization protocol after production of bioengineered SL-1 improved tissue formation in bioengineered SL-2 and SL-3. Vascular and lung tissue development was better in bioengineered SL-3 when compared to SL-2 and for this reason, the cell installation protocol used to bioengineer SL-3 was used to recellularize pediatric whole lung scaffolds and bioengineer PL-1-3.

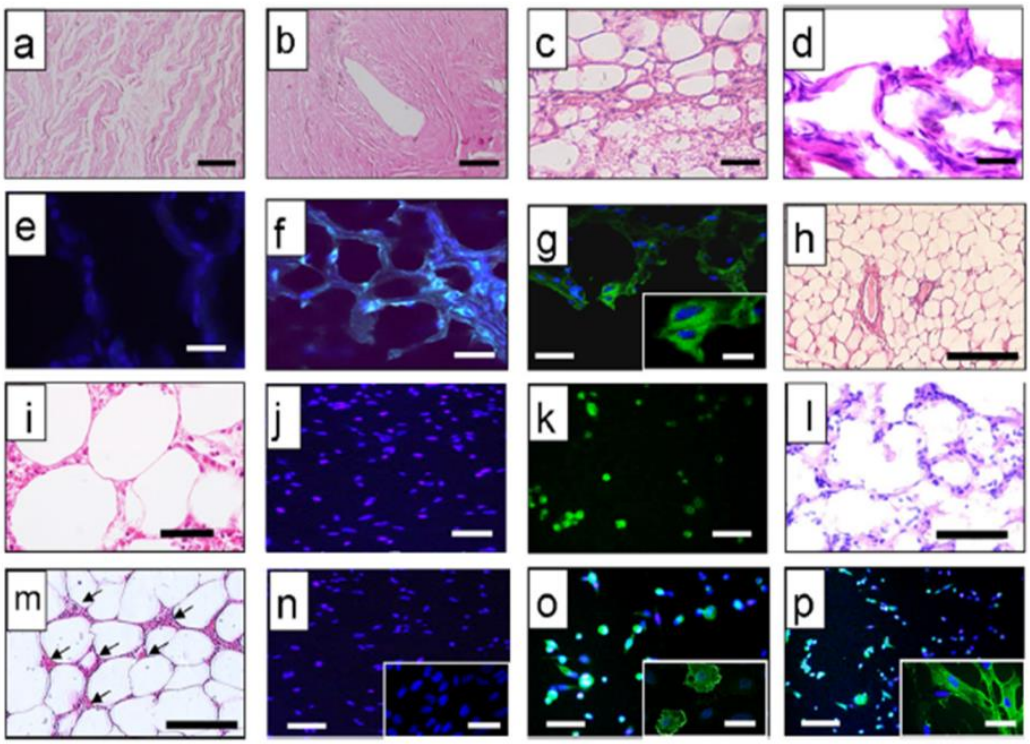

Figure 3.3 Evaluation of cell attachment using immortalized cell lines and examination of tissue formation in bioengineered single lungs 1–3. (A, B) Representative 7 μm sections of AC human lung scaffolds showed **(A)** no cell nuclei and lack of organized tissue structure, except for **(B)** areas containing large blood vessels, bars = **(A, B)** 100 μm. **(C-G)** Representative sections of recellularized SL-1 **(C, D)**, indicating poor cell distribution and poor tissue formation and **(D)** confocal image of section shown in **(C)**, showing that the majority of cells attached to the scaffold were similar in morphology to fibroblasts, bars = **(C)** 100 μm, **(D)** 10 μm; **(E, G)** most cells were fibroblasts, as indicated by **(D)** the morphology of the cells and **(F)** immunostaining; **(E)** staining control; **(F, G)** immunostaining for fibroblast-specific protein-1 (FSP-1), bars = **(D)** 50 μm, **(E, G)** 10 μm, insert in **(G)** 5 μm. **(H-K)** Representative sections of SL-2, showing **(H, I)** improved cell distribution and **(H)** areas of lung tissue and blood vessel formation, bars =(H) 100 μm; **(I)** 50 μm; (K) immunofluorescent staining for P-SPCs indicated that **(K)** most cells were type II AECs; **(J)** staining control, bars = **(J, K)** 50 μm. **(L-P)** Representative sections of SL-3, showing good cell distribution and lung tissue development; **(M)** SL-3 had regions of well-formed blood vessels; black arrows, small capillaries, bars = **(L, M)** 100 μm; **(N)** control and insert, stained with DAPI (nuclei, blue); **(O, P)** sections of SL-3 stained for the presence of **(O)** type II AECs, using P-SPC (green) and **(P)** type I AECs, using AQP-5 (green); **(N-P)** DAPI counterstain (blue) used, bars = **(N-P)** 50 μm, (inserts) 10 μm. Reproduced with permission from Nichols *et al*. 2016.

Evaluation of Lung Tissue Development in Bioengineered Pediatric Lungs 1-3

Before any cell installations, whole pediatric AC lung scaffolds were pre-treated with 10% PRP in SAGM. Only primary cells isolated from adult double-lung sets were used for installations. In order to standardize our cell installation protocol for PL-1, -2 and- 3, the same numbers of cells

were installed in each of the PL scaffolds **(Table 3.1)**. After 30 days in culture, evaluation of PL-1 by CT was done to examine the cell distribution and tissue development. CT examination indicated that were no gross abnormalities, no nodules or masses, no fluid and no areas of lung collapse present in bioengineered PL-1 **(Figure 3.4 A-C)** but the left lung contained some undefined densities. **Figure 3.4 A** shows three representative CT scans of PL-1.

Tissue development in PL-1 also was examined by using 3D CT plots showing only the vascular tissue **(Figure 3.4 B)** or the vascular and parenchymal tissue together **(Figure 3.4 C)**. These 3D CT plots indicated that although some areas of the distal lungs were not evenly recellularized, good tissue development was observed in PL-1 **(Figure 3.4 B, C)**. We realized that the undefined densities in the left lung that were observed in the CT scan were in the region where the left catheter was used for cell installations, terminated. To further examine this, we cut this area of distal lung, and performed a PET-CT scan. The PET-CT scan revealed that only the area where the catheter terminated was FDG-positive **(Figure 3.4 D-F)**. When this same area was examined histologically by H&E staining, it showed that there were many cells present but they did not form organized structures and the tissue was not well developed **(Figure 3.4 G)**. Immunohistological staining showed that most these cells were pro-SPC-positive type II AEC **(Figure 3.4 I)**. Upon identifying this issue in PL-1, we decided to modify the cell installations in PL-1 and PL-3 and maintain cells in suspension to avoid cell deposition in the areas where the catheters terminate.

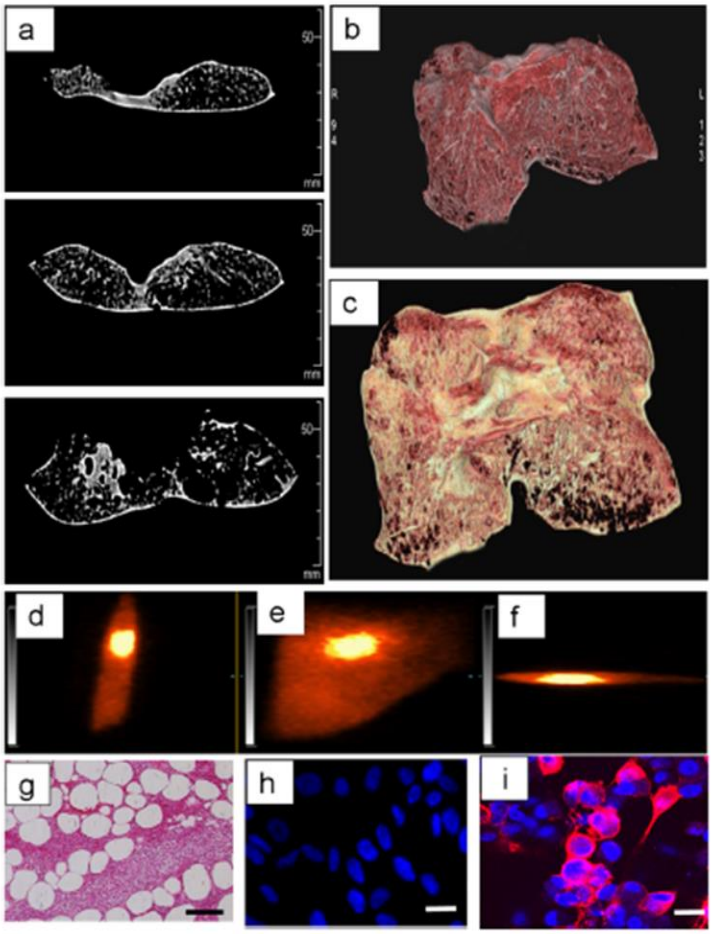

Figure 3. 4 Assessment of cell dispersal and tissue development in PL-2, using positron emission tomography–computed tomography (PET–CT). CT scans were performed following pulmonary function tests of the live bioengineered lungs. **(A)** CT scan of pediatric lung 1 (PL-1) at day 30 of culture: there are undefined densities in the left lung, but there was no fluid in either the right or left lung chambers; three representative scans are shown from the top to the middle of the lung. **(B, C)** 3D representation of the lung CT indicates that the lung parenchyma was well formed, although distal areas near the bottom of the lungs were not well recellularized: **(B)** 3D image of vascular components and **(C)** vascular (red) and tissue (yellow) composition; a portion of the left lobe was used for PET–CT. **(D-F)** PET–CT of the lower left section of the lung: PET–CT shows significant fludeoxyglucose (FDG) signal at the catheter termination site. **(G)** H&E-stained section at the FDG-positive site near the catheter termination point; bar=200 μm. **(H, I)** Confocal images of **(H)** DAPI-stained control and **(I)** sections of lung at the PET-positive site, indicating that the cells were mostly pro-SPC-positive type II AECs; bar=10 μm. Reproduced with permission from Nichols *et al*. 2016.

Histological evaluations of PL-1, -2 and -3 were done after 30 days in culture. Tissue development in bioengineered lungs was compared to native lung tissue from normal pediatric lungs of a 1-month old donor **(Figure 3.5 A-C)**. Good tissue formation was observed in

bioengineered PL-1 **(Figure 3.5 D-F)**, -2 **(Figure 3.5 G-I)** and -3 **(Figure 3.5 J-L)** and it was similar to that of native pediatric lungs **(Figure 3.5 A-C)**. When comparing the cell densities of bioengineered PL-1,-2 and -3 **(Figure 3.5 D-K)** to that of native pediatric lung tissue **(Figure 3.5 A-C)**, bioengineered lungs had a lower cell density. We also observed recellularization of the bronchial airways, H&E staining showed the presence of ciliated bronchial epithelial cells **(Figure 3.5 F, I)**. There were no cells present in the cartilage of the trachea or bronchi of the bioengineered lungs **(Figure 3.5 F)**. Well-developed blood vessels **(Figure 3.5 I, L)** and capillaries **(Figure 3.5 N-T)** also were found in the bioengineered lungs. The average number of blood vessels/tissue section for PL-1 was 101 ± 9, for PL-2 it was 143 ± 23 and for PL-3 it was 168 ± 12.

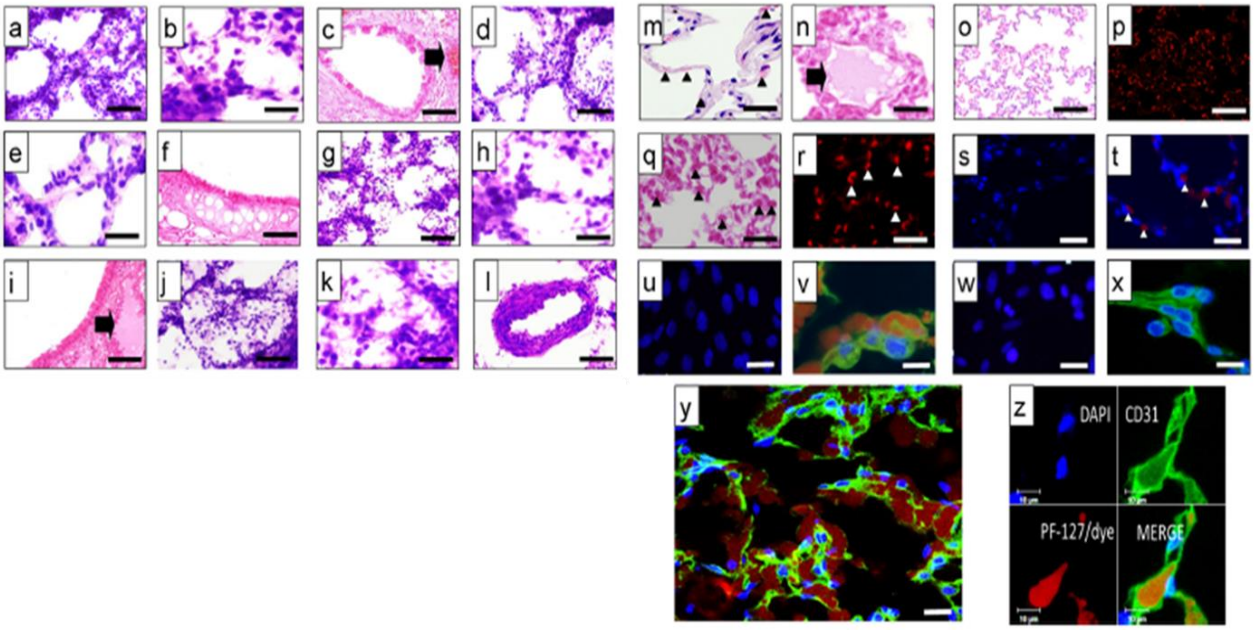

Figure 3.5 Examination of pediatric bioengineered lungs. (A-C) H&E-stained sections of normal human pediatric lung (age 1 month), bars = **(A)** 200 μm, **(B**, H&E high-power image) 50 μm; **(C)** bronchus in normal human pediatric lung; arrow, vessel filled with red blood cells, bar = 200 μm. Pediatric engineered lungs (PL) 1–3 were examined: **(D-F** PL-1; **(G-I)** PL-2; and **(J-L)** PL-3, showing lung tissue and blood vessel formation. **(M)** H&E stain of adult normal human lung alveolus; black arrows, red blood cells in the capillaries, bar = 50 μm. **(N-Z)** Representative sections of PL-2 following injection of rhodamine-PF-127 hydrogel into the pulmonary artery: **(N)** H&E-stained section showing single blood vessel; black arrow, rhodamine PF-127 mixture in the vessel lumen (pink), bar = 20 μm; **(O)** H&E-stained section showing rhodamine PF-127-filled capillaries (pink) in the bioengineered lung, bar = 200 μm; **(P)** fluorescent image of same section, showing rhodamine-PF-127-filled capillaries (red), bar = 200 μm; **(Q)** H&E-stained section of rhodamine-PF-127-filled capillaries, black arrows pointing to dye-filled capillaries, bar = 20 μm;

(R) fluorescent image of rhodamine-PF-127-filled capillaries (red), white arrows pointing to dye-filled capillaries, bar=20 μm; **(S-Z)** confocal images of immunostained sections of bioengineered PL-2; **(S)** DAPI-stained control and **(T)** capillary areas filled with rhodamine-PF-127 mixture (red, white arrows) and DAPI nuclear stain (blue), bars = **(S, T)** 10 μm; **(U)** DAPI-stained control and **(V)** immunofluorescent staining for P-SPCs (type II alveolar epithelial cells (green) and DAPI nuclear stain (blue), bars = **(U, V)** 10 μm; **(W)** DAPI-stained control and **(X)** immunofluorescent staining for aquaporin 5 (AQP-5; type I AECs, green) and DAPI nuclear stain (blue), bars = **(W, X)** 10 μm; **(Y, Z)** immunofluorescent staining for the presence of CD31-positive endothelial cells (green) and DAPI nuclear stain (blue), demonstrating that the CD31-positive cells surround the rhodamine-filled capillaries in bioengineered PL-2, bars = **(Y)** 20 μm; **(Z)** 10 μm. Reproduced with permission from Nichols *et al*. 2016.

Vascular Development in Bioengineered Lungs Leads to the Formation of Capillary Networks

Recellularized blood vessels were present in bioengineered lungs. To examine vascular patency, a mixture of PF-127 hydrogel and rhodamine fluorescent dye was injected into the pulmonary artery of PL-2 before the bioengineered lung was fixed with 2% PAF. In tissue sections of native human lung tissue, capillaries containing red blood cells can be seen throughout the tissue **(Figure 3.5 M)**. When tissue sections of bioengineered PL-2 were examined, the recellularized blood vessels were filled with the PF-127-rhodamine hydrogel **(Figure 3.5 N-T, V, Y, Z)**. We did not observe any indications of vascular leakage as the PF-127-rhodaine hydrogel was well-maintained within the recellularized blood vessels of the bioengineered lungs **(Figure 3.5 N-T, O, Q)**. Small blood vessels containing this hydrogel mixture were found throughout the bioengineered lung tissue and they resembled capillary networks **(Figure 3.5 Y)**. We then examined the cell types that were found in these small recellularized blood vessels and found that these were CD 31-positive endothelial cells **(Figure 3.5 Z)**.

Pulmonary Function Testing of Bioengineered Lungs

Static lung compliance was measured in all 6 bioengineered lungs, including SL-1, -2, and -3 and PL-1, -2 and -3 **(Figure 3.6 A, B)**. Measurements of static lung compliance were also taken for each these lungs right after procurement and of the AC lung scaffolds produced after decellularization. Static lung compliance of all procured lungs was below the 50 – 100 ml/cmH_2O normal range, this may have been caused by blood clots within the airways that caused an obstruction **(Figure 3.6 B)**. All AC lung scaffolds had a significant increase ($p<0.005$) in static lung compliance when compared to the measurements of procured lungs before decellularization **(Figure 3.6 B)**. The static lung compliance of all bioengineered lungs was within the normal range **(Figure 3.6 B)** and was found to be significantly lower ($p<0.05$) than that of AC lung scaffolds.

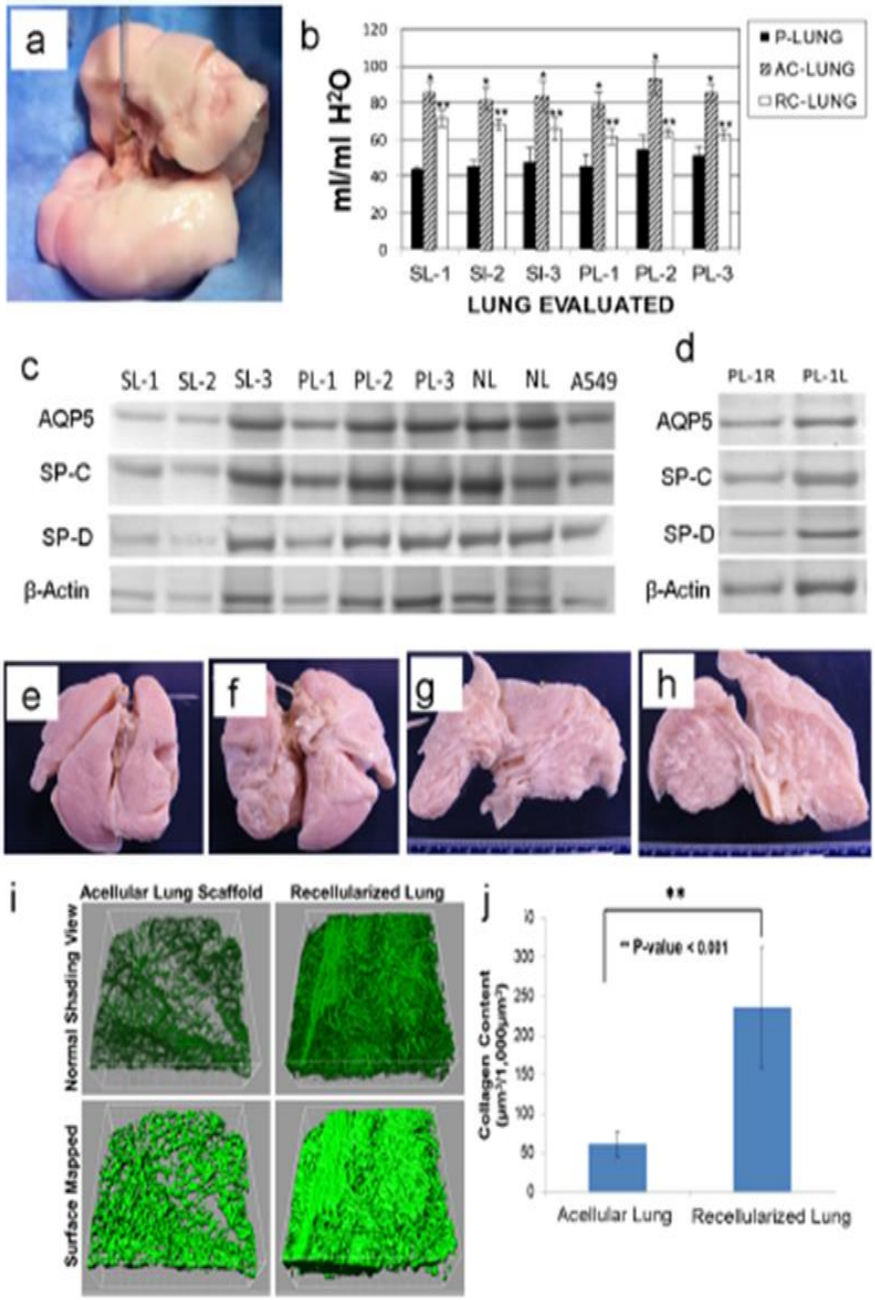

Figure 3.6 Further evaluation of pediatric bioengineered lungs. **(A)** Image of PL-1 during PFT. **(B)** Pulmonary function testing (PFT) was performed on single human adult lungs (SL) 1–3 and pediatric double-lung sets (PL) 1–3; static compliance of each single- or double-lung set was evaluated at procurement (primary lung, P-LUNG), following production of the acellular scaffold (AC-LUNG) and after recellularization (RC-LUNG); the four values for static compliance were collected when the lungs were fully expandedand an average of these four values was plotted on the graph; AC lung scaffolds had a significantly higher static compliance compared to that in donor lungs (*$p<0.0005$), while recellularized lungs had a significantly lower static compliance (**$p<0.05$) and were similar to that of normal procured lung (P-LUNG). **(C)** Immunoprecipitation of lung-specific proteins AQP-5, SP-D and SP-C in SL 1–3 and PL 1–3, normal lung (NL) and A549 cells. **(D)** Immunoprecipitation of AQP-5, SP-D and SP-C of tissue

from the PL1 right (PL-1R) and left (PL-1 L) are shown for comparison; β-actin was used as a loading control. **(E-H)** PL-1 was fixed and cut on a rotary meat slicer: **(E)** anterior view and **(F)** posterior view of the lung; center portions of the PL-1 **(G)** right and **(H)** left lungs. **(I)** Samples of AC scaffold and recellularized lung were compared for collagen content, using a 3D reconstruction of second harmonic generation (SHG) image stacks. **(J)** Analysis of total collagen from SHG image stacks indicates that significantly more collagen was found in recellularized lung scaffolds compared to that in AC lung scaffolds (**p<0.001) and collagen in recellularized lungs had a normal configuration; for SHG analysis, excitation was 840 nm, emission was 420±20 μm, z interval was 1 μm and the objective was 40×1.2 N.A. water c-Apo. Reproduced with permission from Nichols *et al*. 2016.

Production of Lung-Specific Proteins in Bioengineered Lungs

The production of the lung-specific proteins, AQP 5, SP-C, and SP-D was examined in all bioengineered lungs by immunoprecipitation. As a comparison, we also showed production of these proteins in SL-1, -2, -3 and in native human lungs. Levels of AQP5, SP-C and SP-D were lower in bioengineered SL-1 and -2 when compared to SL-3, as expected because these scaffolds were not well recellularized **(Figure 3.6 C)**. Bioengineered PL-1, -2 and -3 produced AQP 5, SP-C and SP-D **(Figure 3.6 C)** and the levels produced by these bioengineered tissues were similar to those of native human lungs. When comparing protein levels in the right and left lung of PL-2, levels of these proteins were similar in both sides **(Figure 3.6 D)**.

Collagen Content in AC Human Lung Scaffolds and Bioengineered Lungs

Gross evaluations of macrosections of bioengineered PL revealed that the lungs were fleshy and their gross functional subunits were similar to that of native lungs **(Figure 3.6 E-H)**. The collagen content in samples of human lung scaffolds and bioengineered lungs was examined with MPM and SHG. 3D MPM and SHG image reconstructions of AC human lung scaffold **(Figure 3.6 I left)** and bioengineered PL **(Figure 3.6 I right)** showed there was a difference in collagen content and quantification of the collagen density indicated that there was significantly more collagen ($p<0.001$) in bioengineered lungs **(Figure 3.6 J)**. This indicated that the ECM of the scaffolds was modified by the cells used for recellularization.

DISCUSSION AND CONCLUSION

Development of tissue-engineered whole organ constructs has been limited by challenges encountered in the development of recellularization procedures that can produce functional lung and vascular tissue. This study demonstrates that whole AC pediatric lung scaffolds and primary cells from discarded human lungs can be used to bioengineer whole human lung constructs. The use of clinical imaging methods such CT and PET-CT allowed us to examine cell distribution, tissue development, metabolic activity and gross morphological structures of bioengineered lungs. The bioengineered lungs we produced had similar histological characteristics of native human lung tissue, they contained alveolar-capillary junctions, contained the presence of both type I and type II AEC, and were capable of producing SP-C and –D. Static compliance of bioengineered lungs was similar to that of the tested native human lungs.

The cell installation protocols we have developed serve as guidelines for the recellularization of bioengineered lungs. Although our study has demonstrated that whole human lung constructs can be bioengineered from discarded human lung tissues, the large numbers of primary cells needed for recellularization represents a limitation in the production of these constructs. The recellularization of pediatric lung scaffolds was accomplished because of their small size and high yields of primary cells obtained from three discarded adult lungs. If these whole lung constructs are to be used as research models, alternative cell sources might be needed. Immortalized cells are a better option because large quantities can be generated.

While developing our recellularization protocols, we learned that pre-treatment of scaffolds with PRP was beneficial for cell attachment and resulted in better formation of parenchymal and vascular tissue. Platelets have been shown to release a variety of growth factors that play key roles

in vascular homeostasis, vasculogenesis, and vascular healing [92, 93]. PRP has been shown to contain angiopoietin-1 [94, 95] and platelet-derived growth factors α, β, C and D which are components of the PDGF-PDGFR pathway involved in development of alveolar epithelium [96] and fibroblast growth factor that has been shown to support lung tissue regeneration [23, 78].

In this study we show the feasibility of bioengineering whole pediatric lungs using AC human lung scaffold and human lung cells isolated from donors lungs. Bioengineered lungs have the potential to be used as large-scale HoC to study lung tissue development, lung physiology or pathological processes.

CHAPTER 4*

In Vivo Validation of Whole Organ Constructs: Production and Transplantation of Bioengineered Lungs into a Large Animal Model

INTRODUCTION

In the previous chapter, we described the production of whole human bioengineered lung constructs and examined their functional characteristics *in vitro*. The aim of the current study was to examine the feasibility of transplanting bioengineered lungs into a large animal model to examine functional characteristics *in vivo*. Left lung pneumonectomies were performed to obtain native porcine single lungs as a source of primary lung cells for recellularization. The methods for recellularization were based on our previously developed cell installations protocols (Chapter 3) with some newly developed modifications. Bioengineered lungs were cultured for 30 days as primary cells were being installed into the vasculature and parenchyma of the porcine AC lung scaffolds. We then designed a method for transplantation of bioengineered single lungs by attaching the main stem bronchus of the bioengineered lungs to the trachea of the native lungs without attaching the pulmonary vasculature. A total of six left single lung bioengineered lungs were produced and four animals received bioengineered single lung transplants. Bioengineered lungs were examined pre- and post-transplant. Pulmonary function tests performed on animals after transplantation of bioengineered revealed that animals had dynamic compliance levels that were within the normal range. Transplanted bioengineered lungs were shown to have better tissue development than bioengineered lungs pre-transplant, which suggests that bioengineered lung tissue continued to develop *in vivo.*

Chapter * published and taken from: Nichols, J.E., La Francesca, S., Niles, J.A., Vega, S.P., Argueta, L.B., Frank, L., Christiani, D.C., Pyles, R.B., Himes, B.E., Zhang, R. and Li, S., 2018. Production and transplantation of bioengineered lung into a large-animal model. Science translational medicine, 10(452), p.eaao3926.

MATERIALS AND METHODS

Animal Care and Surgical Procedures

Animal handling and surgical procedures were performed according to protocols approved by the Institutional Animal Care and Use Committee (IACUC) of University of Texas Medical Branch at Galveston and were compliant with guidelines of the American Association for the Accreditation of Laboratory Animal Care.

Decellularization of Porcine Lungs

Lungs from Yorkshire pigs were obtained as part of a tissue-sharing program from studies approved by the Institutional Care and Use Committee (IACUC) at UTMB or Texas Methodist Hospital Research Institute (TMHRI). Porcine lungs were stored at -80˚C and were kept in storage at least 1 month prior to decellularization. Decellularization was done as previously described (Chapter 2) [88, 89]. On the day of decellularization, lungs were thawed in a 45˚C water bath before being placed in a perfusion bioreactor chamber. To setup the lungs for perfusion, individual cannulas were used to connect the pulmonary artery and main stem bronchus to allow for control of separate pumping systems. Day 1 of decellularization was initiated by immersing the lungs in 1% SDS solution and pumping 1% SDS solution into the individual cannulas of the pulmonary artery and trachea. The pulmonary artery then was perfused with 1% SDS at a rate of 60 ml/min and into the trachea at a rate of 120 ml/min. To fill and expand the lungs, 1-3 liters of 1% SDS were used. Expanded lungs were emptied every hour for 3 hours and at the end of each 3 hour time point, fresh 1% SDS solution was added to the chamber to begin perfusion again. The concertation of SDS was lowered to 0.1% on day 3 of decellularization and the perfusion rates were kept the same. Fresh 0.1% SDS was added to the bioreactor chamber every day for days 4, 5 and 6 of decellularization. By day 5, lungs were perfused with distilled water at a rate of 500 ml/min for 12

hours. Distilled water in the bioreactor chamber was replaced every 3 hours. Lungs were then perfused with 3% H_2O_2 for 1 hour followed by perfusion with sterile water for 12 hours at a rate of 500 ml/h. Sterile water was replaced every 3 hours. Sterile water was then removed from the bioreactor chamber and lungs were perfused with phosphate-buffered saline (PBS) containing streptomycin (90 µg/ml), penicillin (50 U/ml) and amphotericin (90 µg/ml) for 5 hours at rate of 500 ml/h. AC porcine lung scaffolds were stored in fresh PBS containing antibiotic and antimycotic solutions.

Left Pneumonectomy Procedure

A left lung pneumonectomy was performed on the pig that was to receive the bioengineered lung transplant. The recipient pig was anesthetized and placed in the right lateral decubitus position. The pig's left front leg was fixed in a fully extended position and a standard left anterolateral thoracotomy incision was performed one finger below the tip of scapula and extended along the rib. For the donor venous pedicle preparation, the veins were isolated and stapled using an automatic stapler. The inferior pulmonary ligament was released. The hilar dissection was then carried out and the phrenic nerve was left uninjured. Pneumonectomy was performed in a standard fashion beginning with the division of the inferior pulmonary ligament, the sequential encircling of the PA and pulmonary veins followed by multiple firings of an endo GIA stapler staying as peripheral as possible. For the pneumonectomy, the pulmonary vessels were divided first followed by the bronchus.

Isolation of Primary Lung Cells or Primary Vascular Cells

The left lungs obtained from the pneumonectomies were used for primary cell isolations. Single porcine lungs were flushed with 1 liter of PBS containing 100 µg/ml primocin (InvivoGen, San Diego, CA, USA). The lungs were cut to obtain pieces of distal lung while avoiding bronchial

airways and blood vessels. Pieces of distal lung were then minced into smaller fragments that were treated with 1 mg/ml collagenase/dispase (Roche Diagnostics, Indianapolis, IN, USA) for 7 hours at 4˚C.The inner epithelial lining of the trachea and bronchial airways was stripped off the tissue to isolate the tracheal and bronchial cells. The tracheal and bronchial epithelial lining collected was minced and treated with 1mg/ml collagenase/dispase for 4 hours at 4˚C. After incubation with collagenase/dispase, all cells isolated were filtered sequentially through 100 and then 40 µm sterile filters (BD Falcon, San Jose, CA, USA). The filtered solutions containing the cells were centrifuged to collect the pellets of primary human lungs cells and primary human tracheal/bronchial and do cell counts. P-lung cells were cultured in T75 filtered flasks containing SAGM with 1% porcine serum and primocin (100 µm/ml). P-TB cells were cultured in T75 filtered flasks containing bronchial epithelial growth medium (BEGM; Lonza, San Jose, CA, USA) with 1% porcine serum and primocin (100 µm/ml).

Pl-vasc cells were isolated by stripping off the inner endothelial lining of blood vessels from the lungs. These endothelial sheets were then finely minced and treated with 1mg/l collagenase/dispase for 4 hours at room temperature. Sterile 100 µm and 40 µm filters were used to filter the cells followed by centrifugation to collect cell pellets. Primary human vascular cells were cultured in T25 filtered flasks containing endothelial growth medium (EGM; Lonza).

Production of Porcine Platelet-rich Plasma

To isolate the platelet fraction from whole porcine blood, 50 ml aliquots of blood were centrifuged for 15 minutes at 275 x *g* as previously described [91, 92, 93]. The plasma with platelets was collected from the top portion of the tube. PRP was flash-frozen by liquid nitrogen and stored at -80˚C. PRP samples were then thawed and centrifuged at 3000 x g for 20 minutes at 4˚C to maintain low levels of platelet activation. After centrifugation, two-thirds of the supernatant

were removed and the pellet was resuspended in the plasma that remained to calculate the platelet concentration. Platelet concentrations were estimated to be 712.50 ± 22.43 ($x10^4/\mu l$).

Recellularization of Porcine Single Lung Scaffolds

Recellularization was done based on cell installation protocols we previously established and described in Chapter 3. **Table 4.1** describes details of the recellularization procedure.

Table 4. 1 Process for Recellularization of Porcine Left Lung Scaffolds

Day of installation	Cell type or Reagent installed	Number of Installations	Method of Installation	Flow rate for installation
1	VEGF-MP in FGF2-Hydrogel	1	pumped into PA	0.5 ml/hr
1	PRP	2-60 minutes apart	pumped into PA	0.5 ml/hr
1	Primary Vascular Cells	2-3 hrs apart	pumped into PA	0.5 ml/hr
2	EGM+PRP	2-60 minutes apart	pumped into PA	0.5 ml/hr
2	Primary Vascular Cells	2-60 minutes apart	pumped into PA	0.5 ml/hr
3	EGM+PRP	2-60 minutes apart	pumped into PA	0.5 ml/hr
5	Primary Vascular Cells	2-3 hrs apart	pumped into PA	0.5 ml/hr
6	EGM+PRP	2-60 minutes apart	pumped into PA	0.5 ml/hr
7	Primary Vascular Cells	2-3 hrs apart	pumped into PA	0.5 ml/hr
9	EGM+PRP	2-60 minutes apart	pumped into PA	1 ml/hr
10	Primary Vascular Cells	2-3 hrs apart	pumped into PA	1 ml/hr
11	EGM+PRP	2-60 minutes apart	pumped into PA	1 ml/hr
11	MNL	2-60 minutes apart	pumped into PA	0.5 ml/hr
12	Primary Vascular Cells	2-60 minutes apart	pumped into PA	1 ml/hr
15	SAGM+PRP	2-3 hrs apart	pumped into trachea	0.5 ml/hr
16	KGF-Hydrogel	1	pumped into trachea	0.5 ml/hr
16	Primary Lung Cells	2-60 minutes apart	pumped into trachea	1 ml/hr
16	M2 Sup	2-60 minutes apart	pumped into trachea	1 ml/hr
18	PRP+MSC Sup	2-60 minutes apart	pumped into trachea	1 ml/hr
19	Lung cells	2-3 hrs apart	pumped into trachea	0.5 ml/hr
20	M2 Sup	2- 2 hours apart	pumped into trachea	1 ml/hr

21	Primary Lung Cells	2-3 hrs apart	pumped into trachea	0.5 ml/hr
22	SAGM+PRP	2- 2 hours apart	pumped into trachea	1 ml/hr
23	Primary Lung Cells	2-3 hrs apart	pumped into trachea	0.5 ml/hr
24	Primary Lung Cells	2-3 hrs apart	pumped into trachea	0.5 ml/hr
25	Primary Tracheal-Bronchial Cells	2- 2 hours apart	pumped into trachea	0.5 ml/hr
26	M2 Cell Sup	2-3 hrs apart	pumped into trachea and PA	0.5 ml/hr
27	M2 Cells	2- 2 hours apart	pumped into trachea and PA	0.5 ml/hr
28	MSC	2- 2 hours apart	pumped into trachea and PA	0.5 ml/hr
30	MNLs + Serum	1 installation	pumped into PA	1 ml/hr
30	Alveolar Macrophages	1 installation	pumped into trachea	1 ml/hr

Transplantation of the Bioengineered Left Lung into a Porcine Animal Model

The chest was entered through the previous pneumonectomy incision site for each animal. The bronchus was dissected free and cut at the desired length. The trachea of the BEL was trimmed prior to implantation. The bronchial anastomosis was completed using a running 4-0 PDS (Ethicon, Somerville, NJ) suture on the membranous portion of the airway and using interrupted 4-0 PDS sutures on the cartilaginous portion. The anastomosis was immediately inspected using bronchoscopy. The chest cavity then was filled with saline solution and left lung ventilation was gently initiated and the anastomosis was tested for leaks by inflating the lung to up to 30 mmHg of pressure. The chest was then closed in a routine manner. A 21 french tube was left in place and kept under negative pressure until the animal was awake and standing.

RESULTS

Overview of the Bioengineering Process and Transplantation of Bioengineered Lungs

Pig lung scaffolds were produced as previously described in Chapter 2 [88]. Only left lung scaffolds **(Figure 4.1 A)** were used. Individual catheters were placed into the main stem bronchus and the pulmonary artery of the scaffolds **(Figure 4.1 B)**. Pig AC single lung scaffolds were placed in the bioreactor chamber for recellularization **(Figure 4.1 C)**. Only left lung scaffolds were recellularized using autologous primary cells from the pigs that underwent a left lung pneumonectomy. **Figure 4.1 D** shows the culture platform set up with the bioreactor chamber, the fluidic support system and the fluid flow circulation. Bioengineered lungs were harvested after 30 days in culture **(Figure 4.1 E, F)**. Bioengineered lungs were then taken to the operating room and were transplanted via trachea-trachea anastomosis **(Figure 4.1 G)** and they were expanded **(Figure 4.1 H)**.

Bronchoscopies performed on bioengineered lungs before **(Figure 4.2 A)** after transplantation **(Figure 4.2 B)** showed airways were clear of debris. The anastamosis site where the bioengineered lung and native lung were connected was could be seen in the bronchoscopy images **(Figure 4.2 C)**. Computed tomography (CT) of the thorax of pig 1 (survived for two weeks) showed the presence of the bioengineered lung and the native lung **(Figure 4.2 D)**. The presence of collateral blood vessels in the bioengineered lung could be seen in the CT angiogram **(Figure 4.2 D, E)**, indicating collateral circulation had developed. A gross image of the bioengineered lung transplanted into pig 1, two weeks post-transplant can be seen in **Figure 4.2 F**. Micro-CT images demonstrate that both native lung and bioengineered lung contained open bronchial airways and tissue density was similar between both **(Figure 4.3 G, H)**. A CT angiogram of pig 4, survived for one month, showed that regions of the bioengineered lung aerated **(Figure 4.2 I)**. The

bioengineered lung can be seen in the left hemithorax in a coronal image of pig 1, one month post-transplant **(Figure 4.2 J)**. Herniation resulting from hyperinflation of the right lung, restricted the expansion of the bioengineered lung **(Figure 4.2 J)** but the transplanted bioengineered lung was still able to become aerated during breathing **(Figure 4.2 K)**. Magnetic resonance imaging (MRI) provided coronal **(Figure 4.2 L)** and axial **(Figure 4.2 M)** views of the outline of the transplanted bioengineered lung that showed capillary formation, indicating vascularization. An axial image showed a large intercostal vessel **(Figure 4.2 M)** originating from the aorta, branching toward the bioengineered lung. A gross image of the bioengineered lung transplanted to pig 4 is shown in **Figure 4.2 N** and demonstrated the difference in size compared to the native lung.

Tissue Development in Bioengineered Single Lungs Pre-Transplant and Post-Transplant

Transmission electron micrographs (TEM) of AC porcine scaffolds show that the ECM does not have an organized structure **(Figure 4.3 A)**. After 30 days of *in vitro* culture, histological evaluations of bioengineered lungs were done to examine lung tissue development. TEM of bioengineered lungs pre-transplant showed alveolar structures were present with some compressed areas where tissue had not developed properly **(Figure 4.3 B, C)**. TEM revealed the presence of many type II AEC that were identified by the presence of lamellar bodies **(Figure 4.3 D)**. At 1 month post-transplantation, the normal breathing of the animal enhanced aeration of the bioengineered lung and only occasional areas of compressed lung tissue were observed **(Figure 4.3 E, F)**. TEM of bioengineered lungs 10 hours post-transplant, showed the presence of a very few type I AEC **(Figure 4.3 G)**. Immunohistology also showed the presence of AQP5-positie type I AEC in bioengineered lungs transplanted into pig 4 **(Figure 4.3 H-K)**. The numbers of cells and the numbers of type I AEC in bioengineered lungs were significantly increased in animals survived

for 2-weeks ($p<0.05$) and 1 month ($p<0.005$) post-transplant when compared to the bioengineered lung transplanted into animals that were survived for 10 hours **(Figure 4.3 L-N)**. The bioengineered lungs transplanted into pig 5, survived for 2 months, had a lower number of cells and lower number of type I AEC due to an occlusion in the airway that prevented aeration of the tissue **(Figure 4.3 O)**.

Vascular development also was examined in bioengineered lungs pre-transplant and post-transplant. Pre-transplant evaluations of the capillaries in bioengineered lungs showed that there were no red blood cells present **(Figure 4.4 A)**. Although there was no normal blood flow to the transplanted bioengineered lungs, because vascular anastomosis was not performed, there was formation of collateral blood vessels. **Figure 4.4 B** shows an H&E stained tissue section of a collateral blood vessel containing red blood cells and well-developed capillaries within the bioengineered lungs. TEM of the distal lung regions of bioengineered lungs post-transplant confirmed the presence of capillaries that contained red blood cells and the presence of type I and type II AEC **(Figure 4.4 C, D)**. Immunohistochemistry of bioengineered vascular tissue showed CFSE-labeled primary vascular cells repopulated the vasculature and formed blood vessels **(Figure 4.4 E-G)**. The junction region between native lung and bioengineered lungs contained some CFSE-labeled primary vascular cells **(Figure 4.4 H, I)**. Recellularized blood vessels in the bioengineered lungs contained CD-31-positive endothelial cells **(Figure 4.4 J-M)**. The angiogenesis markers, transcription factor early growth response protein 1 (ERG1) **(Figure 4.4 N, O)**, endothelium nitric oxide synthase (eNOS) **(Figure 4.4 P, Q)**, and angiotensin converting enzyme **(Figure 4.4 R, S)** were also expressed. At two weeks **(Figure 4.4 T, U)** and one month **(Figure 4.4 V, W)** post-transplant, bioengineered lungs contained lymphatic vessels that expressed lymphatic vessel endothelial receptor-1 (LYVE-1).

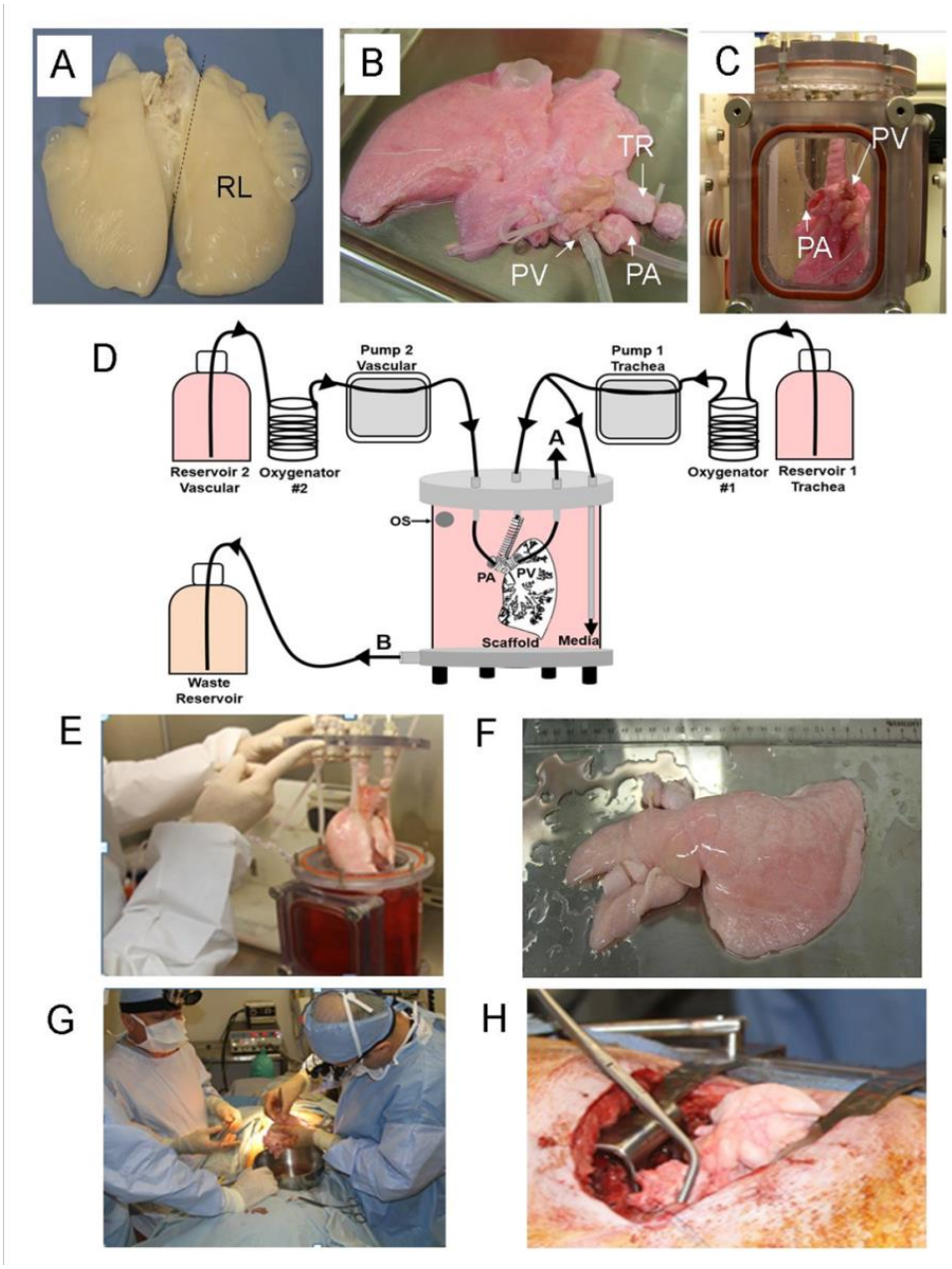

Figure 4.1 Overview of the Bioengineering Process. (A) Left lung scaffolds were produced from whole AC lungs. **(B)** Catheters placed in the trachea and pulmonary artery allowed for cell installation and the scaffold was lowered into the chamber. **(C)** Scaffolds were positioned in the bioreactor chamber to permit visualization of pulmonary artery , pulmonary vein and tracheal catheters. **(D)** Diagram of the fluidic system shows the microfluidic and pumping system supporting the bioreactor. For support of tracheal circulation, media flowed from reservoir-1 (R1) through the oxygenator to pump-1 (P1), then into the trachea (A) or the bioreactor tank and out at B, terminating at a waste container. PA=pulmonary artery, PV=pulmonary vein and TR=trachea. For vascular circulation, media flowed from reservoir-2 (R2) through the oxygenator to pump-2 (P2), into the pulmonary artery and out of the pulmonary vein, returning to reservoir-2 or to a waste container. **(E)** Bioengineered lungs were removed on day 30 and were **(F)** measured and weighed. The bioengineered lung in G was produced using the scaffold shown in B above. **(G)** The trachea as trimmed in the surgical suite. **(H)** Following the trachea to trachea anastomosis, lungs expanded. Reproduced with permission from Nichols *et al*. 2018.

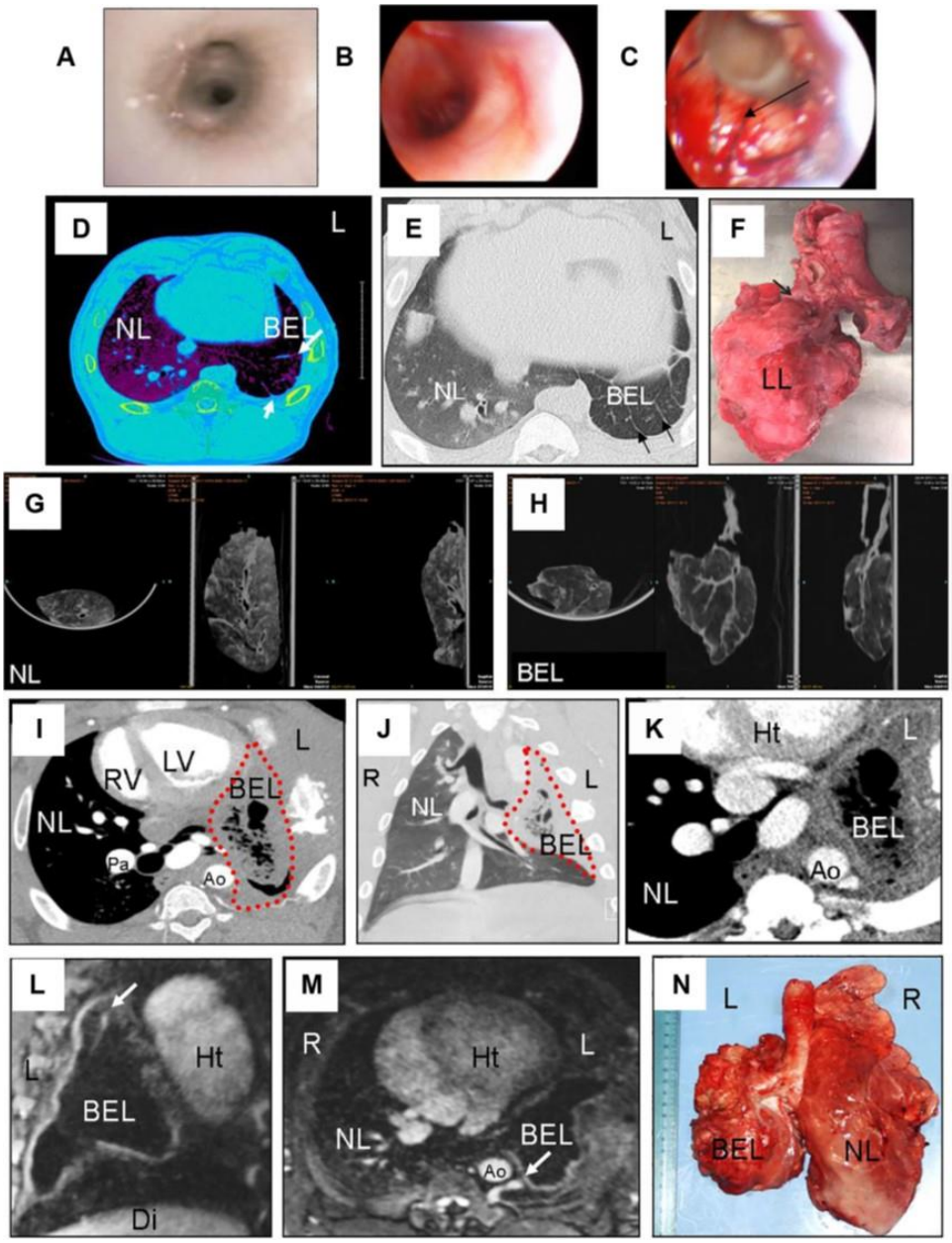

Figure 4.2 Gross assessment of transplanted bioengineered lungs and native lung. (A to C) Bronchoscopy images of **(A)** bioengineered lung (BEL) before and after transplant and of **(B)** the area above the anastomosis site showing left main stem bronchus, and **(C)** BEL trachea-to-trachea anastomosis (black arrow). **(D and E)** CT angiograms of the thorax of pig 1, 2 weeks after transplant. Native lung (NL) and BEL. **(D)** Collateral circulation in BEL is highlighted (white arrows), and aerated regions appear black in this colorized image. **(E)** Collateral vessels formed in BEL after transplantation (black arrows). **(F)** Gross image of BEL [left lung (LL)] from pig 1 after transplant. Black arrow indicates anastomosis site. **(G and H)** Micro-CTs of open airway in nonventilated **(G)** native lung and **(H)** BEL of pig 1. **(I to N)** BEL of pig 4, 1 month after transplant. **(I)** CT angiogram of the thorax in the arterial phase, axial image showing BEL in the left thoracic cavity (red dots denote edges of BEL). The pulmonary artery (Pa), aorta (Ao), right

ventricle (RV), and left ventricle (LV) are shown, as well as the left side (L) of the animal in this coronal image. **(J)** Coronal x-ray image showing BEL in the left hemithorax (red dots denote edges of BEL). **(K)** Axial CT image of both native lung and BEL. The heart (Ht) and left side of the animal are noted. **(L)** Coronal and **(M)** axial images of MRI angiography showing peripheral enhancement outlining the left BEL, indicating capillary vascularization. **(M)** MRI image showing full expansion of both right native lung and left BEL."R"denotes the right side of the animal and "L" the left side. **(L and M)** White arrows point to large collateral vessels in BEL. **(N)** Gross image of the BEL after necropsy showing native lung and the smaller BEL. Reproduced with permission from Nichols *et al*. 2018.

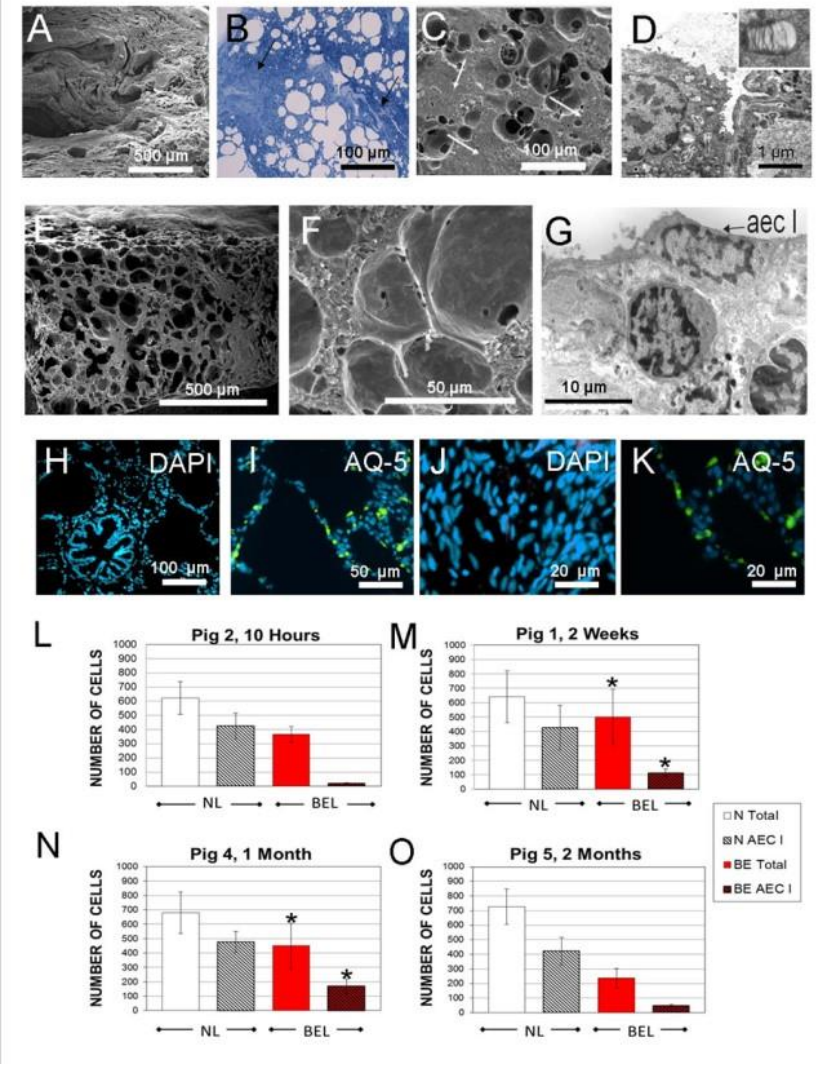

Figure 4.3 Lung tissue development in bioengineered lungs. (A) SEM of distal lung region of AC scaffold. **(B)** Representative image of methylene blue-stained thin section of bioengineered lung pre-transplantation highlighting compressed (non-aerated) regions (arrows) and aerated spaces. **(C)** SEM of alveoli in bioengineered lung pre-transplant. **(D)** TEM image of type II AEC (insert, lamellar body) pre-transplant. **(E-K)** Evaluation of pig-4 bioengineered lung (1 month post-transplant). **(E)** SEM of bioengineered lung post-transplant shows increase in aerated alveolar regions due to normal breathing (arrows). **(F)** SEM of bioengineered lung demonstrating alveolar development. **(G)** TEM of bioengineered lung containing type I AEC. **(H-K)** Histological examination of lung tissue from pig-4, BEL. **(H, J)** DAPI stained controls and **(I, K)** AQ-5 (green) positive type I AEC. **(Q-T)** Averaged counts of number of cells and the number of type II AEC in native lungs or bioengineered lungs for pigs survived for **(Q)** 10 hours, **(R)** 2 weeks, **(S)** 1 month or **(T)** 2 months. Significantly more cells and more type I AEC were found in

the animals survived 2 weeks and 1 month post-transplant than were found at 10 hours or 2 months ($p^*<0.05$). Reproduced with permission from Nichols *et al*. 2018.

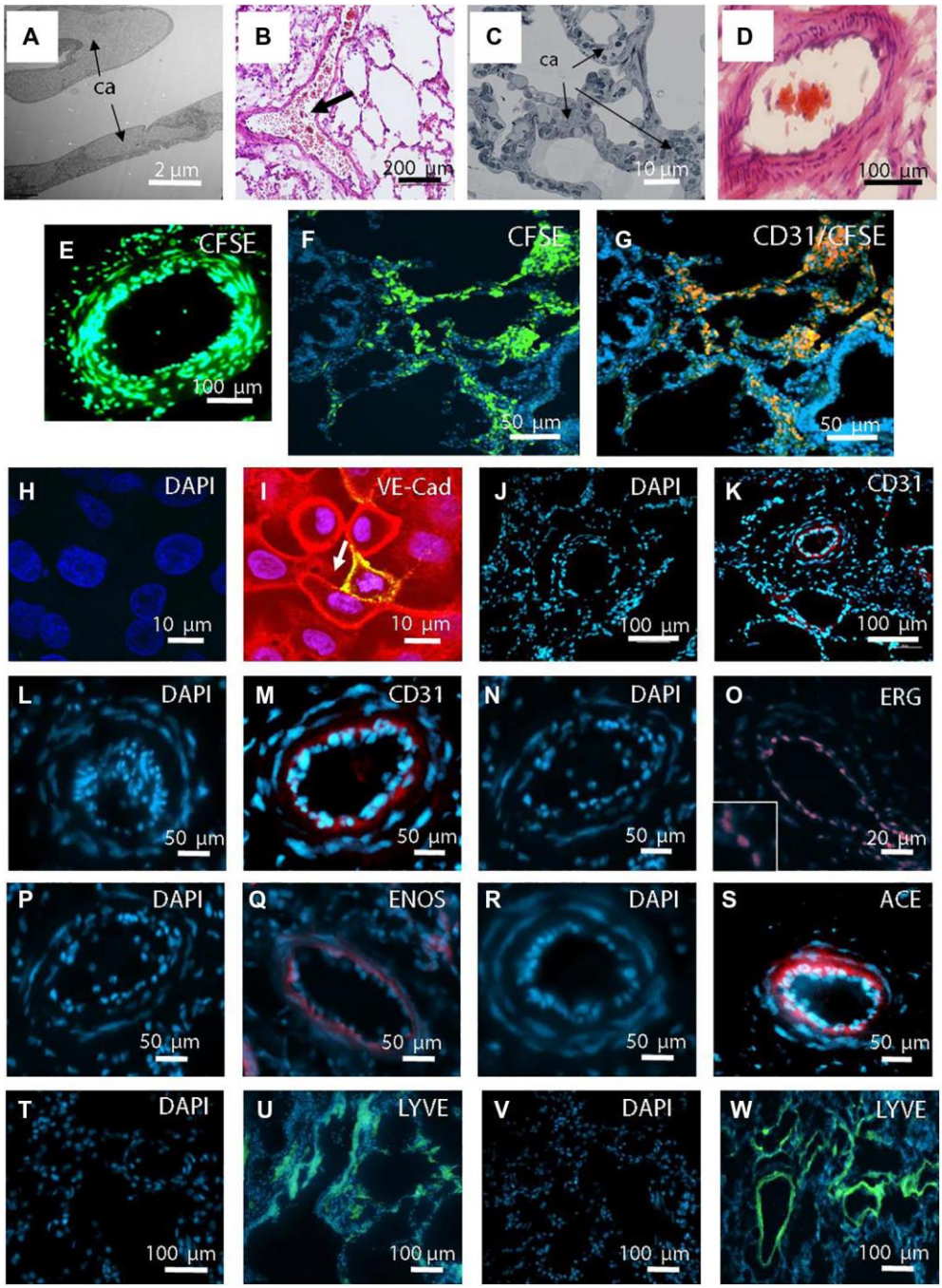

Figure 4.4 Vascular tissue development in bioengineered lungs pre and post transplantation (A) Transmission electron microscopy (TEM) of BEL on day 30 of bioreactor culture demonstrating capillaries (ca; black arrows) without red blood cells. **(B)** Hematoxylin and eosin (H&E) image of BEL at 2 weeks after transplant and **(C)** TEM of red blood cell–filled collateral capillaries (black arrows). **(D)** Cross-sectional H&E image of collateral blood vessels in BEL 2 weeks after transplant. **(E to W)** BEL harvested 1 month after transplant. **(E)** Cross section of CFSE-labeled (green) vessel in BEL. **(F and G)** Blood vessels within BEL formed from CFSE-labeled (green) primary lung–derived vascular cells. **(G)** Overlay of CD31+ (red) staining with CFSE+ (green). **(H)** 4′,6-Diamidino-2-phenylindole (DAPI; blue, nuclei) staining

control lung for **(I)**. **(I)** Junction of collateral vessel outside of the BEL. VE-cadherin+ (VE-Cad; red) endothelial cells and CFSE-labeled primary lung–derived vascular cells (white arrow) were found where collateral vessels joined with the BEL vasculature. **(J to S)**. Cross sections of BEL blood vessels. **(J, L, N, P, and R)** DAPI staining controls and sections stained for **(K and M)** CD31+ (red), **(O)** ERG+ (red), **(Q)** eNOS+ (red), and **(S)** ACE+ (red) cells, all of which are indicators of endothelial cell function in the BEL. **(T and V)** DAPI control and representative image showing LYVE-1+ (green) lymphatic cells at **(U)** 2 weeks and **(W)** 1 month after transplant. Reproduced with permission from Nichols *et al*. 2018.

DISCUSSION AND CONCLUSION

Major accomplishments have been made related to bioengineering of lung [43, 44] and vascular tissue but we have yet to progress to the point where fully functional and transplantable lungs have been created. Whole bioengineered lungs produced on AC lung scaffolds have been transplanted in small animal models, but these lungs failed due to intravascular coagulation and defects in barrier function leading to fluid loss [43, 44]. The lack of ability to bioengineer functional vascular tissues has hindered our advancement of *in vitro* lung tissue development.

For this reason, in this study our recellularization efforts were focused on adequately developing patent pulmonary vasculature. This led us to concentrate on development of blood vessels that could support gas exchange alone. Although the development of pulmonary vasculature needs to be closely correlated with development of the airways we feel that the development of the pulmonary artery and pulmonary vein needs to be managed independently in order to facilitate tissue maturation. In this study, we utilized whole-organ tissue-engineering technologies and methods including biological scaffold production and the use of nanoparticles to deliver growth factors to developing tissues in order to produce bioengineered lungs. We used information related to culture modifications identified in the *in vitro* system to produce large animal whole organs in a newly designed bioreactor culture chamber. The bioreactor facilitated optimization of our recellularization protocol of whole acellular scaffolds and protocols to support

whole-organ culture. Autologous cells isolated from the recipient pig (pig receiving a transplant) and a left lung AC scaffold were used to bioengineer a single bioengineered lung. Pig survival, and tissue development *in vitro* and *in vivo* were evaluated at 10 hours, 2 weeks, 1 month and 2 months post-transplant.

Our results indicated that all pigs who received a bioengineered lung transplant, had development of collateral vessels indicating the development of systemic circulation. This collateral systemic circulation aided in survival of transplanted bioengineered lungs. We did not perform assessments of gas exchange because when transplanted, the bioengineered lungs were supplied with oxygenated blood (unlike native lungs receiving deoxygenated blood) and there was no oxygen gradient to allow for gas exchange. Bioengineered lungs contained well-developed bronchial and alveolar epithelium. We found that the overall cell numbers present in bioengineered lungs increased in pigs survived for 10 hours to 2 months. This indicated that lung tissue and vascular tissue development in transplanted bioengineered lungs was still in progress *in vivo* after being transplanted.

These results support the use of this platform for studies of bioengineered lung development and pulmonary vascular tissue development both *in vitro* and *in vivo*. Future directions involve the subsequent evaluation of the ability of bioengineered lungs to support gas exchange *in vivo* and have pigs receiving a bioengineered lung transplant, rely only on the oxygen the bioengineered lung can provide.

CHAPTER 5

Bleomycin induced Pulmonary Fibrosis

INTRODUCTION

As mentioned in Chapter 1, there is a need for better experimental models that can mimic chronic lung diseases and respiratory infections in humans. HoC composed of bioengineered human lung tissue (mentioned in Chapter 3) can be used as experimental model systems to mimic human disease. ILD is associated with a broad range of more than 200 conditions characterized by progressive lung scarring known as PF [4]. This progressive thickening and scarring of lung tissue may be caused by a variety of environmental factors (e.g. drug exposure, viral and bacterial infections, environmental pollutants,) that provoke lung injury, or genetic factors. In many cases, like in idiopathic pulmonary fibrosis (IPF), causes are still unknown. Adverse effects of some drug therapies may lead to drug-induced development of PF. Many cases of drug-induced PF have been reported in patients being treated with the chemotherapeutic drug bleomycin. Bleomycin-induced PF has been extensively studied in patients and animal models.

BLEOMYCIN CHEMICAL STRUCTURE AND MECHANISM OF ACTION

Bleomycin is a glycopeptide-derived antibiotic and antineoplastic compound that was originally isolated from the bacterium *Streptomyces verticillus* [97]. Bleomycin is well characterized by its antitumor ability and has been used as a chemotherapeutic agent for treatment of a variety of cancers. The chemical structure of bleomycin is composed of four distinct regions, an N-terminal domain, a methylvalerate-threonine linker peptide, C-terminal domain and a disaccharide moiety [98, 99]. The N-terminal domain consists of a pyrimidoblamic acid subunit

and an adjacent β-hydroxyl histidine that are responsible for several functions, including metal binding, activation of oxygen and site-selective DNA cleavage [98, 99]. The methylvalerate-threonine linker connects the N-terminal domain to the C-terminal domain. The C-terminal domain contains a bithiazole moiety that provides DNA-binding affinity. The disaccharide moiety is responsible for in cell-surface recognition, selective accumulation of bleomycin in some cells types and it is also thought to influence metal ion binding [98]. Bleomycin forms complexes with iron that reduce molecular oxygen to superoxide and hydroxyl radicals that can cause DNA strand scission, producing both single- and double- DNA strand breaks and ultimately cell death [100].

BLEOMYCIN-INDUCED PULMONARY TOXICITY AND DEVELOPMENT OF PULMONARY FIBROSIS IN CANCER PATIENTS

Although it is used as a chemotherapeutic agent, the use of bleomycin is now limited due to its severe adverse effects of pulmonary toxicity and subsequent development of pulmonary fibrosis [101, 102]. The mechanisms by which bleomycin leads to the development of pulmonary fibrosis in humans are not well understood. Many cases of bleomycin-induced pulmonary toxicity with development of pulmonary fibrosis have been reported in patients with Hodgkin's lymphoma [103, 104] non-Hodgkin's lymphoma [105], testicular carcinoma [106, 107, 108, 109, 110], ovarian cancer [107, 109, 112] and small cell lung cancer [113]. Some of the risk factors for development of bleomycin-induced pulmonary toxicity and development of pulmonary fibrosis include age, smoking, renal insufficiency, high fraction of inhaled oxygen and radiation therapy [103, 114, 115, 116]. Although advanced age has been recognized as a risk factor, cases of bleomycin-induced pulmonary fibrosis also have been reported in younger patients (< 40 years old) [104, 106]

Symptoms and Diagnosis of Bleomycin-Induced Pulmonary Fibrosis

Symptoms of bleomycin-induced pulmonary toxicity include dyspnea, nonproductive cough, crackles, cyanosis, fever and chest pain or discomfort [rxlist.com]. In patients, symptoms may appear as early as 9 days [117, 118, 119] or 5 months [104, 106] after chemotherapeutic regimens containing bleomycin have been administered. Once patients present with symptoms and a diagnosis is made, extensive damage to the lungs has already been done. Much of the patient data available about bleomycin-induced pulmonary toxicity comes from surgical lung biopsies of patients who suffer from an advanced stage of pulmonary fibrosis and are in respiratory failure. Not much is known about the early pathological changes that occur upon initial exposure to bleomycin during the acute phase of bleomycin-induced pulmonary toxicity before formation of fibrotic lung tissue. Characterization of the early events leading to bleomycin-induced pulmonary toxicity and development of pulmonary fibrosis would help to identify potential targets to prevent the formation or progression of fibrosis.

Diagnosis of bleomycin-induced pulmonary toxicity and pulmonary fibrosis in patients undergoing chemotherapeutic treatment can be difficult because symptoms and clinical signs are not specific to bleomycin-induced lung injury. Diagnosis is most often made by exclusion of other diseases, conditions or malignancies. Patients undergoing chemotherapeutic treatment can be vulnerable to respiratory infections that cause similar symptoms. Bronchoalveolar lavage (BAL) obtained from patients' lungs, blood tests or sputum cultures can be used to identify any infections. Once respiratory infections are ruled out, patients who present these symptoms, can be further examined for bleomycin-induced pulmonary fibrosis through chest X-rays or high resolution computed tomography (HRCT). For a proper diagnosis, it is also important to distinguish differences between progression of cancer malignancies in the lungs and bleomycin-induced

pulmonary fibrosis when identifying and examining lung abnormalities found in a chest X-ray or HRCT.

Similarly to the diagnostic exclusion of respiratory infections, BAL from patients can be used to exclude possible malignancy-induced lung abnormalities that may appear in radiographic findings. In patients with bleomycin-induced pulmonary fibrosis, chest X-rays may reveal nodular densities and unilateral or bilateral, interstitial or alveolar focal infiltrates [102, 120, 121]. HRCT is a more sensitive method when compared to a chest X-ray and it provides detailed images that can help to better characterize the pattern and extent of lung abnormalities [122, 123]. HRCT can help to confirm the presence of bleomycin-induced fibrotic lung tissue by showing patchy unilateral or bilateral ground glass opacities, reticular opacities, airspace consolidation and septal thickening [102]. For patients with end-stage bleomycin-induced pulmonary fibrosis, widespread densely fibrotic lung tissue will appear as clustered cystic air spaces, a condition referred to as honeycombing of the lungs [124].

In instances when an HRCT scan is not sufficient to clearly identify bleomycin-induced fibrotic lung tissue, a surgical lung biopsy is needed for histological examination. Histopathology of lungs from patients with bleomycin-induced pulmonary fibrosis show disarrangement of alveolar structure, infiltration of inflammatory cells into alveoli, increase in the presence of fibroblasts and myofibroblasts and excess deposition of collagen [102].

Treatment for Bleomycin-Induced Pulmonary Toxicity and Fibrosis

Optimal treatment for patients suffering from bleomycin-induced pulmonary toxicity and pulmonary fibrosis has not been established. Upon diagnosis of bleomycin-induced lung injury, the immediate response should be to remove bleomycin from the chemotherapeutic regimen. Glucocorticoids or other immunosuppressive drugs have been used for treatment of bleomycin-

induced pulmonary toxicity and pulmonary fibrosis [125]. The patient response to glucocorticoid treatment after bleomycin-induced pulmonary toxicity and development of pulmonary fibrosis can vary. One study that examined the effects of corticosteroid treatment, reported that seven out of ten patients who received glucocorticoid treatment showed significant improvement in radiographic findings but their PFT remained abnormal [126]. The other three patients who did not receive corticosteroid treatment died [126].

It is uncertain if the degree and extent of lung damage caused by bleomycin-induced pulmonary toxicity at the time of bleomycin cessation is a good predictor of the overall outcome of the patient. The extent of bleomycin-induced lung damage is dependent on many factors (dose of bleomycin, risk factors or delays in diagnosis) and can vary among patients, making it difficult to predict what the outcome of bleomycin-induced pulmonary toxicity will be on patients' overall health.

When bleomycin-induced pulmonary toxicity progresses to pulmonary fibrosis, respiratory complications that are unrelated to the patients' initial cancer diagnosis can arise and result in premature death. The long-term risks of bleomycin-induced pulmonary toxicity in surviving patients who have undergone chemotherapeutic treatment containing bleomycin can vary between patients. There have been few studies that have examined the long-term effects of bleomycin-induced pulmonary toxicity in surviving cancer patients and data currently available shows conflicting results [127, 128]. One study examined the outcome of patients with Hodgkin's lymphoma who were treated with a chemotherapeutic regimen that included bleomycin and developed bleomycin-induced pulmonary toxicity. This study found that the 5-year overall survival rate of patients who developed bleomycin-induced pulmonary toxicity was 63%, a significant decrease when compared to the 90% 5-year overall survival rate of patients without

bleomycin-induced pulmonary toxicity ($p<0.05$) [127]. A different study suggested that bleomycin-induced pulmonary toxicity did not have adverse effects on the overall survival of patients with Hodgkin's lymphoma when compared to patients without bleomycin-induced pulmonary toxicity but they report that at the end of the follow up study; 17% of these patients died due to treatment-related complications [128].

MURINE MODELS OF BLEOMYCIN-INDUCED PULMONARY FIBROSIS

Bleomycin is one of the most commonly used agents for the induction of pulmonary fibrosis in a variety of animal models [129]. Murine models of bleomycin-induced pulmonary fibrosis have been extensively characterized and are the most widely used to study the disease but their strain-dependent susceptibility to bleomycin and resolving nature of fibrotic lesions, prevents their use for studies with clinical relevance. Histopathological features of bleomycin-induced pulmonary fibrosis in murine models also do not accurately reflect those seen in fibrotic human lungs. **Table 5.1** summarizes many of the similarities and differences between human PF and bleomycin-induced PF in murine models. To induce fibrosis, bleomycin can be administered into the airway by intratracheal and intranasal routes or systemically by subcutaneous, intravenous or intraperitoneal routes (129, 130). In murine models, fibrosis develops within 14 – 28 days post exposure to bleomycin. The pathological effects of bleomycin-induced fibrosis in murine models include damage to the alveolar epithelium, induction of type II alveolar epithelial cell metaplasia, infiltration of inflammatory immune cells and deposition of collagen. Key characteristics of usual interstitial pneumonia (UIP) in human fibrotic lungs that are not recapitulated in murine models include formation of fibroblastic foci, hyperplastic epithelium and temporal heterogeneity (131).

Table 5.1 Similarities and differences between human PF and bleomycin-induced PF in murine models

Characteristics of Disease	Human Pulmonary Fibrosis	Bleomycin-Induced Pulmonary Fibrosis in Murine Models	Comments
Disease progression	Pathological characteristics during initiation of disease in humans have not been characterized because of the lack of availability of human lung tissue during the onset of disease. Progression of disease can be slow (years) or rapid (months).	Disease develops between 14 and 21 days, although it may be reversible and completely resolve in some strains of mice.	The initiation of disease in humans has not been defined and is not understood. Most patient lung samples are only available at an advanced stage (symptomatic phase) of disease when clinical symptoms are severe.
Alveolar epithelial cell injury or death	Assessments of AEC injury or death at the initiation of disease are not known due to lack of patient data during the onset of disease	AEC death is observed	Cellular and molecular pathological changes during the initiation of disease are poorly understood in humans.
Pro-inflammatory cytokines	The role of the inflammatory response during initiation of disease is not known. Conflicting studies exist about the involvement of the inflammatory response during the progression of disease	Presence of an inflammatory response characterized by production of pro-inflammatory cytokines and infiltration of immune cells.	Characterization of the inflammatory response during initiation of disease in humans is needed.
Anti-inflammatory cytokines	Increase in the production of anti-inflammatory (pro-fibrotic) cytokines	Increase in the production of anti-inflammatory (pro-fibrotic) cytokines	In this aspect, both are similar. The role of the anti-inflammatory response during progression of the disease is not well-understood.
Fibroblasts	Increase in fibroblasts	Increase in fibroblasts	In this aspect both are similar
Myofibroblasts	Increase in myofibroblasts	Increase in myofibroblasts	In this aspect, both are similar

Fibrosis localization	Temporal and spatial heterogeneity of fibrosis with basal and subpleural fibroblastic foci	Bronchiolocentric distribution of fibrosis and presence of fibroblastic foci	Some similarities but the rodent models are not fully consistent with histopathology of UIP in humans
Clinical features	Clinical course of IPF is characterized by an early asymptomatic phase and a symptomatic phase as disease progresses. As disease progresses, severity of dyspnea worsens, there is a decrease in forced vital capacity and lung compliance	There is uncertainty regarding changes in the forced vital capacity and lung compliance of rodents.	More research is needed to determine similarities and differences of clinical features between human IPF and rodent models

One of the limitations of using a murine model of bleomycin-induced pulmonary fibrosis is that the disease induced by a single dose of the drug is self-limiting and resolves completely in some strains of mice [129]. Studies have reported that in a repetitive dosing bleomycin model, fibrosis persists and is irreversible up to 10 weeks after the last dose is administered but the model still fails to recreate characteristic features of UIP in humans [130, 131]. Susceptibility to bleomycin-induced fibrosis and severity of disease are also dependent on the strains of mice being used [131]. This variability in susceptibility might be due to the differential expression of the bleomycin inactivating enzyme, bleomycin hydrolase amongst mice strains [131]. Differences between murine and human immunological systems are also important to consider when examining the inflammatory response to injury and fibrotic tissue remodeling [131]. The spontaneous resolution of fibrosis, strain-dependent susceptibility, immunological and genetic differences and inability to consistently recreate the histopathology found in human lungs, limit the use of murine models for the study of human disease. Conflicting results on the progression, persistence and pathology of pulmonary fibrosis have been reported due to the variability of

fibrosis development in animal models. While animal models have been indispensable tools for understanding the pathogenesis of disease, they provide a limited correlation with pulmonary fibrosis in humans and are often times not clinically relevant.

IDIOPATHIC PULMONARY FIBROSIS

Incidence and Prevalence

Often times, pulmonary fibrosis develops without a known cause such as in idiopathic pulmonary fibrosis (IPF). Although the initial insult to the lungs may be caused by a different agent or event, IPF and bleomycin-induced PF are both characterized by the formation of fibrotic tissue in the lungs and they share pathological characteristics.

IPF is a chronically progressive fibrotic lung disease that has a poor prognosis with the median survival being 2-3 years after a patient is diagnosed [132]. There are currently no effective treatments for IPF that prevent, stop or reverse progression and damage of lung scarring. The ultimate result of chronically progressive pulmonary fibrosis is respiratory failure. Incidence and mortality of IPF increase with older age [133] although cases also have been reported in younger patients (<50 years of age) with an underlying comorbidity such as a connective tissue disease [132, 134]. Incidence and prevalence of IPF is higher in men than in women. Difficulties in the diagnosis and lack of large scale population studies have made it challenging to form an appropriate estimate of the incidence and prevalence of IPF in the U.S. and around the world [132, 135, 136]. In small-scale population studies within the U.S., incidence has been reported to range from 6.8 – 8.8 per 100,000 in women and 10.7 – 17.4 per 100,000 in men [135, 137, 139, 183]. In these same studies, prevalence in the U.S. has been reported to range from 13.2 – 27.9 per 100,000 in women and 20.2 – 63.0 per 100,000 in men [135, 138].

Although the etiology of IPF is unknown, some risk factors have been identified in patients. Cigarette smoking [140], occupational or environmental exposures to metal dusts such as brass, lead and steel or wood dust, farming, exposure to livestock, exposure to microbial agents such as Epstein-Barr virus [142, 143, 144, 145] hepatitis C virus [146, 147, 148], and some strains of influenza virus [149, 150 151, 152] have all been shown to be associated with an increased risk of developing IPF. Familial forms of pulmonary fibrosis also have been shown to influence the development of IPF [132, 153]

Clinical Course of Idiopathic Pulmonary Fibrosis

In patients, the clinical course of IPF can be slowly or rapidly progressive from the onset of disease to the time of death [154]. Slow, progressive formation of scar tissue, leads to a slow decline in lung function that may involve periods of stability but eventually result in respiratory failure several years after diagnosis of IPF. Patients with rapidly progressive IPF, have a shortened survival due to the rapid formation of fibrotic scar tissue that leads to a faster decline in lung function. The reasons behind these differences in progression of IPF among patients are not entirely known. The unpredictability and variability of clinical progression makes clinical management of IPF difficult. It may be that these are distinct phenotypes for IPF that are influenced by genetic or environmental factors [132]. One study reported that patients with rapid progression of IPF were mostly male cigarette smokers [155]. These patients with rapidly progressing IPF had different gene expression profiles when compared to patients with slowly progressive IPF despite having similar lung function, radiological findings and histopathology upon diagnosis [155]. Another study also reported differences in gene expression profiles in lung surgical biopsies taken at the time of diagnosis from patients with slowly progressive or stable IPF and patients with rapidly progressive IPF [156]. This study suggests that molecular phenotypes identified through

gene expression profiles might be helpful in predicting if the clinical course of IPF will be slowly or rapidly progressive in patients [156]. Lung tissue from patients with rapidly progressive IPF contains significantly higher numbers of macrophages and neutrophils than lungs from patients with slowly progressive IPF [157].

Symptoms and Diagnosis of Idiopathic Pulmonary Fibrosis

Symptoms of IPF are the same as with bleomycin-induced pulmonary fibrosis. In patients, the onset of symptoms often happens at a later time after the onset of disease, when initial pathological changes have already happened and lung damage is significant enough to cause symptoms. Similar to bleomycin-induced pulmonary fibrosis, a delay in the onset of symptoms leads to a delayed diagnosis that may be months or years after the onset of disease and at a later chronic stage of IPF. For this reason, early pathological changes that initiate the irreversible formation of fibrotic lung tissue in patients with IPF are not well understood. Similar to bleomycin-induced pulmonary fibrosis, diagnosis of IPF can be a challenge and must be done by exclusion. A multidisciplinary diagnostic approach involving clinical assessments, radiologic imaging and histopathologic examination is required [132]. The American Thoracic Society and European Respiratory Society have recognized UIP as a characteristic hallmark for the diagnosis of IPF [132]. In all patients with IPF, high resolution computed tomography (HRCT) consistently shows a pattern of UIP where subpleural and basal reticular opacities represent patchy fibrotic lesions [132]. HRCT also will show honeycombing. Although HRCT has been considered an essential component in the diagnosis, relaying on it entirely is not always sufficient to confirm IPF. While less invasive diagnostic methods are preferred, surgical lung biopsies are often required in patients suspected of having IPF. Histological evaluations of surgical lung biopsies from patients with IPF confirm the presence UIP. A key histological feature of UIP is the temporal or spatial

heterogeneous distribution of fibrosis characterized by patchy fibrotic scarring or fibroblastic foci distributed throughout areas of unaffected lung tissue that look histologically normal [132].

Biomarkers of Idiopathic Pulmonary Fibrosis

There are currently no universally accepted biomarkers that are specifically indicative of IPF and can be used in clinical practice. There is a great need for biomarkers that can be used to identify early pathological changes that initiate the development of IPF in order to prevent disease progression and irreversible lung damage. Targeting IPF during its early stages before respiratory function is severely altered will help to improve the overall quality of life and survival of patients. Numerous studies have been done to try and identify potential biomarkers in patients with IPF but most of these studies have used samples from patients with an advanced stage of IPF. Of particular interest is the role of matrix metalloproteinases (MMPs) and their inhibitors, tissue inhibitors of metalloproteinases (TIMPs) in formation of fibrotic lung tissue. MMPs are calcium-dependent, zinc-containing endopeptidases whose main functions involve the turnover and degradation of ECM structural proteins. TIMPs are endogenous inhibitors whose role is to inhibit the functions of MMPs in order to regulate ECM turnover [158] and maintain homeostasis. The literature suggests certain MMPs and TIMPs may be involved in the pathogenesis of IPF.

Increased gene and protein expression of MMP-7 and MMP-9 have been found in lung tissue from patients with IPF, while normal lungs from patients without IPF had minimal to no expression [159, 160, 161 162]. MMP-7 expression has been found to be abundantly localized in the alveolar epithelium and in fibrotic foci of lungs from patients with IPF [160, 161]. MMP-9 expression has been found be localized in dense areas of scar tissue in lungs from patients with IPF [161]. Another study found that concentrations of MMP-1 and MMP-7 were significantly

increased in plasma, bronchoalveolar lavage fluid and lung tissue from patients with IPF when compared to healthy control patients [163].

To examine if increased expression of MMP-1 and MMP-7 was specifically indicative of IPF, this study also compared expression of MMP-1 and MMP-7 in patients with COPD and sarcoidosis and found that these patients did not have increased levels [163]. Levels of TIMP-1 also have been found to be increased in lung tissue and BAL fluid of patients with IPF [159, 164].

Krebs von den Lungen-6 (KL-6) is a mucin-like glycoprotein that is normally expressed at low levels by type II AEC but is also thought to have pathophysiologic functions. Increased levels of KL-6 in patients with IPF have been shown to predict prognosis, as these patients have a reduced survival [165]. KL-6 also has been shown to be a chemoattractant for human fibroblasts, which may further implicate its role in IPF [166].

Some studies have identified SP-A and -D as possible diagnostic markers and predictors of IPF. Serum levels of SP-A and SP-D have been found to be significantly elevated in patients with IPF than in healthy volunteers [167, 168, 169]. In contrast to these findings, patients with IPF also have been found to have significantly lower levels of SP-A in their BAL fluid when compared to BAL from healthy volunteers [169]. Lower levels of SP-A in BAL fluid of patients with IPF also correlate with a shortened survival [170]. On the contrary, significantly increased serum levels of SP-D in patients with IPF are prognostic of a shortened survival [171]. The presence of alternatively activated M2 macrophages has also been documented in lung tissue from patients with IPF [172, 173] but their role in the formation of fibrotic lung tissue is not well-understood.

While there has been some progress in trying to identify potential biomarkers of IPF in humans, one of the limitations of these studies is that patient samples obtained for evaluations are

usually from patients with an advanced stage of the disease. Delayed diagnosis and unavailability of patient samples during the early phase of IPF hinders the possibility of characterizing early pathological changes and identifying early biomarkers of IPF. It is not known if the factors or potential biomarkers identified in the studies mentioned above are also present or differentially expressed during the early stages of IPF when pathological changes begin, before the formation of fibrosis. More research is needed to determine if the factors identified in these studies are specific determinants of IPF that could be used for clinical practice. Identification of biomarkers specific to IPF that can be measured through minimally invasive methods such as serological testing would be helpful for diagnosis, prediction of disease progression and prognostication of mortality [174].

Mechanisms of Pulmonary Fibrosis Pathogenesis

Although the underlying pathological mechanisms of IPF are not well understood it is believed that an aberrant wound healing/tissue repair response is involved in the development of fibrotic lung tissue. The complexity of the cellular and molecular processes that may be involved in the development of IPF make it challenging to study and identify key factors that drive a dysregulated tissue repair response and initiate fibrosis. As mentioned before, much of what we know about the pathogenesis of IPF comes from clinical data obtained from patients with an advanced stage of IPF and our understating about of how fibrotic lung tissue initially develops is limited. Lack of animal models that can closely mimic key pathological characteristics of IPF also represents a barrier in elucidating mechanisms of pathogenesis.

In the past, medical treatments for IPF aimed to minimize inflammation, due to the previous belief that IPF was a chronically inflammatory disease. Data suggests that although inflammation plays a role in pathogenesis it may not be directly involved in the formation and progression of fibrotic lung tissue. Immunosuppressive therapies aimed at reducing inflammation

have proved to be ineffective in patients with IPF [132, 175, 176]. Despite using immunosuppressive therapies to effectively reduce inflammation in the lungs of patients with IPF, there is no positive correlation between reduction of inflammation and improvement of clinical outcome or survival in patients with IPF [132, 177, 178, 179, 180, 181, 182, 183] The paradigm is now shifting, and it is believed that underlying mechanisms of IPF development and progression involve an aberrant tissue repair response. This dysregulated tissue repair response is thought to involve epithelial injury, uncontrolled fibroblast proliferation which leads to an increase in fibroblasts, fibroblast differentiation into myofibroblasts, and excessive deposition of collagen that results in fibrosis [184].

CHAPTER 6*

Validation and Utilization of a 3D Bioengineered Human Lung Construct as a Model to Study Pathogenesis of Lung Disease

INTRODUCTION

Although our bioengineered whole human lung constructs allowed us to develop whole organ recellularization procedures and examine critical factors needed for the development of lung tissue *in vitro*, their use as HoC model systems is limited by complexity of the methods needed for their production and the high cost associated with their production. In our previous studies detailed in Chapters 2 and 3, we have developed small-scale cell-scaffold constructs for initial examinations of cell attachment to human AC lung scaffolds [88, 89], immunogenicity of human AC lung scaffolds [88] and human lung tissue development [89]. Using this same concept, in this study, we have developed a 3D bioengineered human lung construct that is composed of a human AC lung scaffold and primary or immortalized human lung cells (pHLC or iHLC). We provide data to support the ability of 3D engineered human lung constructs to be used as *in vitro* models to examine early pathological changes associated with acute lung injury and initiation of PF. Underlying pathological mechanisms of acute lung injury (ALI) and PF in humans are not well understood. Unavailability of patient lung samples during the early stages of ALI or PF has made it challenging to study early pathological changes or to identify early biomarkers during initiation of lung disease in humans. Obstacles in development of effective treatments are due to the lack of experimental models that mimic key pathological characteristics of human ALI and PF. Persistence and progression of ALI can lead to the development of PF (Johnson et al. 2010). There

are currently no available medical treatments that effectively prevent, reverse or cure the condition, making the elucidation of pathological mechanisms of PF a priority.

Primary human lung cells (pHLC) or immortalized human lung cells (iHLC) from 10 lung donors were used for development of human lung constructs. To examine the role of macrophages in fibrosis development, constructs were bioengineered with or without human peripheral blood monocyte-derived macrophages. After bleomycin-exposure, only constructs containing macrophages had excessive collagen deposition. We demonstrate that constructs produced from either pHLC or iHLC had similar responses when exposed to bleomycin and were able to help identify early pathological changes that occur during acute lung injury as PF develops. Type II AEC were found to express MMP-7 after bleomycin-induced lung injury.. Significant increases in the amount of collagen deposition that distorted alveolar structure and increases in the percentages of fibroblasts and myofibroblasts after exposure to bleomycin confirmed fibrosis development. Constructs recreated histopathological characteristics of PF similar to those described in patients such as UIP. Examination of areas with dense collagen deposition which resembled fibrotic foci contained M2 macrophages that expressed TIMP-1. Total numbers of M2 macrophages significantly increased as fibrosis developed.

MATERIALS AND METHODS

Procurement of human lungs

Human lungs used for this study, were obtained as discarded specimens through protocols approved by the Institutional Review Board (IRB) at the University of Texas Medical Branch (UTMB) and The Methodist Hospital Research Institute (MHRI). Procurement and handling of lungs was done as previously described (Nichols *et al*. 2013, Nichols *et al*. 2016). Lungs used for

the production of acellular scaffolds were flash frozen in dry ice and stored at -80˚C until use for decellularization. Human lungs with viable tissue were used for primary cell isolation, 2-3 hours after procurement. Only lungs from individuals with no history of smoking, lung disease or infectious disease were used for decellularization and the isolation of primary human lung cells.

Decellularization and production of whole human lung scaffold and scaffold pieces

Upon procurement, human lungs were stored at -80˚C and were kept in storage at least 1 month prior to decellularization. Decellularization was done as previously described [88, 89]. On the day of decellularization, lungs were thawed in a 45˚C water bath before being placed in a perfusion bioreactor chamber. To setup the lungs for perfusion, individual cannulas were used to connect the pulmonary artery and main stem bronchus to allow for control of separate pumping systems. Day 1 of decellularization was initiated by immersing the lungs in 1% SDS solution and pumping 1% SDS solution into the individual cannulas of the pulmonary artery and trachea. 1% SDS was perfused into the pulmonary artery at a rate of 60 ml/min and into the trachea at a rate of 120 ml/min. 1-3 liters of 1% SDS were used to fill and expand the lungs. Expanded lungs were emptied every hour for 3 hours and at the end of each 3 hour time point, fresh 1% SDS solution was added to the chamber to begin perfusion again. The concertation of SDS was lowered to 0.1% on day 3 of decellularization and the perfusion rates were kept the same. Fresh 0.1% SDS was added to the bioreactor chamber every day for days 4, 5 and 6 of decellularization. By day 5, lungs were perfused with distilled water at a rate of 500 ml/min for 12 hours. Distilled water in the bioreactor chamber was replaced every 3 hours. Lungs were then perfused with 3% H_2O_2 for 1 hour followed by perfusion with sterile water for 12 hours at a rate of 500 ml/h. Sterile water was replaced every 3 hours. Sterile water was then removed from the bioreactor chamber and lungs were perfused with phosphate-buffered saline (PBS) containing streptomycin (90 µg/ml),

penicillin (50 U/ml) and amphotericin (90 µg/ml) for 5 hours at rate of 500 ml/h. AC human lung scaffolds were stored in fresh PBS containing antibiotic and antimycotic solutions. For development of the lung construct, distal areas of the whole lung scaffold were cut into equal-sized 1.5 cm^3 pieces.

Sterilization of human lung scaffold pieces

Human lung scaffold pieces were sterilized before cells were seeded to ensure that were was no bacterial or fungal contamination during culture. Scaffold pieces were treated with 0.05% H_2O_2 for 5 minutes. Pieces were washed in sterile water 5 times and were kept in water for 30 minutes to remove any H_2O_2. Pieces then were treated with 70% ethanol for 15 minutes, washed in sterile water 5 times and then kept in water for 1 hour to remove any remaining ethanol. Scaffold pieces were placed in DPBS containing penicillin (50 U/ml), streptomycin (90 µg/ml), and 25µg/ml amphotericin for 24 hours. After 24 hours, scaffold pieces were placed in Dulbecco's modified eagle medium (DMEM) containing 10% fetal calf serum (FCS), penicillin (50 U/ml), streptomycin (90 µg/ml), and 25µg/ml amphotericin at 5% CO_2 37˚C overnight to verify sterility. Sterile scaffold pieces were incubated in DMEM until use for recellularization.

Isolation of Human Monocyte-Derived Macrophages

The MNL fraction was isolated from whole human peripheral blood using Ficoll density gradient separation medium (Amersham-Biosciences, Piscataway, NJ). Cells were plated in 75 or 150 cm^2 tissue culture flasks in Dulbecco's Modified Eagle's Medium (DMEM, Sigma, St Louis MO), 0.1 mM nonessential amino acids, 100-U/ml penicillin and streptomycin. Attached macrophages then were collected for experiments.

Isolation of primary human lung cells from donor lungs

Primary lung cells were isolated from both male and female adult donors ranging in age from 29 – 71 years old. No other information about the donors was provided. Human lungs were flushed with 1L of DPBS containing 100µg/ml primocin (InvivoGen, San Diego, CA, USA). Pieces of tissue were cut from the distal regions of the lungs avoiding bronchi, bronchioles and blood vessels and were minced into $1mm^3$ fragments. Minced tissue was treated with 1mg/ml collagenase/dispase (Roche Diagnostics, Indianapolis, IN, USA) for 7 h at 4°C. The cell suspension was filtered through 100 µm and 40 µm filters and was then centrifuged to collect the cell pellet. Cells were counted and plated in T75 Primaria™ (BD Falcon) flasks containing small airway growth medium (SAGM; Lonza, San Jose, CA, USA) with 100µg/ml primocin and 10% FCS and were incubated at 37˚C with 5% CO_2.

Development of immortalized human lung cells

Primary human lung cells were immortalized by retroviral vector transduction using supernatant from the PA317 LXSN 16E6E7 cell line (ATCC, Manassas, VA, USA). The pLXSN16E6E7 retrovirus vector contains the human papilloma virus type 16 E6 and E7 genes and a neomycin resistance gene. For immortalization, a transduction mixture containing 200 µl PA317 LXSN 16E6E7 cell supernatant, 20 µl protamine sulfate (1µg/µl; MP Biomedical, Santa Ana, CA, USA) and 1800 µl serum-free small airway growth medium (SAGM; Lonza, San Jose, CA, USA) was prepared. Cells were washed with sterile DPBS without Ca^{2+} and Mg^{2+}. Cells were treated with the transduction mixture and were incubated at 5% CO_2 37˚C for 6 hours with occasional rocking. After 6 hours, serum-free medium was replaced with SAGM and cells were incubated at 5% CO_2 37˚C overnight. Medium was replaced again after 24 h of transduction with

fresh SAGM. At 48 hours post-transduction, antibiotic selection of immortalized cells was done by replacing the medium with SAGM containing 50 µg/ml geneticin.

Characterization of human lung cells

Both primary and immortalized human lung cells were characterized by examining their expression of phenotype-specific markers. Type I alveolar epithelial cells were identified by positive expression of aquaporin 5 (AQP 5). Type II alveolar epithelial cells were identified as pro-surfactant protein C (pro-SPC)-positive cells. Fibroblasts were identified as fibroblast specific protein-1 (FSP-1)-positive cells. Smooth muscle cells were identified as α-smooth muscle actin (α-SMA)-positive cells. Cells were cultured on 8-chamber polystyrene vessel tissue culture treated glass slides (BD biosciences, San Jose, CA) with SAGM and were incubated at 5% CO2 37˚C. When the cells reached 50% confluence they were fixed with 2 % formaldehyde in PBS for 1 hour. Cells in chamber slides then were washed in DPBS 5 times before immunofluorescent staining. Cells stained for pro-SPC, FSP-1 and α-SMA were first permeabilized with 0.5% Triton X-100 in PBS for 15 minutes. The respective primary antibodies were added and incubated overnight. The cells were then washed with DPBS and the secondary antibodies were added and incubated for 1 hour. For negative staining controls, the primary antibodies were omitted and cells were only stained with secondary antibodies to set baseline values for imaging. All slides were washed with DBPS and mounted in Slow Fade GOLD with 4',6-diamidino-2-phenylindole (DAPI;Molecular Probes, Eugene, OR)

Recellularization of human lung scaffold pieces

For recellularization, sterile lung scaffold pieces were each seeded with primary or immortalized human lung cells from each of the ten donors. A total of 7 x 10^6 pHLC or iHLC were seeded into each 2.5 cm^3 scaffold piece. Cells were resuspended in SAGM containing 15% PF-

127 and 100 µl of cell suspension was used to seed each scaffold piece. Cells were injected through a 19-gauge catheter into the scaffold following the pattern shown in **Figure 6.1 A** to ensure an even distribution of cells within scaffold pieces. After scaffold pieces were seeded with cells on day 1, they were centrifuged at 100 x g to help spread the cells throughout the scaffold. The seeded scaffolds were placed into individual wells of a six-well culture plate containing SAGM with 100µg/ml primocin and were incubated for 1 day at 5% CO_2 37˚C. On day 2 of culture, cell-scaffold constructs were placed in a bioreactor chamber where an air liquid interphase was provided. Triplicate cell-scaffold constructs produced from pHLC or iHLC of each of the 10 donors were cultured in the bioreactor chambers for 7 days **(Figure 6.1 B)**. Monocyte-derived macrophages were seeded after this 7 day culture. Recellularized human lung constructs were used for experiments. Constructs were fixed for histology and immunohistochemistry, used for preparation of tissue lysate or used for exposure experiments. Conditioned medium from each of the constructs was collected for further analysis.

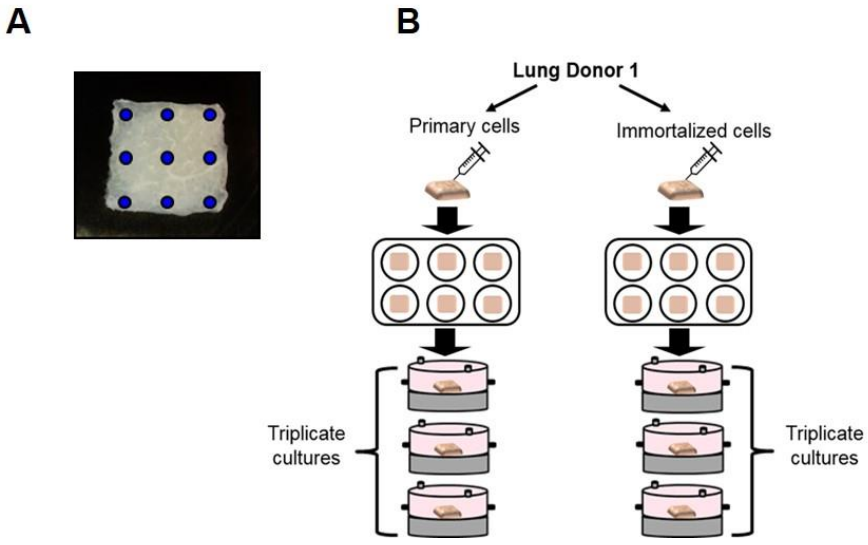

Figure 6.1 Recellularization and experimental design for human lung constructs produced from pHLC or iHLC. (A) Cells were injected into scaffolds following this pattern. **(B)** Primary cells are isolated from each of the 10 donor lungs. For each of the 10 lung donors, primary cells are immortalized. The final result is two cell populations

(pHLC and iHLC) from each of the 10 donors. Constructs are then produced from either pHLC or iHLC and cultured in triplicate for use in separate experiments (N=10).

Histology and immunohistochemistry

Tissue samples used for histology and immunohistochemistry were fixed with 2% formaldehyde for 24 hours at room temperature. Samples were taken out of the fixative and washed in sterile DPBS for 24 hours before being sectioned. Human lung tissue was frozen in tissue freezing medium (Triangle Biomedical Sciences) and serial sections were cut at a 5 μm thickness using a Microm cryomicrotome (Thermo Scientific). Primary antibodies and dilutions used included: anti-AQP-5 (1:50; Santa Cruz Biotechnology); anti-pro-SPC (1:100; Chemicon, Temecula, CA, USA); anti-SMA (1:100; Sigma); anti-FSP-1 (1:100; Millipore); anti CD 14 (Millipore); anti CD 163 (Santa Cruz Biotechnology); anti CD 68 (1:100 Millipore); anti CD 80 (1:100 Millipore). The slides were then prepared for imaging by mounting in Slow Fade GOLD with 4,6-diamidino-2-phenylindole (DAPI; Molecular Probes, OR, USA).

Fluorescent microscopy

Location and extent of fluorescent labels were examined using a Nikon T300 Inverted Fluorescent microscope (Nikon Corp.).

Assessment of cell viability

Cell viability was examined using vital fluorescent staining (calcein-AM and ethidium homodimer-1; Molecular Probes) as previously described (Nichols *et al*. 2013). Both live and dead cells were counted from all cells isolated. Each slide was scored by counting live or dead fluorescently labeled cells in five different fields by two observers using a fluorescence

microscope. Cell counts were performed using a cell counter (Coulter) and mean counts were used to calculate and assess percent viability.

Assessment of apoptosis

Assessment of apoptosis was done on fixed tissue sections using In Situ Cell Death Detection Kit (Roche) according to the manufacturer's protocol. Slides were first rinsed with DPBS. 50 μL of TUNEL reaction mixture was added to the sections and slides were incubated for 1 h at 37°C. Negative control slides were incubated with Label Solution alone. After incubation, tissue sections were rinsed with DPBS and embedded in antifade mountant. Tissue sections were evaluated under a fluorescence microscope. 5 random fields of the tissue sections were evaluated by two observers to count the number of TUNEL-positive cells. Mean counts were used to calculate and assess percent apoptosis.

Picrosirius red stain

Picro-Sirius Red Stain Kit (for collagen) (Diagnostic Biosystems, Pleasanton, CA) was used for histological evaluations of collagen content. Fixed tissue sections of the constructs were stained with Picro-Sirius Red Stain and evaluated for collagen content at days 7 and 14 post exposure to bleomycin. Tissue sections of normal human lung and were also stained and used as a controls for collagen content. Staining was performed according to the manufacturer's instructions. Slides were washed in DI water to remove freezing medium. Picro-sirisus red solution was added to the tissue sections and slides were incubated for 60 minutes at room temperature. Slides were then rinsed quickly in two changes of acetic acid solution followed by a rinse in absolute alcohol. A final rinse was done in two changes of absolute alcohol to dehydrate tissue sections. Slides were cleared in xylene and mounted in Permount Mounting Medium.

Ashcroft scale

The Ashcroft numerical scale was originally developed to histologically determine the severity of pulmonary fibrosis in lung tissue sections from patients. The numerical scale consists of scores ranging from 0 – 8, with the higher numbers indicating more severe fibrosis. A score of 0 is given to normal lung tissue sections that have no fibrotic histopathological changes, while an 8 represents total fibrous obliteration in the majority of lung tissue. Severity of fibrosis was determined in human lung constructs at days 7 and 14 post-bleomycin exposure. Slides with lung tissue sections stained with Picro-sirius Red Stain were systematically scanned under a microscope to view extent of collagen deposition and 5 different fields were examined. Each field was assigned a score between 0 – 8. The mean score for all the fields was used as the representative fibrosis score.

Multiphoton microscopy and second harmonic generation

Human lung model samples were imaged using multiphoton microscopy (MPM) and second harmonic generation (SHG) microscopy to examine structural changes in the ECM and measure collagen content. MPM detects tissue autofluorescence, from elastin and cells within tissues, and SHG microscopy detects autofluorescence from fibrillar collagen. MPM evaluation was done with a customized Zeiss 410 Confocal Laser Scanning Microscope modified for multiphoton excitation and detection along nondescanned optics as previously described (Nichols *et al*. 2016). Briefly, multiphoton excitation was produced from a femtosecond titanium sapphire laser (Tsunami; Spectra-Physics) with a 5W frequency-doubled Nd:YVO pump laser that was routed into the scanhead and through the sample objective. An epi-configuration was used for collection of emitted light and detected using a cooled PMT placed in a nondescanned configuration (R6060; Hamamatsu). Excitation for AF was 780 nm and for SHG was 840 nm.

Fluorescence emission in the spectral region of 450–650 nm was collected for detection of broadband AF from the lung tissue pieces. SHG was collected using a 420±14 nm bandpass filter in the nondescanned detector path. Each of the human lung tissues pieces being evaluated was placed on an imaging dish with a #1.5 coverslip and immersed in PBS. Several sites for each of the human lung tissue pieces were chosen. At each site a z-stack was obtained from the outer lung surface using a z-interval of 1 μm to depths >150 μm using a 40×, 1.2 N.A. water immersion objective, which provided a field of view of 320×320 μm. Image reconstructions of micrograph stacks were constructed using Metamorph (Molecular Devices, Sunnyvale, CA) or Image J 3D viewer.

Cytokine profile - Cytometric bead array

Conditioned medium was collected from all human lung tissue cultures and examined for the presence of interleukin-1β (IL-1β), interleukin-2 (IL-2), interleukin-4 (IL-4), interleukin-6 (IL-6), interleukin-10 (IL-10), tumor necrosis factor (TNF), and interferon-γ (IFN-γ) using the BD™ Cytometric Bead Array Human Th1/Th2 Cytokine Kits (BD Biosciences, San Jose, CA). The array was performed according to the manufacturer's instructions. Flow cytometry was used for analysis.

Immunoprecipitation

Construct tissue samples were placed in 1ml cold RIPA lysis buffer (50 mM Tris-HCI, pH 8, 150 mM NaCl, 1% NP-40, 0.5% sodium deoxycholate) containing 1X Protease Inhibitor Cocktail (Sigma). Lysate from each tissue sample was centrifuged at 10 000 x g for 15 minutes. After centrifugation the supernatants were collected. Immunoprecipitation was done for TIMP-1 as previously described in Chapter 3. The lysate was pre-cleared then centrifuged at 10,000 x g for 10 minutes at 4˚C and then placed in a fresh microcentrifuge tube. Lysates were incubated with 10

µg of TIMP-1 antibody for one hour at 4˚C. Sepharose protein A beads were added and incubated for one hour at 4˚C. Samples containing sepharose protein A beads were then washed and after a third final wash, samples were centrifuged, the supernatant was removed and the beads were collected. Laemmli sample buffer was added and samples were vortexed, and then heated at 90˚-100˚C for 10 minutes to elute proteins from the beads. Samples containing beads were then centrifuged and the supernatants were collected and loaded onto a SDS-PAGE gel. Coomassie blue was used to stain the gels.

Statistical analysis

Statistical analyses were performed using two-way ANOVA. Mean differences between samples were determined by a two sample T-test. P-values of <0.05 were considered significant. Data are presented as mean values and standard deviations.

RESULTS

Cell sources used for development of the 3D human lung constructs

PHLC isolated from 10 lung donors **(Figure 6.2 A)** were immortalized to produce iHLC. Phenotypic profiling by flow cytometry showed the mixture of iHLC were predominately type II AEC (74.3%) **(Figure 6.2 B)**. Lower percentages of type I AEC (6.5%), fibroblasts (7.7%) and smooth muscle cells (5.3%) were present **(Figure 6.2 B)**. Examination of iHLC by immunocytochemistry showed morphology of aquaporin-5 (AQP-5)-positive type I AEC **(Figure 6.2 C, D)**, pro-surfactant protein C (pro-SPC)-positive type II AEC **(Figure 6.2 E, F)**, α-smooth muscle actin (α-SMA)-positive smooth muscle cells **(Figure 6.2 G, H)** and fibroblast specific proteins-1 (FSP-1)-positive fibroblasts **(Figure 6.2 I, J)**. PHLC demonstrated a similar phenotypic profile as iHLC **(Figure 6.2 K)**. Examination of pHLC by immunocytochemistry showed the

morphology of type I AEC **(Figure 6.2 L, M)**, type II AEC **(Figure 6.2 N, O)**, smooth muscle cells **(Figure 6.2 P, Q)** and fibroblasts **(Figure 6.2 R, S)**. Both iHLC and pHLC contained a mixture of cells that were phenotypically and morphologically similar.

A

	Donor 1	Donor 2	Donor 3	Donor 4	Donor 5	Donor 6	Donor 7	Donor 8	Donor 9	Donor 10
Gender	male	male	male	female	female	male	male	male	female	male
Age	54	65	71	37	62	48	29	37	62	62

Gender and age of 10 lung donors from which pHLC were isolated.

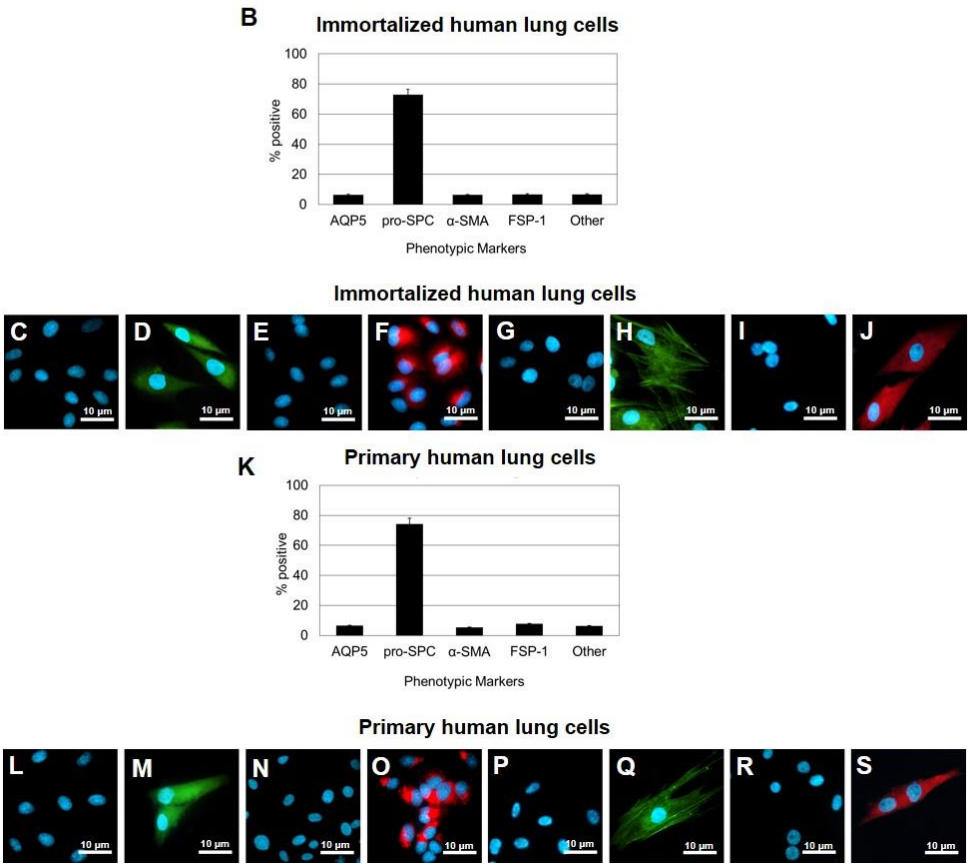

Figure 6.2 Cell sources used for development of human lung constructs (A) Gender and age of 10 lung donors from which pHLC were isolated from. **(B)** Phenotypic profile of iHLC. **(C-J)** Morphology of iHLC **(C, E, G, I)** Staining controls **(D)** AQP-5-positive (green) type I AEC. **(f)** pro-SPC-positive (red) type II AEC. **(H)** α-SMA-positive (green) smooth muscle cells **(J)** FSP-1-positive (red) fibroblasts. **(K)** Phenotypic profile of pHLC. **(L-S)** Morphology of pHLC. **(L, N, P, R)** Staining controls, DAPI (blue). **(M)** AQP-5-positive (green) type I AEC. **(O)** pro-SPC-positive (red) type II AEC. **(Q)** α-SMA-positive (green) smooth muscle cells. **(S)** FSP-1-positive (red) fibroblasts.

Development of 3D human lung constructs

For development of replicate constructs, one whole human lung AC scaffold was used **(Figure 6.3 A)** and 2.5 cm^3 pieces of AC human lung scaffold **(Figure 6.3 B, C)** were cut from distal regions (~300 pieces). Histological examination by H&E staining showed there were no cell nuclei after decellularization **(Figure 6.3 D, E)**.

Individual 2.5 cm^3 pieces of AC lung scaffold were seeded with $7x10^6$ iHLC or pHLC from each of the 10 donors to bioengineer iHLC or pHLC constructs. IHLC or pHLC were injected into AC scaffold pieces as described in **Figure 6.1 A**. Lung constructs were cultured in 6-well plates for 24 hours **(Figure 6.3 F)** and then in bioreactor culture for 13 days **(Figure 6.3 G-I)**.

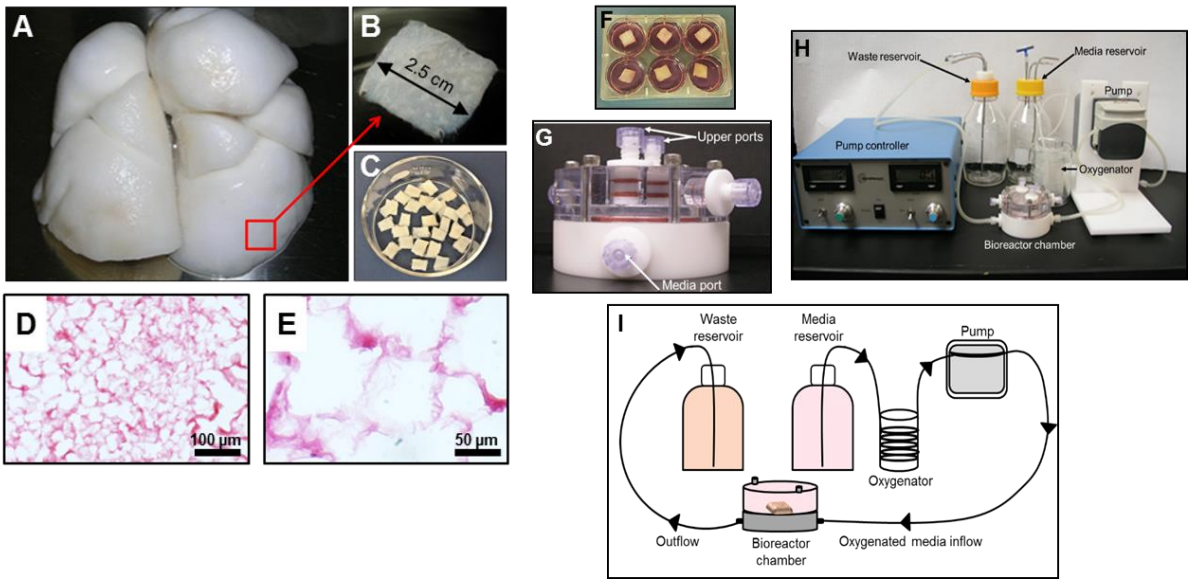

Figure 6.3 Production of human lung constructs (A) Whole human lung scaffold **(B-C)** 2.5 cm^3 lung scaffold pieces from the distal regions (red box in A) of the whole lung scaffold. **(D-E)** H&E stain of AC lung scaffold showing no cells **(D)** scale bar = 100 µm **(E)** scale bar = 50 µm. **(F)** Cell-scaffold constructs cultured in 6-well plates for 24 hours. **(G)** Bioreactor chamber **(H, I)** Bioreactor setup.

H&E stained tissue sections of native human lung **(Figure 6.4 A, B)** were compared to 14-day iHLC constructs **(Figure 6.4 C, D)** or pHLC constructs **(Figure 6.4 E, F)**. Although there were fewer cells in iHLC and pHLC constructs than in native human lung, structures were similar.

Immunofluorescent staining of AQP-5-postive cells in native human lung **(Figure 6.4 G, H)**, iHLC constructs **(Figure 6.4 I, J)** and pHLC constructs **(Figure 6.4 K, L)** shows distribution of type I AEC. Fewer type I AEC were present in constructs compared to native human lung tissue. Staining of pro-SPC-positive cells in native human lung **(Figure 6.4 M, N)**, iHLC constructs **(Figure 6.4 O, P)** and pHLC constructs **(Figure 6.4 Q, R)** indicates the presence of type II AEC.

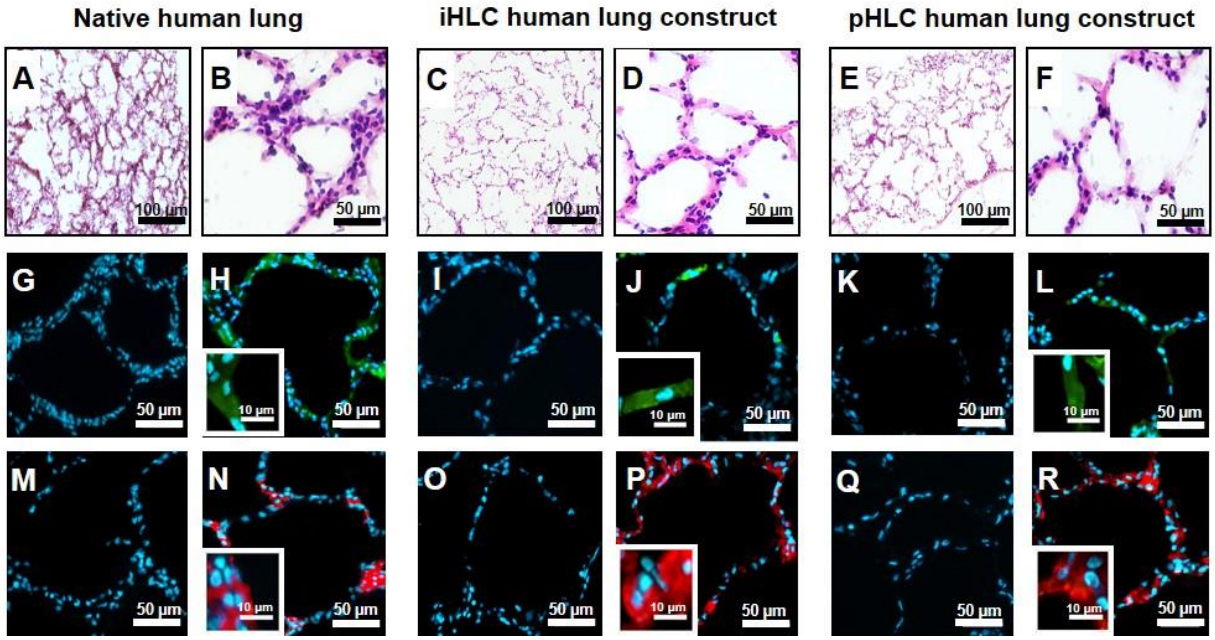

Figure 6.4 Tissue development in human lung constructs. (A-F) H&E staining of **(A, B)** native human lung, **(C, D)** iHLC and **(E, F)** pHLC constructs. **(A, C, E** scale bars = 100 µm**) (B, D**, **F** scale bars = 50 µm**)**. **(G-R)** Immunofluorescent staining of **(G, H, M, N)** native human lung, (**I**, **J**, **O**, **P**) iHLC and **(K, L, Q, R)** pHLC constructs. (**G**, **M**, **I**, **O**, **K**, **Q**) Staining controls, DAPI (blue). **(H, J, L)** AQP-5-positive (green) type I AEC, DAPI (blue). **(N, P, R**) pro-SPC-positive (red) type II AEC, DAPI (blue). **(G-R** scale bars = 50 µm, inserts scale bars = 10 µm**)**.

Bleomycin Exposure leads to decreased cell viability in human lung constructs

Biopsies from patients with bleomycin-induced lung injury demonstrate destruction and desquamation of AEC. To assess the ability of constructs to mimic human responses to bleomycin exposure, iHLC constructs from each of the 10 donors were exposed to 0.1 U/ml of bleomycin. A

significant decrease in cell viability was observed at 12 hours ($p<0.05$) and 24 hours ($p<0.01$) post-bleomycin exposure compared to sham-exposed constructs **(Figure 6.5 A)**.

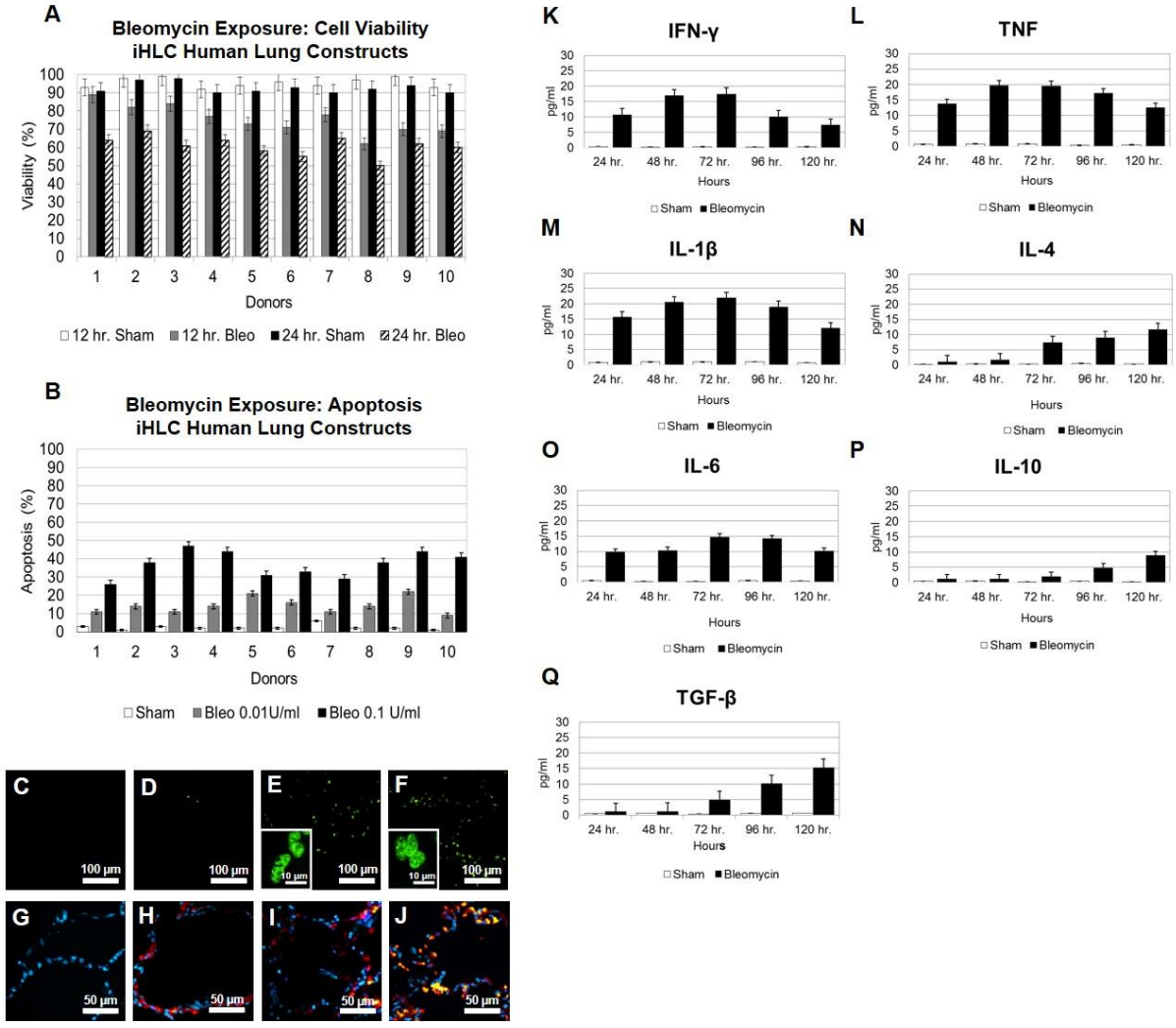

Figure 6.5 Bleomycin exposure of human lung construct. (A) Cell viability of iHLC constructs from 10 donors at 12 and 24 hours post-exposure to 0.1U/ml bleomycin. **(B)** Apoptosis in iHLC constructs from 10 donors post-exposure to 0.01 U/ml or 0.1U/ml bleomycin. **(C-F)** TUNEL-positive (green) apoptotic cells in iHLC construct. **(C)** Negative control **(D)** Sham-exposed **(E)** 0.01 U/ml bleomycin exposure **(F)** 0.1 U/ml bleomycin exposure. **(G-J)** Immunofluorescent staining of iHLC constructs. **(G)** Staining control, DAPI (blue) (**H**) Sham-exposed (**I**) 0.01 U/ml bleomycin exposure **(J)** 0.1 U/ml bleomycin exposure. **(K-Q)** Cytokine profile of iHLC constructs post-exposure to 0.1 U/ml bleomycin. (**C-J** scale bars = 50 µm, inserts scale bars = 10 µm).

Bleomycin Exposure induces apoptosis of alveolar epithelial cells in human lung constructs

Apoptosis of AEC occurs in murine models of bleomycin-induced PF and is thought to occur in PF patients. In this study, apoptosis was examined in iHLC constructs 24 hours post-bleomycin exposure using the TUNEL assay. Exposure to 0.01U/ml or 0.1 U/ml of bleomycin resulted in a significant increase in numbers of apoptotic cells ($p<0.001$ for both concentrations) when compared to sham-exposed constructs **(Figure 6.5 B)**. Higher numbers of apoptotic cells ($p<0.001$) were observed in constructs exposed to 0.1U/ml of bleomycin than those exposed to 0.01 U/ml bleomycin **(Figure 6.5 B)**. There was variability in levels of apoptosis in iHLC constructs produced from each of the 10 donors but levels of apoptosis consistently increased **(Figure 6.5 B)**. Immunohistochemistry showed the presence of TUNEL-positive apoptotic cells in constructs exposed to 0.01 or 0.1 U/ml bleomycin when compared to negative controls and sham-exposed constructs **(Figure 6.5 C-F)**. We found that many TUNEL-positive cells were pro-SPC-positive type II AEC **(Figure 6.5 G-J)**. Previous studies indicate that loss of type II AEC alters normal alveolar epithelial repair by limiting the number of type II AEC available to support re-epithelization

Cytokine profile of human lung constructs after bleomycin exposure

In murine models, the initial response to bleomycin exposure is induction of an inflammatory response characterized by production of pro-inflammatory cytokines. In patients with PF, the early immune response immediately after exposure to PF-inducing agents has not been well characterized. Cytokine profiles of iHLC constructs were evaluated after bleomycin

exposure. Levels of IFN-γ, TNF, IL-1β, and IL-6 increased from 24 hours - 120 hours post-bleomycin exposure when compared to sham-exposed constructs ($p<0.01$**) (Figure 6.5 K-M, O)**. Levels of IL-4, IL-10 and TGF-β were lower between 24 hours – 48 hours post-bleomycin exposure but began to increase significantly ($p<0.05$) between 72 hours - 120 hours **(Figure 6.5 N, P, Q)**.

Development of fibrosis in human lung constructs after bleomycin exposure

Extent of fibrosis is indicated by an increase in collagen deposition. Picrosirius red is a histochemical technique used to visualize collagen. Tissue sections of non-fibrotic human lung **(Figure 6.6 A)** or fibrotic human lung **(Figure 6.6 B)** stained with Picrosirius red show the range in collagen levels. In non-fibrotic human lung, collagen fibers are well organized and line alveolar septum **(Figure 6.6 A)**. Fibrotic human lungs have excessive collagen deposition that obliterates tissue structure **(Figure 6.6 B)**. Picrosirius red staining of AC human lung scaffold alone **(Figure 6.6 C)** and of culture day 14 constructs prior to exposure shows base line levels of collagen content **(Figure 6.6 D)**. MPM and SHG were used to examine regional differences in collagen content and validate Picrosirius red staining. MPM and SHG 3D reconstructions show spatial collagen distribution in regions of interest in non-fibrotic human lung **(Figure 6.6 E)**, fibrotic human lung **(Figure 6.6 F)**, AC lung scaffold **(Figure 6.6 G)** and culture day 14 iHLC constructs **(Figure 6.7 H)**. In non-fibrotic human lung collagen is evenly distributed **(Figure 6.6 E)**. Fibrotic human lung contains excessive collagen deposition **(Figure 6.6 F)**. Collagen density of AC scaffolds **(Figure 6.6 G)** is less than in day 14 iHLC constructs **(Figure 6.6 H)**.

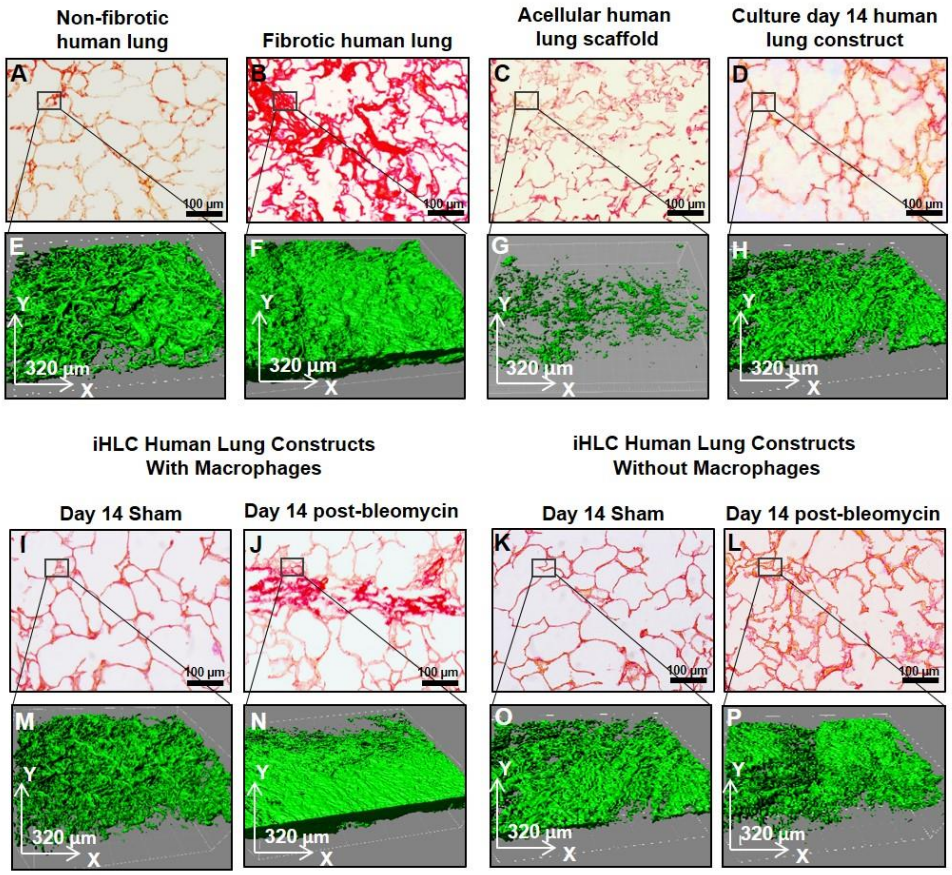

Figure 6.6 Collagen content in native human lungs and human lung constructs. Picrosirius red staining **(A-D, I-L)** and MPM SHG 3D reconstructions **(E-H, M-P)** of **(A, E)** Non-fibrotic human lung **(B, F)** Fibrotic human lung **(C, G)** AC human lung scaffold **(D, H)** Day 14 iHLC construct. IHLC constructs **(I, J, M, N)** with and **(K, L, O, P)** without macrophages. **(I, M, K, O)** Day 14 sham-exposed constructs **(J, N, L, P)** Day 14 bleomycin-exposed constructs. MPM SHG collagen density analysis of iHLC constructs with **(Q)** and without macrophages **(R)** at 7 and 14 days post-bleomycin exposure.

To examine the role of human peripheral blood monocyte-derived macrophages (macrophages) in fibrosis development, iHLC constructs with or without macrophages were sham- or bleomycin- exposed. Picrosirius red staining of day 14 bleomycin-exposed iHLC constructs containing macrophages demonstrated increased collagen deposition and distorted tissue structure when compared to sham-exposed constructs **(Figure 6.6 I, J)**. Not all areas of bleomycin-exposed constructs underwent fibrotic remodeling. Collagen deposition was patchy although some areas displayed normal lung structure **(Figure. 6.6 J)**. This pattern resembles spatial and temporal

heterogeneity, a characteristic feature of UIP in human PF. IHLC constructs without macrophages did not have increased collagen deposition as evaluated by Picrosirius red staining **(Figure 6.6 K, L)**. MPM and SHG 3D reconstructions of day 14 sham- or bleomycin-exposed constructs with **(Figure 6.6 M, N)** or without **(Figure 6.6 O, P)** macrophages demonstrate these differences in collagen content. Macrophage-containing iHLC constructs had a significant increase in collagen density ($p<0.01$) at days 7 and 14 post-bleomycin exposure compared to sham-exposed constructs **(Figure 6.7 A)**. Collagen density was significantly higher ($p<0.05$) in day 14 post-bleomycin exposed constructs than in day 7 post-bleomycin exposed constructs **(Figure 6.7 A)**. IHLC constructs without macrophages did not have an increase in collagen density **(Figure 6.7 B)**. These results indicate that macrophages are necessary for fibrosis development after bleomycin exposure.

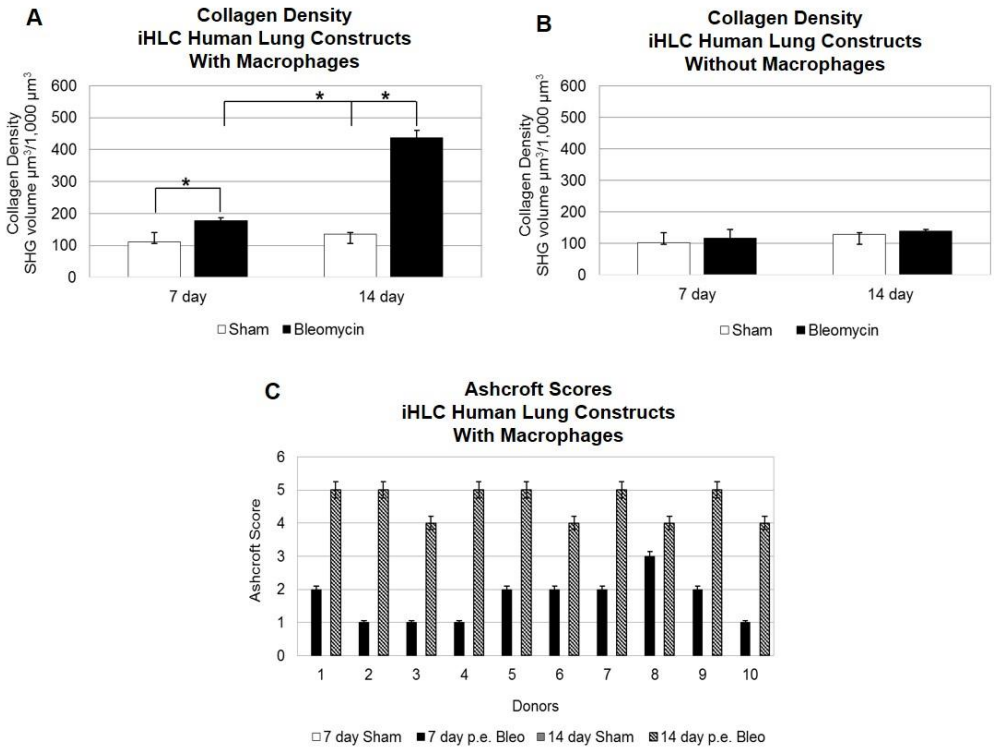

Figure 6.7 Collagen density and Ashcroft scores (A) Collagen density in iHLC constructs with macropahges **(B**) Collagen density in iHLC constructs without macrophages **(C)** Ashcroft scores of iHLC constructs (produced from 10 donors) with macrophages at 7 day sham-exposed, 7 day post-bleomycin-exposed, 14 day sham-exposed and 14 day post-bleomycin exposed.

The Ashcroft numerical scale was used to determine degree of fibrosis in iHLC constructs containing macrophages. In blinded assessments of constructs 7 days post-bleomycin exposure, Ashcroft scores between 1 – 3 were assigned, indicating minimal fibrosis **(Figure 6.7 C)**. Moderate to high fibrotic scores of 4 – 5 were assigned to constructs 14 days post-bleomycin exposure **(Figure 6.7 C)**.

Fibroblasts and myofibroblasts are collagen-producing cells that are the main source of increased collagen in PF. Numbers of fibroblasts and myofibroblasts were determined by immunohistochemistry at days 7 and 14 post-bleomycin exposure in iHLC constructs with and without macrophages. Immunohistochemistry and cell counts from non-fibrotic **(Figure 6.8 A-D)** or fibrotic **(Figure 6.8 E-H)** human lungs served as negative or positive controls. Fibrotic human lungs have significantly higher percentages of fibroblasts ($p<0.001$) **(Figure 6.8 I)** and myofibroblasts ($p<0.001$) **(Figure 6.8 J)** compared to non-fibrotic human lungs. Constructs containing macrophages had a significant increase in percentages of fibroblasts **(Figure 6.8 K)** and myofibroblasts **(Figure 6.8 L)** at 7 and 14 days post-exposure to bleomycin compared to sham-exposed constructs. Constructs without macrophages had no significant increase in fibroblasts **(Figure 6.8 M)** or myofibroblasts **(Figure 6.8 N)** at days 7 or 14 post-bleomycin exposure compared to sham-exposed constructs.

MMP-7 is increased in the alveolar epithelium of PF patients compared to healthy patients. MMP-7 expression in AEC is induced in response to lung injury and tissue repair. In the previous section, we show increased collagen deposition in macrophage-containing constructs by days 7 and 14 post-bleomycin exposure. To assess MMP-7 expression as fibrosis develops, MMP-7 expression was examined in macrophage-containing iHLC constructs at these time

points. At day 0 pre-exposure, constructs did not express MMP-7 **(Figure 6.9 A, B)**. At days 7 **(Figure 6.9 C, D)** and 14 **(Figure 6.9 E, F)** post-bleomycin exposure, MMP-7 expression in constructs was predominately localized to pro-SPC-positive type II AEC **(Figure 6.9 D, F)**. Other MMP-7-positive cells were also present at day 7 post-bleomycin exposure **(Figure 6.9 D)**

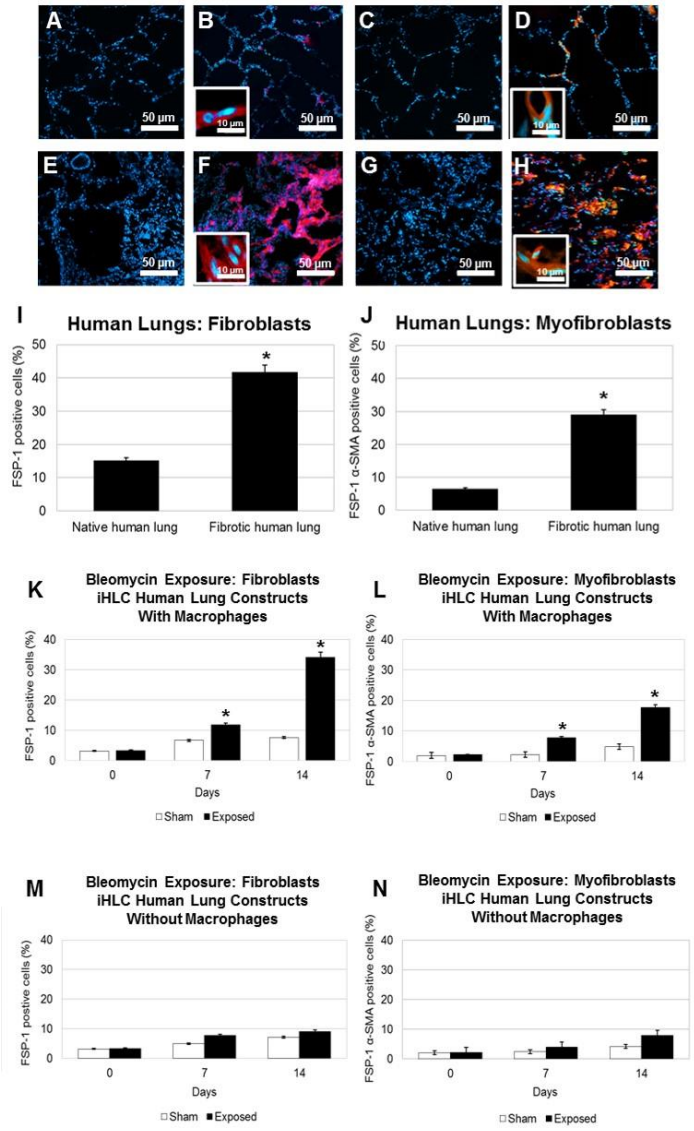

Figure 6.8 Increase in fibroblasts and myofibroblasts in iHLC constructs after bleomycin exposure. (A-H) Immunohistochemistry of **(A-D)** Non-fibrotic human lung, **(E-H)** Fibrotic human lung. **(A, C, E, G)** Staining controls, DAPI (blue) **(B, F)** FSP-1-positive (red) fibroblasts, DAPI (blue). **(D, H)** α-SMA-(green) and FSP-1-positive (red) myofibroblasts, DAPI (blue). Numbers of fibroblasts **(I)** and myofibroblasts **(J)** in non-fibrotic and fibrotic human lungs. Numbers of fibroblasts and myofibroblasts in sham- or bleomycin-exposed iHLC constructs with **(K, L)** and without **(M, N)** macrophages.

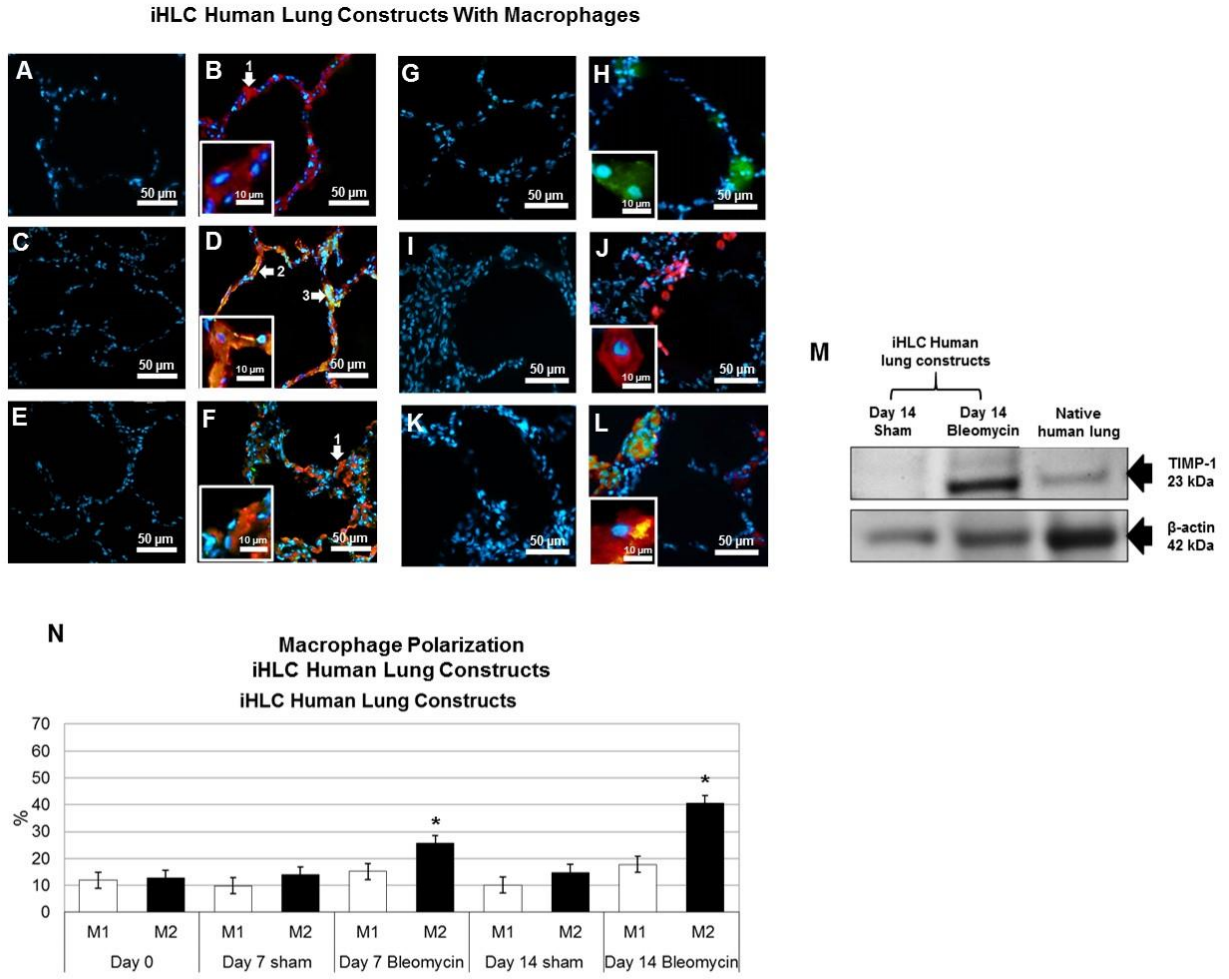

Figure 6.9 MMP-7, TIMP-1 and M2 macrophages in iHLC constructs after bleomycin exposure. (A-L) Immunohistochemistry of iHLC constructs with macrophages. **(A, C, E, G, I, K)** Staining controls, DAPI (blue). **(B, D, F)** MMP-7- (green) and pro-SPC-positive (red) type II AEC at **(B)** Day 0 pre-exposure **(D)** Day 7 and **(F)** Day 14 post-bleomycin exposure. **(H)** CD 14-positive macrophages at day 0 pre-exposure. (**J, L**) CD-163-positive (red) M2 macrophages at day 14 post-bleomycin exposure. **(L)** TIMP-1-postive (green) M2 macrophages. **(M)** Immunoprecipitation of TIMP-1 in day 14 sham-exposed or bleomycin-exposed constructs and native human lung. **(N)** Numbers of M1 (CD 68-, CD 80-positive) and M2 (CD 163-, CD 206-positive) macrophages in sham-exposed or bleomycin-exposed iHLC constructs at days 0, 7 and 14 (* $p < 0.05$).

TIMP-1 expression is increased in PF patients. Increased expression of TIMP-1 is associated with a pro-fibrotic microenvironment in animal models of bleomycin-induced PF.

Although varieties of cells within the human respiratory tract are capable of producing TIMP-1, macrophages are a main source of TIMP-1 in tissues from PF patients. Since excessive collagen deposition was observed by day 14 post-bleomycin exposure, we examined TIMP-1 expression at this time point in macrophage-containing iHLC constructs. At day 0 pre-bleomycin-exposure constructs contained unpolarized CD14-positve macrophages that were generally found in corners of alveoli **(Figure 6.9 G, H)**. CD 163 is a well-known marker used for the characterization of M2 macrophages. On day 14 post-bleomycin exposure, constructs contained CD 163-positive M2 macrophages in regions of dense collagen deposition **(Figure 6.9 I, J)**. No CD-68-positive M1 macrophages were present in these areas of collagen deposition **(Figure 6.9 I, J)**. CD-163-positive M2 macrophages in regions with dense collagen deposition expressed TIMP-1 **(Figure 6.9 K, L)**. Expression of TIMP-1 at day 14 post-bleomycin exposure was also validated by immunoprecipitation **(Figure 6.9 M)**. There was a significant increase ($p<0.01$) in CD-163- and CD 206-positive M2 macrophages at days 7 and 14 post-bleomycin exposure compared to sham-exposed constructs and day 0 pre-exposure **(Figure 6.9 N)**.

Comparison between iHLC and pHLC human lung constructs

We compared data generated from constructs developed from iHLC and constructs developed from pHLC to validate functionality of constructs. The phenotypic profile and morphological characteristics of pHLC **(Figure 6.2 K-S)** were similar to iHLC **(Figure 6.2 B-J)**. Bleomycin exposure of pHLC constructs resulted in decreased cell viability **(Figure 6.10 A)**, and increased apoptosis **(Figure 6.10 B-J)**. Cytokine profiles for pHLC constructs with **(Figure 6.10 K-Q)** were similar to iHLC constructs with **(Figure 6.3 K-Q)**. Picrosirius red staining of collagen **(Figure 6.11 A-D)**, MPM SHG collagen density analysis **(Figure 6.11 E-J)**, Ashcroft scores **(Figure 6.11 K)** numbers of fibroblasts **(Figure 6.12 A, C)**, and myofibroblasts **(Figure 6.12 B,**

D) in pHLC constructs with and without macrophages were similar to iHLC constructs **(Figure 6.7 I-P, Figure 6.8 A-C)**. We concluded that iHLC constructs provide a comparable reproducible alternative to pHLC constructs to mimic features of fibrotic tissue remodeling when exposed to bleomycin.

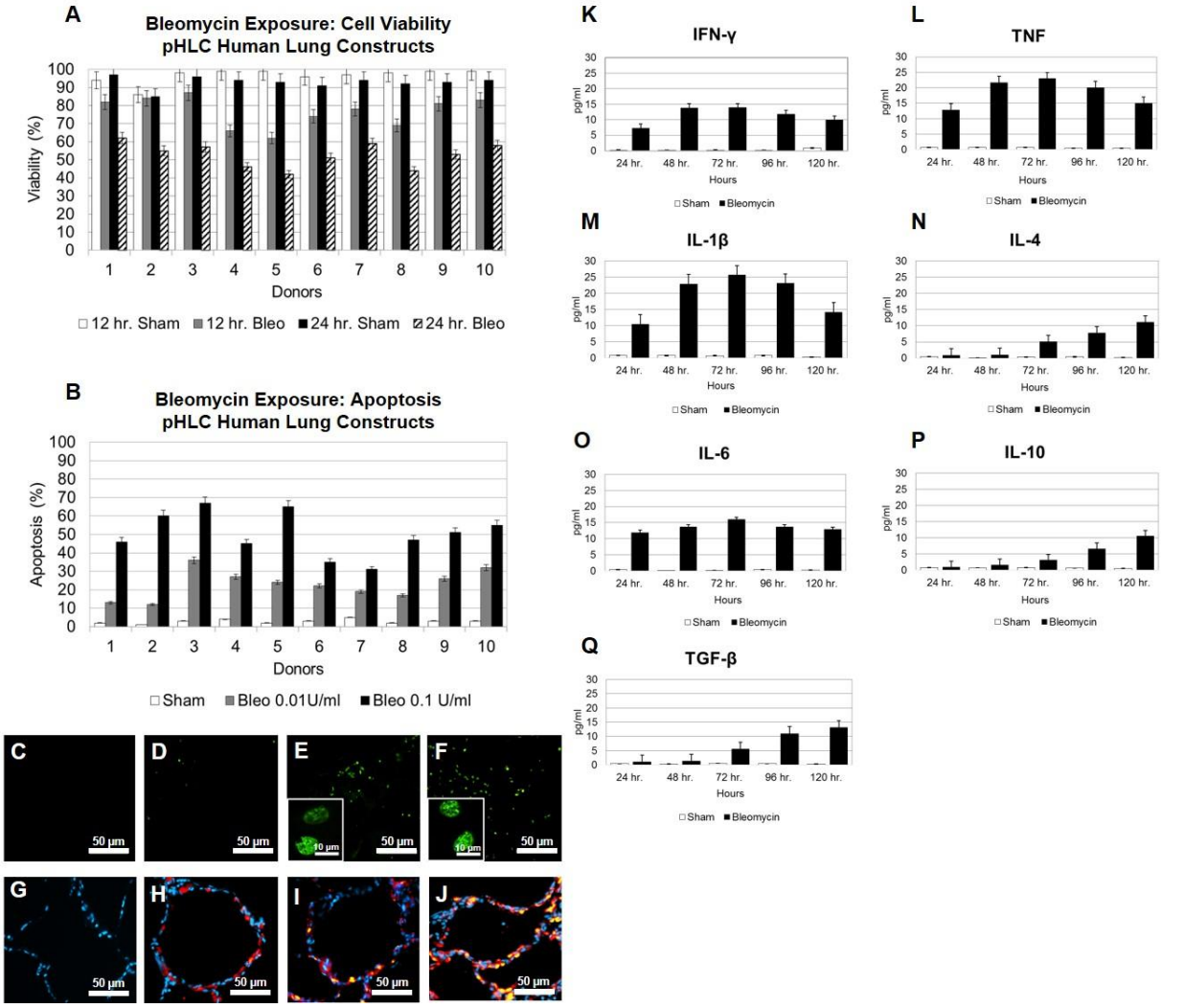

Figure 6.10 Bleomycin exposure of pHLC human lung construct. (A) Cell viability of iHLC constructs from 10 donors at 12 and 24 hours post-exposure to 0.1U/ml bleomycin. **(B)** Apoptosis in iHLC constructs from 10 donors post-exposure to 0.01 U/ml or 0.1U/ml bleomycin. **(C-F)** TUNEL-positive (green) apoptotic cells in iHLC construct. **(C)** Negative control **(D)** Sham-exposed **(E)** 0.01 U/ml bleomycin exposure **(F)** 0.1 U/ml bleomycin exposure. **(G-J)** Immunofluorescent staining of iHLC constructs. **(G)** Staining control, DAPI (blue) **(H)** Sham-exposed **(I)** 0.01 U/ml bleomycin exposure **(J)** 0.1 U/ml bleomycin exposure. **(K-Q)** Cytokine profile of iHLC constructs post-exposure to 0.1 U/ml bleomycin. (c-j scale bars = 50 µm, inserts scale bars = 10 µm).

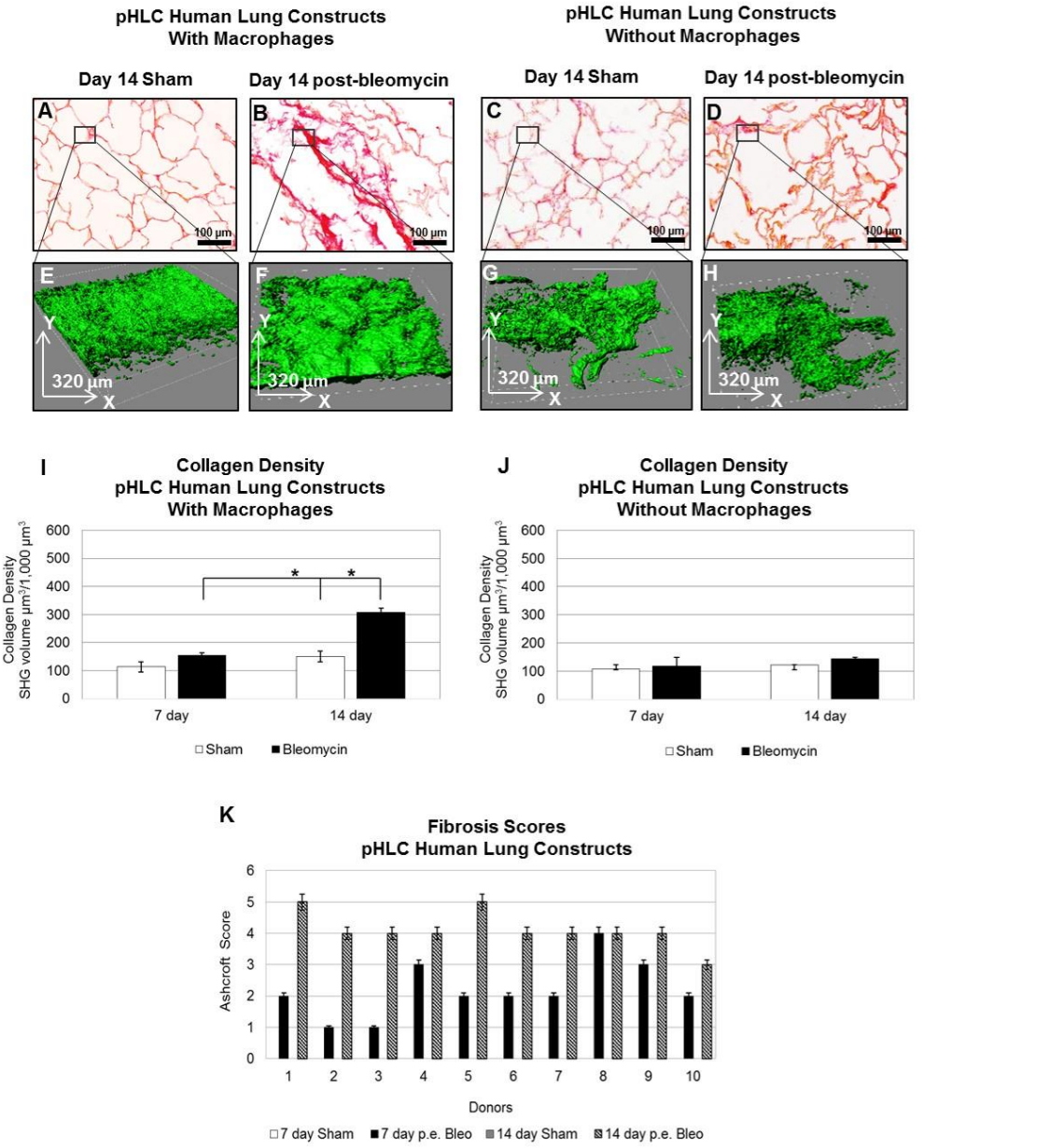

Figure 6.11 Collagen content in pHLC constructs. (A-D) Picrosirius red staining of **(A)** Day 14 sham-exposed pHLC constructs with macrophages **(B)** Day 14 bleomycin-exposed pHLC constructs with macrophages **(C)** Day 14 sham-exposed pHLC constructs without macrophages **(D)** Day 14 bleomycin-exposed pHLC constructs without macrophages **(E-H)** MPM and SHG 3D reconstructions of **(E)** Day 14 sham-exposed pHLC constructs with macrophages **(F)** Day 14 bleomycin-exposed pHLC constructs with macrophages **(G)** Day 14 sham-exposed pHLC constructs without macrophages **(H)** Day 14 bleomycin-exposed pHLC constructs without macrophages **(I)** Collagen density in pHLC constructs with macrophages **(J)** Collagen density in pHLC constructs without macrophages **(K)** Ashcroft scores for pHLC with macrophages.

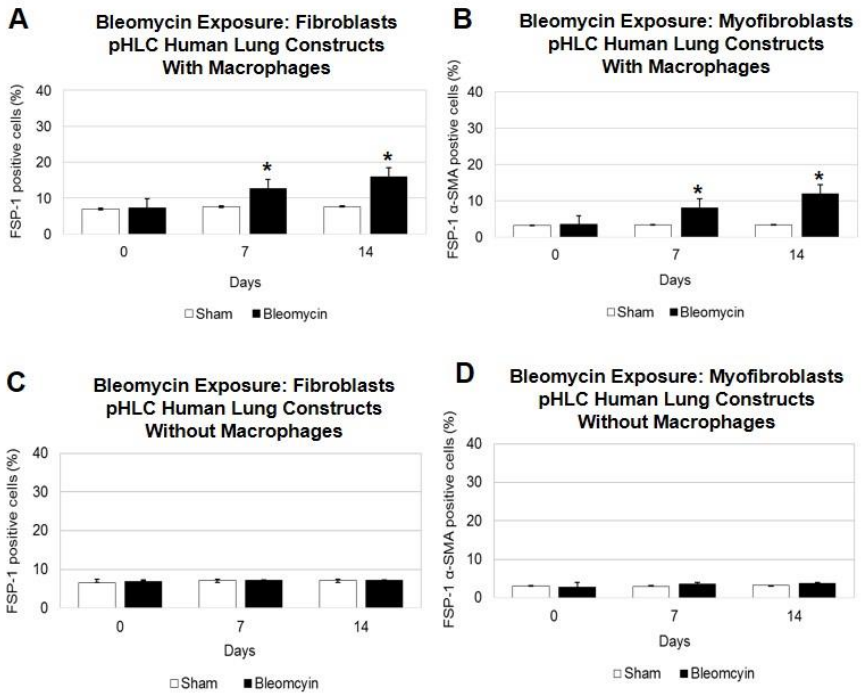

Figure 6.12 Increase in fibroblasts and myofibroblasts in pHLC post-bleomycin exposure. (A) Numbers of fibroblasts in pHLC constructs with macrophages **(B)** Numbers of myofibroblasts in pHLC constructs with macrophages **(C)** Numbers of fibroblasts in pHLC constructs without macrophages **(D)** Numbers of myofibroblasts in pHLC constructs without macrophages.

DISCUSSION AND CONCLUSION

In this study, we developed a bioengineered 3D human lung construct as an *in vitro* model of ALI and PF. This model has allowed for the examination of the early human response to acute lung injury and fibrosis development after exposure to bleomycin. Functionality of the model was evaluated by directly comparing responses between pHLC and iHLC, and determining if iHLC were able to reliably recreate similar responses as pHLC. Following bleomycin exposure, lung constructs exhibited: (1) AEC injury that lead to a decreases in cell viability and (2) increase in apoptotic loss of type II AEC (3) an initial pro-inflammatory response with l (4) only constructs containing monocyte-derived macrophages developed fibrosis (5) increased and accumulation of fibroblasts (6) increase in myofibroblasts (7) excessive deposition of collagen leading to formation

of fibrotic tissue in a temporal heterogeneous distribution (8) expression of MMP-7 in injured alveolar epithelium after exposure to bleomycin (9) polarization of M2-macrophages expressing TIMP-1 in collagen-dense areas of fibrotic lung tissue. Upon exposure, the cytotoxic effects of bleomycin significantly decreased cell viability and increased the percentage of apoptotic type II AEC in all constructs. Use of a native human lung AC scaffold allowed for examination of interactions between epithelial cells and the native lung ECM leading to fibrotic changes. This human lung construct allowed us to deconstruct complex mechanisms involved the formation of fibrosis by examining the responses of specific cell types during the early acute phase (0-14 days) of fibrosis development. We have also shown that monocyte-derived macrophages play a critical role in the development of PF. Similar to data from patients with IPF, alternatively activated macrophages were found in our constructs. M2-polorized monocyte-macrophages were consistently found in collagen-dense areas resembling fibrotic foci.

Deciphering early pathological changes of AEC injury that lead to fibrotic remodeling will help in the identification of events at early stages of the disease before there is significant fibrous scarring of patients' lungs and pulmonary function is altered. This construct provides a platform that can be used to make more accurate predictions for efficacy testing of therapeutics aimed at limiting or preventing the formation of PF.

This bioengineered human lung construct can also be used as a personalized medicine model. Patients' own cells can be used to bioengineer constructs to examine disease susceptibility or drug efficacy based on patient-specific parameters, including age, gender, race, and genetics.

FUTURE DIRECTIONS

The human lung construct we have developed can be used as model for a broad range of studies. In our future studies we will use the construct as a model of respiratory infections. Of particular interest is the role of influenza virus in development of PF after infection. Some patients with influenza infection recover without any trace of illness in lungs but in some cases and with some strains of virus such as with the H1N1 2009 pandemic strain, pulmonary fibrosis develops and becomes progressive [151]. The mechanisms by which influenza virus strains may promote, cause or exacerbate pulmonary fibrosis are unknown. We have performed some studies using the highly pathogenic H1N1 2009 pandemic influenza virus and a seasonal H1N1 virus to examine how differences in pathogenicity may induce PF formation. In our future studies we plan on exposing constructs to other strains of influenza such as the highly pathogenic avian influenza H5N1 to examine if highly pathogenic strains may employ mechanisms that induce formation of fibrotic lung tissue.

REFERENCES

1. Luca, A.C., Mersch, S., Deenen, R., Schmidt, S., Messner, I., Schäfer, K.L., Baldus, S.E., Huckenbeck, W., Piekorz, R.P., Knoefel, W.T. and Krieg, A., 2013. Impact of the 3D microenvironment on phenotype, gene expression, and EGFR inhibition of colorectal cancer cell lines. *PloS one*, *8*(3), p.e59689.

2. Spagnolo, P. and Maher, T.M., 2017. Clinical trial research in focus: why do so many clinical trials fail in IPF?. *The Lancet Respiratory Medicine*, *5*(5), pp.372-374.

3. National Center for Health Statistics (US, 2016. Health, United States, 2015: with special feature on racial and ethnic health disparities.

4. Schraufnagel, D., 2014. 'Interstitial Lung Disease', Breathing in America: diseases, progress, and hope. American Thoracic Society.

5. American Thoracic Society, 2000. Idiopathic pulmonary fibrosis: diagnosis and treatment: international consensus statement. *Am J Respir Crit Care Med*, *161*, pp.646-664.

6. Ferkol, T. and Schraufnagel, D., 2014. The global burden of respiratory disease. *Annals of the American Thoracic Society*, *11*(3), pp.404-406.

7. Wikswo, J.P., Curtis, E.L., Eagleton, Z.E., Evans, B.C., Kole, A., Hofmeister, L.H. and Matloff, W.J., 2013. Scaling and systems biology for integrating multiple organs-on-a-chip. *Lab on a Chip*, *13*(18), pp.3496-3511.

8. Nichols, J.E., Niles, J.A., Vega, S.P., Argueta, L.B., Eastaway, A. and Cortiella, J., 2014. Modeling the lung: Design and development of tissue engineered macro-and micro-physiologic lung models for research use. *Experimental biology and medicine*, *239*(9), pp.1135-1169.

9. Franks, T.J., Colby, T.V., Travis, W.D., Tuder, R.M., Reynolds, H.Y., Brody, A.R., Cardoso, W.V., Crystal, R.G., Drake, C.J., Engelhardt, J. and Frid, M., 2008. Resident cellular components of the human lung: current knowledge and goals for research on cell phenotyping and function. *Proceedings of the American Thoracic Society*, *5*(7), pp.763-766.

10. Eglen, R. and Reisine, T., 2011. Primary cells and stem cells in drug discovery: emerging tools for high-throughput screening. *Assay and drug development technologies*, *9*(2), pp.108-124.

11. Chakir, J., Pagé, N., Hamid, Q., Laviolette, M., Boulet, L.P. and Rouabhia, M., 2001. Bronchial mucosa produced by tissue engineering: a new tool to study cellular interactions in asthma. *Journal of allergy and clinical immunology*, *107*(1), pp.36-40.

12. Paquette, J.S., Moulin, V., Tremblay, P., Bernier, V., Boutet, M., Laviolette, M., Auger, F.A., Boulet, L.P. and Goulet, F., 2004. Tissue-engineered human asthmatic bronchial equivalents. *Eur Cell Mater*, *7*(1), p.11.

13. Matrosovich, M.N., Matrosovich, T.Y., Gray, T., Roberts, N.A. and Klenk, H.D., 2004. Human and avian influenza viruses target different cell types in cultures of human airway epithelium. *Proceedings of the National Academy of Sciences of the United States of America*, *101*(13), pp.4620-4624.

14. Pugin, J., Dunn, I., Jolliet, P., Tassaux, D., Magnenat, J.L., Nicod, L.P. and Chevrolet, J.C., 1998. Activation of human macrophages by mechanical ventilation in vitro. *American Journal of Physiology-Lung Cellular and Molecular Physiology*, *275*(6), pp.L1040-L1050.

15. Hermanns, M.I., Unger, R.E., Kehe, K., Peters, K. and Kirkpatrick, C.J., 2004. Lung epithelial cell lines in coculture with human pulmonary microvascular endothelial cells: development of an alveolo-capillary barrier in vitro. *Laboratory investigation*, *84*(6), p.736.

16. Huh, D., Matthews, B.D., Mammoto, A., Montoya-Zavala, M., Hsin, H.Y. and Ingber, D.E., 2010. Reconstituting organ-level lung functions on a chip. *Science*, *328*(5986), pp.1662-1668.

17. Cordes, N., Blaese, M.A., Plasswilm, L., Rodemann, H.P. and Van Beuningen, D., 2003. Fibronectin and laminin increase resistance to ionizing radiation and the cytotoxic drug Ukrain® in human tumour and normal cells in vitro. *International journal of radiation biology*, *79*(9), pp.709-720.

18. Mishra, D.K., Creighton, C.J., Zhang, Y., Gibbons, D.L., Kurie, J.M. and Kim, M.P., 2014. Gene expression profile of A549 cells from tissue of 4D model predicts poor prognosis in lung cancer patients. *International journal of cancer*, *134*(4), pp.789-798.

19. Lin, Y.M., Zhang, A., Rippon, H.J., Bismarck, A. and Bishop, A.E., 2010. Tissue engineering of lung: the effect of extracellular matrix on the differentiation of embryonic stem cells to pneumocytes. *Tissue Engineering Part A*, *16*(5), pp.1515-1526.

20. Ghaedi, M., Calle, E.A., Mendez, J.J., Gard, A.L., Balestrini, J., Booth, A., Bove, P.F., Gui, L., White, E.S. and Niklason, L.E., 2013. Human iPS cell–derived alveolar epithelium repopulates lung extracellular matrix. *The Journal of clinical investigation*, *123*(11), pp.4950-4962.

21. Huang, S.X., Islam, M.N., O'neill, J., Hu, Z., Yang, Y.G., Chen, Y.W., Mumau, M., Green, M.D., Vunjak-Novakovic, G., Bhattacharya, J. and Snoeck, H.W., 2014. Efficient generation of lung and airway epithelial cells from human pluripotent stem cells. *Nature biotechnology*, *32*(1), p.84.

22. Nakayama, K.H., Lee, C.C.I., Batchelder, C.A. and Tarantal, A.F., 2013. Tissue specificity of decellularized rhesus monkey kidney and lung scaffolds. *PloS one*, *8*(5), p.e64134

23. Cortiella, J., Niles, J., Cantu, A., Brettler, A., Pham, A., Vargas, G., Winston, S., Wang, J., Walls, S. and Nichols, J.E., 2010. Influence of acellular natural lung matrix on murine embryonic stem cell differentiation and tissue formation. *Tissue Engineering Part A*, *16*(8), pp.2565-2580.

24. Coraux, C., Nawrocki-Raby, B., Hinnrasky, J., Kileztky, C., Gaillard, D., Dani, C. and Puchelle, E., 2005. Embryonic stem cells generate airway epithelial tissue. *American journal of respiratory cell and molecular biology*, *32*(2), pp.87-92.

25. Cortiella, J., Niles, J.A., Vega, S.P., Argueta, L.B., Eastaway, A. and Nichols, J.E., 2016. Use of Hydrogels in the Engineering of Lung Tissue. In *GELS HANDBOOK: Fundamentals, Properties and Applications Volume 2: Applications of Hydrogels in Regenerative Medicine* (pp. 397-426).

26. Ahmed, E.M., 2015. Hydrogel: Preparation, characterization, and applications: A review. *Journal of advanced research*, *6*(2), pp.105-121.

27. Vukicevic, S., Kleinman, H.K., Luyten, F.P., Roberts, A.B., Roche, N.S. and Reddi, A.H., 1992. Identification of multiple active growth factors in basement membrane Matrigel suggests caution in interpretation of cellular activity related to extracellular matrix components. *Experimental cell research*, *202*(1), pp.1-8.

28. Fetal type 2 pneumocytes form alveolar-like structures and maintain long-term differentiation on extracellular matrix.

29. Chinoy, M.R., Antonio-Santiago, M.T. and Scarpelli, E.M., 1994. Maturation of undifferentiated lung epithelial cells into type II cells in vitro: a temporal process that parallels cell differentiation in vivo. *The Anatomical Record*, *240*(4), pp.545-554.

30. Zhang, W.J., Lin, Q.X., Zhang, Y., Liu, C.T., Qiu, L.Y., Wang, H.B., Wang, Y.M., Duan, C.M., Liu, Z.Q., Zhou, J. and Wang, C.Y., 2011. The reconstruction of lung alveolus-like structure in collagen-matrigel/microcapsules scaffolds in vitro. *Journal of cellular and molecular medicine*, *15*(9), pp.1878-1886.

31. Xu, J., Liu, M., Liu, J., Caniggia, I. and Post, M., 1996. Mechanical strain induces constitutive and regulated secretion of glycosaminoglycans and proteoglycans in fetal lung cells. *Journal of Cell Science*, *109*(6), pp.1605-1613.

32. Xu, J., Liu, M. and Post, M., 1999. Differential regulation of extracellular matrix molecules by mechanical strain of fetal lung cells. *American Journal of Physiology-Lung Cellular and Molecular Physiology*, *276*(5), pp.L728-L735.

33. Nakamura, T., Liu, M., Mourgeon, E., Slutsky, A. and Post, M., 2000. Mechanical strain and dexamethasone selectively increase surfactant protein C and tropoelastin gene expression. *American Journal of Physiology-Lung Cellular and Molecular Physiology*, *278*(5), pp.L974-L980.

34. Andrade, C.F., Wong, A.P., Waddell, T.K., Keshavjee, S. and Liu, M., 2007. Cell-based tissue engineering for lung regeneration. *American journal of physiology-lung cellular and molecular physiology*, *292*(2), pp.L510-L518.

35. Khattak, S.F., Bhatia, S.R. and Roberts, S.C., 2005. Pluronic F127 as a cell encapsulation material: utilization of membrane-stabilizing agents. *Tissue engineering*, *11*(5-6), pp.974-983.

36. Gioffredi, E., Boffito, M., Calzone, S., Giannitelli, S.M., Rainer, A., Trombetta, M., Mozetic, P. and Chiono, V., 2016. Pluronic F127 hydrogel characterization and biofabrication in cellularized constructs for tissue engineering applications. *Procedia CIRP*, *49*, pp.125-132.

37. Cortiella, J., Nichols, J.E., Kojima, K., Bonassar, L.J., Dargon, P., Roy, A.K., Vacant, M.P., Niles, J.A. and Vacanti, C.A., 2006. Tissue-engineered lung: an in vivo and in vitro comparison of polyglycolic acid and pluronic F-127 hydrogel/somatic lung progenitor cell constructs to support tissue growth. *Tissue engineering*, *12*(5), pp.1213-1225.

38. Gilding, D.K. and Reed, A.M., 1979. Biodegradable polymers for use in surgery—polyglycolic/poly (actic acid) homo-and copolymers: 1. *Polymer*, *20*(12), pp.1459-1464.

39. Giuliani, A., Moroncini, F., Mazzoni, S., Belicchi, M.L.C., Villa, C., Erratico, S., Colombo, E., Calcaterra, F., Brambilla, L., Torrente, Y. and Albertini, G., 2013. Polyglycolic acid–polylactic acid scaffold response to different progenitor cell in vitro cultures: a demonstrative and comparative X-ray synchrotron radiation phase-contrast microtomography study. *Tissue Engineering Part C: Methods*, *20*(4), pp.308-316.

40. Crapo, P.M., Gilbert, T.W. and Badylak, S.F., 2011. An overview of tissue and whole organ decellularization processes. *Biomaterials*, *32*(12), pp.3233-3243.

41. Lwebuga-Mukasa, J.S., Ingbar, D.H. and Madri, J.A., 1986. Repopulation of a human alveolar matrix by adult rat type II pneumocytes in vitro: a novel system for type II pneumocyte culture. *Experimental cell research*, *162*(2), pp.423-435.

42. Price, A.P., England, K.A., Matson, A.M., Blazar, B.R. and Panoskaltsis-Mortari, A., 2010. Development of a decellularized lung bioreactor system for bioengineering the lung: the matrix reloaded. *Tissue engineering Part A*, *16*(8), pp.2581-2591.

43. Ott, H.C., Clippinger, B., Conrad, C., Schuetz, C., Pomerantseva, I., Ikonomou, L., Kotton, D. and Vacanti, J.P., 2010. Regeneration and orthotopic transplantation of a bioartificial lung. *Nature medicine*, *16*(8), p.927.

44. Petersen, T.H., Calle, E.A., Zhao, L., Lee, E.J., Gui, L., Raredon, M.B., Gavrilov, K., Yi, T., Zhuang, Z.W., Breuer, C. and Herzog, E., 2010. Tissue-engineered lungs for in vivo implantation. *Science*, *329*(5991), pp.538-541.

45. Carey, L.E., Dearth, C.L., Johnson, S.A., Londono, R., Medberry, C.J., Daly, K.A. and Badylak, S.F., 2014. In vivo degradation of 14C-labeled porcine dermis biologic scaffold. *Biomaterials*, *35*(29), pp.8297-8304.

46. Frantz, C., Stewart, K.M. and Weaver, V.M., 2010. The extracellular matrix at a glance. *J Cell Sci*, *123*(24), pp.4195-4200.

47. Nichols, J.E., Niles, J.A. and Cortiella, J., 2012. Production and utilization of acellular lung scaffolds in tissue engineering. *Journal of cellular biochemistry*, *113*(7), pp.2185-2192.

48. Luque, T., Melo, E., Garreta, E., Cortiella, J., Nichols, J., Farré, R. and Navajas, D., 2013. Local micromechanical properties of decellularized lung scaffolds measured with atomic force microscopy. *Acta biomaterialia*, *9*(6), pp.6852-6859.

49. Van Den Berg, A., Craighead, H.G. and Yang, P., 2010. From microfluidic applications to nanofluidic phenomena. Chemical Society Reviews, 39(3), pp.899-900

50. Liu, Y. and Singh, A.K., 2013. Microfluidic platforms for single-cell protein analysis. *Journal of laboratory automation*, *18*(6), pp.446-454.

51. Delamarche, E., Tonna, N., Lovchik, R.D., Bianco, F. and Matteoli, M., 2013. Pharmacology on microfluidics: multimodal analysis for studying cell–cell interaction. *Current opinion in pharmacology*, *13*(5), pp.821-828

52. Ruiz, S.A. and Chen, C.S., 2007. Microcontact printing: A tool to pattern. *Soft Matter*, *3*(2), pp.168-177.

53. Sin, M.L., Gao, J., Liao, J.C. and Wong, P.K., 2011. System integration-A major step toward lab on a chip. *Journal of biological engineering*, *5*(1), p.6.

54. Ren, K., Chen, Y. and Wu, H., 2014. New materials for microfluidics in biology. *Current opinion in biotechnology*, *25*, pp.78-85.

55. Bhatia, S.N. and Ingber, D.E., 2014. Microfluidic organs-on-chips. *Nature biotechnology*, *32*(8), p.760.

56. Huh, D., Matthews, B.D., Mammoto, A., Montoya-Zavala, M., Hsin, H.Y. and Ingber, D.E., 2010. Reconstituting organ-level lung functions on a chip. *Science*, *328*(5986), pp.1662-1668.

57. Engineering an artificialalveolar-capillary membrane: a novel continuously perfused modelwithin microchannels.

58. Huh, D., Leslie, D.C., Matthews, B.D., Fraser, J.P., Jurek, S., Hamilton, G.A., Thorneloe, K.S., McAlexander, M.A. and Ingber, D.E., 2012. A human disease model of drug toxicity–induced pulmonary edema in a lung-on-a-chip microdevice. *Science translational medicine*, *4*(159), pp.159ra147-159ra147.

59. Higuita-Castro, N., Nelson, M.T., Shukla, V., Agudelo-Garcia, P.A., Zhang, W., Duarte-Sanmiguel, S.M., Englert, J.A., Lannutti, J.J., Hansford, D.J. and Ghadiali, S.N., 2017. Using a Novel Microfabricated Model of the Alveolar-Capillary Barrier to Investigate the Effect of Matrix Structure on Atelectrauma. *Scientific reports*, *7*(1), p.11623.
60. Stahlman, M.T., Gray, M.E. and Whitsett, J.A., 1996. Expression of thyroid transcription factor-1 (TTF-1) in fetal and neonatal human lung. *Journal of Histochemistry&Cytochemistry*, *44*(7), pp.673-678.

61. Stoner, G.D., Katoh, Y., Foidart, J.M., Trump, B.F., Steinert, P.M. and Harris, C.C., 1981. Cultured human bronchial epithelial cells: blood group antigens, keratin, collagens, and fibronectin. *In vitro*, *17*(7), pp.577-587.

62. Twort, C. and Van Breemen, C., 1988. Human airway smooth muscle in culture. *Tissue and Cell*, *20*(3), pp.339-344.

63. Cozens, A.L., Yezzi, M.J., Kunzelmann, K., Ohrui, T., Chin, L., Eng, K., Finkbeiner, W.E., Widdicombe, J.H. and Gruenert, D.C., 1994. CFTR expression and chloride secretion in polarized immortal human bronchial epithelial cells. *American journal of respiratory cell and molecular biology*, *10*(1), pp.38-47.

64. Fogh, J., Fogh, J.M. and Orfeo, T., 1977. One hundred and twenty-seven cultured human tumor cell lines producing tumors in nude mice. *Journal of the National Cancer Institute*, *59*(1), pp.221-226.

65. Bell, M.R., Meredith, D.J. and Gill, P.G., 1985. Role of carbon monoxide diffusing capacity in the early detection of major bleomcyin-induced pulmonary toxicity. *Internal Medicine Journal*, *15*(2), pp.235-240.

66. Giard, D.J., Aaronson, S.A., Todaro, G.J., Arnstein, P., Kersey, J.H., Dosik, H. and Parks, W.P., 1973. In vitro cultivation of human tumors: establishment of cell lines

derived from a series of solid tumors. *Journal of the National Cancer Institute*, *51*(5), pp.1417-1423.

67. Jaffe, E.A., Nachman, R.L., Becker, C.G. and Minick, C.R., 1973. Culture of human endothelial cells derived from umbilical veins. Identification by morphologic and immunologic criteria. *The Journal of clinical investigation*, *52*(11), pp.2745-2756.

68. Hewett, P.W. and Murray, J.C., 1993. Human microvessel endothelial cells: isolation, culture and characterization. *In Vitro Cellular&Developmental Biology-Animal*, *29*(11), pp.823-830.

69. Jacobs, J.P., Jones, C.M. and Baille, J.P., 1970. Characteristics of a human diploid cell designated MRC-5. *Nature*, *227*(5254), p.168.

70. Hayflick, L., 1965. The limited in vitro lifetime of human diploid cell strains. *Experimental cell research*, *37*(3), pp.614-636.

71. He, J.Q., Ma, Y., Lee, Y., Thomson, J.A. and Kamp, T.J., 2003. Human embryonic stem cells develop into multiple types of cardiac myocytes: action potential characterization. *Circulation research*, *93*(1), pp.32-39

72. Takahashi, K., Tanabe, K., Ohnuki, M., Narita, M., Ichisaka, T., Tomoda, K. and Yamanaka, S., 2007. Induction of pluripotent stem cells from adult human fibroblasts by defined factors. *cell*, *131*(5), pp.861-872.

73. Lwebuga-Mukasa, J.S., Ingbar, D.H. and Madri, J.A., 1986. Repopulation of a human alveolar matrix by adult rat type II pneumocytes in vitro: a novel system for type II pneumocyte culture. *Experimental cell research*, *162*(2), pp.423-435.

74. Sugihara, H., Toda, S., Miyabara, S., Fujiyama, C. and Yonemitsu, N., 1993. Reconstruction of alveolus-like structure from alveolar type II epithelial cells in three-dimensional collagen gel matrix culture. *The American journal of pathology*, *142*(3), p.783.

75. Chen, P., Marsilio, E., Goldstein, R.H., Yannas, I.V. and Spector, M., 2005. Formation of lung alveolar-like structures in collagen–glycosaminoglycan scaffolds in vitro. *Tissue engineering*, *11*(9-10), pp.1436-1448.

76. Choe, M.M., Tomei, A.A. and Swartz, M.A., 2006. Physiological 3D tissue model of the airway wall and mucosa. *Nature protocols*, *1*(1), p.357.

77. Mondrinos, M.J., Koutzaki, S., Jiwanmall, E., Li, M., Dechadarevian, J.P., Lelkes, P.I. and Finck, C.M., 2006. Engineering three-dimensional pulmonary tissue constructs. *Tissue engineering*, *12*(4), pp.717-728.

78. Mondrinos, M.J., Koutzaki, S., Lelkes, P.I. and Finck, C.M., 2007. A tissue-engineered model of fetal distal lung tissue. *American journal of physiology-lung cellular and molecular physiology*, *293*(3), pp.L639-L650.

79. Birkness, K.A., Guarner, J., Sable, S.B., Tripp, R.A., Kellar, K.L., Bartlett, J. and Quinn, F.D., 2007. An in vitro model of the leukocyte interactions associated with granuloma formation in Mycobacterium tuberculosis infection. *Immunology&Cell Biology*, *85*(2), pp.160-168.

80. Zani, B.G., Kojima, K., Vacanti, C.A. and Edelman, E.R., 2008. Tissue-engineered endothelial and epithelial implants differentially and synergistically regulate airway repair. *Proceedings of the National Academy of Sciences*, *105*(19), pp.7046-7051.

81. Miller, C., George, S. and Niklason, L., 2010. Developing a tissue-engineered model of the human bronchiole. *Journal of tissue engineering and regenerative medicine*, *4*(8), pp.619-627.

82. Hoang, A.T.N., Chen, P., Juarez, J., Sachamitr, P., Billing, B., Bosnjak, L., Dahlén, B., Coles, M. and Svensson, M., 2011. Dendritic cell functional properties in a three-dimensional tissue model of human lung mucosa. *American Journal of Physiology-Lung Cellular and Molecular Physiology*, *302*(2), pp.L226-L237.

83. Kloxin, A.M., Lewis, K.J., DeForest, C.A., Seedorf, G., Tibbitt, M.W., Balasubramaniam, V. and Anseth, K.S., 2012. Responsive culture platform to examine the influence of microenvironmental geometry on cell function in 3D. *Integrative Biology*, *4*(12), pp.1540-1549.

84. Patel, H. and Kwon, S., 2012. Multi-walled carbon nanotube-induced inflammatory response and oxidative stress in a dynamic cell growth environment. *Journal of biological engineering*, *6*(1), p.22

85. Booth, M.J., Branco, M.R., Ficz, G., Oxley, D., Krueger, F., Reik, W. and Balasubramanian, S., 2012. Quantitative sequencing of 5-methylcytosine and 5-hydroxymethylcytosine at single-base resolution. *Science*, *336*(6083), pp.934-937.

86. Daly, A.B., Wallis, J.M., Borg, Z.D., Bonvillain, R.W., Deng, B., Ballif, B.A., Jaworski, D.M., Allen, G.B. and Weiss, D.J., 2011. Initial binding and recellularization of decellularized mouse lung scaffolds with bone marrow-derived mesenchymal stromal cells. *Tissue Engineering Part A*, *18*(1-2), pp.1-16.

87. Horie, M., Saito, A., Mikami, Y., Ohshima, M., Morishita, Y., Nakajima, J., Kohyama, T. and Nagase, T., 2012. Characterization of human lung cancer-associated fibroblasts in three-dimensional in vitro co-culture model. *Biochemical and biophysical research communications*, *423*(1), pp.158-163.

88. Nichols, J.E., Niles, J., Riddle, M., Vargas, G., Schilagard, T., Ma, L., Edward, K., La Francesca, S., Sakamoto, J., Vega, S. and Ogadegbe, M., 2013. Production and assessment of decellularized pig and human lung scaffolds. *Tissue Engineering Part A*, *19*(17-18), pp.2045-2062

89. Nichols, J.E., La Francesca, S., Vega, S.P., Niles, J.A., Argueta, L.B., Riddle, M., Sakamoto, J., Vargas, G., Pal, R., Woodson, L. and Rhudy, J., 2017. Giving new life to old lungs: methods to produce and assess whole human paediatric bioengineered lungs. *Journal of tissue engineering and regenerative medicine*, *11*(7), pp.2136-2152.

90. Comhair, S.A., Xu, W., Mavrakis, L., Aldred, M.A., Asosingh, K. and Erzurum, S.C., 2012. Human primary lung endothelial cells in culture. *American journal of respiratory cell and molecular biology*, *46*(6), pp.723-730.

91. Wirz, S., Dietrich, M., Flanagan, T.C., Bokermann, G., Wagner, W., Schmitz-Rode, T. and Jockenhoevel, S., 2011. Influence of platelet-derived growth factor-AB on tissue development in autologous platelet-rich plasma gels. *Tissue Engineering Part A*, *17*(13-14), pp.1891-1899.

92. Sánchez-González, D.J., Méndez-Bolaina, E. and Trejo-Bahena, N.I., 2012. Platelet-rich plasma peptides: key for regeneration. *International journal of peptides*, *2012*.

93. Araki, J., Jona, M., Eto, H., Aoi, N., Kato, H., Suga, H., Doi, K., Yatomi, Y. and Yoshimura, K., 2011. Optimized preparation method of platelet-concentrated plasma and noncoagulating platelet-derived factor concentrates: maximization of platelet concentration and removal of fibrinogen. *Tissue Engineering Part C: Methods*, *18*(3), pp.176-185.

94. Alsousou, J., Ali, A., Willett, K. and Harrison, P., 2013. The role of platelet-rich plasma in tissue regeneration. *Platelets*, *24*(3), pp.173-182.

95. Thurston, G., Rudge, J.S., Ioffe, E., Zhou, H., Ross, L., Croll, S.D., Glazer, N., Holash, J., McDonald, D.M. and Yancopoulos, G.D., 2000. Angiopoietin-1 protects the adult vasculature against plasma leakage. *Nature medicine*, *6*(4), p.460.

96. Huang, Y.Q., Sauthoff, H., Herscovici, P., Pipiya, T., Cheng, J., Heitner, S., Szentirmai, O., Carter, B. and Hay, J.G., 2008. Angiopoietin-1 increases survival and reduces the development of lung edema induced by endotoxin administration in a murine model of acute lung injury. *Critical care medicine*, *36*(1), pp.262-267.

97. Umezawa, H., Ishizuka, M., Maeda, K. and Takeuchi, T., 1967. Studies on bleomycin. *Cancer*, *20*(5), pp.891-895.

98. Claussen, C.A. and Long, E.C., 1999. Nucleic acid recognition by metal complexes of bleomycin. *Chemical reviews*, *99*(9), pp.2797-2816.

99. Della Latta, Veronica, A. Cecchettini, S. Del Ry, and M. A. Morales. "Bleomycin in the setting of lung fibrosis induction: From biological mechanisms to counteractions." *Pharmacological research* 97 (2015): 122-130.

100. Hecht, S.M., 2000. Bleomycin: new perspectives on the mechanism of action. Journal of natural products, 63(1), pp.158-168.

101. Muggia, F.M., Louie, A.C. and Sikic, B.I., 1983. Pulmonary toxicity of antitumor agents. *Cancer treatment reviews*, *10*(4), pp.221-243.

102. Reinert, T., Baldotto, C.S.D.R., Nunes, F.A.P. and Scheliga, A.A.D.S., 2013. Bleomycin-induced lung injury. *Journal of Cancer Research, 2013*.

103. Brugge, S.S., Claasen, H.R. and Dawson, L., 2013. Drug induced lung injury-a case of fatal Bleomycin interstitial pneumonitis. *Netherlands J Critical Care*, *17*, pp.25-29.

104. Patil, N., Paulose, R.M., Udupa, K.S., Ramakrishna, N. and Ahmed, T., 2016. Pulmonary Toxicity of Bleomycin–A Case Series from a Tertiary Care Center in Southern India. *Journal of clinical and diagnostic research: JCDR*, *10*(4), p.FR01.

105. Ngan, H.Y., Liang, R.H., Lam, W.K. and Chan, T.K., 1993. Pulmonary toxicity in patients with non-Hodgkin's lymphoma treated with bleomycin-containing combination chemotherapy. *Cancer chemotherapy and pharmacology*, *32*(5), pp.407-409.

106. Nachman, J.B., Baum, E.S., White, H. and Cruissi, F.G., 1981. Bleomycin-induced pulmonary fibrosis mimicking recurrent metastatic disease in a patient with testicular carcinoma: Case report of the CT scan appearance. *Cancer*, *47*(2), pp.236-239.

107. Simpson, A.B., Paul, J., Graham, J. and Kaye, S.B., 1998. Fatal bleomycin pulmonary toxicity in the west of Scotland 1991-95: a review of patients with germ cell tumours. *British journal of cancer*, *78*(8), p.1061.

108. Keijzer, A. and Kuenen, B., 2007. Fatal pulmonary toxicity in testis cancer with bleomycin-containing chemotherapy. *Journal of clinical oncology*, *25*(23), pp.3543-3544.

109. Usman, M., Faruqui, Z.S., ud Din, N. and Zahid, K.F., 2010. Bleomycin induced pulmonary toxicity in patients with germ cell tumours. *Journal of Ayub Medical College Abbottabad*, *22*(3), pp.35-37.

110. Daphale, A., Acharya, S., Shukla, S. and Alegaonkar, S., 2017. Bleomycin Induced Acute Respiratory Distress Syndrome. *Journal of Case Reports*, *7*(1), pp.55-57.

111. Doi, M., Okamoto, Y., Yamauchi, M., Naitou, H. and Shinozaki, K., 2012. Bleomycin-induced pulmonary fibrosis after tumor lysis syndrome in a case of advanced yolk sac

tumor treated with bleomycin, etoposide and cisplatin (BEP) chemotherapy. *International Journal of Clinical Oncology*, *17*(5), pp.528-531.

112. Rodríguez, J.C., Morales, M.D.C.J. and Casero, M.A.R., 2016. Death by bleomycin pulmonary toxicity in ovarian dysgerminoma with pathologic complete response to chemotherapy. A case report. *Respiratory medicine case reports*, *18*, pp.48-50.

113. Einhorn, L.H. and Donohue, J., 1977. Cis-diamminedichloroplatinum, vinblastine, and bleomycin combination chemotherapy in disseminated testicular cancer. *Annals of internal medicine*, *87*(3), pp.293-298.

114. Sleijfer, S., 2001. Bleomycin-induced pneumonitis. *Chest*, *120*(2), pp.617-624.

115. O'sullivan, J.M., Huddart, R.A., Norman, A.R., Nicholls, J., Dearnaley, D.P. and Horwich, A., 2003. Predicting the risk of bleomycin lung toxicity in patients with germ-cell tumours. *Annals of Oncology*, *14*(1), pp.91-96.

116. Mulder, R.L., Thönissen, N.M., van der Pal, H.J., Bresser, P., Hanselaar, W., Koning, C.C., Oldenburger, F., Heij, H.A., Caron, H.N. and Kremer, L.C., 2011. Pulmonary function impairment measured by pulmonary function tests in long-term survivors of childhood cancer. *Thorax*, *66*(12), pp.1065-1071.

117. Patel, A.S., Lin, L., Geyer, A., Haspel, J.A., An, C.H., Cao, J., Rosas, I.O. and Morse, D., 2012. Autophagy in idiopathic pulmonary fibrosis. *PloS one*, *7*(7), p.e41394.

118. Comis, R.L., 1992, April. Bleomycin pulmonary toxicity: current status and future directions. In *Seminars in oncology* (Vol. 19, No. 2, pp. 64-70). Elsevier.

119. Rudders, R.A., 1973. Bleomycin: pulmonary toxicity. *Annals of internal medicine*, *78*(4), pp.616-618.

120. Sleijfer, S., 2001. Bleomycin-induced pneumonitis. *Chest*, *120*(2), pp.617-624.

121. Abid, S.H., Malhotra, V. and Perry, M.C., 2001. Radiation-induced and chemotherapy-induced pulmonary injury. *Current opinion in oncology*, *13*(4), pp.242-248.

122. Bellamy, E.A., Husband, J.E., Blaquiere, R.M. and Law, M.R., 1985. Bleomycin-related lung damage: CT evidence. *Radiology*, *156*(1), pp.155-158.

123. Comis, R.L., 1992, April. Bleomycin pulmonary toxicity: current status and future directions. In *Seminars in oncology* (Vol. 19, No. 2, pp. 64-70). Elsevier.

124. Arakawa, H. and Honma, K., 2011. Honeycomb lung: history and current concepts. *American Journal of Roentgenology*, *196*(4), pp.773-782.

125. Shippee, B.M., Bates, J.S. and Richards, K.L., 2016. The role of screening and monitoring for bleomycin pulmonary toxicity. *Journal of Oncology Pharmacy Practice*, *22*(2), pp.308-312.

126. White, D.A. and Stover, D.E., 1984. Severe bleomycin-induced pneumonitis: clinical features and response to corticosteroids. *Chest*, *86*(5), pp.723-728.

127. Martin, W.G., Ristow, K.M., Habermann, T.M., Colgan, J.P., Witzig, T.E. and Ansell, S.M., 2005. Bleomycin pulmonary toxicity has a negative impact on the outcome of patients with Hodgkin's lymphoma. *Journal of Clinical Oncology*, *23*(30), pp.7614-7620.

128. Sun, H., Atenafu, E.G., Tsang, R., Kukreti, V., Marras, T.K., Crump, M. and Kuruvilla, J., 2017. Bleomycin pulmonary toxicity does not adversely affect the outcome of patients with Hodgkin lymphoma. *Leukemia&lymphoma*, *58*(11), pp.2607-2614.

129. Moore, B.B. and Hogaboam, C.M., 2008. Murine models of pulmonary fibrosis. *American Journal of Physiology-Lung Cellular and Molecular Physiology*, *294*(2), pp.L152-L160.

130. Degryse, A.L., Tanjore, H., Xu, X.C., Polosukhin, V.V., Jones, B.R., McMahon, F.B., Gleaves, L.A., Blackwell, T.S. and Lawson, W.E., 2010. Repetitive intratracheal bleomycin models several features of idiopathic pulmonary fibrosis. *American Journal of Physiology-Lung Cellular and Molecular Physiology*, *299*(4), pp.L442-L452.

131. Degryse, A.L. and Lawson, W.E., 2011. Progress toward improving animal models for idiopathic pulmonary fibrosis. *The American journal of the medical sciences*, *341*(6), pp.444-449.

132. Raghu, G., Collard, H.R., Egan, J.J., Martinez, F.J., Behr, J., Brown, K.K., Colby, T.V., Cordier, J.F., Flaherty, K.R., Lasky, J.A. and Lynch, D.A., 2011. An official ATS/ERS/JRS/ALAT statement: idiopathic pulmonary fibrosis: evidence-based guidelines for diagnosis and management. *American journal of respiratory and critical care medicine*, *183*(6), pp.788-824.

133. Olson, A.L., Swigris, J.J., Lezotte, D.C., Norris, J.M., Wilson, C.G. and Brown, K.K., 2007. Mortality from pulmonary fibrosis increased in the United States from 1992 to 2003. *American journal of respiratory and critical care medicine*, *176*(3), pp.277-284.

134. Nadrous, H.F., Myers, J.L., Decker, P.A. and Ryu, J.H., 2005, January. Idiopathic pulmonary fibrosis in patients younger than 50 years. In *Mayo Clinic Proceedings* (Vol. 80, No. 1, pp. 37-40). Elsevier

135. Raghu, G., Weycker, D., Edelsberg, J., Bradford, W.Z. and Oster, G., 2006. Incidence and prevalence of idiopathic pulmonary fibrosis. *American journal of respiratory and critical care medicine*, *174*(7), pp.810-816.

136. Ley, B. and Collard, H.R., 2013. Epidemiology of idiopathic pulmonary fibrosis. *Clinical epidemiology*, *5*, p.483.

137. Idiopathic Pulmonary Fibrosis Clinical Research Network, 2012. Prednisone, azathioprine, and N-acetylcysteine for pulmonary fibrosis. *New England Journal of Medicine*, *366*(21), pp.1968-1977.

138. Coultas, D.B., Zumwalt, R.E., Black, W.C. and Sobonya, R.E., 1994. The epidemiology of interstitial lung diseases. *American journal of respiratory and critical care medicine*, *150*(4), pp.967-972.

139. Pérez, E.R.F., Daniels, C.E., Sauver, J.S., Hartman, T.E., Bartholmai, B.J., Eunhee, S.Y., Ryu, J.H. and Schroeder, D.R., 2010. Incidence, prevalence, and clinical course of idiopathic pulmonary fibrosis: a population-based study. *Chest*, *137*(1), pp.129-137.

140. Baumgartner, K.B., Samet, J.M., Stidley, C.A., Colby, T.V. and Waldron, J.A., 1997. Cigarette smoking: a risk factor for idiopathic pulmonary fibrosis. *American journal of respiratory and critical care medicine*, *155*(1), pp.242-248.

141. Miyake, Y., Sasaki, S., Yokoyama, T., Chida, K., Azuma, A., Suda, T., Kudoh, S., Sakamoto, N., Okamoto, K., Kobashi, G. and Washio, M., 2005. Occupational and environmental factors and idiopathic pulmonary fibrosis in Japan. *Annals of Occupational Hygiene*, *49*(3), pp.259-265.

142. Stewart, J.P., Egan, J.J., Ross, A.J., Kelly, B.G., Lok, S.S., Hasleton, P.S. and Woodcock, A.A., 1999. The detection of Epstein-Barr virus DNA in lung tissue from patients with idiopathic pulmonary fibrosis. *American journal of respiratory and critical care medicine*, *159*(4), pp.1336-1341.

143. Tsukamoto, K., Hayakawa, H., Sato, A., Chida, K., Nakamura, H. and Miura, K., 2000. Involvement of Epstein-Barr virus latent membrane protein 1 in disease progression in patients with idiopathic pulmonary fibrosis. *Thorax*, *55*(11), pp.958-961.

144. Lok, S.S., Stewart, J.P., Kelly, B.G., Hasleton, P.S. and Egan, J.J., 2001. Epstein–Barr virus and wild p53 in idiopathic pulmonary fibrosis. *Respiratory medicine*, *95*(10), pp.787-791.

145. Kelly, B.G., Lok, S.S., Hasleton, P.S., Egan, J.J. and Stewart, J.P., 2002. A rearranged form of Epstein–Barr virus DNA is associated with idiopathic pulmonary fibrosis. *American journal of respiratory and critical care medicine*, *166*(4), pp.510-513.

146. Ueda, T., Ohta, K., Suzuki, N., Yamaguchi, M., Hirai, K., Horiuchi, T., Watanabe, J., Miyamoto, T. and Ito, K., 1992. Idiopathic Pulmonary Fibrosis and High Prevalence of Serum Antibodies to Hepatitis C Virus1• 2. *Am Rev Respir Dis*, *1*(148), pp.268-268.

147. Irving, W.L., Day, S. and Johnston, I., 1993. Virus Infertion. *Am Rev Respir Dis*, *148*, pp.1683-1684.

148. Meliconi, R., Andreone, P., Fasano, L., Galli, S., Pacilli, A., Miniero, R., Fabbri, M., Solforosi, L. and Bernardi, M., 1996. Incidence of hepatitis C virus infection in Italian patients with idiopathic pulmonary fibrosis. *Thorax*, *51*(3), pp.315-317.

149. Laraya-Cuasay, L.R., DeForest, A., Huff, D., Lischner, H. and Huang, N.N., 1977. Chronic pulmonary complications of early influenza virus infection in children. *American Review of Respiratory Disease*, *116*(4), pp.617-625.

150. Ortiz, J.R., Neuzil, K.M., Victor, J.C., Wald, A., Aitken, M.L. and Goss, C.H., 2010. Influenza-associated cystic fibrosis pulmonary exacerbations. *Chest*, *137*(4), pp.852-860.

151. Singh, N., Singh, S., Sharma, B.B. and Singh, V., 2016. Swine flu fibrosis: Regressive or progressive?. *Lung India: official organ of Indian Chest Society*, *33*(2), p.219.

152. Keyvani, H., Moghoofei, M., Bokharaei-Salim, F., Mostafaei, S., Mousavi, S.A.J., Monavari, S.H. and Esghaei, M., 2017. Prevalence of respiratory viruses in Iranian patients with idiopathic pulmonary fibrosis. *Journal of medical microbiology*, *66*(11), pp.1602-1606.

153. García-Sancho, C., Buendía-Roldán, I., Fernández-Plata, M.R., Navarro, C., Pérez-Padilla, R., Vargas, M.H., Loyd, J.E. and Selman, M., 2011. Familial pulmonary fibrosis is the strongest risk factor for idiopathic pulmonary fibrosis. *Respiratory medicine*, *105*(12), pp.1902-1907.

154. Ley, B., Collard, H.R. and King Jr, T.E., 2011. Clinical course and prediction of survival in idiopathic pulmonary fibrosis. *American journal of respiratory and critical care medicine*, *183*(4), pp.431-440.

155. Selman, M., Carrillo, G., Estrada, A., Mejia, M., Becerril, C., Cisneros, J., Gaxiola, M., Pérez-Padilla, R., Navarro, C., Richards, T. and Dauber, J., 2007. Accelerated variant of idiopathic pulmonary fibrosis: clinical behavior and gene expression pattern. *PloS one*, *2*(5), p.e482.

156. Boon, K., Bailey, N.W., Yang, J., Steel, M.P., Groshong, S., Kervitsky, D., Brown, K.K., Schwarz, M.I. and Schwartz, D.A., 2009. Molecular phenotypes distinguish patients with relatively stable from progressive idiopathic pulmonary fibrosis (IPF). *PloS one*, *4*(4), p.e5134.

157. Balestro, E., Calabrese, F., Turato, G., Lunardi, F., Bazzan, E., Marulli, G., Biondini, D., Rossi, E., Sanduzzi, A., Rea, F. and Rigobello, C., 2016. Immune inflammation and disease progression in idiopathic pulmonary fibrosis. *PloS one*, *11*(5), p.e0154516.

158. Nagase, H., Visse, R. and Murphy, G., 2006. Structure and function of matrix metalloproteinases and TIMPs. *Cardiovascular research*, *69*(3), pp.562-573.

159. Selman, M., Ruiz, V., Cabrera, S., Segura, L., Ramírez, R., Barrios, R. and Pardo, A., 2000. TIMP-1,-2,-3, and-4 in idiopathic pulmonary fibrosis. A prevailing nondegradative lung microenvironment?. *American Journal of Physiology-Lung Cellular and Molecular Physiology*, *279*(3), pp.L562-L574.

160. Cosgrove, G.P., Schwarz, M.I., Geraci, M.W., Brown, K.K. and Worthen, G.S., 2002. Overexpression of matrix metalloproteinase-7 in pulmonary fibrosis. *Chest*, *121*(3), pp.25S-26S.

161. Zuo, F., Kaminski, N., Eugui, E., Allard, J., Yakhini, Z., Ben-Dor, A., Lollini, L., Morris, D., Kim, Y., DeLustro, B. and Sheppard, D., 2002. Gene expression analysis reveals matrilysin as a key regulator of pulmonary fibrosis in mice and humans. *Proceedings of the National Academy of Sciences*, *99*(9), pp.6292-6297.

162. Huh, J.W., Kim, D.S., Oh, Y.M., Shim, T.S., Lim, C.M., Do Lee, S., Koh, Y., Kim, W.S., Kim, W.D. and Kim, K.R., 2008. Is metalloproteinase-7 specific for idiopathic pulmonary fibrosis?. *Chest*, *133*(5), pp.1101-1106

163. Rosas, I.O., Richards, T.J., Konishi, K., Zhang, Y., Gibson, K., Lokshin, A.E., Lindell, K.O., Cisneros, J., MacDonald, S.D., Pardo, A. and Sciurba, F., 2008. MMP1 and MMP7 as potential peripheral blood biomarkers in idiopathic pulmonary fibrosis. *PLoS medicine*, *5*(4), p.e93.

164. Beeh, K.M., Beier, J., Kornmann, O. and Buhl, R., 2003. Sputum matrix metalloproteinase-9, tissue inhibitor of metalloprotinease-1, and their molar ratio in patients with chronic obstructive pulmonary disease, idiopathic pulmonary fibrosis and healthy subjects. *Respiratory medicine*, *97*(6), pp.634-639.

165. Yokoyama, A., Kondo, K., Nakajima, M., Matsushima, T., Takahashi, T., Nishimura, M., Bando, M., Sugiyama, Y., Totani, Y., Ishizaki, T. and Ichiyasu, H., 2006. Prognostic value of circulating KL-6 in idiopathic pulmonary fibrosis. *Respirology*, *11*(2), pp.164-168.

166. Hirasawa, Y., Kohno, N., Yokoyama, A., Inoue, Y., Abe, M. and Hiwada, K., 1997. KL-6, a human MUC1 mucin, is chemotactic for human fibroblasts. *American journal of respiratory cell and molecular biology*, *17*(4), pp.501-507.

167. Greene, K.E., King, T.E., Kuroki, Y., Bucher-Bartelson, B., Hunninghake, G.W., Newman, L.S., Nagae, H. and Mason, R.J., 2002. Serum surfactant proteins-A and-D as

biomarkers in idiopathic pulmonary fibrosis. *European Respiratory Journal*, *19*(3), pp.439-446.

168. Ohnishi, H., Yokoyama, A., Kondo, K., Hamada, H., Abe, M., Nishimura, K., Hiwada, K. and Kohno, N., 2002. Comparative study of KL-6, surfactant protein-A, surfactant protein-D, and monocyte chemoattractant protein-1 as serum markers for interstitial lung diseases. *American journal of respiratory and critical care medicine*, *165*(3), pp.378-381.

169. Ishii, H., Mukae, H., Kadota, J., Kaida, H., Nagata, T., Abe, K., Matsukura, S. and Kohno, S., 2003. High serum concentrations of surfactant protein A in usual interstitial pneumonia compared with non-specific interstitial pneumonia. *Thorax*, *58*(1), pp.52-57.

170. McCormack, F.X., King Jr, T.E., Voelker, D.R., Robinson, P.C. and Mason, R.J., 1991. Idiopathic pulmonary fibrosis: abnormalities in the bronchoalveolar lavage content of surfactant protein A. *American Review of Respiratory Disease*, *144*(1), pp.160-166.

171. Barlo, N.P., van Moorsel, C.H.M. and Ruven, H.J.T., 2009. Surfactant protein-D predicts survival in patients with idiopathic pulmonary fibrosis. *Sarcoidosis vasculitis and diffuse lung disease*, *26*(2), pp.155-161.

172. Stahl, M., Schupp, J., Jäger, B., Schmid, M., Zissel, G., Müller-Quernheim, J. and Prasse, A., 2013. Lung collagens perpetuate pulmonary fibrosis via CD204 and M2 macrophage activation. *PloS one*, *8*(11), p.e81382.

173. Pechkovsky, D.V., Prasse, A., Kollert, F., Engel, K.M., Dentler, J., Luttmann, W., Friedrich, K., Müller-Quernheim, J. and Zissel, G., 2010. Alternatively activated alveolar macrophages in pulmonary fibrosis—mediator production and intracellular signal transduction. *Clinical immunology*, *137*(1), pp.89-101.

174. Vij, R. and Noth, I., 2012. Peripheral blood biomarkers in idiopathic pulmonary fibrosis. *Translational Research*, *159*(4), pp.218-227.

175. Selman, M., King, T.E. and Pardo, A., 2001. Idiopathic pulmonary fibrosis: prevailing and evolving hypotheses about its pathogenesis and implications for therapy. *Annals of internal medicine*, *134*(2), pp.136-151.

176. Gauldie, J., Kolb, M. and Sime, P.J., 2001. A new direction in the pathogenesis of idiopathic pulmonary fibrosis?. *Respiratory research*, *3*(1), p.1.

177. Ueda, T., Ohta, K., Suzuki, N., Yamaguchi, M., Hirai, K., Horiuchi, T., Watanabe, J., Miyamoto, T. and Ito, K., 1992. Idiopathic Pulmonary Fibrosis and High Prevalence of Serum Antibodies to Hepatitis C Virus1• 2. *Am Rev Respir Dis*, *1*(148), pp.268-268.

178. Mapel, D.W., Samet, J.M. and Coultas, D.B., 1996. Corticosteroids and the treatment of idiopathic pulmonary fibrosis: past, present, and future. *Chest*, *110*(4), pp.1058-1067.

179. Douglas, W.W., Ryu, J.H. and Schroeder, D.R., 2000. Idiopathic pulmonary fibrosis: impact of oxygen and colchicine, prednisone, or no therapy on survival. *American journal of respiratory and critical care medicine*, *161*(4), pp.1172-1178.

180. Grijm, K., Verberne, H.J., Krouwels, F.H., Weller, F.R., Jansen, H.M. and Bresser, P., 2005. Semiquantitative 67Ga scintigraphy as an indicator of response to and prognosis after corticosteroid treatment in idiopathic interstitial pneumonia. *Journal of Nuclear Medicine*, *46*(9), pp.1421-1426.

181. Raghu, G., Brown, K.K., Bradford, W.Z., Starko, K., Noble, P.W., Schwartz, D.A. and King Jr, T.E., 2004. A placebo-controlled trial of interferon gamma-1b in patients with idiopathic pulmonary fibrosis. *New England Journal of Medicine*, *350*(2), pp.125-133.

182. Raghu, G., Collard, H.R., Anstrom, K.J., Flaherty, K.R., Fleming, T.R., King Jr, T.E., Martinez, F.J. and Brown, K.K., 2012. Idiopathic pulmonary fibrosis: clinically meaningful primary endpoints in phase 3 clinical trials. *American journal of respiratory and critical care medicine*, *185*(10), pp.1044-1048.

183. Papiris, S.A., Kagouridis, K., Kolilekas, L., Papaioannou, A.I., Roussou, A., Triantafillidou, C., Baou, K., Malagari, K., Argentos, S., Kotanidou, A. and Karakatsani, A., 2015. Survival in Idiopathic pulmonary fibrosis acute exacerbations: the non-steroid approach. *BMC pulmonary medicine*, *15*(1), p.162.

184. Wolters, P.J., Collard, H.R. and Jones, K.D., 2014. Pathogenesis of idiopathic pulmonary fibrosis. *Annual Review of Pathology: Mechanisms of Disease*, *9*, pp.157-179.

Curriculum Vitae

NAME: Stephanie P. Vega, Ph.D.

PRESENT POSITION: Ph.D., Microbiology & Immunology Graduate Program
Graduate School of Biomedical Sciences
University of Texas Medical Branch
301 University Boulevard, Galveston, Texas 77555-1070
Telephone: (409) 772-0367
Email: spvega@utmb.edu

BIOGRAPHICAL: Birthplace: Brownsville, Texas
Languages: English and Spanish

EDUCATION:

University of Texas at Brownsville (UTB) Brownsville, Texas	B.S.	May 2010	Biology
University of Texas Medical Branch (UTMB) Galveston, Texas	Ph.D.	August 2018	Microbiology & Immunology

A. PROFESSIONAL AND TEACHING EXPERIENCE:

Professional Experience:

2011 – 2018	PhD Candidate, Microbiology & Immunology Graduate Program, UTMB
2010 – 2011	Scholar, NIH-Funded Post baccalaureate Research Education Program (PREP), UTMB
2009 – 2010	Scholar, NIH-Funded Minority Biomedical Research Support, Research Initiative for Scientific Enhancement (MBRS RISE) Program, UTB

Technical Skills and Experience

- Decellularization procedures - production of acellular human, porcine and rodent organ scaffolds
- Cell culture - primary cell isolations, adult and embryonic stem cell growth and expansion, characterization of cell populations, immortalization of primary cells, isolation of peripheral blood mononuclear cells, installation procedures for recellularization of scaffolds

- Recellularization and development of tissue-engineered human lung constructs
- Experience in the use, assessment and maintenance of whole-organ perfusion bioreactors and small rotary bioreactors for use in the production of organ scaffolds
- Immunofluorescence staining, immunohistochemistry, immunocytochemistry, fluorescent microscopy, basic histology, tissue sectioning, flow cytometry, immunological assays and immunoprecipitation
- BSL-3 laboratory training for experiments involving the exposure and infection of human lung models to respiratory pathogens such as Influenza A virus.

Training and Supervision of High School, Undergraduate, Medical and Graduate Students:

2016 – 2017	Paulina Horton, PREP student, University of Texas Medical Branch
2015 – 2016	Daniil Weaver, High School Student, Ball High School
2015 – 2016	Maria Grimaldo, High School Student, Clear Lake High School
2014 – 2016	Jeffrey Michael Smith, Medical Student, University of Texas Medical Branch
2015	David Brown, Medical Student, University of Texas Medical Branch
2013 – 2016	Adriene Eastaway, Medical Student, University of Texas Medical Branch
2013 – 2014	Lissenya B. Argueta, PREP student, University of Texas Medical Branch
2012 - 2013	Marie Martins, PREP student, University of Texas Medical Branch
2012	Emy Usheva, High School Student, Clear Springs High School
2012	Kevin Cyr, High School Student, Clear Lake High School

B. AREA OF RESEARCH:

- *In vitro* tissue-engineering of three-dimensional human lung model systems as experimental tools to study pathogenesis of chronic lung disease, respiratory infections caused by influenza virus, for toxicology studies or for screening of drug therapies with potential for clinical applications.
- Pathogenesis of pulmonary fibrosis induced by xenobiotic agents or respiratory viruses (influenza A) – involvement of macrophage subsets (M1 and M2) and other innate immune cells in chronic inflammation or regulation of pro-fibrotic microenvironments and tissue remodeling in the formation of fibrotic lung tissue.
- Development of stem cell therapies and examination of pro-inflammatory and regulatory immune responses in nervous system injuries such as traumatic brain injury.

C. COMMITTEE RESPONSIBILITIES:

Departmental

2013 – 2016	Student Representative, Curriculum Committee, Microbiology & Immunology Graduate Program, UTMB

UTMB

2015 – Present	Student Representative for the Graduate School of Biomedical Sciences, Student Fee Advisory Committee, UTMB
2014 – Present	Student Representative for the Graduate School of Biomedical Sciences, Professionalism Committee, UTMB

D. ACTIVITIES AND PROFESSIONAL MEMBERSHIPS:

2018 – Present	Member, American Association for the Advancement of Science (AAAS)
2018 – Present	Scholar, National Society of Leadership and Success
2015 – Present	Scholar, Interprofessional Scholars Program, UTMB
2016	Galveston National Lab High School Outreach Program, UTMB
2015 – 2016	High School Student Mentor, Biomedical Research Training for High School Students Training Program, UTMB
2014 – 2016	Vice President, Microbiology & Immunology Student Organization (MISO), Department of Microbiology & Immunology, UTMB
2014	Student Speaker, Community of Scholars, Graduate School of Biomedical Sciences, UTMB
2012 – Present	Peer Mentor, Post baccalaureate Research Education Program (PREP), UTMB
2011 – 2013	Member, American Association of Microbiology
2009 – 2011	Student Member, Society for Advancement of Hispanics/Chicanos and Native Americans in Science (SACNAS)

E. HONORS AND AWARDS:

2018-present	Scholar, National Society of Leadership and Success
2017	Recipient, Robert Shope PhD Endowed Scholarship
2016	Recipient, Robert Shope PhD Endowed Scholarship
2016	Recipient, Who's Who among Students in American Universities and Colleges
2015	Recipient, James E. Beall II Memorial Scholarship
2015	Travel Award Recipient, Best Poster Presentation for Microbiology & Immunology National Student Research Forum
2015	Recipient, Edith and Robert Zinn Presidential Scholarship
2014	Recipient, Edith and Robert Zinn Presidential Scholarship
2014	Travel award recipient, 8th Symposium on Biologic Scaffolds for Regenerative Medicine
2009 – 2010	Recipient, TSC Trustee Scholarship
2009 – 2010	Recipient, Pell Grant
2011	Molecular Biophysics Educational Tract Award for Research Excellence, Summer Undergraduate Research Program Poster Presentation

F. COMMUNITY SERVICE AND VOLUNTEER ACTIVITIES

2016	Judge, Galveston County Science and Engineering Fair
2011	Volunteer, Frontera de Salud, UTMB
2011	Volunteer, D'Feet Breast Cancer Race, Galveston, Texas
2009 – 2010	Volunteer, The World Birding Center, Resaca de La Palma State Park, Brownsville Texas

G. BIBLIOGRAPHY

Abstracts:

1. **Stephanie P. Vega**, Jean A. Niles, Joaquin Cortiella, Joan E. Nichols. Immune Modulatory Potential of Human Stem Cell Populations as a Therapeutic Strategy for Traumatic Brain Injury. 27TH Annual Keck Center Research Conference and Poster Session: Innovations in Interdisciplinary Neuroscience. 2017. Houston, Texas.

2. **Stephanie P. Vega**, Jean A. Niles, Joaquin Cortiella, Joan E. Nichols. Development of a 3D Tissue-Engineered Human Lung Model to Study Pathogenesis of Lung Disease. National Student Research Forum. 2017. Galveston, Texas.

3. **Stephanie P. Vega**, Jean A. Niles, Joaquin Cortiella, Joan E. Nichols. A Large Animal Model for Transplanting Bioengineered Lungs. Biomedical Research Awareness Day. 2016. UTMB, Galveston, Texas.

4. **Stephanie P. Vega**, Jean A. Niles, Joaquin Cortiella, Joan E. Nichols. Immune Modulatory Potential of Human Stem Cell Populations as a Therapeutic Strategy for Traumatic Brain Injury. Moody Project TBI Symposium. 2016. Galveston, Texas

5. Oluwarotimi Folorunso, **Stephanie P. Vega**, Kara Michaelsen, Madiha Merchant, Sheryar Khan. Interprofessional Collaborative Team Needed to Treat COPD Effectively. Professionalism Summit. 2016. Galveston Texas

6. **Stephanie P. Vega**, Jean A. Niles, Joaquin Cortiella, Joan E. Nichols. Production and Assessment of Bioengineered Human Pediatric Lungs. National Student Research Forum. 2016. Galveston, Texas

7. **Stephanie P. Vega**, Jean A. Niles, Joaquin Cortiella, Joan E. Nichols. Tissue Engineered Human Lung Models to Study Pathogenesis of Lung Disease. National Student Research Forum. 2015. Galveston, Texas

8. **Stephanie P. Vega**, Jean A. Niles, Joaquin Cortiella, Joan E. Nichols. Development of Human Lung Model to Study Pathogenesis of Lung Disease. McLaughlin Colloquium on Infection and Immunity. 2015. Galveston, Texas

9. **Stephanie P. Vega,** Jean A. Niles, Joaquin Cortiella, Joan E. Nichols. Tissue-Engineered Human Lungs. Gulf Coast Consortium for Regenerative Medicine Symposium. 2014. Houston Texas

10. **Stephanie P. Vega**, Lissenya B. Argueta, Adriene C. Eastaway, Jean A. Niles, Joaquin Cortiella and Joan E. Nichols. Tissue Engineered Human Lung Model System. Clinical and Translational Research Forum. 2014. Galveston, Texas

11. **Stephanie P. Vega**, David Briley. Translational Science Research. Professionalism Summit. 2014. Galveston Texas

12. **Stephanie P. Vega**, Lissenya B. Argueta, Adriene C. Eastaway, Joaquin Cortiella, Joan E. Nichols. Tissue-Engineered Human Lungs: Cellular and Immune Responses to

Natural Acellular Scaffolds. Biologic Scaffolds for Regenerative Medicine 8th Symposium. 2014. Napa Valley, California

13. **Stephanie P. Vega**, Jean A. Niles, Lissenya B. Argueta, Joaquin Cortiella, Joan E. Nichols. Evaluation of the Human Immune Response to Natural Acellular Lung Scaffolds. McLaughlin Colloquium on Infection and Immunity. 2014. Galveston, Texas

14. **Stephanie P. Vega**, Jean A. Niles, Joaquin Cortiella, Joan E. Nichols. Use of a 3D Tissue Engineered (TE) Human Lung Model To Study The Role of M1 and M2 cells in Pulmonary Fibrosis Development. McLaughlin Colloquium on Infection and Immunity. 2013. Galveston Texas

15. **Stephanie P. Vega**, Jean A. Niles, Joaquin Cortiella, Joan E. Nichols. Production of Engineered Lung. Summer Undergraduate Research Program Poster Presentations. 2011. Galveston, Texas

Oral Presentations:

1. **Stephanie P. Vega**, Jean A. Niles, Joaquin Cortiella, Joan E. Nichols. Development of a 3D Tissue-Engineered Human Lung Model to Study Pathogenesis of Lung Disease. National Student Research Forum. 2017. Galveston, Texas.

2. **Stephanie P. Vega**, Jean A. Niles, Joaquin Cortiella, Joan E. Nichols. Immune Modulatory Potential of Human Stem Cell Populations as a Therapeutic Strategy for Traumatic Brain Injury. Moody Project TBI Symposium. 2016. Galveston, Texas

3. **Stephanie P. Vega**, Joan E. Nichols. Tissue-Engineered Human Lungs. Galveston National Lab High School Outreach Program. UTMB. 2016. Galveston, Texas

4. **Stephanie P. Vega**, Jean A. Niles, Joaquin Cortiella, Joan E. Nichols. Production and Assessment of Bioengineered Human Pediatric Lungs. National Student Research Forum. 2016. Galveston, Texas

5. **Stephanie P. Vega**. Survival Tips for Graduate Students. Community of Scholars, Graduate School of Biomedical Sciences, UTMB. 2014. Galveston, Texas

6. **Stephanie P. Vega**. Development of Tissue-Engineered Human Lung Model to Study Pathogenesis of Lung Disease. Student Research Update Seminar, Department of Microbiology & Immunology, UTMB. 2012 -2017. Galveston, Texas

Publications:

Peer-reviewed Journals

1. **Vega SP**. Nichols JE, Niles JA, Cortiella J. Development and Utilization of a 3D Bioengieered Human Lung Model to Study Pathogenesis of Lung Disase. Preparing manuscript for publication.

2. Nichols, J.E., La Francesca, S., Niles, J.A., **Vega, S.P.**, Argueta, L.B., Frank, L., Christiani, D.C., Pyles, R.B., Himes, B.E., Zhang, R. and Li, S., 2018. Production and transplantation of bioengineered lung into a large-animal model. *Science translational medicine*, *10*(452), p.eaao3926.

3. Nihcols JE, La Francesca S, Niles JA, **Vega SP**, Argueta LB, Frank L, Christiani DC, Pyles R, Hynes B, Zhang R, Miller A, Sakamoto J, Rhudy J, Hendricks G, Begarani F, Liu X, Vargas G, Pal R, Wacher A, Usheva E, Patrikeev I, Woodson L, Grimaldo M, Weaver D, Mlcak R, Cortiella J. The Next Step in the Production of Bioengineered Lungs for Clinical Application: Transplantation of Bioengineered Lung into a Large Animal Model. Science Translational Medicine. Sent for review.

4. Nichols JE, La Francesca S, **Vega SP**, Niles JA, Argueta LB, Riddle M, Sakamoto J, Vargas G, Pal R, Woodson L, Lee D, Seanor D, Campbell G, Schnadig V, Rhudy J, Cortiella J. Giving New Life to Old Lungs; Methods to Produce and Assess Whole Human Pediatric Bioengineered Lungs. *J Tissue Eng* Regen Med. 2016.

5. Nichols JE, Niles JA, **Vega SP**, Argueta LB, Eastaway A, Cortiella J. Modeling the lung: Design and development of tissue engineered macro- and micro-physiologic lung models for research use. *Exp Biol Med*. 2014 Sep;239(9):1135-69

6. Nichols JE, Niles JA, **Vega SP**, Cortiella J. Novel in vitro respiratory models to study lung development, physiology, pathology and toxicology. *Stem Cell Res Ther*. 2013;4 Suppl 1:S7

7. Nichols JE, Niles J, Riddle M, Vargas G, Schilagard T, Ma L, Edward K, La Francesca S, Sakamoto J, **Vega S**, Ogadegbe M, Mlcak R, Deyo D, Woodson L, McQuitty C, Lick S, Beckles D, Melo E, Cortiella J. Production and assessment of decellularized pig and human lung scaffolds. *Tissue Eng Part A*. 2013 Sep;19(17-18):2045-62

8. Nichols JE, Niles JA, DeWitt D, Prough D, Parsley M, **Vega S**, Cantu A, Lee E, Cortiella J. Neurogenic and neuro-protective potential of a novel subpopulation of peripheral blood-derived CD133+ ABCG2+CXCR4+ mesenchymal stem cells: development of autologous cell-based therapeutics for traumatic brain injury. *Stem Cell Res Ther.* 2013 Jan 6;4(1):3

Book Chapters:

1. Nichols JE, **Vega SP**, Argueta LB, Niles JA, Smith JM, Eastaway A, Cortiella J. " From 2D Culture to 3D Microchip Models: Trachea, Bronchi/Bronchiole and Lung Biomimetic Models for Disease Modeling, Drug Discovery and Personalized Medicine." *Regenerative Medicine Technology: On-a-chip Applications for Disease Modeling, Drug Discovery and Personalized Medicine.* CRC Press. Florida, Boca Raton. 2016.

2. Cortiella J, Niles JA, **Vega SP**, Eastaway A, Cortiella J. Applications of Hydrogels in Lung Regenerative Medicine. "Use of Hydrogels in the Engineering of Lung Tissue." *Gels Handbook*: *Fundamentals, Properties, Applications*. World Scientific Publishing Company. Hackensack, NJ. 2015. Print

H. REFERENCES:

Available upon request